QUENCH - SAFEST: Scientific Report NUSAFE 3574

Results of the bundle test QUENCH-19 with FeCrAl claddings

J. Stuckert, M. Große, M. Steinbrück

Karlsruher Institut für Technologie

Karlsruher Institut für Technologie

in der Helmholtz-Gemeinschaft

Wissenschaftliche Berichte

NUSAFE 3574

Results of the bundle test QUENCH-19 with FeCrAl claddings

J. Stuckert, M. Große, M. Steinbrück

Institut für Angewandte Materialien:
Angewandte Werkstoffphysik (IAM-AWP)

Programm Nukleare Sicherheitsforschung

Karlsruher Institut für Technologie

2022

DOI : 10.5445/IR/1000148370

Impressum

Karlsruher Institut für Technologie (KIT)
Institut für Angewandte Materialien
Angewandte Werkstoffphysik IAM-AWP-KOR
Nukleare Sicherheitsforschung
Hermann-von-Helmholtz-Platz 1
76344 Eggenstein-Leopoldshafen
www.iam.kit.edu/awp/666.php

Abstract

The QUENCH-19 bundle experiment was the worldwide first bundle test simulating severe accident conditions with ATF cladding materials. It was conducted with FeCrAl(Y) cladding tubes (alloy B136Y3, developed by the Oak Ridge National Lab, USA) and 4 Kanthal AF spacer grids as well as 7 Kanthal APM corner rods and Kanthal APM shroud was conducted at KIT on 29th August 2018. All Kanthal materials used are made of FeCrAl alloys too. The test objective was the comparison of FeCrAl(Y) and ZIRLO™ claddings under similar electrical power and gas flow conditions. The experiment was performed in four stages. The electrical power supply was the same as in the reference test QUENCH-15 (ZIRLO) during the first two stages (pre-oxidation and transient). The third stage with constant electrical power was performed to extend the temperature increase period. The test was terminated at peak cladding temperature of about 1800 K by water flooding similar to QUENCH-15 (stage four).

As expected, the hydrogen release during this test with FeCrAl cladding was significantly lower than for the reference test QUENCH-15 with ZIRLO cladding tubes. The total hydrogen production was 9.2 g (47.6 g for QUENCH-15), even the test duration at maximum power input was 2000 s longer. The post-test observation of the bundle showed the damage of several claddings at the bundle elevations between 850 and 1000 mm. The claddings failed either due to interaction with melted thermocouples (mostly) or by spalling of small annular cladding parts. Furthermore, unexpectedly some rods circumferentially broke most probably during reflood due the larger coefficients of thermal expansion of FeCrAl compared to Zr alloys.

Contents

List of Tables

List of Figures

Introduction

The main goal of the QUENCH program at KIT is to investigate the core thermal response, the cladding oxidation with accompanying hydrogen release and the cooling efficacy of water injection under design basis (DBA) and beyond design basis (BDBA) accident conditions. The program was initiated in 1996 and is still on-going [1], [2], [3]. Nineteen high temperature bundle tests were performed so far under severe accident conditions (Table 1). Bundle experiments as well as separate-effects tests are conducted to provide data for the development of models and the validation of severe fuel damage code systems.

The severe accident test QUENCH-19 was the worldwide first large-scale bundle test with ATF cladding. It was conducted with FeCrAl(Y) claddings (alloy B136Y3) in cooperation with the Oak Ridge National Laboratory (ORNL), USA. The QUENCH-15 bundle test with ZIRLO claddings was used as the reference test with similar bundle geometry and equal electric power injection during the pre-oxidation and power transient stages [4], [5].

1 Test facility

The main component of the QUENCH test facility is the test section with the test bundle (Figure 1…Figure 4). The test rods were arranged within the QUENCH-19 bundle as shown in the schematic cross section of Figure 5. The facility can be operated in two modes: (a) a forced-convection mode and (b) a boil-off mode with the steam inlet line closed. QUENCH-19 was conducted in forced-convection mode, in which superheated steam from the steam generator and super-heater together with argon as a carrier gas for off-gas measurements enter the test bundle at the bottom. The system pressure in the test section is usually around 0.2 MPa absolute.

The design characteristics of the QUENCH-19 bundle are presented in Table 2. The chemical compositions of used FeCrAl materials and comparison of physical properties of FeCrAl and ZIRLO are presented in Table 3 and Table 4, respectively. The test bundle is made up of 24 approximately 2.5 m long heated fuel rod simulators (Figure 6). Heating is electric by 5 mm diameter tungsten heaters installed in the rod centers, and the heated length is 1024 mm (between bundle elevations 0 and 1024 mm). At each end, molybdenum heaters coupled with copper electrodes are connected to the tungsten heaters. The copper electrodes are connected by gold-plated slide contacts to the cable leading to the DC electrical power supply. The electrical resistance of Cu/Mo/W/Mo/Cu composition was measured before and after the test for each rod simulator (Table 5). The tungsten heaters of heated rods are surrounded by annular ZrO_2 pellets simulating UO_2 fuel. The pellet properties are listed in Table 6. The pellets are surrounded by test material B136Y3 (Fe-6.2Al-13Cr-0.03Y).

The fuel rod simulators are held in position by five grid spacers at bundle elevations -200, 50, 550, 1050 and 1410 mm (Figure 7). The lower grid spacer was the standard AREVA Inconel spacer; the other four spacers were manufactured by ORNL from the Kanthal AF material. The rod cladding of the fuel rod has 9.52 mm outside diameter and 8.76 mm inner diameter. All test rods were filled with Kr at a pressure of approximately 0.23 MPa after bundle heating to cladding peak temperature of 800 K. The rods were connected to a relative large reservoir that, on the one, hand limited pressure increase during the heating (no ballooning risk), and, on the other hand, compensated minor gas losses and allowed observation of the first cladding failure as well as the failure progression.

Seven corner rods were installed in the bundle. Four of them, i.e. rods “A”, “C”, “E”, and “G” were made of a solid rod (Kanthal APM, Ø6 mm) at the top and a tube at the bottom (Kanthal D, Ø6 mm, wall 0.4 mm), and were used for thermocouple instrumentation. The other three rods, i.e. rods “B”, “D”, and “F” (solid rods of 6 mm diameter) are designed to be withdrawn from the bundle to check the amount of oxidation at specific times. Two solid rods (B and F) were withdrawn during the test, whereas the solid rod D was withdrawn after the test.

The test bundle was surrounded by a shroud of Kanthal APM with a 34 mm thick ZrO_2 fiber insulation extending from the bottom (-300 mm) to the upper end of the heated zone (+1024 mm) and a double-walled cooling jacket of Inconel 600 (inner)/stainless steel (outer) over the entire length. The properties of fiber insulation are listed in Table 7.The annulus between shroud and cooling jacket with the fiber insulation was purged (after several cycles of evacuation) and then filled with stagnant argon. The annulus is connected to a flow- and pressure-controlled argon feeding system in order to keep the pressure constant at the target of 0.23 MPa (beyond this pressure gas is released) and to prevent an access of steam to the annulus after possible shroud failure (argon feeding below the target value). The 6.7 mm annulus of the cooling jacket is cooled by argon from the upper end of the heated zone to the bottom of the bundle and by water in the upper electrode zone. Both the absence of ZrO_2 insulation above the heated region and the water cooling are to avoid too high temperatures of the bundle in that region.

2 Instrumentation and data acquisition

The assignment of measuring channels is listed in Table 8.

For temperature measurements, the test bundle, corner rods, shroud, and cooling jackets are equipped with thermocouples (TCs) (Figure 8…Figure 12). The thermocouples attached to the outer surface of the rod cladding at elevations between -250 and 1350 mm are designated “TFS” for all heated rods. The shroud thermocouples (designation “TSH”) are mounted at the outer surface between -250 and 1250 mm. The thermocouples that are installed inside the instrumentation rods at the two corner positions of the bundle (positions A, C, E and G) are designated “TIT”.

The thermocouples in the hot zone and above are high-temperature thermocouples with W5Re/W26Re wires, MgO insulation, and a sheath of stainless steel AISI 304 with an outside diameter of about 2.4 mm and wall thickness of about 500 µm (Table 9). All “TIT” thermocouples are also of the high-temperature type. The thermocouples in the lower bundle region, i.e. up to 550 mm elevation, were NiCr/Ni thermocouples with stainless steel sheath/MgO insulation and an outside diameter of 1.0 mm, used for measurements of the rod cladding and shroud temperatures. The distribution of the TFS thermocouples in the bundle is presented in Table 10.

The thermocouple measurement accuracies are:

at bundle elevations between 0 and 500 mm (NiCr/Ni thermocouples): ± 2 K (up to 600 K), ± 0.005*T K (above 600 K);

at bundle elevations between 600 and +1300 mm (W/Re thermocouples): ± 5 K (up to 700 K), ± 0.01*T K (above 700 K).

The hydrogen release is analyzed by a quadrupole mass spectrometer Balzers “GAM300” with the sampling position located at the off-gas pipe of the test facility (Figure 13, Figure 14). The ion currents representing the concentrations of the respective gases are determined. From these data the mass production rate of hydrogen as well as of the other gases is calculated with the ratio of the concentration of the particular gas and that one of argon (carrier gas) and multiplied by the argon flow rate through the test bundle.

The operational data, e.g. voltage, current, electric power, pressure, and temperatures were recorded by a data acquisition system with a frequency of 1 Hz as were the temperatures of the test section.

3 Test performance and results of online measurements

The detailed sequence of the test events is described in Table 11.

In the QUENCH-19 experiment the test sequence can be distinguished in the following stages:

Pre-oxidation	0 – 6018 s (similar to QUENCH-15),
Heat-up	6018 – 7127 s (similar to QUENCH-15),
Extended period	7127 – 9100 s (constant electrical power),
Quench	≈9115 – 9285 s with water flow rate 48 g/s (similar to QUENCH-15).

The heating of Ar and steam before injection into the bundle is illustrated in Figure 15 - Figure 17 for both tests QUENCH-15 and -19. The reason for the lower gas temperatures inside the superheater during QUENCH-19 was the lower power of trace heating of tubes before the superheater due to a changed heating during the QUENCH-LOCA program. The coolant data as the argon and steam flow rates and the temperature at the bundle inlet, as well as system pressure are shown in Figure 18. QUENCH-15 and -19 have quite similar gas inlet conditions except the inlet gas temperature: while the QUENCH-15 gas temperature was constant during the test (720 K), the corresponding QUENCH-19 temperature increased from 640 to 700 K.

The boundary conditions were noticeably different for two bundle tests (Figure 19). Whereas the porous heat insulation of QUENCH-15 was filled with dry Ar, the QUENCH-19 insulation contained humid Ar due to leakage of steam (or water) during the pre-tests through a small gap at the upper shroud flange. The penetrated steam condensed and was collected in the pores of insulation and has been evaporated during the pre-oxidation stage. The dewetting of the TCI thermocouples (inner surface of cooling jacket) in Figure 19 shows sequential boiling starting from the elevation 850 mm (at 2200 s) to 350 mm (at 5500 s). Also the TSH thermocouple at the elevation 150 mm showed dewetting behavior at about 2250 s (Figure 28). The TCI thermocouples at elevation 950 mm were not dewetted, and the temperature at 1150 mm is relative low due to cooling of the cooling jacket upper part with water at about 75°C. Figure 20 shows intermittent injection of Ar into the annulus due to loss of gas (Ar and steam) from annulus into the bundle. The noticeable release of the so formed steam through the gap was detected by mass spectrometer after the start of the transient at about 6000 s (Figure 21). The corresponding amount of steam released through the gap was estimated to be 320 g. During the post-test disassembly of the bundle, about 7300 g of water leaked out from the annulus between the shroud and the cooling jacket. Additionally, the post-test weighing of humid heat insulation showed that about 400 g was collected in insulation pores. So, the total water mass penetrated into the annulus during pre-tests and in the early test stage is estimated to be about 8000 g. Figure 22 shows different temperature behavior at the inner and outer boundaries of heat insulation for QUENCH-15 and -19, illustrating strong heat losses through the humid insulation in the QUENCH-19 test.

The power input history for the QUENCH-19 test is provided together with the measured peak cladding temperature in Figure 23.The different boundary conditions could be the main reason for the fact, that the peak cladding temperature was about 210 K lower during *pre-oxidation* than in QUENCH-15. Furthermore, the radial temperature gradient across the QUENCH-19 bundle was larger than the gradient for QUENCH-15. The influence of the chemical heat released due to exothermic interaction between steam and cladding tubes is minimal during this stage because the corresponding electrical energy was about 64 MJ, whereas the chemical energy release was only 3.5 MJ for the Zr/steam interaction (and much less for the FeCrAl/steam interaction). This energy relationship was changed during the power *transient* stage; the significant higher contribution of the chemical heat (6.8 MJ vs. 16.5 MJ of electrical energy) caused strong temperature escalation during QUENCH-15. In contrast to this, no temperature escalation during the *extended* stage of the QUENCH-19 test was observed.

Figure 24 - Figure 40 show the TFS, TIT and TSH thermocouple readings separately for each bundle elevation. It should be mentioned, that during the pre-oxidation the radial temperature gradient across the QUENCH-19 bundle (max 165 K between central rods and shroud) was larger than the gradient for QUENCH-15 (max 120 K); the reason of this should be the above discussed higher heat loss in QUENCH-19 through the wetted heat insulation to the cooling jacket. The temperatures at the inner and outer jacket walls are shown in Figure 41, Figure 42. The temperature of the cooling jacket at 350 mm remained constant until about 6200 s due to the boiling of water in the annulus, which mainly reached there during the preliminary tests. The level of this water dropped to 350 mm after starting the transient stage. The porous heat insulation between the shroud and the cooled jacket below the elevation of 350 mm remained filled with water during the entire experiment (at least along the cooling jacket).

At the beginning of the *transient*, lower temperatures were observed at all elevations of the QUENCH-19 bundle in comparison to QUENCH-15 (Figure 43, Figure 44). The hottest elevation of the QUENCH-19 was the level 850 mm unlike 950 mm for QUENCH-15. At the *end of the transient* stage, the temperatures were very similar between -250 and 650 mm, whereas at higher elevations the QUENCH-15 temperatures were significantly higher due to the strong exothermal reaction between the Zr alloy and steam in this bundle at T>1500 K. The average heating rate during the QUENCH-19 transient was 0.14 K/s (8.7 K/min).

In contrast to QUENCH-15, the transient in QUENCH-19 was not followed by the reflood stage. A *2000 s long period with constant electrical power* at maximum level for delayed observation of the effect of rising temperatures until the moment the claddings begin to melt (FeCrAl melting point ≈1510 °C=1783 K). Temperatures gradually increased from a peak cladding temperature of 1470 K to 1810 K until the reflood stage. Approximately in the middle of this period, at a peak cladding temperature of 1620 K, the depressurization of the claddings began, which was indicated by Kr release (Figure 45).

The initial evaporation rate was higher in QUENCH-15 compared to QUENCH-19 due to the higher temperatures at the *onset of reflooding*. Therefore, the duration of water level increase up to the bundle head was shorter in QUENCH-19 (270 s instead 330 s in QUENCH-15). The wetting of the cladding surface thermocouples TFS occurred earlier than the collapsed water front reached the corresponding thermocouple elevation (Figure 46, Figure 47). The reason is the relatively extended region of two-phase fluid.

Only a small amount of hydrogen yield (0.4 g) was measured towards the end of the *power transient* (41 g for QUENCH-15). The increase of the hydrogen release rate corresponded to first cladding failures during the QUENCH-19 *extended stage* at t≈7700 s and measured T_{pct}≈1550 K at 850 and 950 mm. The strong increase of hydrogen release occurred during the massive cladding failures at t>8260 s and T≈1700 K. The probable reason for the sharp increase of hydrogen release could be the strong oxidation of iron after vanishing of the protective Al_2O_3 layer with the following formation of molten FeO at T_{pct}≈1650 K. The corresponding catastrophic acceleration of FeCrAl oxidation was observed by separate-effect tests [6]. The generation rate of hydrogen released due to oxidation of claddings, corner rods, shroud, grid spacers and thermocouples showed the maximal value of 280 mg/s at during reflood (QUENCH-15: 1830 mg/s). The total hydrogen release at the end of the test was 9.2 g, what corresponds about 20% of total hydrogen in QUENCH-15 (Figure 48). The amount of hydrogen released by the oxidation of solid and melted QUENCH-19 thermocouples can be estimated as 2 g.

4 Posttest investigations

4.1 Inspection of corner rods

The two KANTHAL APM corner rods withdrawn during the test (rod B - at the end of pre-oxidation, and rod F - at the end of transient) showed an only slightly oxidized surface (thickness of oxide layer less than 1 µm). Similar observations were made also for the corner rod (rod D) withdrawn after the test (Figure 49).

4.2 Visual and videoscope inspection

The inspection of some peripheral rods by videoscope showed the formation of cladding circumferential breaks, probably developed due to thermal axial expansion followed by quench shrinkage (Figure 50). As result, pellets (partially fragmented) and tungsten heaters were exposed to steam. However, several other peripheral rods remained intact. No spalling of tube segments or large circumferential break of cladding segments was observed after the reference test QUENCH-15 with a lower thermal expansion coefficient of the applied Zr alloy cladding material (see Table 4), only thin circumferential cracks were indicated.

Another character of cladding damage is associated with interaction between claddings and thermocouple sheaths. The claddings of the thermocouples made of the AISI-304 stainless steel (melting range

1400…1450 °C) and located at the elevations 850, 950 and 1050 mm were melted with downwards melt relocation (Figure 51). The relocated melt attacked the FeCrAl claddings and caused partial dissolution of these claddings (Figure 53). It means that during the short period with temperatures above 1400 °C the behavior of the instrumented claddings was no longer prototypical. However, the metallographic investigations showed that the cladding temperature of the hot inner rods reached even the melting point of FeCrAl, and the FeCrAl melt was found at the surface of claddings (unfortunately, it was not registered by thermocouples because the corresponding TCs failed before quenching and were no more available). In contrast to this, the QUENCH-15 test with ZIRLO cladding showed that the metallic melt of the cladding was trapped between the pellet and the outer oxide layer and did not escape into the space between the rods (Figure 51).

All four FeCrAl grid spacer were outside the hottest area and remained intact.

4.3 Metallographic examination of bundle cross sections

The test bundle was extracted from the test section (Figure 52) and embedded in epoxy resin Epotec 277 with the pertinent hardener Epikure 350. The mixture of these two components gives good result concerning formation of hardened mass without cracks and pores. However, the hardening process was very long and the final material was relatively soft. Though it was yet possible to cut the bundle into necessary slices (Table 12), the grinding and polishing processes were quite difficult and requested the development of special slice holders.

The melting of the thermocouple sheaths was confirmed by the observation of the cross section 1050 mm (Figure 54). The failures of thermocouples due to melting of TC sheaths occurred also at the end of the QUENCH-15 test. However, in this case the melting points of TC sheaths (Zr alloy) and ZIRLO claddings were very similar. Furthermore, no interaction between TC melt and cladding metal occurred due to relative thick outer oxide layer at TC and cladding surfaces: the cladding metal melt in QUENCH-15 was practically trapped between the stable outer oxide layer and the pellets (Figure 51).

Observation of the lower cross sections revealed the change in color of some ZrO_2 pellets (Figure 55). Especially, the rods with failed claddings have dark pellets. The detailed investigations (see below) showed, that these pellets are surrounded by frozen FeO melt. The oxygen was partially transported from the pellets to the melt. Similar interaction of molten FeO with UO_2 pellets were observed already 1998 [7].

Other dark pellets are observed in rods 17, 18, and 23 in which the claddings remain intact. In this case, steam did not penetrate to the pellets, and oxygen from the pellets was transported to the tungsten heater or to the claddings at the points of contact with them. In this case, the pellets acquired a dark shade typical of sub-stoichiometric zirconium oxide.

Elevation 950 mm

The FeCrAl claddings of all center rods failed (Figure 56). Similar to the elevation 1050 mm (Figure 54), the sheaths of thermocouples were molten and oxidized (Figure 57): metallic precipitates are surrounded by FeO melt formed at relatively low temperature of about 1380 °C (Figure 58). The dark pellets of the rods 1 and 2 are very porous (Figure 59, Figure 60). The detailed optical (Figure 61) and SEM/EDX investigations showed, that claddings were mostly oxidized and the FeO melt formed at the cladding position (Figure 62) penetrated also between the pellet grains (Figure 63). The dark color of the pellets could be explained by partial oxygen transport from zirconium oxide to the melt and formation of dark sub-stoichiometric ZrO_{2-x} grains. The FeO melt interacted with pellets not only at the outer pellet surface, but the FeO melt has penetrated between ZrO_{2-x} grains in the whole pellet of rod 3 (Figure 64). On the inner edge of the pellet, side effects of the very hot W heater could also be here observed: some of the oxygen from the pellet was transported to the heater. Similar microstructure was observed for the dark and porous pellet of the rod 4: the molten FeO from cladding has penetrated through the pellet grains (Figure 65). The pores could be caused by metallographic processing: some clusters of grains fell out during grinding and polishing.

In the ring of rods surrounding the four internal heaters, not all claddings were completely destroyed and formed the molten FeO. Only small cladding segments of rod 5 were oxidized at the outer cladding surface (Figure 66). The pellet of this rod kept intact and has typical white color of stoichiometric ZrO_2. Similar white color have also the halves of the pellets of rods 6 and 7 at the positions with intact metal claddings (Figure 67, Figure 68). The other halves of these pellets is dark due to interaction with cladding oxidized and melted at corresponding positions. Similar dark and porous pellet structures were observed for rods 9 through 15 of the second inner row of heaters (Figure 69 through Figure 79) as well as for outer rods 19, 20, and 21 (Figure 56). The dark pellet color of outer rods 17, 18 and 23 should be caused by interaction of these pellets with the FeO melt relocated in the pellet-cladding gap from above.

Elevation 850 mm

The claddings of most of the rods at elevation 850 mm remained almost not damaged (Figure 80). While the reason for the violation of cladding integrity for the rods 8 and 19, as well as 21 and 22, could be the interaction with the molten stainless steel claddings of the thermocouples, the claddings of the inner rods 3 and 9 could have been damaged due to their own high-temperature oxidation and melting after the destruction of the outer protective Al_2O_3 layer.

For rod 3 (Figure 81), on the remaining part of the cladding, one can see a protective layer of aluminum oxide Al_2O_3 formed on the inner and outer surfaces of the cladding (Figure 82). Most of the cladding of rod 3 is missing - only small fragments of the melt remain, which reacted with the pellet (Figure 83). A number of rods are characterized by local oxidation and melting of the inner surface of the cladding; the typical structure of the frozen FeO melt (with ceramic precipitates) and the interaction of the FeO melt with the pellet of the rod 4 is shown in Figure 84 and Figure 85.

A thin protective Al_2O_3 layer was detected at the outer and inner cladding surfaces of rod 16 (Figure 86). At the same time, in some places on the inner cladding side of this rod, melt is observed, which in some cases was formed at this elevation, and in some cases moved from the upper elevations. In both cases, the thinning of metal cladding was observed. However, more complex structure of intermediate layers was observed for the relocated melt (Figure 87): the melt has interacted with Cr_2O_3 and Al_2O_3 sub-layers formed before.

For the outer rod 18 (Figure 88), the whole cladding remained practically intact. The SEM/EDX investigation (Figure 89) 1) revealed formation of thin Al_2O_3 oxide layer (thickness between 2 and 3 µm) at the outer cladding surface, 2) absence of metal cladding thinning (no cladding oxidation). The metal in the cladding-pellet gap is an artifact that appeared due to formation of shavings during sawing and polishing.

Figure 90 illustrates an interaction of molten stainless steel thermocouple cladding with cladding and pellet of rod 19. On the other hand, the rod cladding was damaged near to failed thermocouple due to its own strong oxidation and formation of FeO melt which interacted with pellet. SEM/EDX analyses confirm these observations (Figure 91).

Figure 92 presents two interesting phenomena in the gap of rod 24: 1) cladding-pellet interaction (before materials shrinkage during quench; 2) relocation of FeCrAl melt. The complex multilayer structure was formed at the pellet-cladding interaction location due to oxygen transport from pellet to cladding (Figure 93). The downwards relocation of the melt in the gap is accompanied by the oxidation of the metal components of the melt by oxygen diffused from the pellet (Figure 94). Similar to rod 16 (Figure 86), a complex structure of intermediate layers was observed at the interaction boundary between relocated melt and inner cladding surface covered by thin Al_2O_3 layer (Figure 95).

Elevation 750 mm

The peak cladding temperatures at the outer cladding surface here were below 1600 K, i.e. below the FeO melting point (1650 K). The claddings of all the rods at this elevation retained their integrity (Figure 96). But they often thinned as a result of interaction with the oxidized melt flowing in the gap between pellet and cladding from the upper elevations. The claddings of the inner rods were thinned by half at many circumferential positions (Figure 97 through Figure 102). The FeO_x melt relocated downwards along the oxidized inner surface of claddings. Whereas the outer cladding surface oxidized only slightly (<3 µm Al_2O_3, Figure 98), the inner oxide is quite thick (up to 70 µm), and additionally there is a transient layer (with similar thickness) between oxide and residual cladding (Figure 100). Such layer structure was formed due to redistribution of oxygen between the FeO melt and cladding. Often, mixed layer with precipitates of (Fe, Cr, Al)-oxides inside the FeO_x melt formed between the homogeneous FeO_x melt and the solid cladding (Figure 101, Figure 103).

It is interesting to note the accumulation of shavings in the gap between the cladding and the pellets, which appeared during sawing and grinding of the claddings, which were not damaged at any of the elevations. For these claddings, no protective alumina layer was formed at the inner cladding surface, and the burrs of relatively tough FeCrAl material were pressed during sawing and grinding into the gap between cladding and pellet at all investigated bundle elevations. This can be seen for the intact claddings 17, 18, 23 in Figure 104, Figure 105, and Figure 106.

5 Summary and Conclusions

The QUENCH-19 test with bundle containing 24 heated rods with B136Y3 cladding tubes and 4 Kanthal AF spacer grids as well as 7 KANTHAL APM corner rods and KANTHAL APM shroud was performed at KIT on August 29, 2018 with similar electrical power history as reference test QUENCH-15 (ZIRLO™ claddings). Non comparable conditions were 1) cooler steam-Ar flow, and 2) moist Ar inside the thermal insulation for QUENCH-19.

The QUENCH-19 test was performed in four test stages:

1. pre-oxidation during about 6000 s (similar to QUENCH-15),
2. transient during about 1130 s (similar to QUENCH-15),
3. extended period with constant electrical power of 18.32 kW during 1970 s (to extend the temperature increase stage),
4. test termination by water flooding with rate of 48 g/s (similar to QUENCH-15).

The peak cladding temperatures during the pre-oxidation stage were about 200 K lower in comparison to QUENCH-15. The radial temperature gradient was noticeable larger in comparison to QUENCH-15. The reasons for these test differences could be the different properties of the bundle materials (lower thermal conductivity and higher heat capacity and thermal expansion of FeCrAl) as well as the different boundary conditions (cooler gas flow, humid heat insulation).

Compared to QUENCH-15, a much lower heating rate was measured. A temperature of about 1150 °C was reached at the time point as local melting of QUENCH-15 claddings occurred. No temperature escalation was observed during the extended transient. Maximum cladding temperature measured before reflood was about 1800 K (extrapolated from measured data at the elevation of 950 mm).

The coping time was about 3200 s (≈1200 s for QUENCH-15). The conclusion about increased coping time in QUENCH-19 in comparison with the reference test QUENCH-15 is only qualitative: quantitative assessments for reactor conditions should be made with care due to artificial extension of transient before reflood.

In the axial hottest zone between 800 and 1000 mm, a thin (2-3 µm) protective layer of aluminum oxide formed and remained on the claddings of some peripheral rods. But in many cases (especially for the inner rods) this layer was destroyed and the claddings were completely oxidized, which is in accordance with results of single effect tests, showing catastrophic oxidation of nuclear grade FeCrAl alloys with lower Cr content already from 1350°C. Many claddings were damaged at elevations between 850 and 1000 mm: 1) by formation of circumferential cracks (probably due to thermal expansion followed by quench shrinkage), 2) by high-temperature inner oxidation in steam, penetrated through the damaged cladding regions, and formation of molten FeO, 3) due to FeCrAl melting and relocation of melt inside the gap between pellet and cladding, 4) due to eutectic interaction of claddings with stainless steel thermocouple sheaths. The molten FeO penetrated between the grains of the ZrO_2 pellets and dissolved them at their edges. The remaining parts of the pellets became loose and porous due to the penetration of the FeO melt between the grains of the pellets throughout the entire volume of the pellets. Additionally, FeO melt formed at the contact between pellets and cladding due to transport of oxygen from pellets to cladding. The interaction of the FeO melt with the ZrO_2 pellet is an important degradation effect of the pellet. The appearance of liquid phases was also observed in three-phase systems Fe-U-O already at 1335 °C [8], and this effect was early checked for the interaction of molten FeO with UO_2 pellets [7]: the dissolution of UO_2 was observed at 1400 °C with a penetration of iron oxide in the fuel grain boundaries and, finally, a decohesion of the fuel structure.

At the relatively cold level of 750 mm, the integrity of the claddings was preserved, but several claddings were significantly thinned (up to half) due to the interaction with the molten oxidized melt that formed at this elevation or flowed down from the upper elevations through the cladding-pellet gap.

All four FeCrAl grid spacers were outside the hottest area and remained intact.

A sharp increase of the hydrogen release rate was observed about 800 s before reflooding. A trigger of this event should be the melting of steel thermocouple claddings. However, the main reasons are the disappearance of the protective layer of aluminum oxide and the melting of the claddings of the inner rods. The maximum hydrogen release rate reached during reflood was 280 mg/s (1830 mg/s for QUENCH-15). The total hydrogen production was 9.2 g (47.6 g for QUENCH-15). The first modelling of QUENCH-19 by integral codes showed much lower total hydrogen release [9]. The probable reason of this is the applied oxidation correlation for FeCrAl, which could be not correct at temperatures between 1300 and 1500 °C.

The influence of different boundary conditions in the QUENCH-15 and -19 tests (condensed water inside the heat insulation and the lower gas inlet temperature for QUENCH-19) on the different bundle behaviors will be analyzed during a benchmark planed in the framework of the ongoing IAEA CRP project ATF-TS.

6 Acknowledgments

The QUENCH-19 experiment was supported by the KIT program NUSAFE and partly sponsored by ORNL. The cladding materials and thermocouples were provided by ORNL. IKET/KIT colleagues were involved into bundle dismounting. The authors thank all colleagues involved in the investigations, particularly J. Moch and U. Peters for bundle preparation, U. Stegmaier for mass spectrometer measurements and SEM/EDX investigations, and J. Laier for data processing.

7 References

1. J. Stuckert, M. Steinbrueck, M. Grosse, "Experimental program QUENCH at KIT on core degradation during reflooding under LOCA conditions and in the early phase of a severe accident," *Proceedings of Meeting on Modelling of Water Cooled Fuel Including Design Basis and Severe Accidents*, Chengdu/China, 28 October–1 November 2013, IAEA-TECDOC-CD-1775, pp. 281-297,2013, https://www-pub.iaea.org/MTCD/Publications/PDF/TE-1775_CD_web.pdf.

2. T. Haste, M. Steinbrück, M. Barrachin, O. de Luze, M. Grosse, J. Stuckert, "A comparison of core degradation phenomena in the CORA, QUENCH, Phébus SFD and Phébus FP experiments," *Nuclear Engineering and Design*, 283 (2015), pp. 8–20, https://doi.org/10.1016/j.nucengdes.2014.06.035.

3. M. Steinbrück, M. Große, L. Sepold, J. Stuckert. "Synopsis and outcome of the QUENCH experimental program", *Nuclear Engineering and Design*, 240 (7), pp. 1714-1727, 2010, https://doi.org/10.1016/j.nucengdes.2010.03.021.

4. J. Stuckert, J. Birchley, M. Große, B. Jaeckel, M. Steinbrück. „Experimental and calculation results of the integral reflood test QUENCH-15 with ZIRLO™ cladding tubes in comparison with results of previous QUENCH tests". *Nuclear Engineering and Design*, 241 (2011), pp. 3224–3233. https://doi.org/10.1016/j.nucengdes.2011.05.004.

5. J. Stuckert; M. Große, U. Stegmaier, M. Steinbrück. "Results of Severe Fuel Damage Experiment QUENCH-15 with ZIRLO cladding tubes". *Scientific report KIT-7576* (2011), https://www.doi.org/10.5445/KSP/1000022788.

6. C. Kim, C Tang, M Grosse, Y. Maeng, C. Jang, M. Steinbrueck. "Oxidation mechanism and kinetics of nuclear-grade FeCrAl alloys in the temperature range of 500–1500 °C in steam*". Journal of Nuclear Materials*, 564 (2022), 153696, https://www.doi.org/10.1016/j.jnucmat.2022.153696.

7. P. Pacenti, F. Toci, R. Nannicini (ENEA-ERG Ispra), R.A.H. Edwards, U. Montaretto (grant holder), M. Della Rossa, G. Buscaglia. Dissolution of UO_2 by FeO melts. Project CIT (Corium Interactions and Thermochemistry). EU Report EUR 18661 EN (1998). https://op.europa.eu/en/publication-detail/-/publication/83b33290-c77c-11e6-a6db-01aa75ed71a1.

8. S.V. Bechta, E.V. Krushinov, V.I. Almjashev, S.A. Vitol, L.P. Mezentseva, Yu.B. Petrov, D.B. Lopukh, V.B. Khabensky, M. Barrachin, S. Hellmann, K. Froment, M. Fisher, W. Tromm, D. Bottomley, F. Defoort, V.V. Gusarov. "Phase diagram of the UO_2–FeO_{1+x} system". *Journal of Nuclear Materials*, 362 (2007), pp. 46–52, https://www.doi.org/10.1016/j.jnucmat.2006.11.004.

9. M. Cherubini, G. Pastore, S. Penttilä, M. Ševeček, J. Stuckert, M. Veshchunov, P. Xu, I. Zozulia. Analysis of Options and Experimental Examination of Fuels for Water Cooled Reactors with Increased Accident Tolerance (ACTOF). *IAEA Report TECDOC-1921* (2020). ISBN 978–92–0–114220–7. Chapter 6.

10. IAEA CRP project "Testing and Simulation for Advanced Technology and Accident Tolerant Fuels (ATF-TS)", 2020-2024, https://nucleus.iaea.org/sites/connect/NFEpublic/Pages/ATF-TS.aspx

Tables and Figures

Table 1 QUENCH Test Matrix 1997 – 2019

Test	Quench medium and injection rate	Temp. at onset of flooding[1)]	Max. ZrO_2 before transient[2)]	Max. ZrO_2 (X s) before flooding[2)]	Posttest average ZrO_2 thickness[3)]	H_2 production before / during cooldown	Remarks, objectives
QUENCH-00 Oct. 9 - 16, 97	Water 80 g/s	≈ 1800 K			completely oxidized		Commissioning tests.
QUENCH-01 Febr 26, 98	Water 52 g/s	≈ 1830 K	312 µm		500 µm at 913 mm	36 / 3	COBE Project; partial fragmentation of pre-oxidized cladding.
QUENCH-02 July 7, 98	Water 47 g/s	≈ 2400 K			completely oxidized	20 / 140	COBE Project; no additional pre-oxidation; quenching from high temperatures.
QUENCH-03 January 20, 99	Water 40 g/s	≈ 2350 K			completely oxidized	18 / 120	No additional pre-oxidation, quenching from high temperatures.
QUENCH-04 June 30, 99	Steam 50 g/s	≈ 2160 K	82 µm		280 µm	10 / 2	Cool-down behavior of slightly pre-oxidized cladding by cold steam injection.
QUENCH-05 March 29, 2000	Steam 48 g/s	≈ 2020 K	160 µm		420 µm	25 / 2	Cool-down behavior of pre-oxidized cladding by cold steam injection.
QUENCH-06 Dec 13 2000	Water 42 g/s	≈ 2060 K	207 µm[5)]	300 µm, (60 s), SVECHA modeling	630 µm[4)]	32 / 4	OECD-ISP 45; prediction of H_2 source term by different code systems.
QUENCH-07 July 25, 2001	Steam 15 g/s	≈ 2100 K	230 µm		completely oxidized	66 / 120	COLOSS Project; impact of B_4C absorber rod failure on H_2, CO, CO_2, and CH_4 generation.
QUENCH-09 July 3, 2002	Steam 49 g/s	≈ 2100 K			completely oxidized	60 / 400	As QUENCH-07, steam-starved conditions prior to cooldown.

Test	Quench medium and injection rate	Temp. at onset of flooding[1)]	Max. ZrO_2 before transient[2)]	Max. ZrO_2 (*X* s) before flooding[2)]	Posttest average ZrO_2 thickness[3)]	H_2 production before / during cooldown	Remarks, objectives
QUENCH-08 July 24, 2003	Steam 15 g/s	≈ 2090 K	274 µm		completely oxidized	46 / 38	As QUENCH-07, no absorber rod.
QUENCH-10 July 21, 2004	Water 50 g/s	≈ 2200 K	514 µm	613 µm (at 850 mm)	completely oxidized	48 / 5	LACOMERA Project; Air ingress.
QUENCH-11 Dec 08, 2005	Water 18 g/s	≈ 2040 K		170 µm	completely oxidized	9 / 132	LACOMERA Project; Boil-off.
QUENCH-12 Sept 27, 2006	Water 48 g/s	≈ 2100 K	160 µm, breakaway	300 µm, (110 s), breakaway	completely oxidized	34 / 24	ISTC Project #1648.2; VVER bundle with E110 claddings.
QUENCH-13 Nov 7, 2007	Water 52 g/s	≈ 1820 K		400 µm,after AgInCd rod failure	750 µm	42 / 1	SARNET; impact of AgInCd absorber rod failure on aerosol generation.
QUENCH-14 July 2, 2008	Water 41 g/s	≈ 2100 K	170 µm[6)]	470 µm[6)] (30 s)	900 µm	34 / 6	ACM series: M5® cladding
QUENCH-15 May 27, 2009	Water 48 g/s	≈ 2100 K	145 µm[6)]	380 µm[6)] (30 s)	620 µm	41 / 7	ACM series: ZIRLO™ cladding.
QUENCH-16 July 27, 2011	Water 53 g/s	≈ 1870 K*	135 µm	130 µm at 450-950 mm, breakaway	1075 µm at 550-650 mm	144 / 128	LACOMECO Project; Air ingress.
QUENCH-17 Jan. 31, 2013	Water 10 g/s	≈ 1800 K		completely oxidized	completely oxidized	110 / 1	SARNET-2; Debris formation and coolability.
QUENCH-18 Sept. 27, 2017	Water 53 g/s	≈ 1950 K	80 µm	completely oxidized	completely oxidized	57 / 238	ALISA Project; air ingress; AgInCd absorber rods
QUENCH-19 Aug. 29, 2018	Water 48 g/s	≈ 1800 K	-	-	-	8 / 1.2	Bundle with FeCrAl materials; cooperation with ORNL

1) Maximum measured bundle temperature at 950 mm elevation.
2) Measured (or calculated for LOCA tests) at the withdrawn corner rod at 950 mm elevation.
3) Measured posttest at the bundle elevation of maximum temperature, i.e. 950 mm.
4) Some claddings were completely oxidized at 950 mm elevation.
5) Oxide thickness during transient stage.
6) Zircaloy-4 corner rods.

Revised: June 2021

Table 2 Design characteristics of the QUENCH-19 test bundle

Bundle type		PWR
Bundle size (heated rods)		24 rods
Pitch		12.6 mm
Coolant channel area		34.57 cm^2
Hydraulic diameter		12.27 mm
Cladding outside / inside diameter		9.52 ± 0.04 / 8.76 ± 0.04 mm
Cladding material		cold drawing B136Y3 (Fe-6.2Al-13Cr-0.03Y)
Cladding length (elevations)		2280 mm (-595 to 1685 mm)
Cladding thickness		381 ± 9 µm
Full rod length (elevations)		2480 mm (-690 to 1790 mm)
Material of main heater surface roughness		Tungsten (W) Ra = 1.6 µm
W heater length		1024 mm
W heater diameter		5 mm
Annular pellet	material dimensions	ZrO_2; Y_2O_3-stabilized ∅ 8.58/5.2 mm; L=11 mm
Pellet stack		0 mm to ≈ 1020 mm
Internal rod pressure (gas)		0.22 MPa abs. (Kr)
Corner rod (7)	material instrumented (A, C, E, G) not instrumented (B, D, F)	*Kanthal D tube (Fe22%Cr4.8%Al)* Kanthal APM rod (Fe22%Cr5.8%Al) *tube ∅ 6x0.4 (bottom: -1140 mm)* rod ∅ 6 mm (top: +1300 mm) rod ∅ 6 mm (-1350 to +1155 mm)
Grid spacer (GS)	material length sheet thickness elevation of lower side	Inconel (1 GS), Kanthal AF (4 GS) 48 mm (1 GS), ≈ 16 mm (4 GS) 0.5 mm -200; 50; 550; 1050, 1410 mm
Shroud	material wall thickness outside diameter length (extension)	Kanthal APM tube OBE (Fe22%Cr5.8%Al) 2 flanges: APMT (Fe21%Cr5%Al3%Mo) 3.03±0.15 mm (ultrasound) 89 mm 1600 mm (-300 mm to 1300 mm)
Shroud insulation	material insulation thickness elevation	ZrO_2 fiber ≈ 34 mm -300 mm to ≈ 1000 mm
Molybdenum heaters and copper electrodes	length of upper parts length of lower parts diameter of electrodes: - prior to coating - after coating with ZrO_2 coating surface roughness	766 mm (576 Mo, 190 mm Cu) 690 mm (300 Mo, 390 mm Cu) 8.0 mm 8.4 mm Ra = 6-12 µm
Cooling jacket	Material: inner/outer tube inner tube outer tube	Inconel 600 (2.4816) / SS (1.4571) ∅ 158.3 / 168.3 mm ∅ 181.7 / 193.7 mm

Table 3 Chemical compositions of FeCrAl alloys

Material	Fe	Cr	Al	Y	Si	Mn	C	comment
Conventional Kanthal APM	Balance	22	5.8	-	0.7	0.4	0.08	used for shroud and corner rods in QUENCH-19
FeCrAl(Y) alloy B136Y3 (ORNL)	**Balance**	**13***	**6.2**	**0.03**			**0.01**	used for **claddings** of heated rods in QUENCH-19

Table 4 Physical properties of FeCrAl and ZIRLO materials

	heat capacity	heat conductivity	thermal expansion	melting point
FeCrAl (Kanthal)	≈ 460 J/(kg·K)	≈ 11 W/(m·K)	$14 \cdot 10^{-6}$ /K	≈ 1790 K
ZIRLO	≈ 270 J/(kg·K)	≈ 23 W/(m·K)	$5.7 \cdot 10^{-6}$ /K	≈ 2030 K

Table 5 QUENCH-19; Electrical resistances of heated rods at 20 °C [mΩ]

Rod #	1	2	3	4	5	6	7	8	9	10	11	12	ave-rage	12 rods parallel
Pre-test	7.2	4.7	4.8	4.7	4.7	5.3	4.4	4.5	4.4	4.7	5.3	4.8	4.96	0.41
Post-test	12.6	4.5	4.3	4.6	7.1	8.2	4.9	4.4	4.3	4.3	4.5	4.5	5.68	0.42

Rod #	13	14	15	16	17	18	19	20	21	22	23	24	ave-rage	12 rods parallel
Pre-test	4.9	4.7	4.8	4.9	4.7	4.9	4.6	4.5	4.7	5.0	5.2	4.9	4.82	0.40
Post-test	4.3	4.4	4.3	4.3	4.3	4.3	4.4	4.3	4.4	4.4	4.3	4.1	4.32	0.36

Note: Measured values include the resistance of slide contacts R_s=0.75 mΩ

All 12 rods were connected to one DC generator with 4 parallel bonded cables. The resistance of each cable is Rc=1.2 mΩ. Therefore, the external (outside) resistance corresponding to each heated rod (indicated by SCDAP/RELAP as fxwid) is Re=Rs+12*Rc/4=4.35 mΩ.

Table 6 Main characteristics of the ZrO_2 pellet material, yttria-stabilized (type ZYK3)

Property	Data
Y_2O_3 content	5 %
Density	6.07 ± 0.03 g/cm^3
Open porosity	0
Average crystallite size	0.8 µm
Specific heat at 20 °C	400 J/kg K
Thermal conductivity at 100 °C	2.5 W/m K
Linear expansion, 20-1000 °C	11 x 10^{-6}/K
Vickers Hardness HV10	> 12000 N/mm^2
Bending strength	> 1150 MPa
Elastic modulus	> 200 GPa
Weibull modulus	20
Fracture toughness K_{1C}	12 MPa•m$^{1/2}$

According to Barat Ceramics GmbH, 07955 Auma

Table 7 Properties of zirconia fiber insulating boards of type ZYFB3

Chemical composition

Oxide	ZrO_2	Y_2O_3	HfO_2	TiO_2	SiO_2	CaO	MgO	Fe_2O_3	Al_2O_3	Na_2O
typical wt%	88	10	2	0.14	0.12	0.09	0.03	0.04	0.01	0.01

Physical properties

bulk density	porosity	shrinkage (1 hour @1925 K)	shrinkage (24 hours @1925 K)	thermal expansion coefficient @298-1453K	melting point	max service temperature	flexural strength	compressive strength @10% compression
g/cm^3	%	%		1/K	K	K	MPa	MPa
0.48	92	1.2	2.8	$10.7*10^{-6}$	2866	2500	0.59	0.29

Thermal conductivity

temperature, K	673	1073	1373	1673	1923
conductivity, W/(m*K)	0.08	0.11	0.14	0.19	0.24

Specific heat capacity

temperature, K	366	2644
specific heat capacity, J/(kg*K)	544	754

According to specifications of manufacturer ZIRCAR PRODUCTS

Table 8 List of instrumentation for the QUENCH-19 test

Chan	Designation	Instrument, location	Unit
0	**TFS 3/17**	TC (W/Re), surface of fuel rod simulator 3, group 1, 1350 mm	K
1	**TFS 6/17**	TC (W/Re), surface of fuel rod simulator 6, group 2, 1350 mm	K
2	**TFS 8/16**	TC (W/Re), surface of fuel rod simulator 8, group 2, 1250 mm	K
3	**TFS 13/16**	TC (W/Re), surface of fuel rod simulator 13, group 3, 1250 mm	K
4	**TFS 12/15**	TC (W/Re), surface of fuel rod simulator 12, group 2, 1150 mm	K
5	**TSH 16/180**	TC (W/Re), shroud outer surface, 1250 mm, 201°, behind shroud insulation	K
6	**TFS 22/12**	TC (W/Re), surface of fuel rod simulator 22, group 4, 850 mm	K
7	**TFS 19/14**	TC (W/Re), surface of fuel rod simulator 19, group 4, 1050 mm	K
8	**TFS 14/14**	TC (W/Re), surface of fuel rod simulator 14, group 2, 1050 mm	K
9	**TFS 5/14**	TC (W/Re), surface of fuel rod simulator 5, group 2, 1050 mm	K
10	**TFS 2/14**	TC (W/Re), surface of fuel rod simulator 2, group 1, 1050 mm	K
11	**TFS 21/13**	TC (W/Re), surface of fuel rod simulator 21, group 4, 950 mm	K
12	**TIT A/13 defect**	TC (W/Re), center line of corner rod A, 950 mm	K
13	**TFS 17/13**	TC (W/Re), surface of fuel rod simulator 17, group 4, 950 mm	K
14	**TFS 15/13**	TC (W/Re), surface of fuel rod simulator 15, group 2, 950 mm	K
15	**TFS 9/13 defect**	TC (W/Re), surface of fuel rod simulator 9, group 2, 950 mm	K
16	**TFS 9/15**	TC (W/Re), surface of fuel rod simulator 9, group 2, 1150 mm	K
17	**TSH 15/0**	TC (W/Re), shroud outer surface, 1150 mm, 21°	K
18	**TSH 15/180**	TC (W/Re), shroud outer surface, 1150 mm, 201°	K
19	**TSH 16/0**	TC (W/Re), shroud outer surface, 1250 mm, 21°, behind shroud insulation	
20	**TSH 14/270 defect**	TC (W/Re), shroud outer surface, 1050 mm, 289°, behind shroud insulation	K
21	**TSH 14/90 defect**	TC (W/Re), shroud outer surface, 1050 mm, 101°, behind shroud insulation	K
22	TFS 22/9	TC (NiCr/Ni), surface of fuel rod simulator 22, group 4, 550 mm	K
23	TFS 17/9	TC (NiCr/Ni), surface of fuel rod simulator 17, group 4, 550 mm	K
24	F 902	Reserve	
25	Fm 401 r	Reserve (rotameter)	g/s
26..31		TC (W/Re), Reserve	K
32	**TIT C/12 defect**	TC (W/Re), center line of corner rod C, 850 mm	K

Chan	Designation	Instrument, location	Unit
33	**TFS 3/10 defect**	TC (W/Re), surface of fuel rod simulator 3, group 1, 650 mm	K
34		Reserve (W/Re)	K
35	TSH 4/270	TC (NiCr/Ni), shroud outer surface, 50 mm, 291°	K
36	TSH 5/0	TC (NiCr/Ni), shroud outer surface, 150 mm, 21°	K
37	**TFS 4/15 defect**	TC (W/Re), surface of fuel rod simulator 4, group 1,1150 mm	K
38	TFS 14/9	TC (NiCr/Ni), surface of fuel rod simulator 14, group 2, 550 mm	K
39	TFS 8/9	TC (NiCr/Ni), surface of fuel rod simulator 8, group 2, 550 mm	K
40	**TIT E/11**	TC (W/Re), centerline of central rod, 750 mm	
41	**TFS 6/10**	TC (W/Re), surface of fuel rod simulator 6, group 2, 650 mm	K
42	TFS 4/9	TC (NiCr/Ni), surface of fuel rod simulator 4, group 1, 550 mm	K
43	TFS 2/9	TC (NiCr/Ni), surface of fuel rod simulator 2, group 1, 550 mm	K
44	TFS 9/8	TC (NiCr/Ni), surface of fuel rod simulator 9, group 2, 450 mm	K
45	TFS 6/8	TC (NiCr/Ni), surface of fuel rod simulator 6, group 2, 450 mm	K
46	TFS 3/8	TC (NiCr/Ni), surface of fuel rod simulator 3, group 1, 450 mm	K
47	**TFS 3/13 defect**	TC (W/Re), surface of fuel rod simulator 3, group 1, 950 mm	K
48	**TFS 1/13**	TC (W/Re), centerline of central rod, 950 mm	K
49	**TSH 11/180**	TC (W/Re), shroud outer surface, 750 mm, 201° behind shroud insulation	K
50		Reserve (W/Re)	
51	**TIT G/13**	TC (W/Re), center line of corner rod G, 950 mm	K
52	**TSH 10/270**	TC (W/Re), shroud outer surface, 650 mm, 289°	K
53	**TSH 12/180**	TC (W/Re), shroud outer surface, 850 mm, 201° behind shroud insulation	K
54	**TSH 11/0**	TC (W/Re), shroud outer surface, 750 mm, 21°, behind shroud insulation	K
55	**TSH 13/90**	TC (W/Re), shroud outer surface, 950 mm, 101° behind shroud insulation	K
56	**TFS 14/11 defect**	TC (W/Re) surface of fuel rod simulator 14, group 2, 750 mm	K
57	**TFS 1/11 defect**	TC (W/Re) surface of fuel rod simulator 1, group 1, 750 mm	K
58	TSH 6/270	TC (NiCr/Ni), shroud outer surface, 250 mm, 281°	K
59	**TFS 16/12**	TC (W/Re) surface of fuel rod simulator 16, group 3, 850 mm	K
60	**TSH 10/90**	TC (W/Re), shroud outer surface, 650 mm,109°	K
61	T 206	Temperature upstream steam flow instrument location 1 g/s	K
62	P 206	Reserve	
63	F 206	Reserve	

Chan	Designation	Instrument, location	Unit
64	T 402 b	TC (NiCr/Ni), Ar super heater	K
65	**TFS 8/12**	TC (W/Re), surface of fuel rod simulator 8, group 2, 850 mm	K
66	**TSH 13/270**	TC (W/Re), shroud outer surface, 950 mm, 281° behind shroud insulation	K
67	**TSH 12/0 defect**	TC (W/Re) shroud outer surface, 850 mm, 11°, behind shroud insulation	K
68	T 512	TC (NiCr/Ni), gas temperature bundle outlet	K
69		Reserve (W/Re)	K
70	**TFS 2/12**	TC (W/Re) surface of fuel rod simulator 2, group 1, 850 mm	K
71	*Ref. T01*	*Temperature of measuring crate 1 (reference temperature)*	K
72	TFS 1/2	TC (NiCr/Ni, surface of fuel rod simulator 1, group 1, -150 mm	
73	TFS 1/7	TC (NiCr/Ni), surface of fuel rod simulator 1, group 1, 350 mm	K
74	TFS 11/6	TC (NiCr/Ni), surface of fuel rod simulator 11, group 2, 250 mm	K
75	TFS 4/1	TC (NiCr/Ni), surface of fuel rod simulator 4, fluid, -250 mm	K
76	TFS 17/5	TC (NiCr/Ni), surface of fuel rod simulator 17, group 4, 150 mm	K
77	TFS 2/5	TC (NiCr/Ni), surface of fuel rod simulator 2, group 1, 150 mm	K
78	TFS 14/4	TC (NiCr/Ni), surface of fuel rod simulator 14, group 2, 50 mm	K
79	TSH 9/0	TC (NiCr/Ni), shroud outer surface, 550 mm, 11°	K
80	TFS 5/6	TC (NiCr/Ni), surface of fuel rod simulator 5, group 2, 250 mm	K
81	TSH 9/180	TC (NiCr/Ni), shroud outer surface, 550 mm, 191°	K
82	TSH 8/90	TC (NiCr/Ni), shroud outer surface, 450 mm, 109°	K
83	TSH 8/270	TC (NiCr/Ni), shroud outer surface, 450 mm, 289°	K
84	TSH 7/0	TC (NiCr/Ni), shroud outer surface, 350 mm, 11°	K
85	TSH 7/180	TC (NiCr/Ni), shroud outer surface, 350 mm, 191°	K
86	TSH 6/90	TC (NiCr/Ni), shroud outer surface, 250 mm, 109°	K
87	TSH 5/180	TC (NiCr/Ni), shroud outer surface, 150 mm, 191°	K
88	TSH 4/90	TC (NiCr/Ni), shroud outer surface, 50 mm, 109°	K
89	TSH 3/180	TC (NiCr/Ni), shroud outer surface, -50 mm, 191°	K
90	TSH 1/0	TC (NiCr/Ni), shroud outer surface, -250 mm, 11°	K
91	TCI 9/270	TC (NiCr/Ni), cooling jacket inner tube wall, 550 mm, 270°	K
92	TCI 10/270	TC (NiCr/Ni), cooling jacket inner tube wall, 650 mm, 270°	K
93	TCI 11/270 defect	TC (NiCr/Ni), cooling jacket inner tube wall, 750 mm, 270°	K
94	TCI 13/270	TC (NiCr/Ni), cooling jacket inner tube wall, 950 mm, 270°	K
95	TFS 21/7	TC (NiCr/Ni), surface of fuel rod simulator 21 group 4, 350 mm	

Chan	Designation	Instrument, location	Unit
96	TCI 1/180 defect	TC (NiCr/Ni), cooling jacket inner tube wall, -250 mm, 180°	K
97	TCI 4/180	TC (NiCr/Ni), cooling jacket inner tube wall, 50 mm, 180°	K
98	TCI 7/180	TC (NiCr/Ni), cooling jacket inner tube wall, 350 mm, 180°	K
99	TCI 11/180 defect	TC (NiCr/Ni), cooling jacket inner tube wall, 750 mm, 180°	K
100	TCI 12/180	TC (NiCr/Ni), cooling jacket inner tube wall, 850 mm, 180°	K
101	TCI 13/180	TC (NiCr/Ni), cooling jacket inner tube wall, 950 mm, 180°	K
102	TCI 15/180	TC (NiCr/Ni), cooling jacket inner tube wall, 1150 mm, 180°	K
103	T 002	TC (NiCr/Ni), cooling water, inlet of off-gas tube	K
108	TFS 8/4	TC (NiCr/Ni), surface of fuel rod simulator 8, group 2, 50 mm	K
109	TCI 1/0	TC (NiCr/Ni), cooling jacket inner tube wall, -250 mm, 0°	K
110	TCI 4/0	TC (NiCr/Ni), cooling jacket inner tube wall, 50 mm, 0°	K
111	TCI 7/0	TC (NiCr/Ni), cooling jacket inner tube wall, 350 mm, 0°	K
112	TCI 11/0	TC (NiCr/Ni), cooling jacket inner tube wall, 750 mm, 0°	K
113	TCI 12/0	TC (NiCr/Ni), cooling jacket inner tube wall, 850 mm, 0°	K
114	TCI 13/0	TC (NiCr/Ni), cooling jacket inner tube wall, 950 mm, 0°	K
115	TCI 15/0	TC (NiCr/Ni), cooling jacket inner tube wall, 1150 mm, 0°	K
116	T 003	TC (NiCr/Ni), cooling water, outlet of off-gas tube	K
117	T 309	TC (NiCr/Ni), Ar bundle top	K
118		Reserve (NiCr/Ni)	
119	TFS 3/3	TC (NiCr/Ni), surface of fuel rod simulator 3, group 1, -50 mm	K
120	TCO 1/0	TC (NiCr/Ni), cooling jacket outer tube surface, -250 mm, 0°	K
121	TCO 7/0	TC (NiCr/Ni), cooling jacket outer tube surface, 350 mm, 0°	K
122	TCO 13/0	TC (NiCr/Ni), cooling jacket outer tube surface, 950 mm, 0°	K
123	T 310	TC (NiCr/Ni), aerosol extraction tube in off-gas pipe	K
124	T 513	Temperature bundle head top (wall)	K
125	T 514	Temperature bundle head, cooling water inlet	K
126	T 307	TC (NiCr/Ni), inner surface of inlet of off-gas pipe	K
127	TSH 2/90	TC (NiCr/Ni), shroud outer surface, -150 mm, 111°	K
128	T 104	Temperature quench water	K
129	T 201	Temperature steam generator heating pipe	K
130		Reserve	K
131	T 205	Temperature upstream steam flow instrument location 10 g/s	K
132	T 301A	Temperature downstream superheater	K

Chan	Designation	Instrument, location	Unit
133	T 302	Temperature superheater heating pipe	K
134	T 303	Temperature upstream total flow instrument location	K
135	T 401	Temperature upstream Ar flow instrument (orifice) location	K
136	T 403	Temperature of Ar at inlet cooling jacket	K
137	T 404	Temperature of Ar at outlet cooling jacket	K
138	T 501	Temperature in containment (near from bundle head)	K
139	T 502	Temperature at outer surface of containment, 0°, 2.4 m	K
140	T 503	Temperature at outer surface of containment, 270°, 2.2 m	K
141	T 504	Temperature at outer surface of containment, 270°, 3.2 m	K
142	T 505	Temperature at outer surface of containment, 90°, 3.2 m	K
143	T 506	Temperature at outer surface of containment, 270°, 3.6 m	K
144	T 507	Temperature at outer surface of containment, 90°, 3.6 m	K
145	T 508	Temperature at outer surface of containment, 180°, 4.0 m	K
146		Reserve	K
147	T 510	Temperature at outer surface of containment, 270°, 4.4 m	K
148	T 511	Gas temperature at bundle inlet	K
149	T 901	Reserve	K
150	T 304	Reserve (valve V 302)	K
151	*Ref. T02*	*Temperature of measuring crate 2 (reference temperature)*	K
152	P 201	Pressure steam generator	bar
153	P 204	Reserve	
154	P 205	Pressure at steam flow instrument location 10 g/s	bar
155	P 303	Pressure upstream total flow instrument (orifice) location	bar
156	P 401	Pressure upstream gas flow instrument location	bar
157	P 511	Pressure at bundle inlet	bar
158	P 512	Pressure at bundle outlet	bar
159	P 601	Pressure upstream off-gas flow instrument (orifice) F 601	bar
160		Reserve	
161	L 201	Liquid level steam generator	mm
162	L 501	Liquid level quench water	mm
163	L 701	Liquid level condensation vessel	mm
164	Fm 401	Argon gas mass flow rate, (20 mA), Bronkhorst	g/
165	P 411	Pressure Kr supply for heated rods	bar
166	P 403	Pressure Ar cooling of cooling jacket	bar

Chan	Designation	Instrument, location	Unit
167	P 406	Pressure insulation shroud/cooling jacket	bar
168	Fm 104	Flow rate quench water	g/s
169	F 204	Reserve	
170	Fm 205	Flow rate steam 10 g/s	g/s
171	F 303	Flow rate at bundle inlet (steam + argon), orifice	mbar
172	F 401	Reserve	
173	Fm 403	Flow rate cooling gas	g/s
174	F 601	Flow rate off-gas (orifice), 2000 mm from test section outlet (flange)	mbar
175	Fm 406	Flow rate argon into room between shroud and cooling jacket	g/s
176	E 201	Electric current steam generator	A
177	E 301	Electric current superheater	A
178	E 501	Electric current of left group of fuel rod simulators	A
179	E 502	Electric current of right group of fuel rod simulators	A
180	E 503	Electric voltage of left group of fuel rod simulators	V
181	E 504	Electric voltage of right group of fuel rod simulators	V
182	Hub_V302	Gas supply valve lift	%
183	*Ref. T03*	*Temperature of buffer amplifier (reference temperature)*	K
184…..199		Binary inputs	
200…..215		Analog outputs	
250	E 505	Electric power inner ring of fuel rod simulators	W
251	E 506	Electric power outer ring of fuel rod simulators	W
252	EP	Gross electrical power	kW

Indications:
TFS – TC at the surface of fuel rod simulators;
TSH – TC at the outer surface of shroud;
TIT – TC inside corner rods.

Table 9 QUENCH-19: diameters of the materials used at ORNL for the manufacture of High-Temperature Thermocouples [mm]

Material	As-received	Final
W/Re wires		0.25
MgO insulation OD	1.2	
steel tube of **SAE 304** material; OD / ID		2.4 / 1.4

Table 10 QUENCH-19; map of TFS thermocouples

elevation, mm	-250	-150	-50	50	150	250	350	450	550	650	750	850	950	1050	1150	1250	1350
elev. No. / rod No.	1	2	3	4	5	6	7	8	9	10	11	12	13	14	15	16	17
1		N					N				W*		W				
2					N				N			W		W			
3			N					N		W*			W*				W
4	N								N						W*		
5						N								W			
6								N		W							W
7																	
8				N					N			W				W	
9								N					W*		W		
10																	
11						N											
12															W		
13																W	
14				N					N		W*			W			
15													W				
16												W					
17					N				N				W				
18																	
19														W			
20																	
21							N						W				
22									N			W					
23																	
24																	
TC quantity:	1	1	1	2	2	2	2	3	6	2	2	4	6	4	3	2	2

TC to bundle bottom: 8 W/Re + 20 NiCr/Ni

TC to bundle top: 17 W/Re

N NiCr/Ni (totally 20)

W W/Re (totally 25)

W* failed during pre-tests

Table 11 QUENCH-19; Sequence of events

Time, s	Event
0 (11:29:36)	Start data recording. TFS 2/12 = 857 K, el. power at 4.86 kW.
260	System pressure: at bundle bottom P511 = 2.1 bar, at bundle top P512 = 2.05 bar; rod inner pressure (Kr) P411 2.16 bar; TFS 2/12 = 873 K
1586	Rod inner pressure regulated from P411 = 2.4 to 2.2 bar; system pressure P511 = 2.14 bar; TFS 2/12 = 1103 K
4083	Temperature plateau of TFS 2/12 = 933 K reached; Pel=11.27 kW
2200…6450	Downwards relocation of collapsed *water front in annulus* between shroud and cooling jacket (sequential reaction of TCI 12/180…TCI 7/180…TCI 9/270)
5953	Corner rod B removed from bundle (reaction of TFS 8/12, TFS 19/14)
6018	Transient stage start with electrical power rate of 5.88 W/s
6570…8260	Continuous increase of hydrogen release rate
6834	Onset of drop of rod inner pressure: P411 decrease. Probable leakage at Kr inlet at bundle bottom
7127	Switch to *constant* electrical power of 18.32 kW
7700	First indication of Kr release (mass spectrometer): first cladding failure. *Increase of hydrogen release rate*.
8260	*Sharp increase of hydrogen release rate*. Beginning of continuous Kr release (*cladding failures*).
8838	Corner rod F removed from bundle (reaction of TFS 14/4, TFS 22/9)
9107	Initiation of *fast water injection* (4 L). First indication of cooling (T 511)
9107…9185	Intensive reflood water evaporation indicated by mass spectrometer
9108…9126	Decrease of electrical power from 18.32 to 4.34 kW
9109…9129	Quick wetting of cladding surface thermocouples at elevations -250…+350 mm
9110	*Temperature maximum reached: extrapolated TFS 1/13 ≈* ***1800 K*** *and TFS 2/12 = 1730 K*; TSH 12/180 = 1469 K
9112…9140	Quick temporary cooling of bundle at elevation 1050…1350 mm due to steam condensation at bundle head
9114	Switch of carry Ar flow from bundle bottom to bundle top
9116	*Start of quench* water flow (Fm 104), water at 150 mm (L 501)
9119	Probable massive failures of claddings: decrease of inner rod pressure to system pressure (2.3 bar -> 2.15 bar): P 411 ≤ P 511
9136	Maximal flow rate of quench water reached: Fm 104 = 46 g/s
9150	Start of water level raising, delayed by a gradual increase in flow rate Fm 104 (20 s, feature of the diaphragm pump) and a varying water evaporation rate
9173…9285	Sequential wetting of cladding surface thermocouples at elevations 450…1250 mm
9482	Maximum of water level reached: L 501 = 1319 mm
9760	Quench pump shut off. Electrical power shut off
10281 (14:20:57)	End of data recording
15:30:00	Corner rod D removed from bundle

Table 12 Cross sections of the QUENCH-19 test bundle for metallographic examination

Sample	Sample length (mm)	Axial position (mm)		Remarks
		bottom	top	
			54	Remainder
Cut	4	54	58	
QUE-19-1	16	**58**	**64**	Spacer 2, 58 mm, 64 mm polished
Cut	4	56	60	
QUE-19-a	70	60	130	
Cut	4	130	134	
QUE-19-2	16	134	**150**	TC elevation 5, 150 mm polished
Cut	4	150	154	
QUE-19-b	276	154	430	
Cut	4	430	434	
QUE-19-3	16	434	**450**	TC elevation 8, 450 mm polished
Cut	4	450	454	
QUE-19-c	82	454	536	
Cut	4	536	540	
QUE-19-4	16	540	**556**	Spacer 3, 556 mm polished
Cut	4	556	560	
QUE-19-5	16	**560**	576	
Cut	4	576	580	
QUE-16-d	50	580	630	
Cut	4	630	634	
QUE-19-6	16	634	**650**	TC elevation 10, 650 mm polished
Cut	4	650	654	
QUE-19-e	76	654	730	
Cut	4	730	734	
QUE-19-7	16	734	**750**	***sent to ORNL***
Cut	4	750	754	
QUE-19-8	16	**754**	770	**TC elevation 11, 754 mm polished**
Cut	4	770	774	
QUE-19-f	56	774	830	
Cut	4	830	834	
QUE-19-9	16	834	**850**	***sent to ORNL***
Cut	4	850	854	
QUE-19-10	16	**854**	870	**TC elevation 12, 854 mm polished**
Cut	4	870	874	
QUE-19-g	54	874	928	
Cut	4	928	932	
QUE-19-11	16	932	**948**	***sent to ORNL***
Cut	4	948	952	
QUE-19-12	16	**952**	968	**TC elevation 13, 952 mm polished**
Cut	4	968	972	
QUE-19-h	66	972	1038	
Cut	4	1038	1042	
QUE-19-13	16	**1042**	1058	Spacer 4, 1042 mm polished
Cut	4	1058	1062	
		1062		Remainder

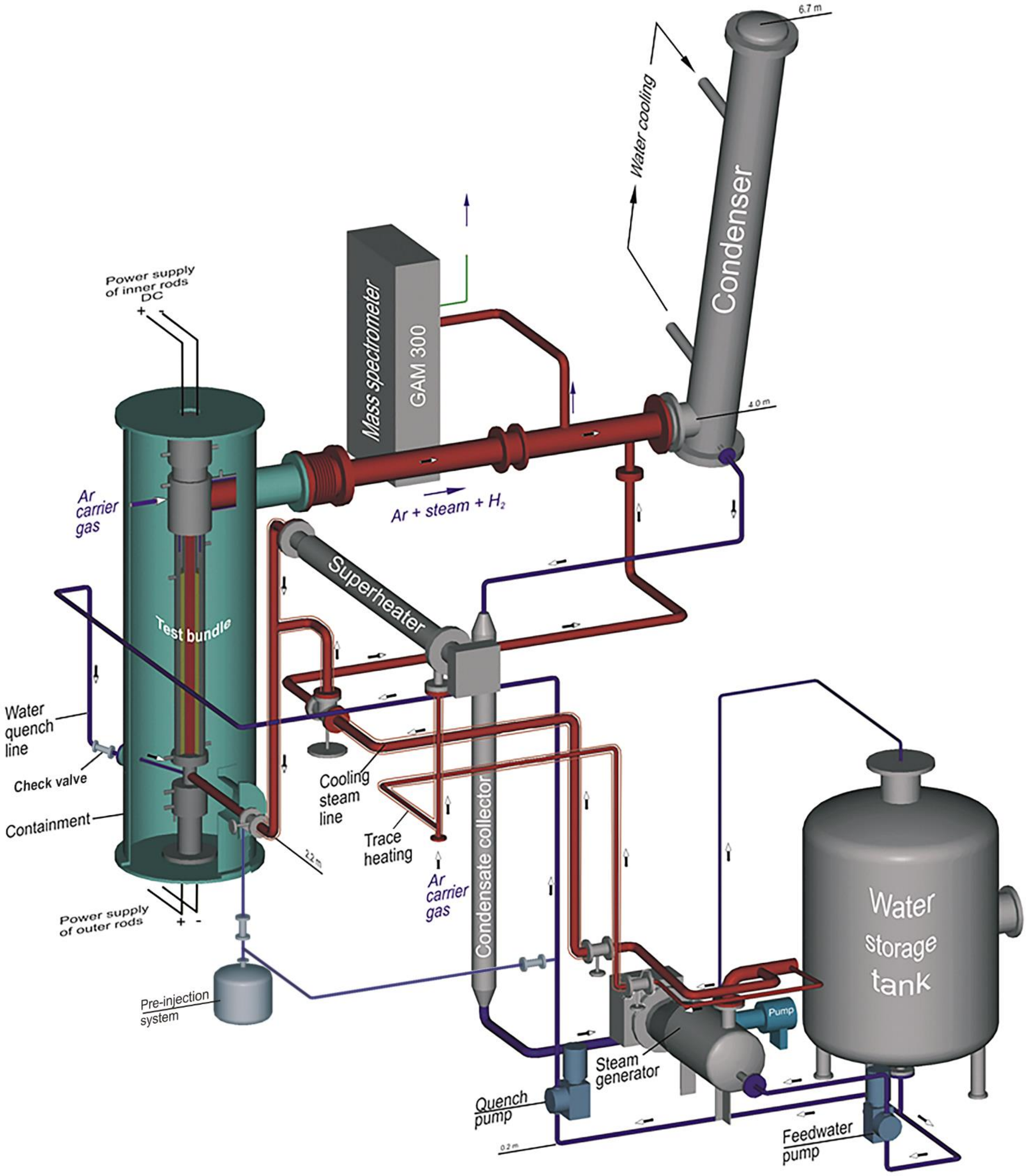

Figure 1 QUENCH Facility - Main components.

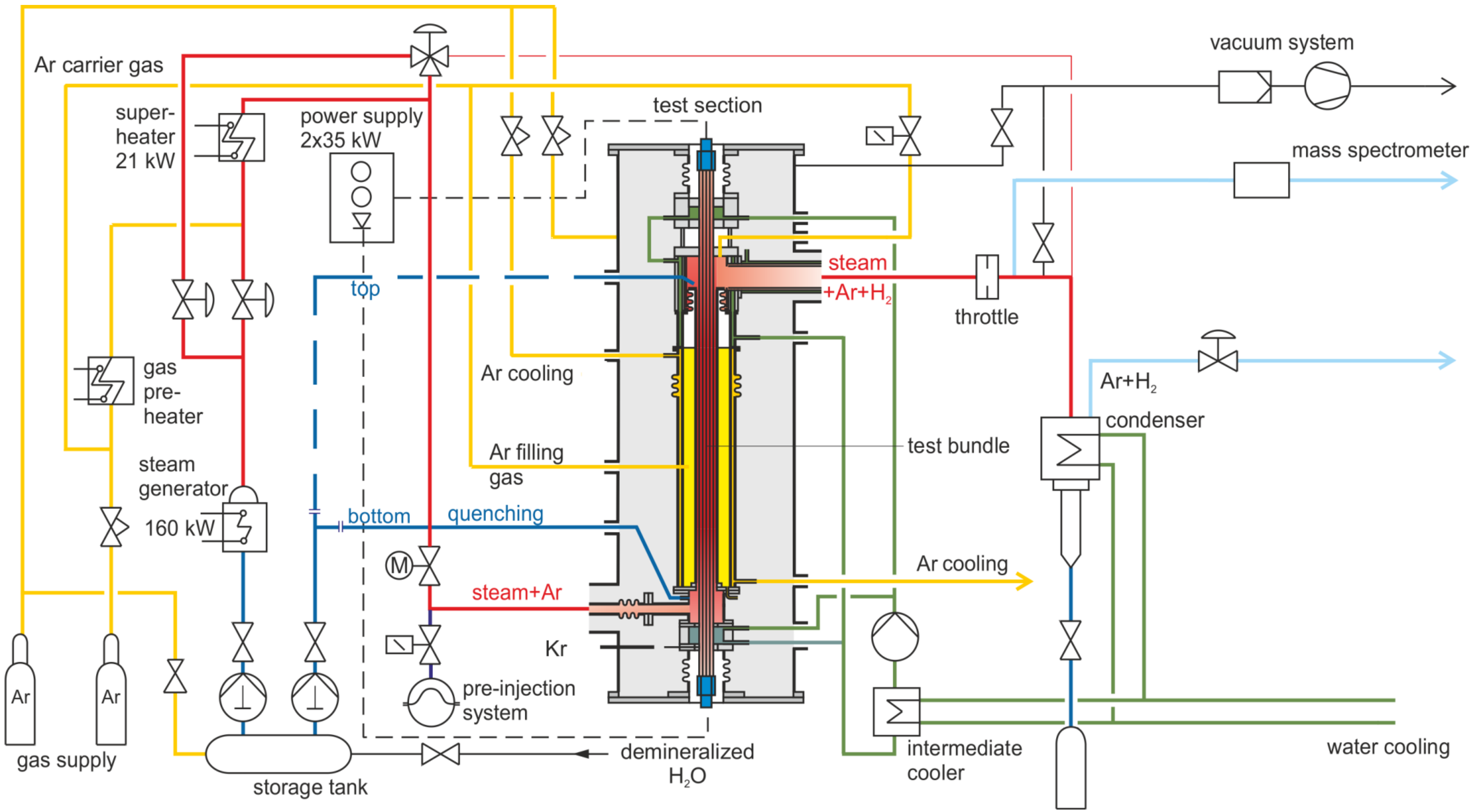

Figure 2 QUENCH-19; flow diagram of the QUENCH facility.

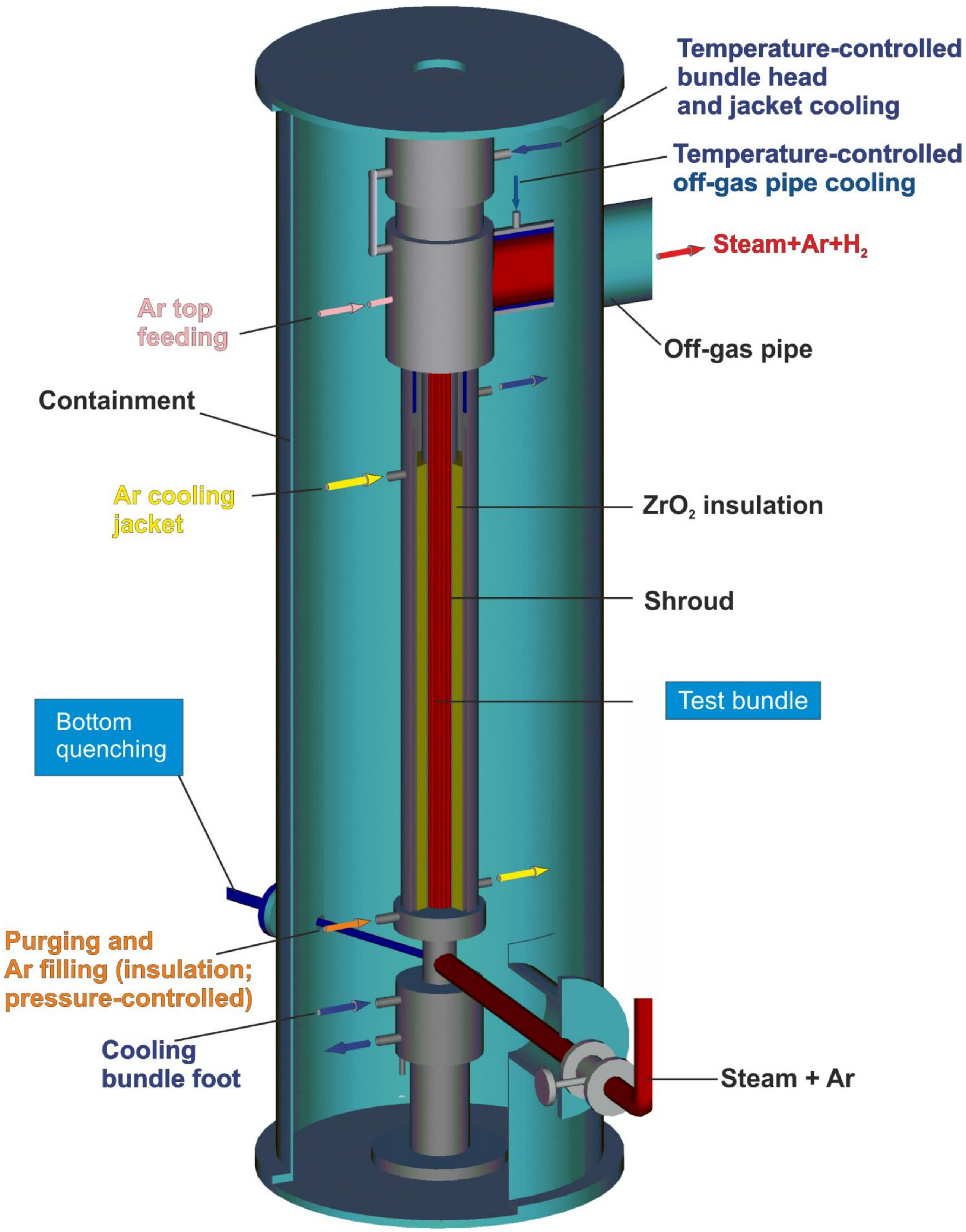

Figure 3 QUENCH-19; containment and test section.

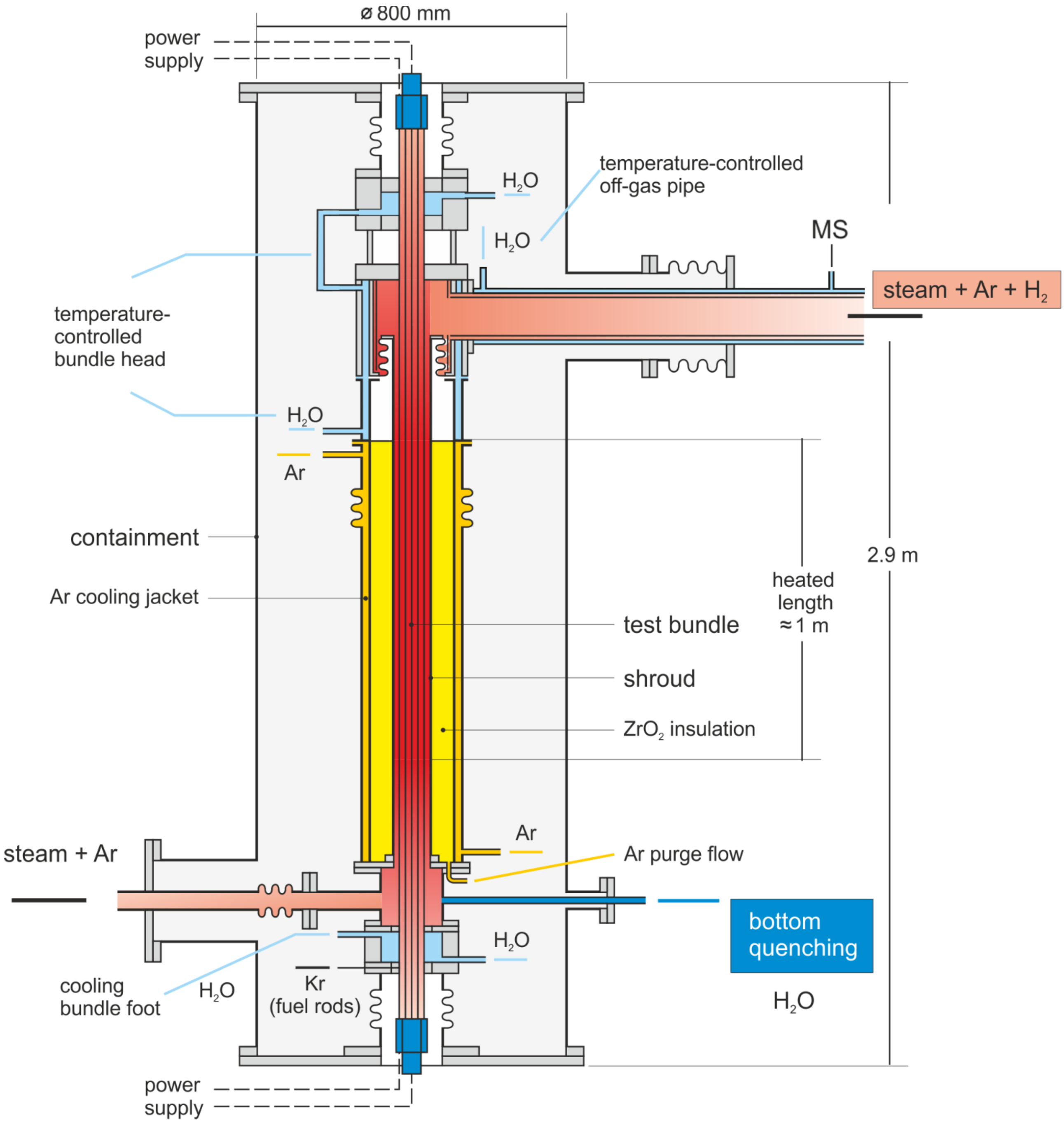

Figure 4 QUENCH-19; test section with flow lines.

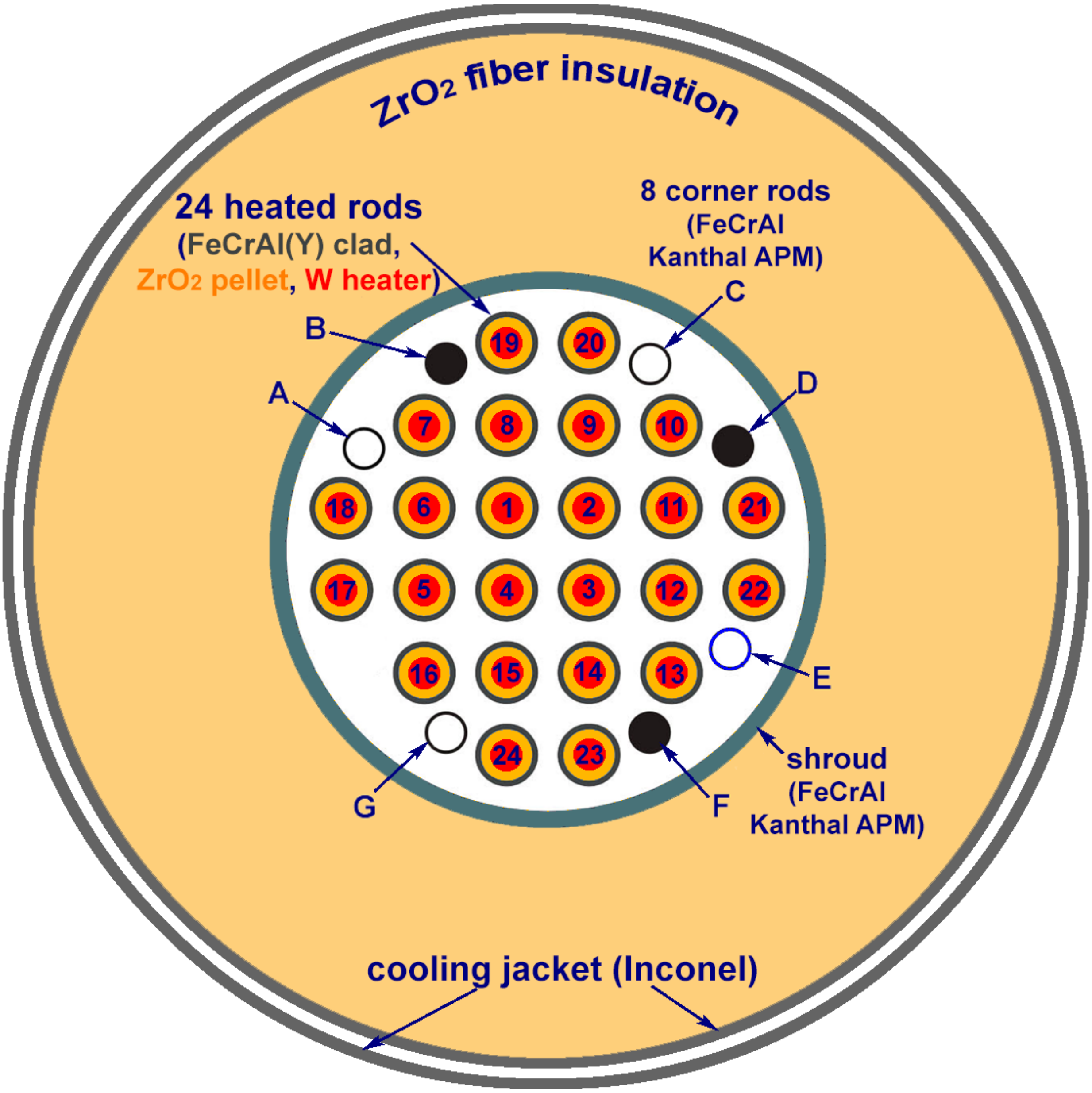

Figure 5 QUENCH-19; cross section of the test bundle.

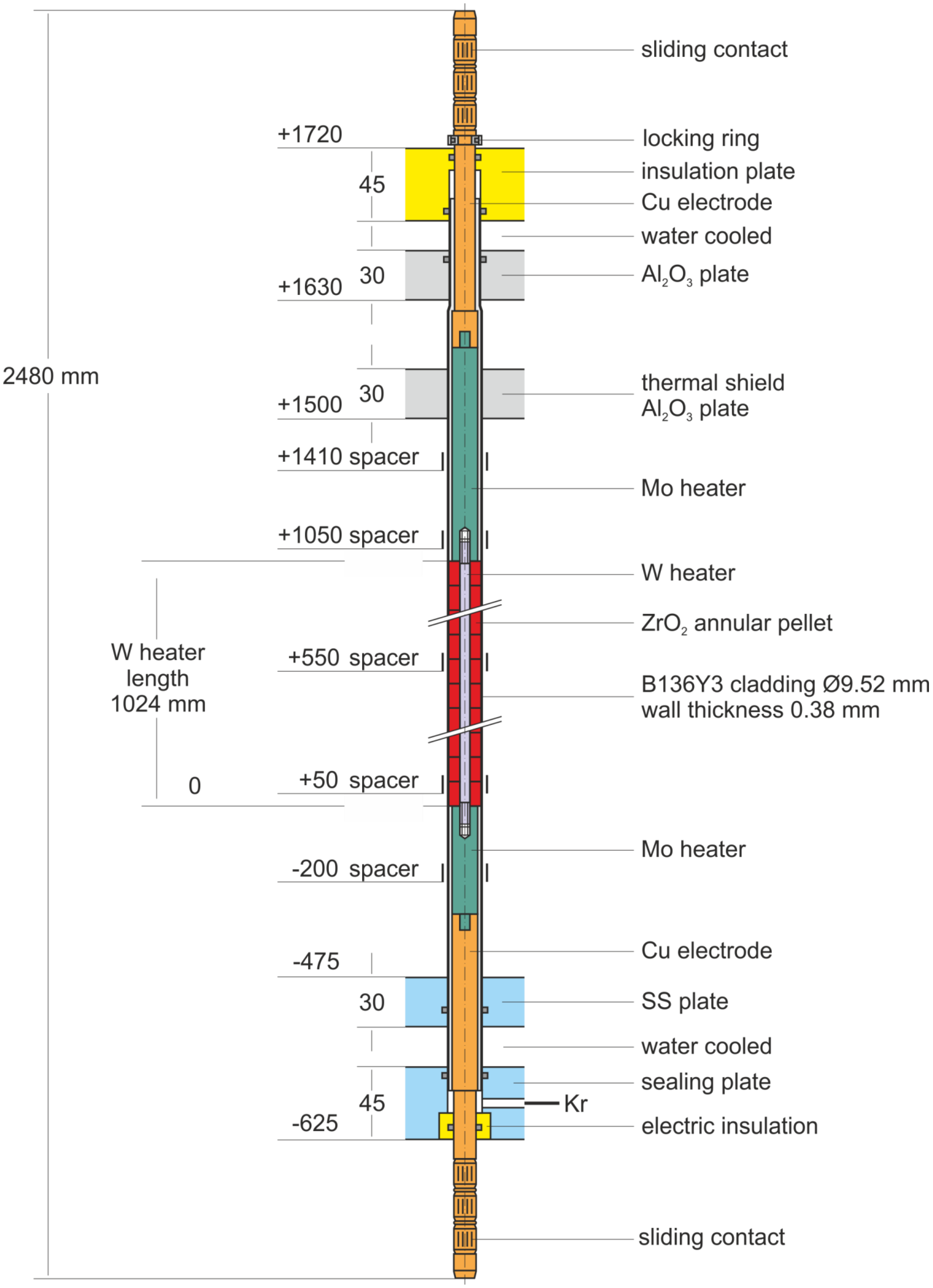

Figure 6 QUENCH-19; heated rod.

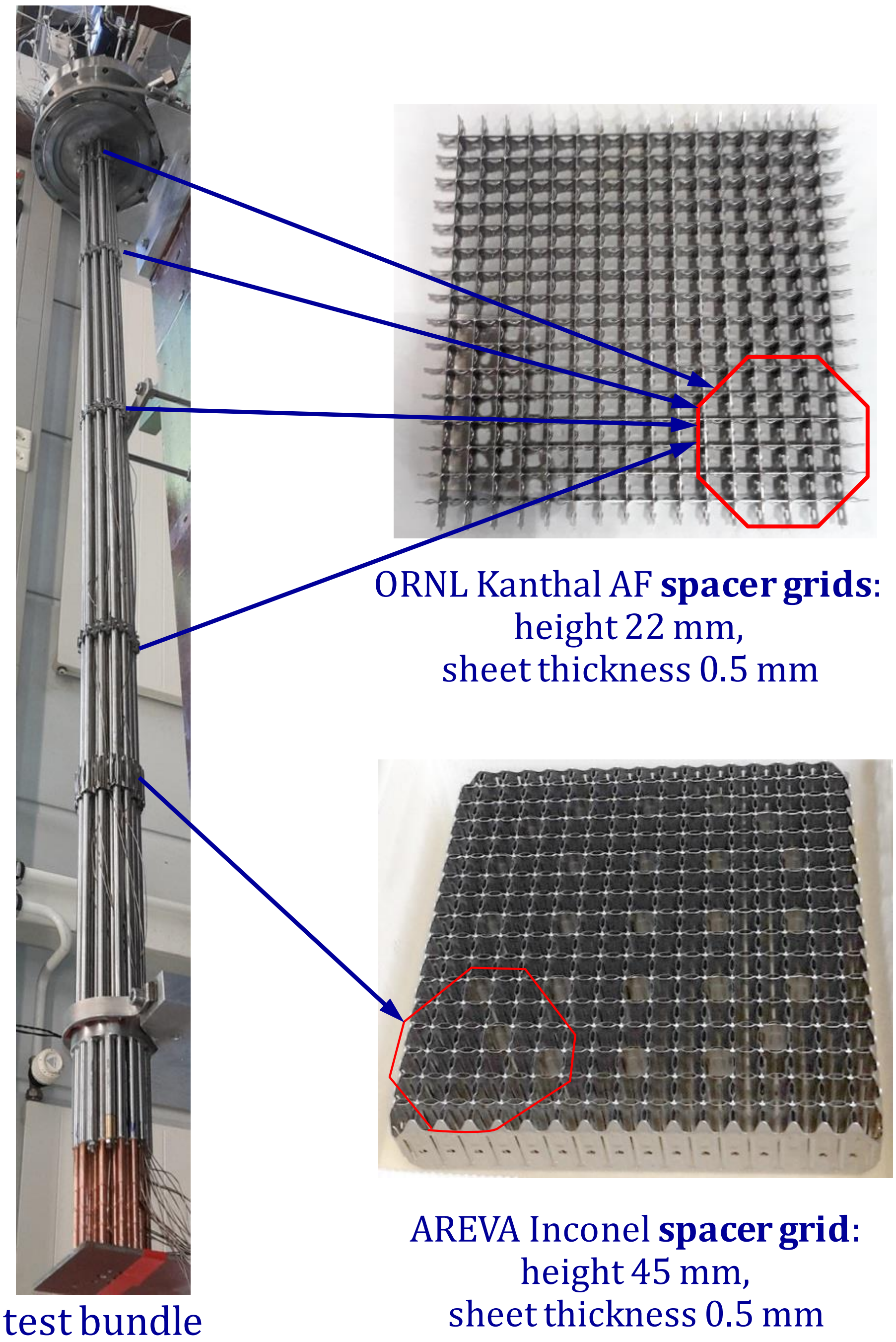

Figure 7 QUENCH-19; spacer grids.

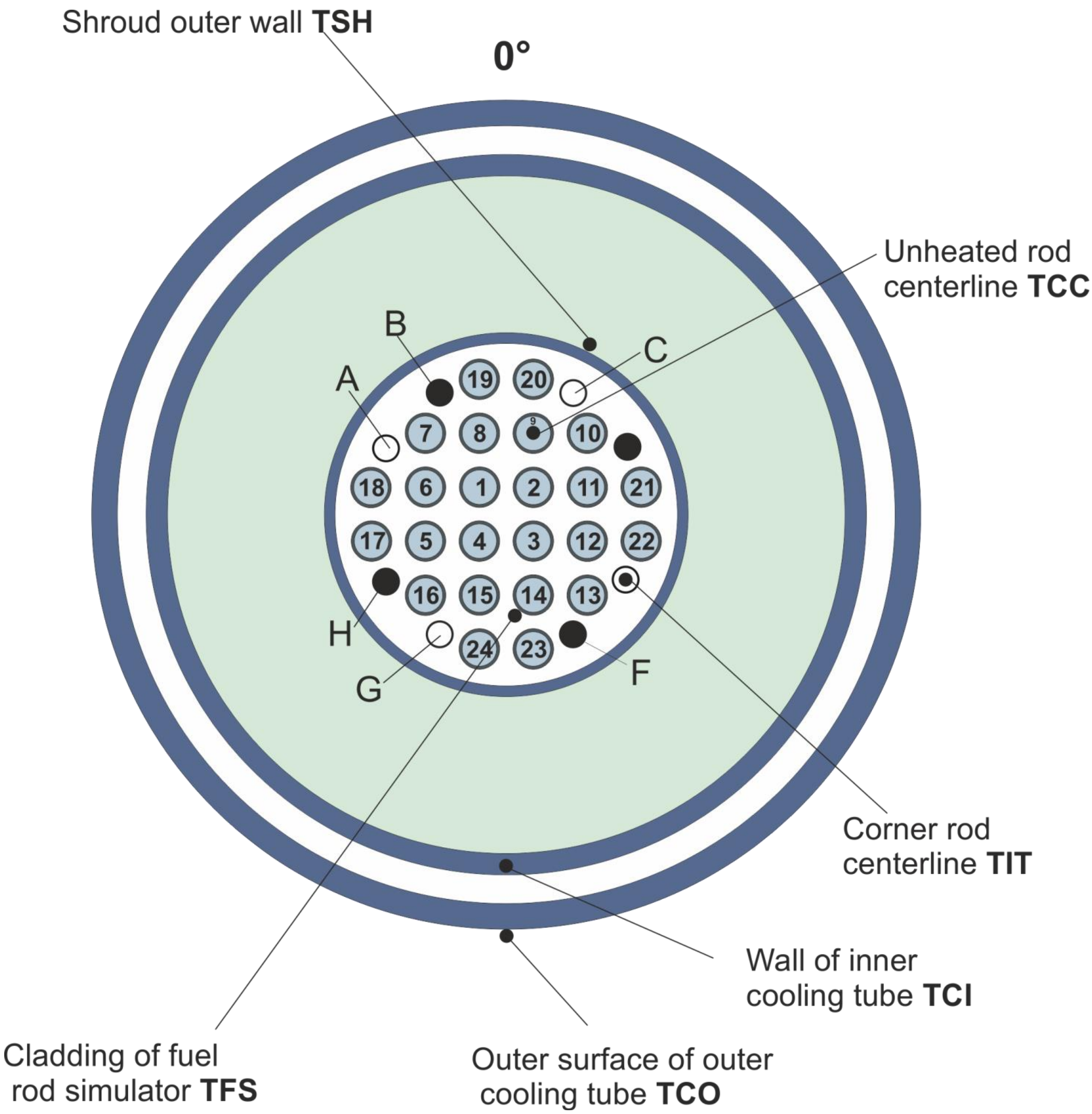

Figure 8 QUENCH-19; designation of the various thermocouples.

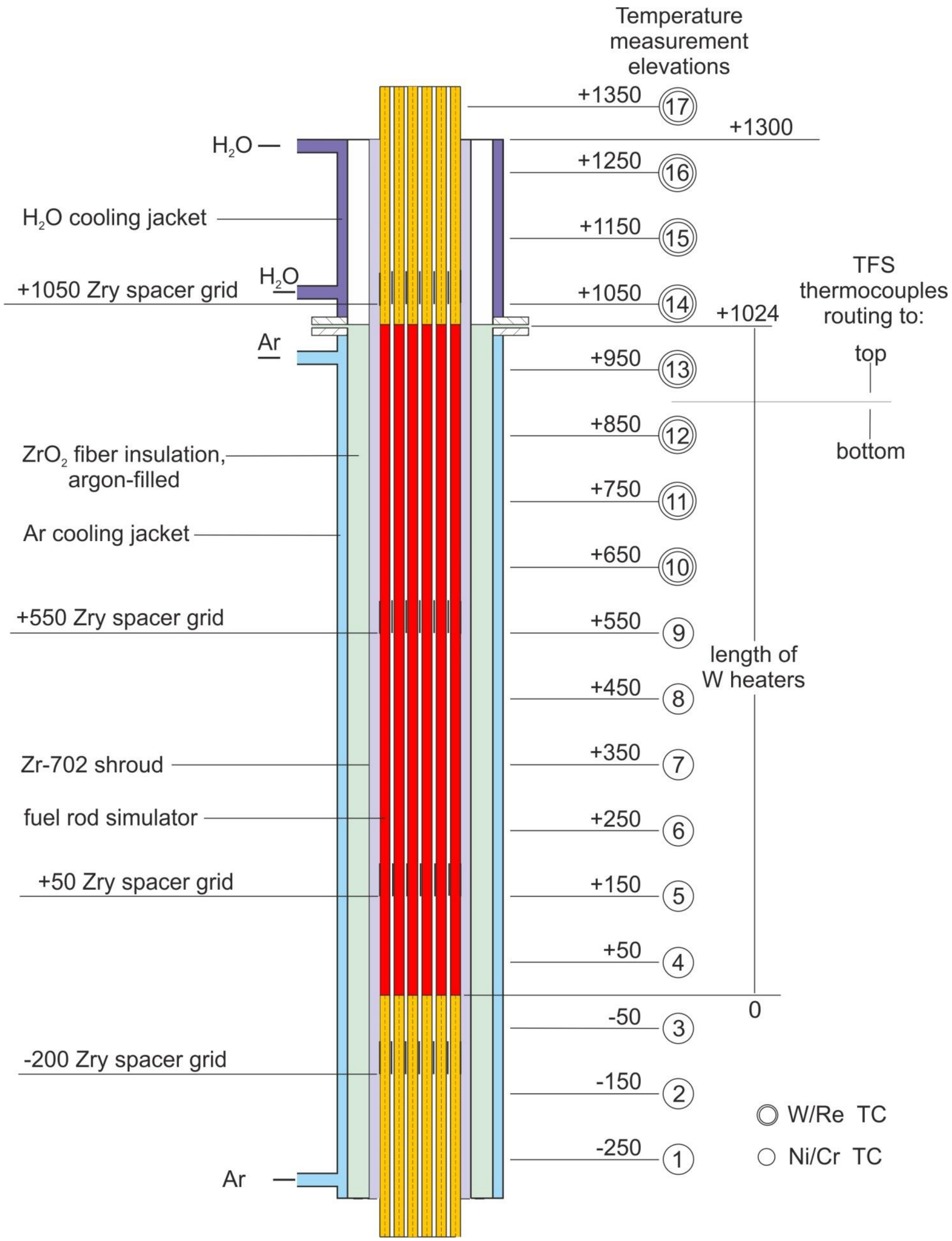

Figure 9 QUENCH-19; axial locations of thermocouples.

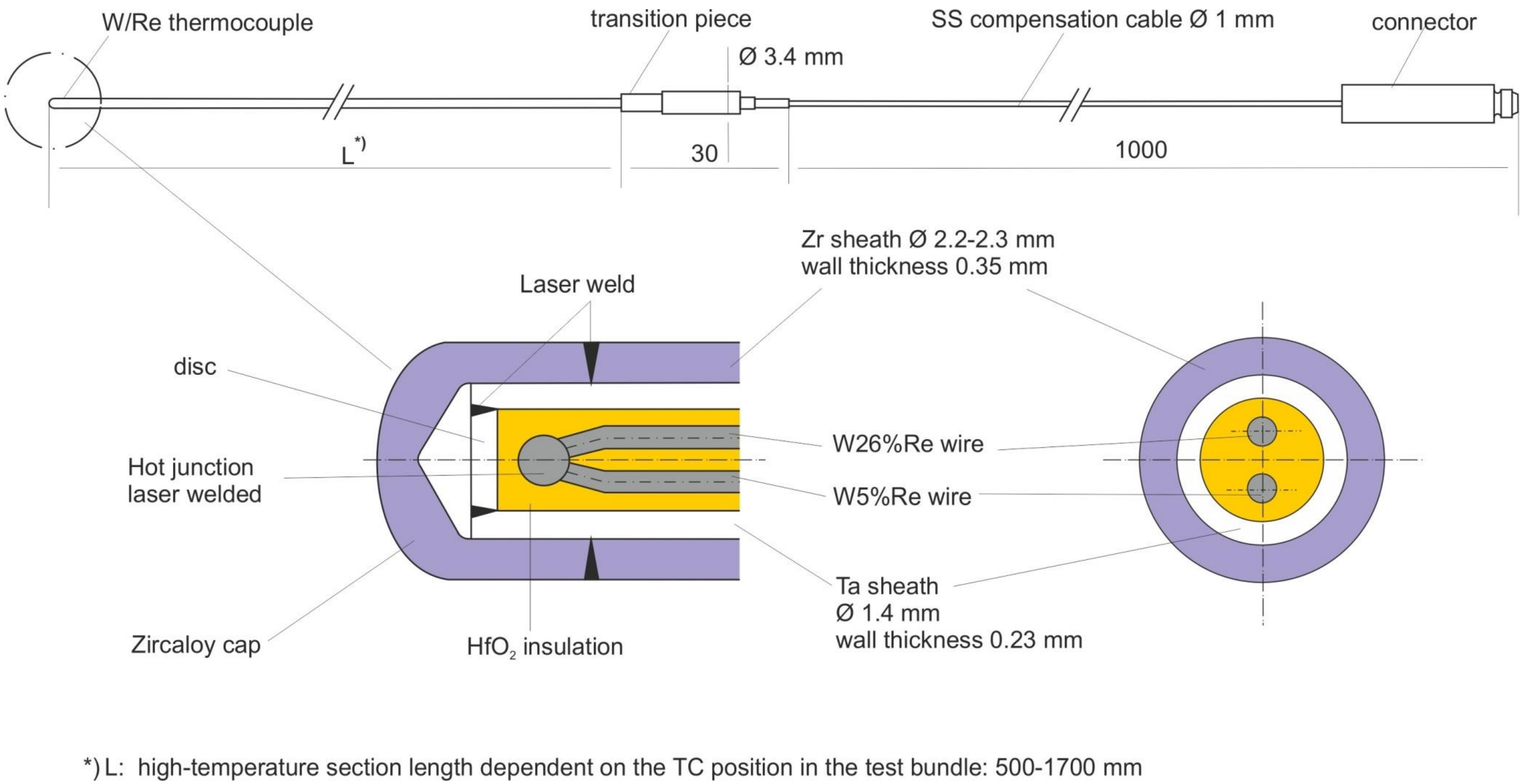

Figure 10 QUENCH-19; high temperature thermocouple.

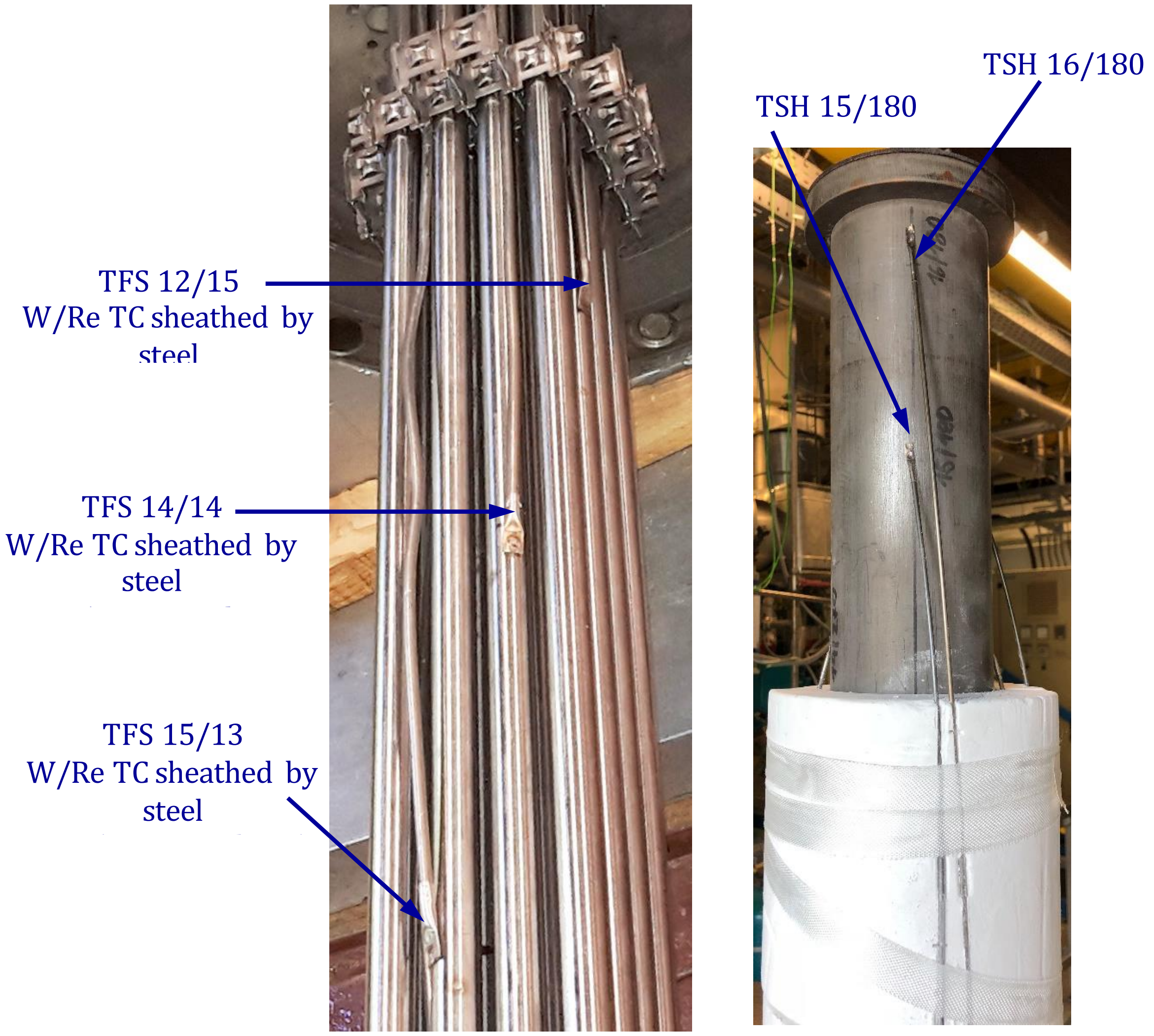

Figure 11 QUENCH-19; TC fastening at cladding (TFS) and shroud (TSH)

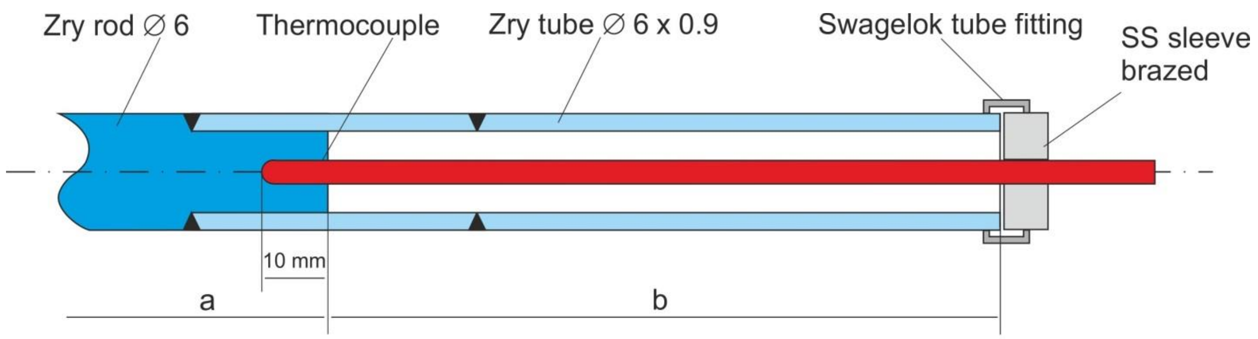

Rod A: TIT/ A12 (850 mm), W/Re, ∅ 2.1 mm, a = 460 mm, b = 1980 mm

Rod C: TIT/ C11 (750 mm), W/Re, ∅ 2.1 mm, a = 560 mm, b = 1880 mm

Rod E: TIT/ E10 (650 mm), W/Re, ∅ 2.1 mm, a = 660 mm, b = 1780 mm

Rod G: TIT G/9 (550 mm), W/Re, ∅ 2.1 mm, a = 760 mm, b = 1680 mm

Figure 12 QUENCH-19; arrangement of the thermocouples inside the corner rods.

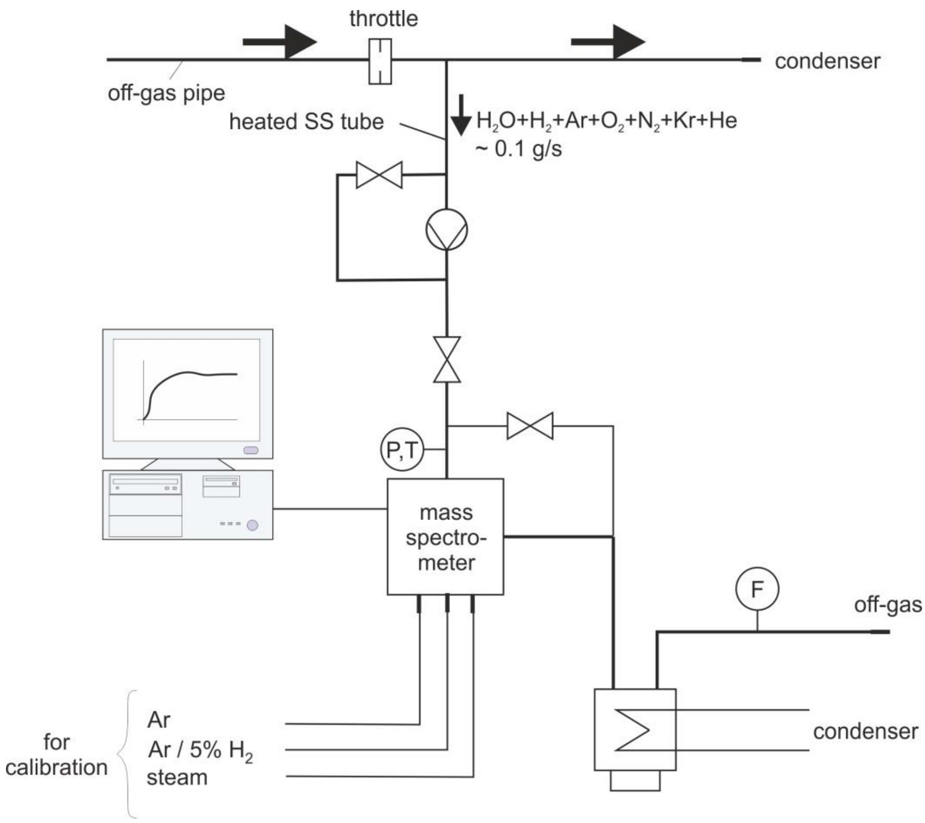

Figure 13 QUENCH-19; gas measurement with the GAM 300 mass spectrometer.

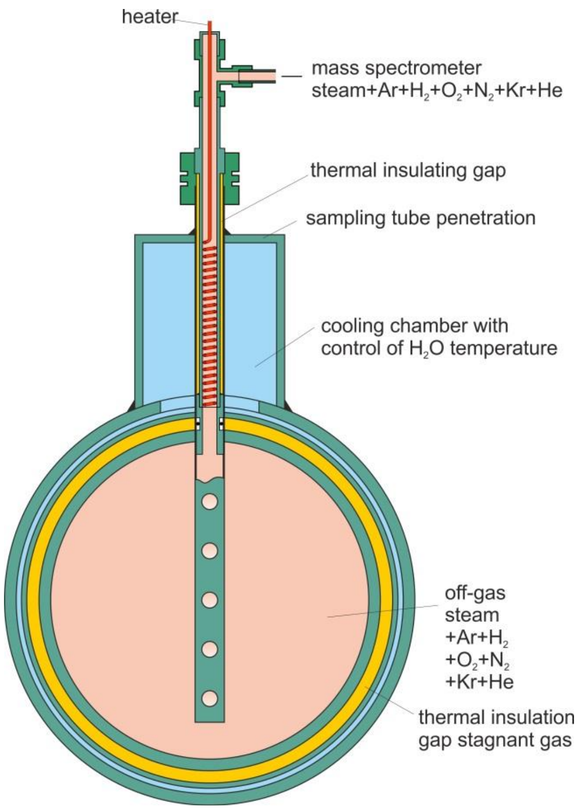

Figure 14 QUENCH-19; mass spectrometer sampling position at the off-gas pipe.

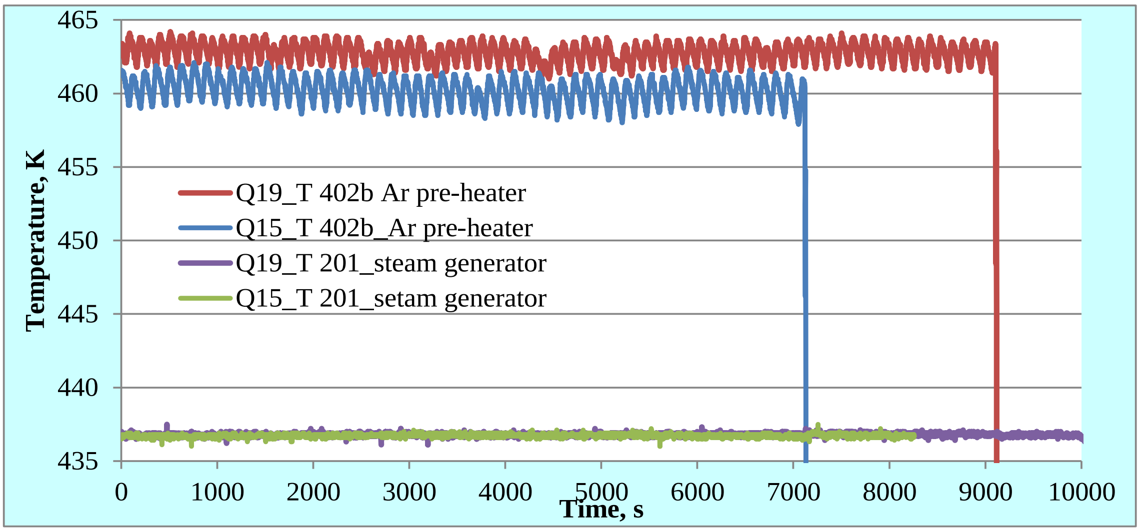

Figure 15 Ar and steam temperatures before superheater: comparison of QUENCH-15 and -19

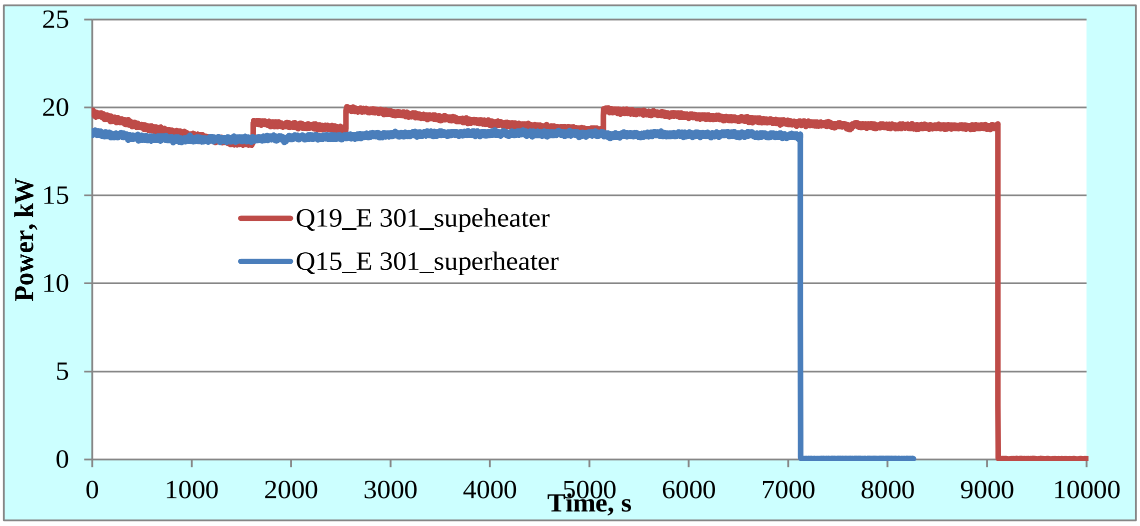

Figure 16 Power of gas superheater: comparison of QUENCH-15 and -19.

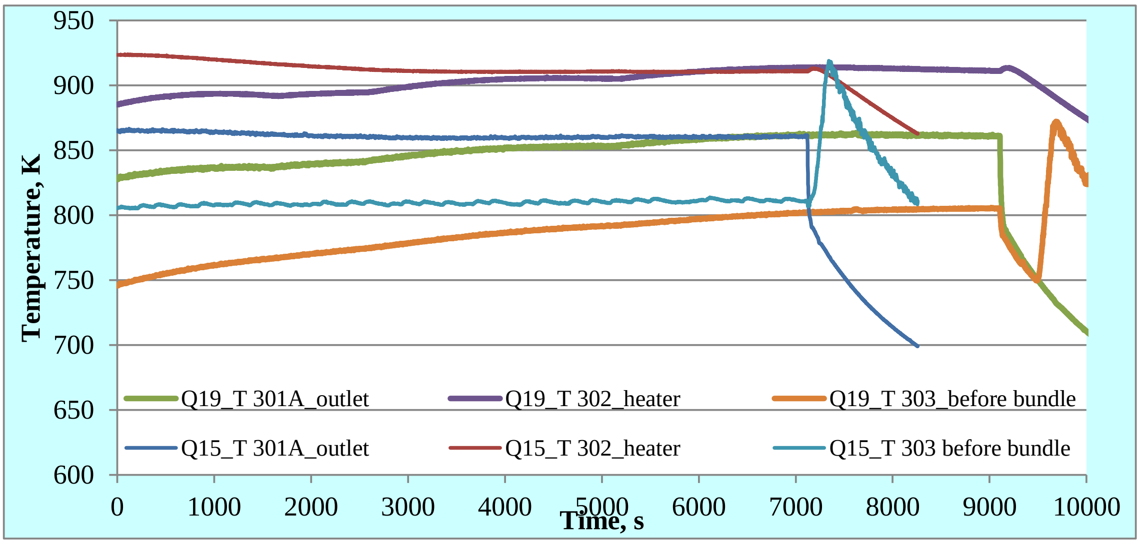

Figure 17 Temperatures of superheater heaters, at superheater outlet, before bundle inlet: comparison of QUENCH-15 and -19.

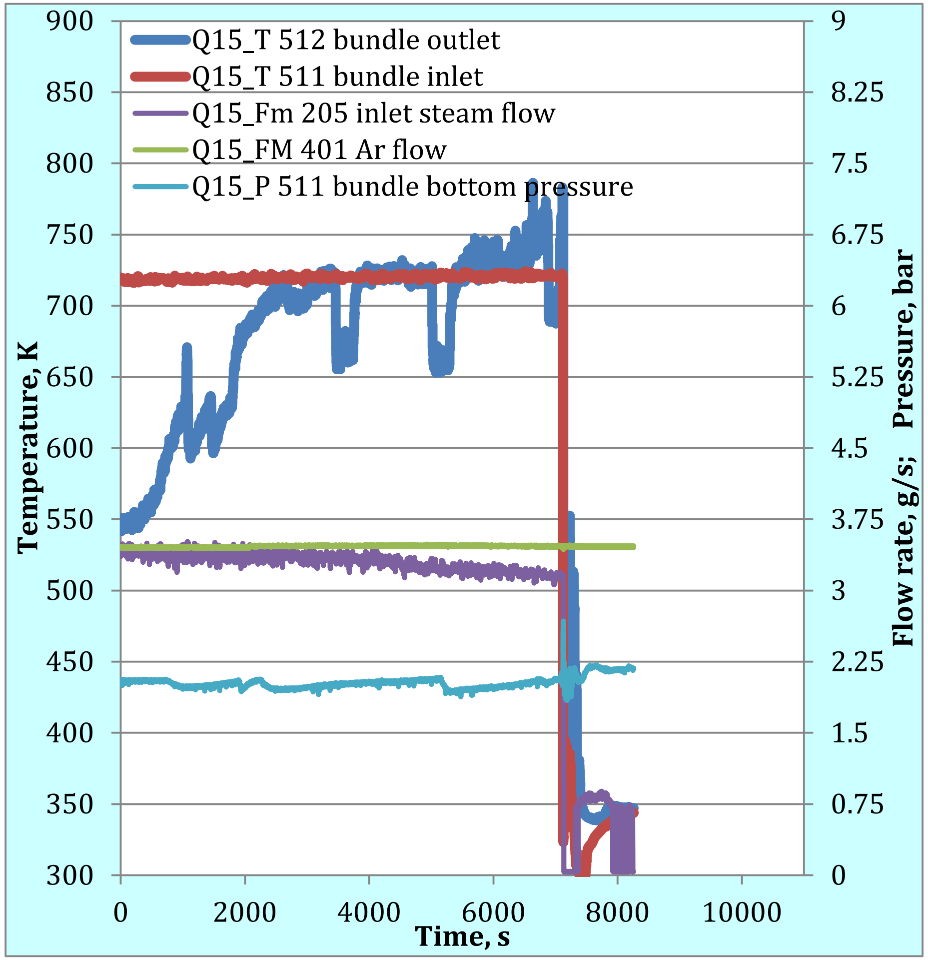

QUENCH-15: inlet gas (steam + Ar) $T_g \approx 720$ K; steam flow rate 3.2 < Fs <3.4 g/s; Ar flow rate F_{Ar} = 3.5 g/s

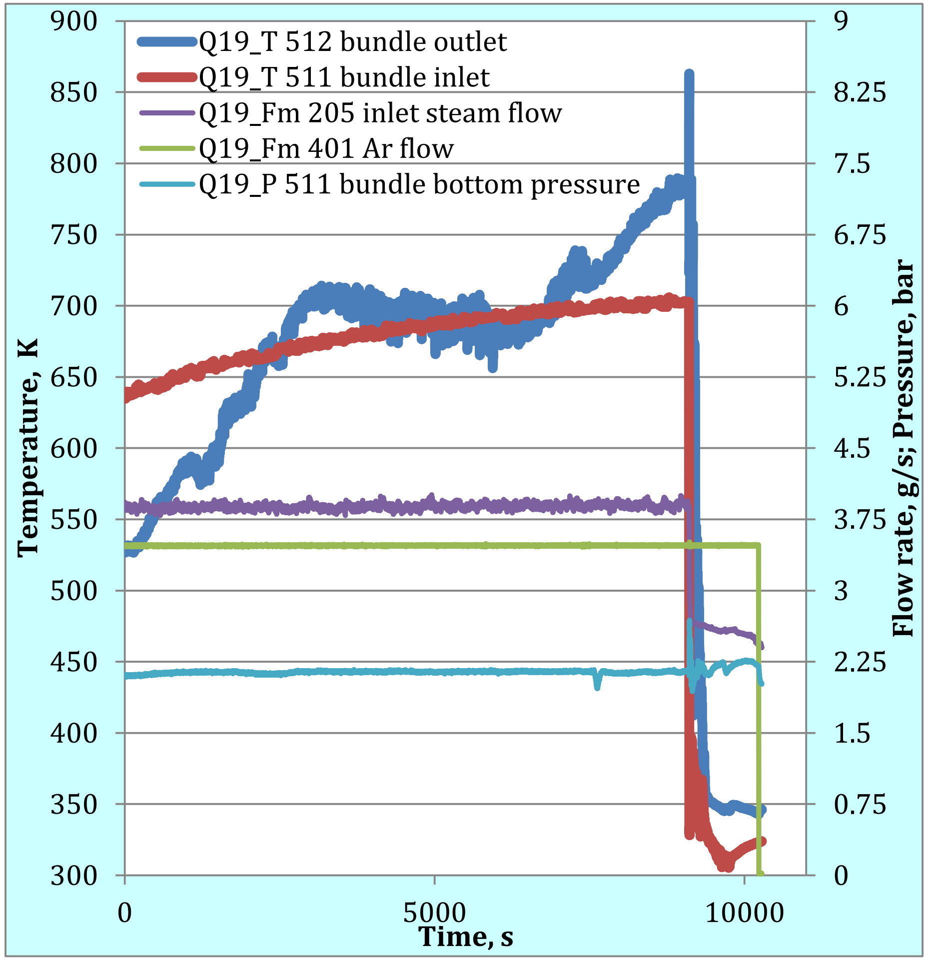

QUENCH-19: inlet gas (steam + Ar) 640 < T_g < 700 K; steam flow rate Fs ≈ 3.8 g/s; Ar flow rate F_{Ar} = 3.5 g/s

Figure 18 Parameters of gas atmosphere at bundle inlet and outlet for QUENCH-15 and -19.

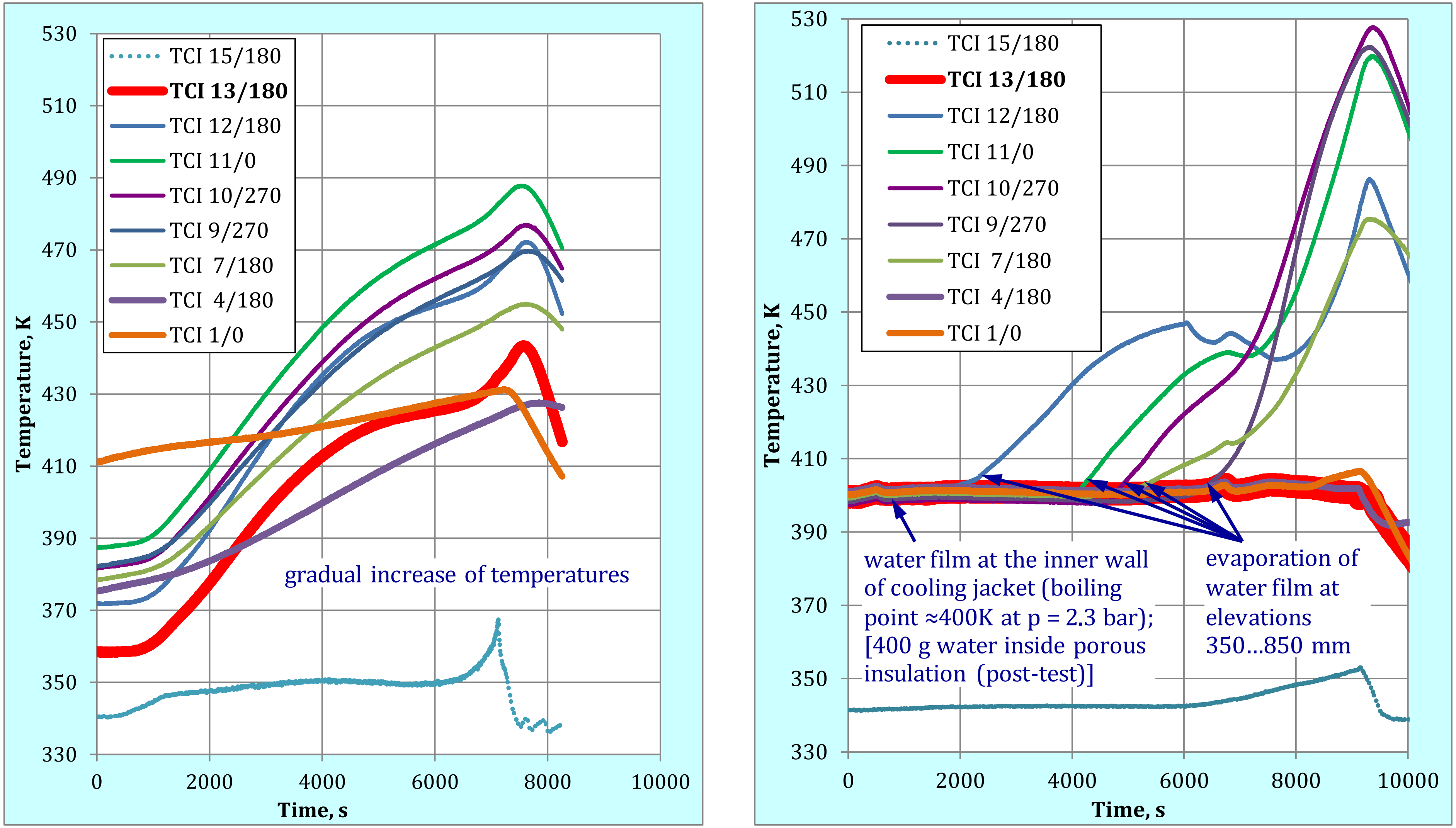

Figure 19 Comparison of readings of the TCI thermocouples installed inside the inner tube of cooling jacket for QUENCH-15 and QUENCH-19.

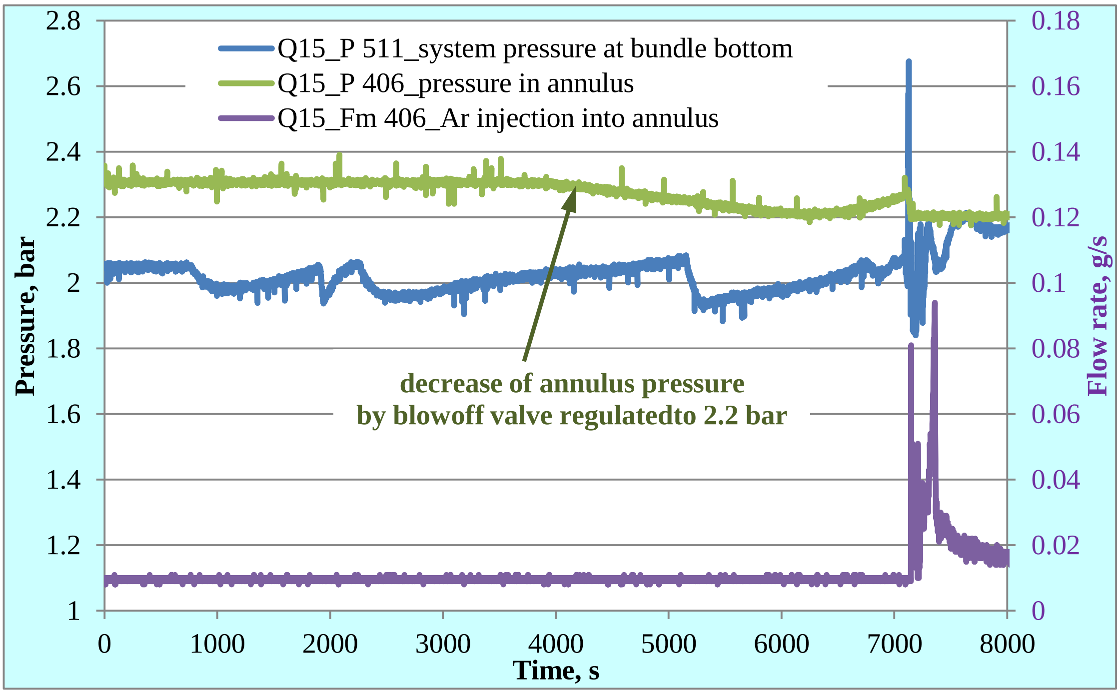

QUENCH-15: behavior of Ar in annulus (bundle system pressure for comparison)

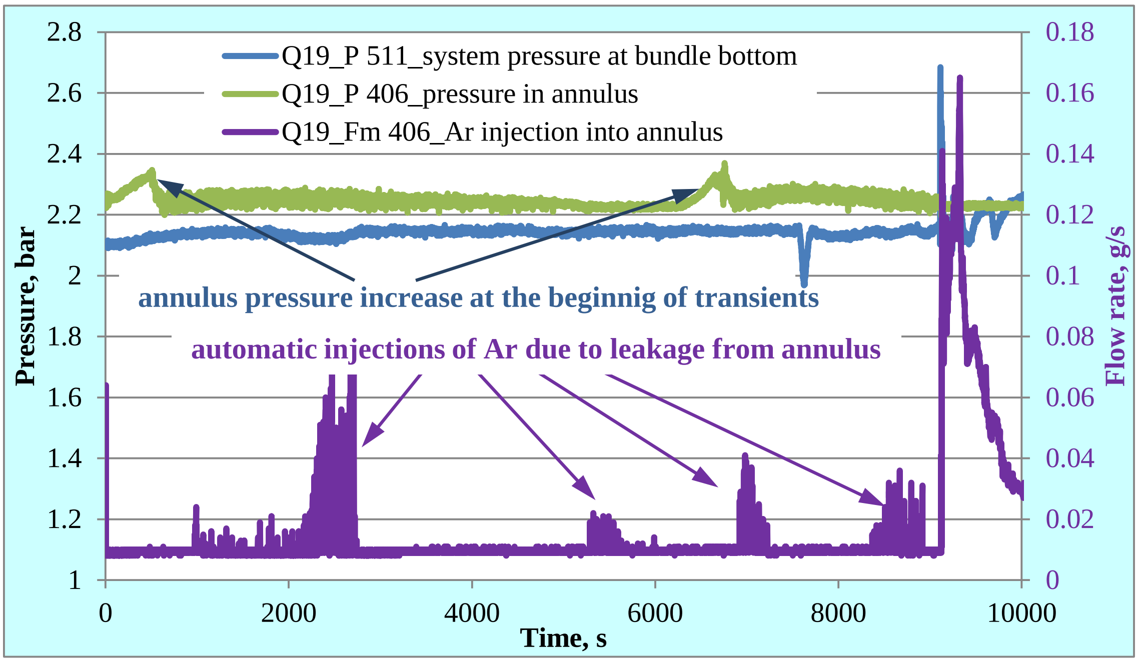

QUENCH-15: behavior of Ar in annulus (bundle system pressure for comparison)

Figure 20 Comparison of Ar behavior in annulus between shroud and cooling jacket for QUENCH-15 and QUENCH-19: intermittent automatic Ar injection during QUENCH-19 evidences gas leakage from the annulus.

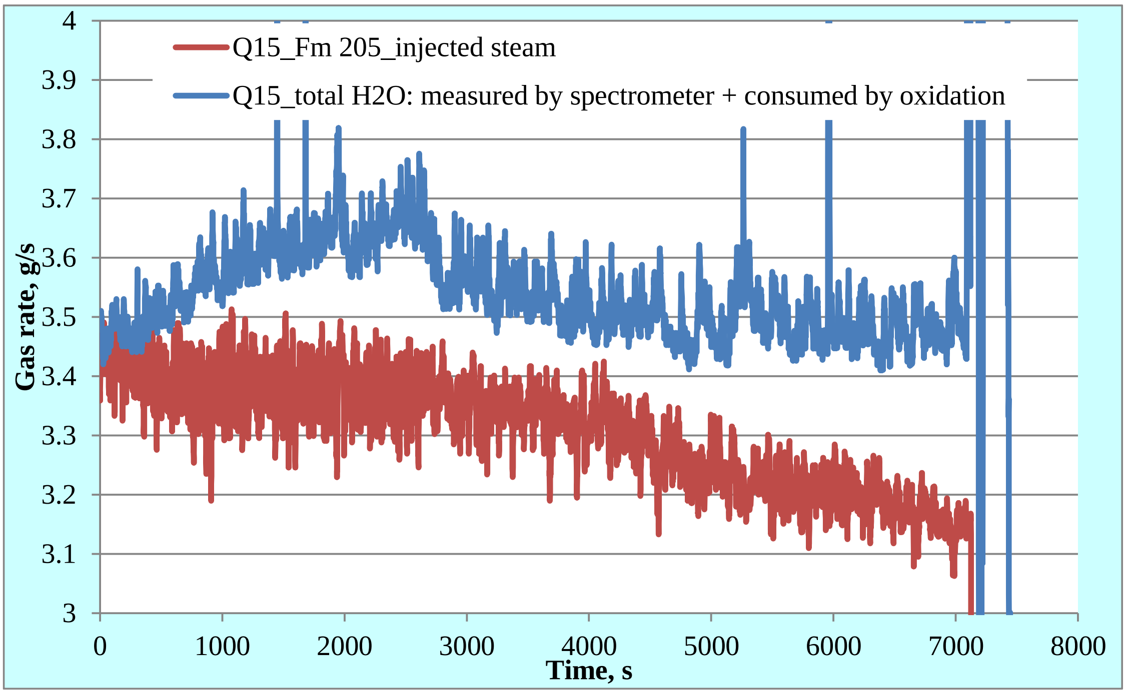

QUENCH-15: injected steam (estimation) as well as sum of outlet steam and steam consumed for ZIRLO oxidation

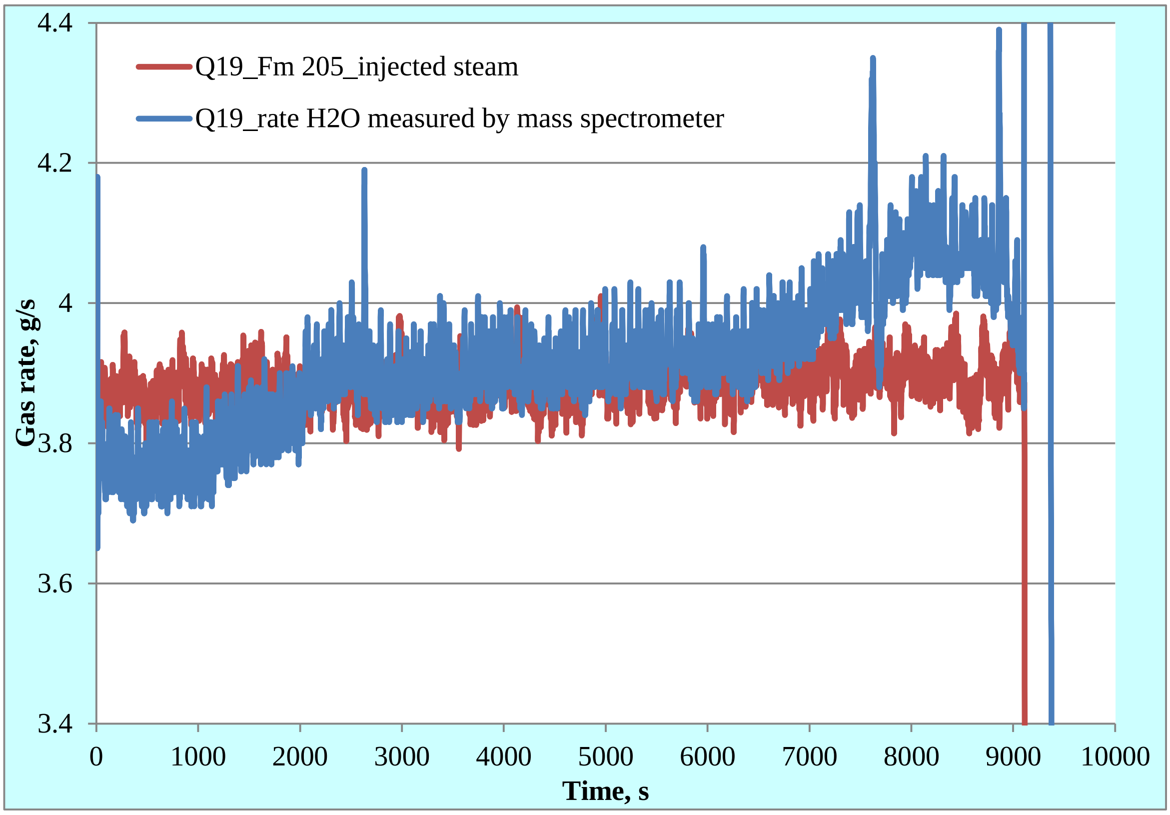

QUENCH-19: injected steam and sum steam in off-gas pipe

Figure 21 Comparison of steam balance for QUENCH-15 and -19: the reason of increase of steam output at about 6200 s is release of steam from annulus into bundle through the gap at upper shroud flange.

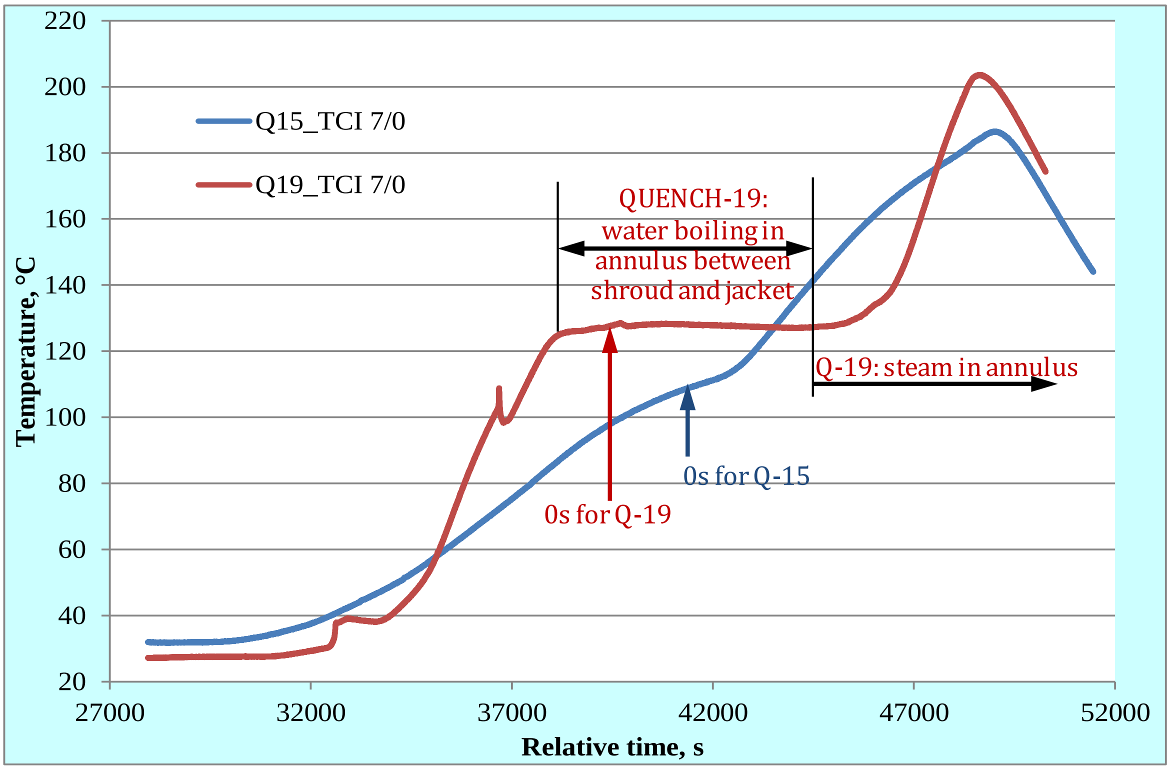

Period of constant temperature in annulus between shroud and cooling jacket of the QUENCH-19 bundle in comparison to continuous temperature increase for QUENCH-15

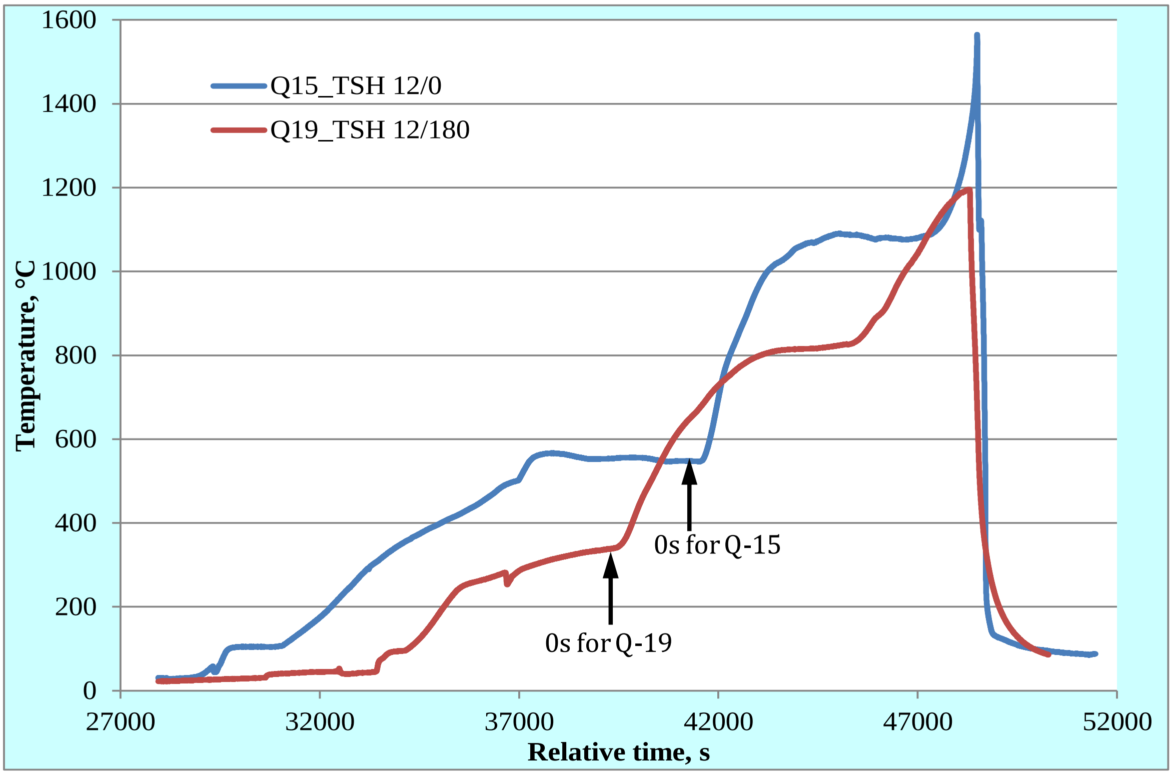

Decreased shroud temperatures for the QUENCH-19 bundle in comparison to QUENCH-15 due to heat loss through the humid heat insulation

Figure 22 Comparison of temperatures at inner and outer boundaries of heat insulation for QUENCH-15 and -19 (time axis accords the day time in seconds for the QUENCH-15 test)

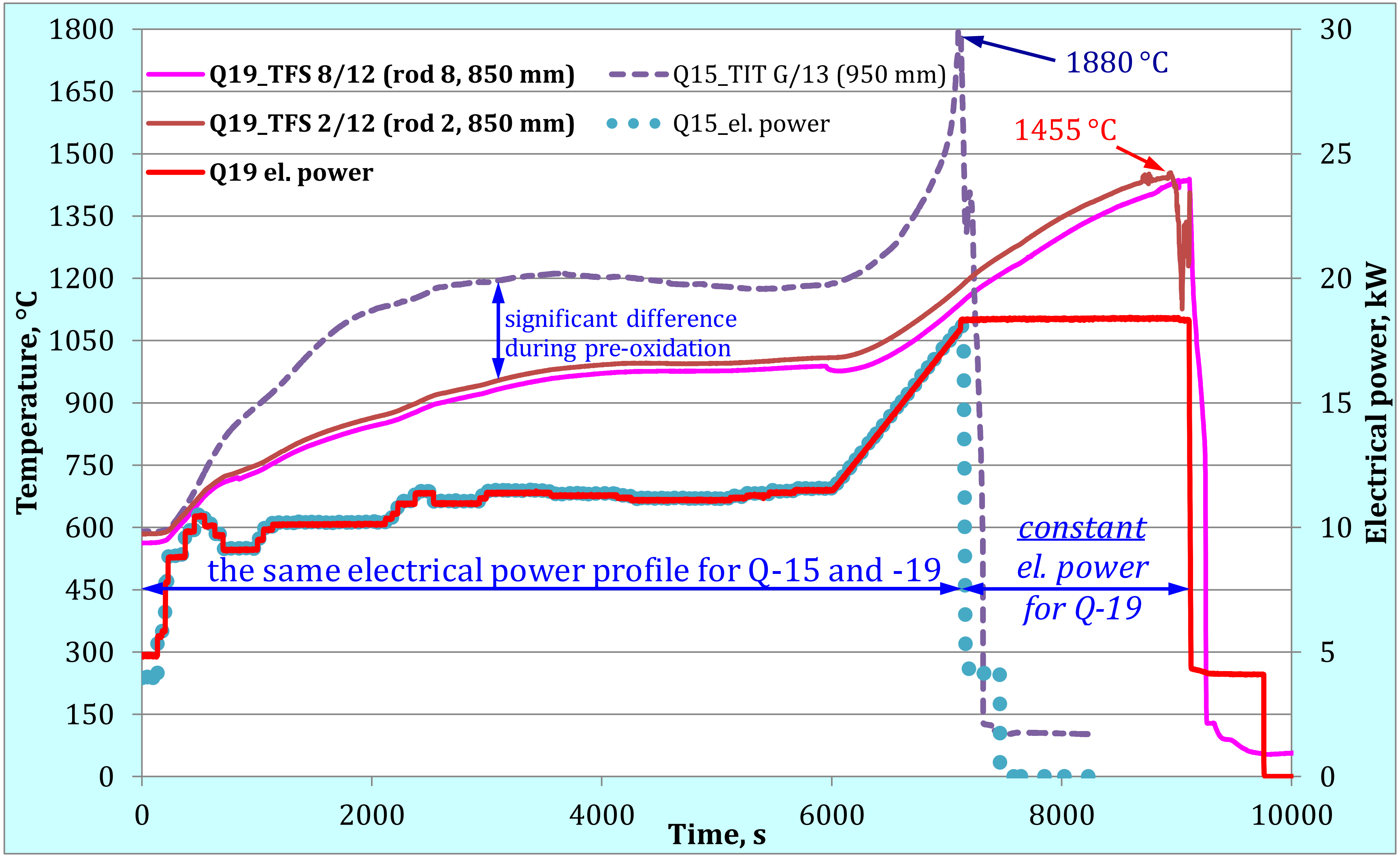

Figure 23 QUENCH-19; Test performance in comparison to QUENCH-15.

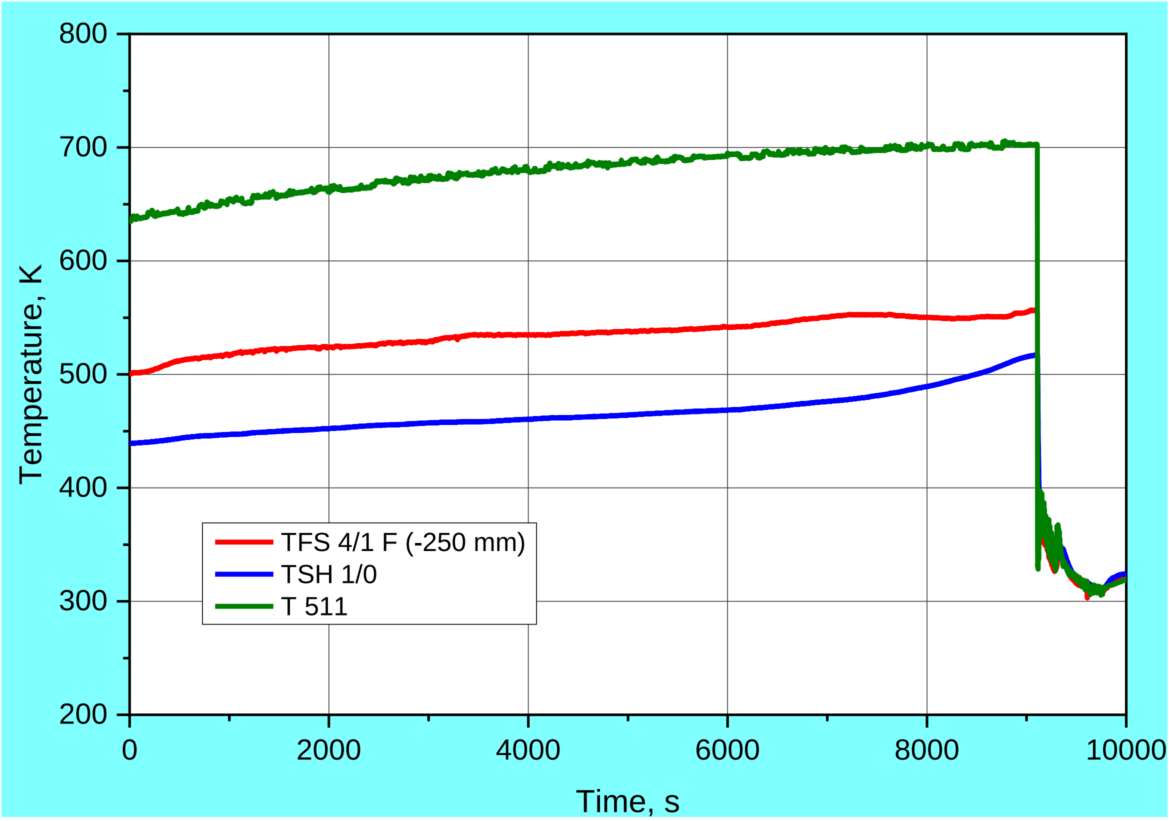

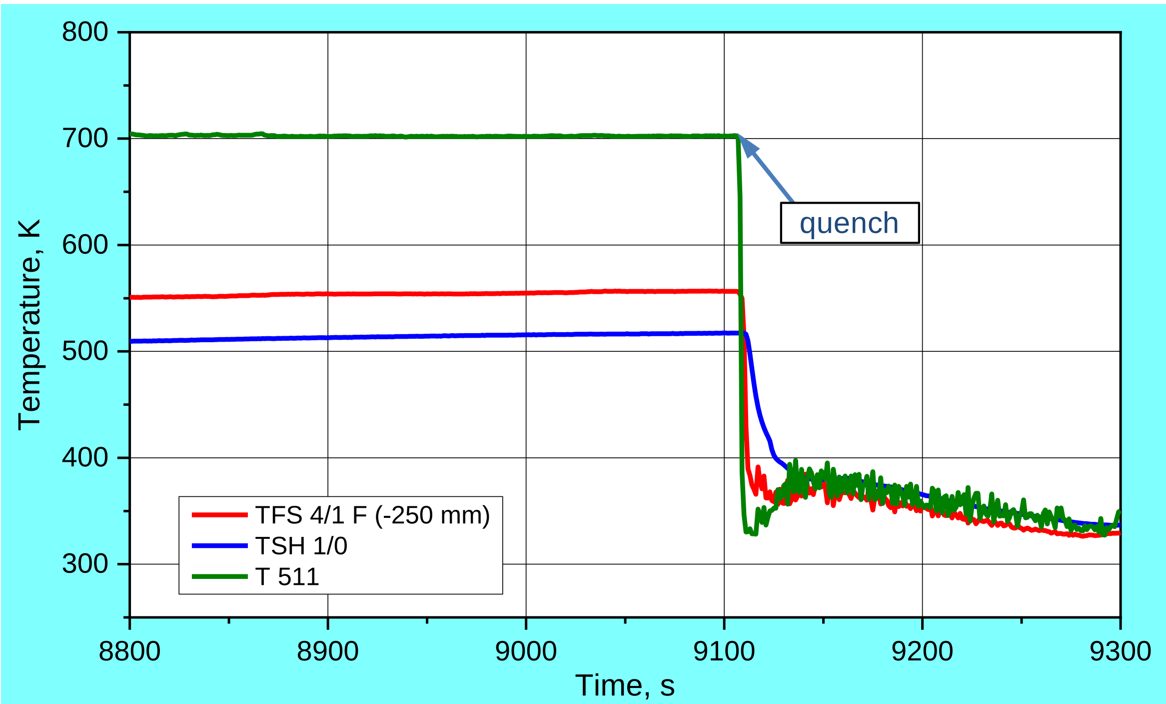

Figure 24 QUENCH-19; Temperatures measured by gas inlet thermocouple (T 511) at -412 mm, rod cladding thermocouple (TFS 4/1F) and shroud (TSH 1/0) thermocouples at -250 mm elevation

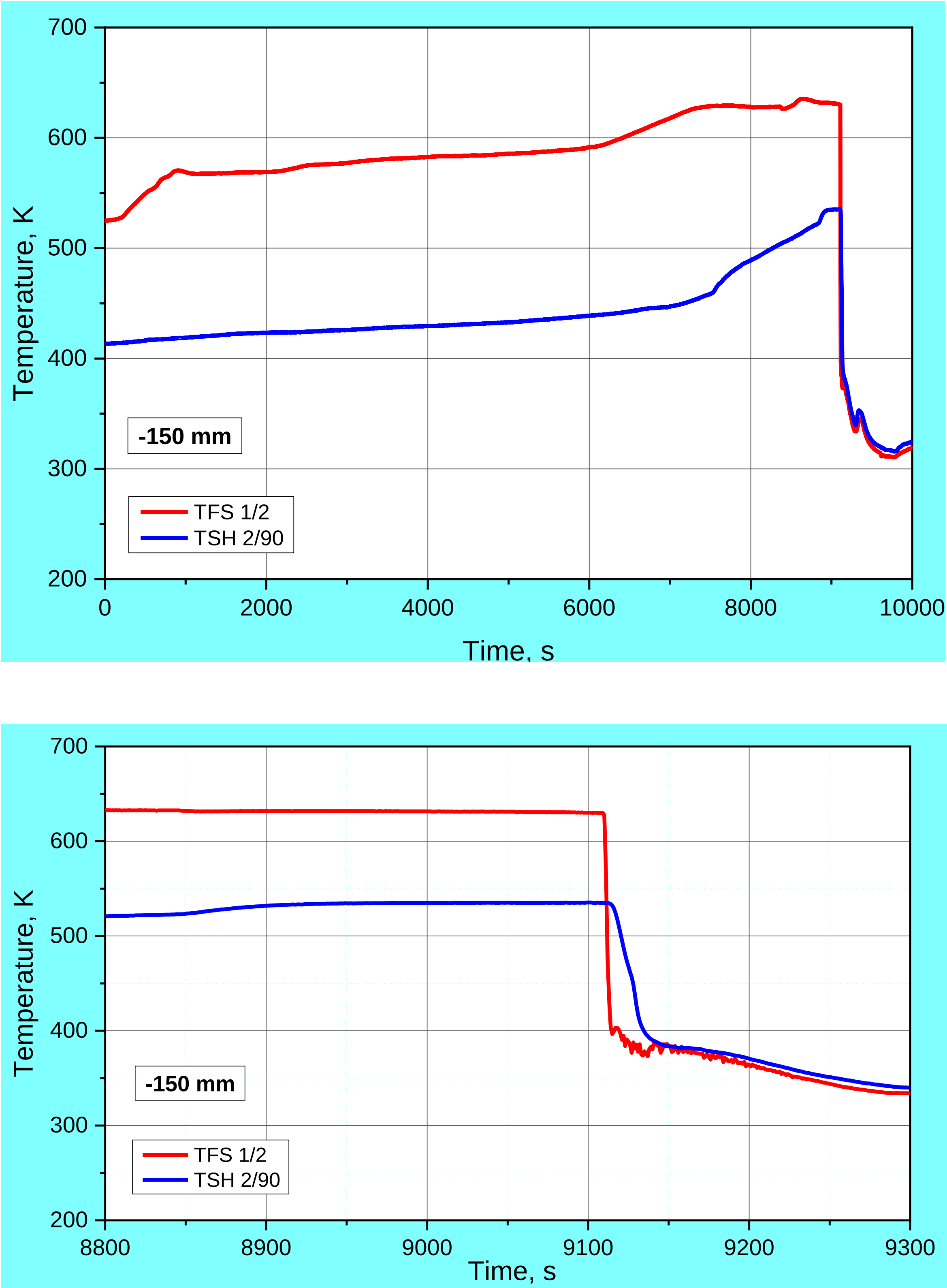

Figure 25 QUENCH-19; Temperatures measured by rod cladding (TFS 1/2) and shroud (TSH 2/90) thermocouples thermocouple at -150 mm elevation.

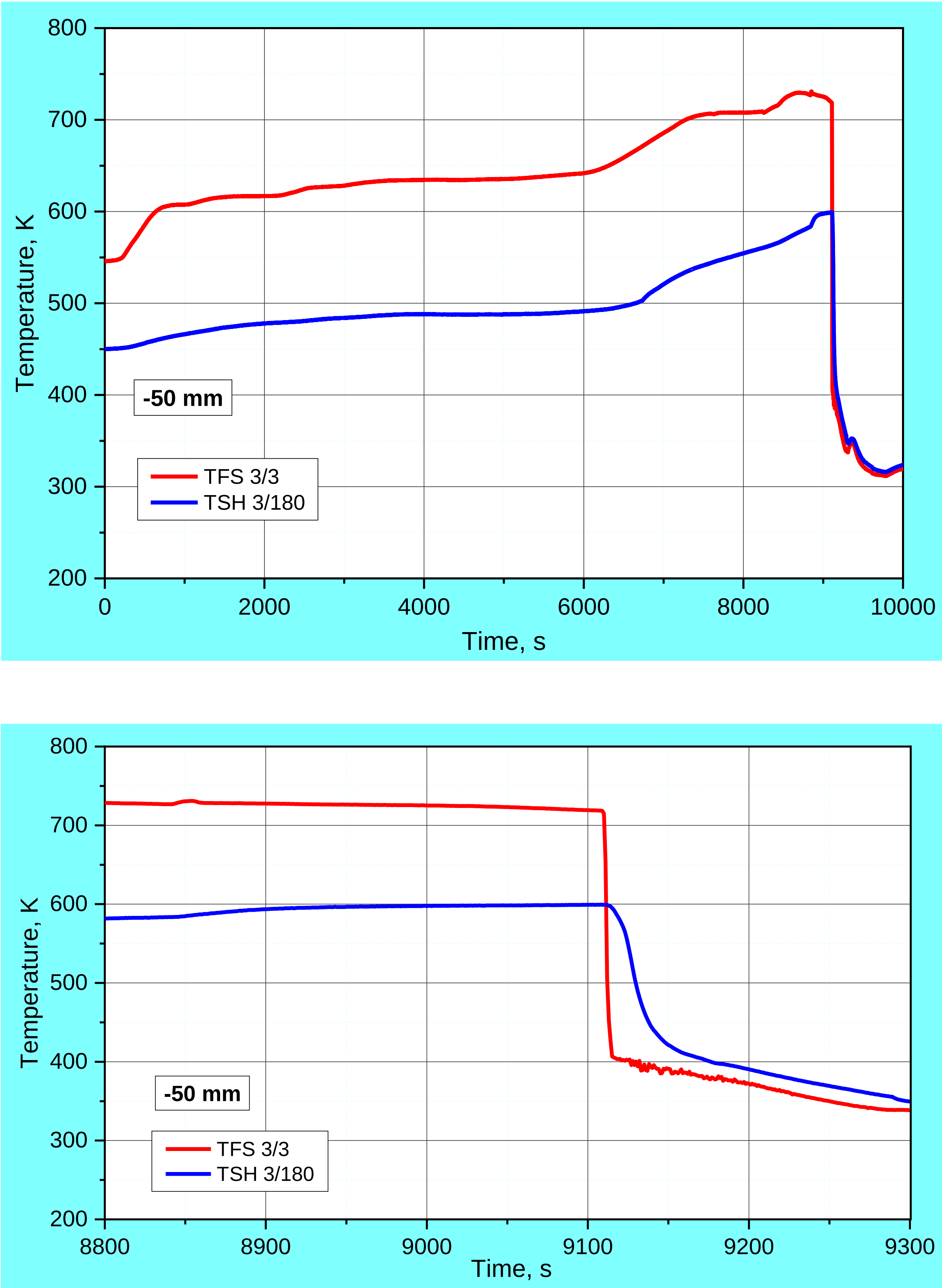

Figure 26 QUENCH-19; Temperatures measured by rod cladding (TFS 3/3) and shroud (TSH 3/180) thermocouples at -50 mm elevation.

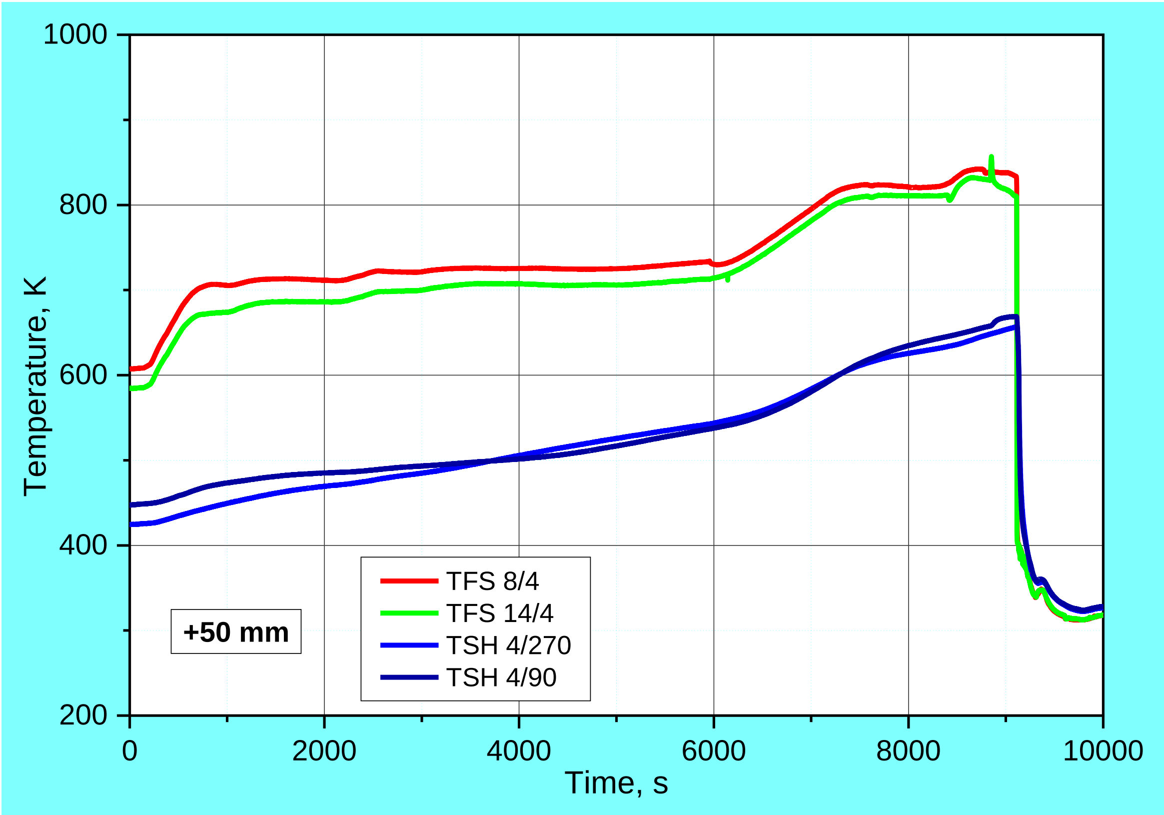

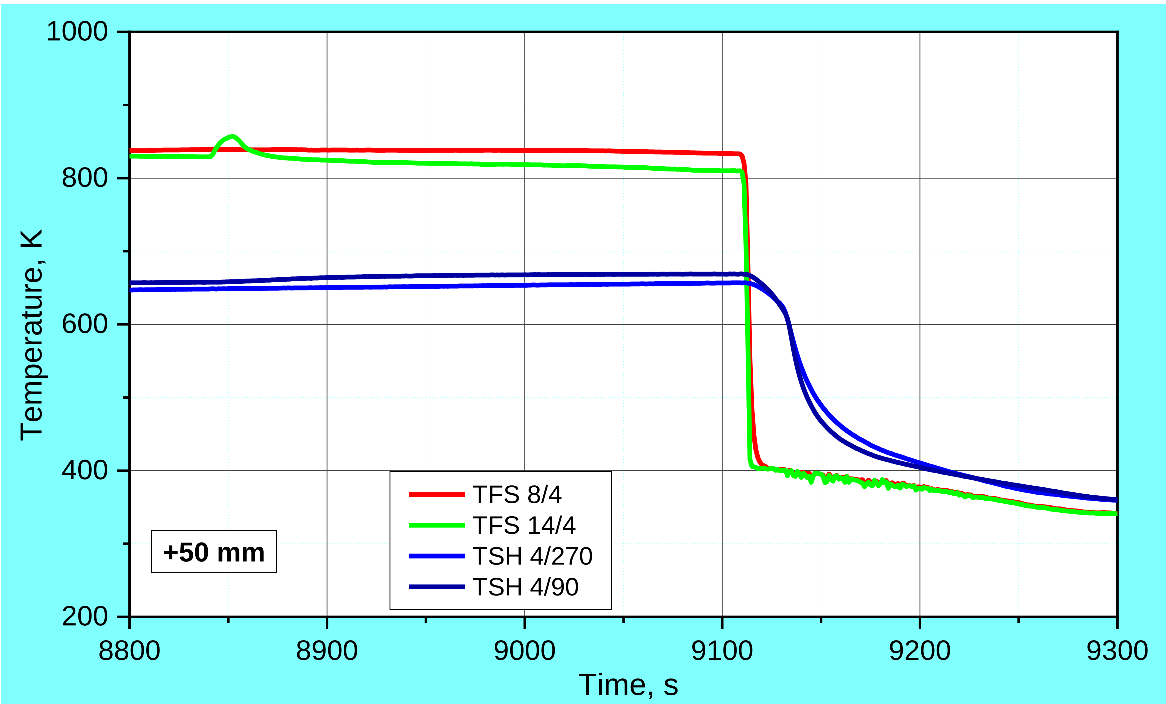

Figure 27 QUENCH-19; Temperatures measured by rod cladding (TFS) and shroud (TSH) thermocouples at 50 mm elevation

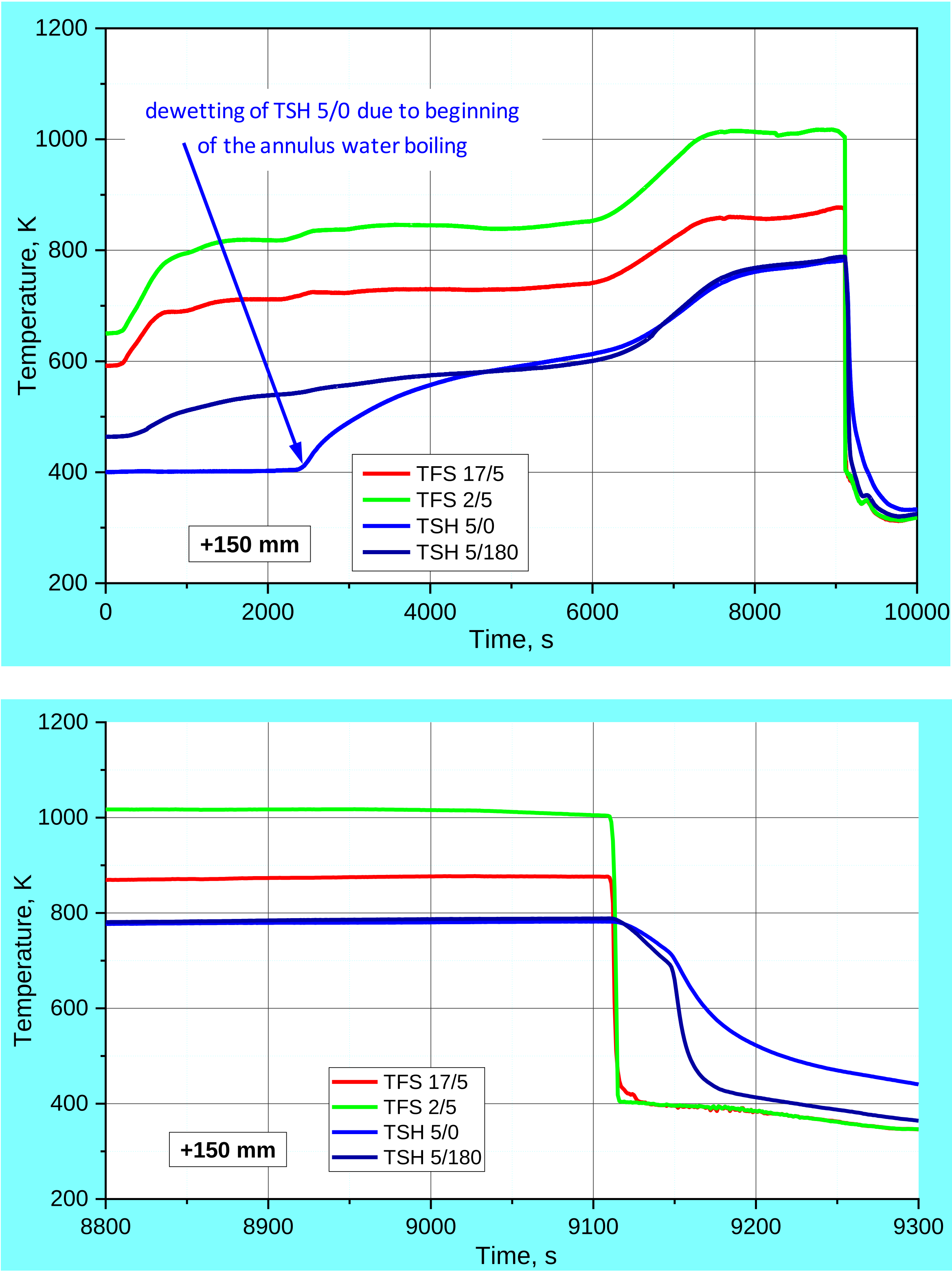

Figure 28 QUENCH-19; Temperatures measured by rod cladding (TFS) and shroud (TSH) thermocouples at 150 mm elevation

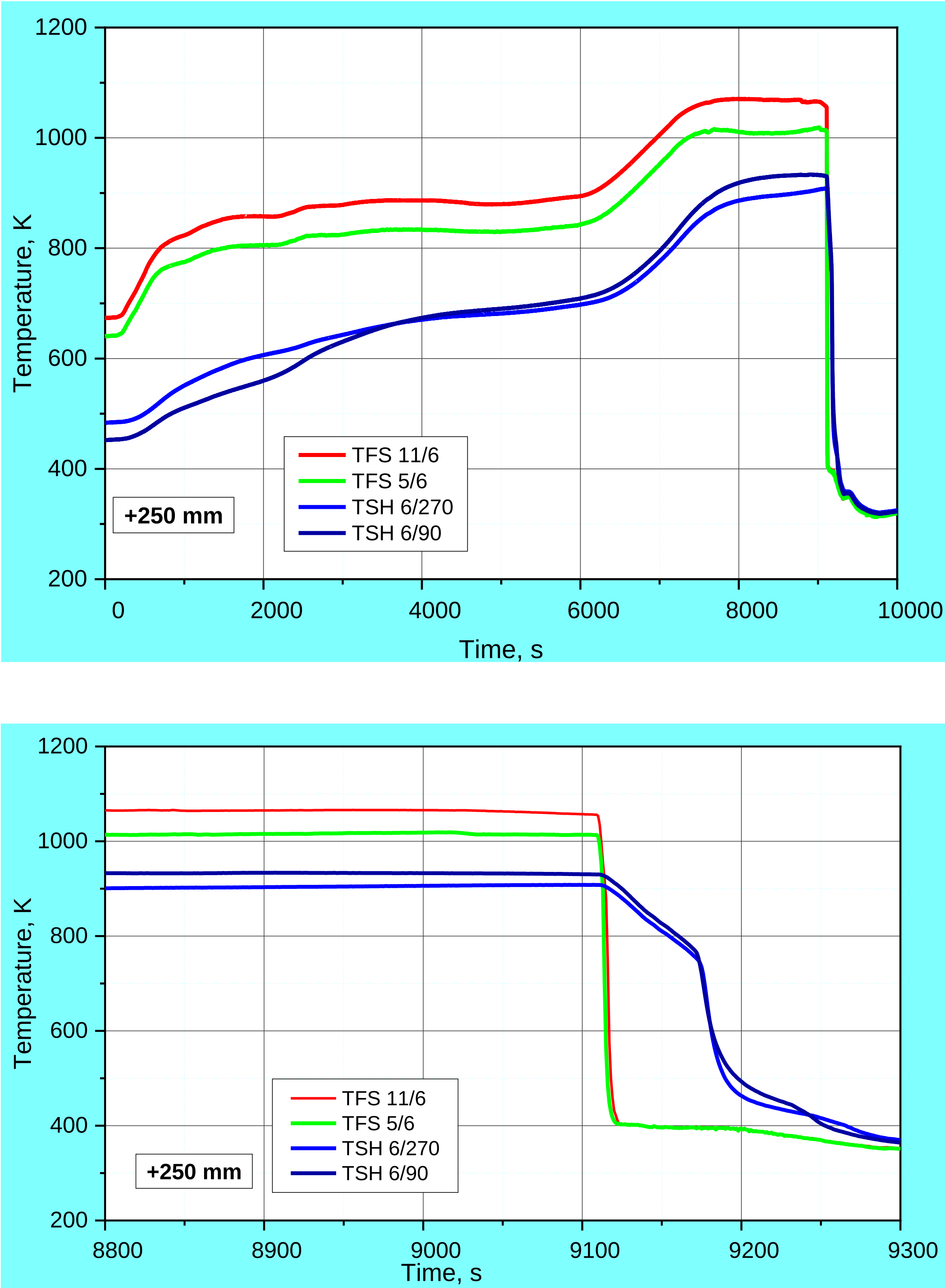

Figure 29 QUENCH-19; Temperatures measured by rod cladding (TFS) and shroud (TSH) thermocouples at 250 mm elevation.

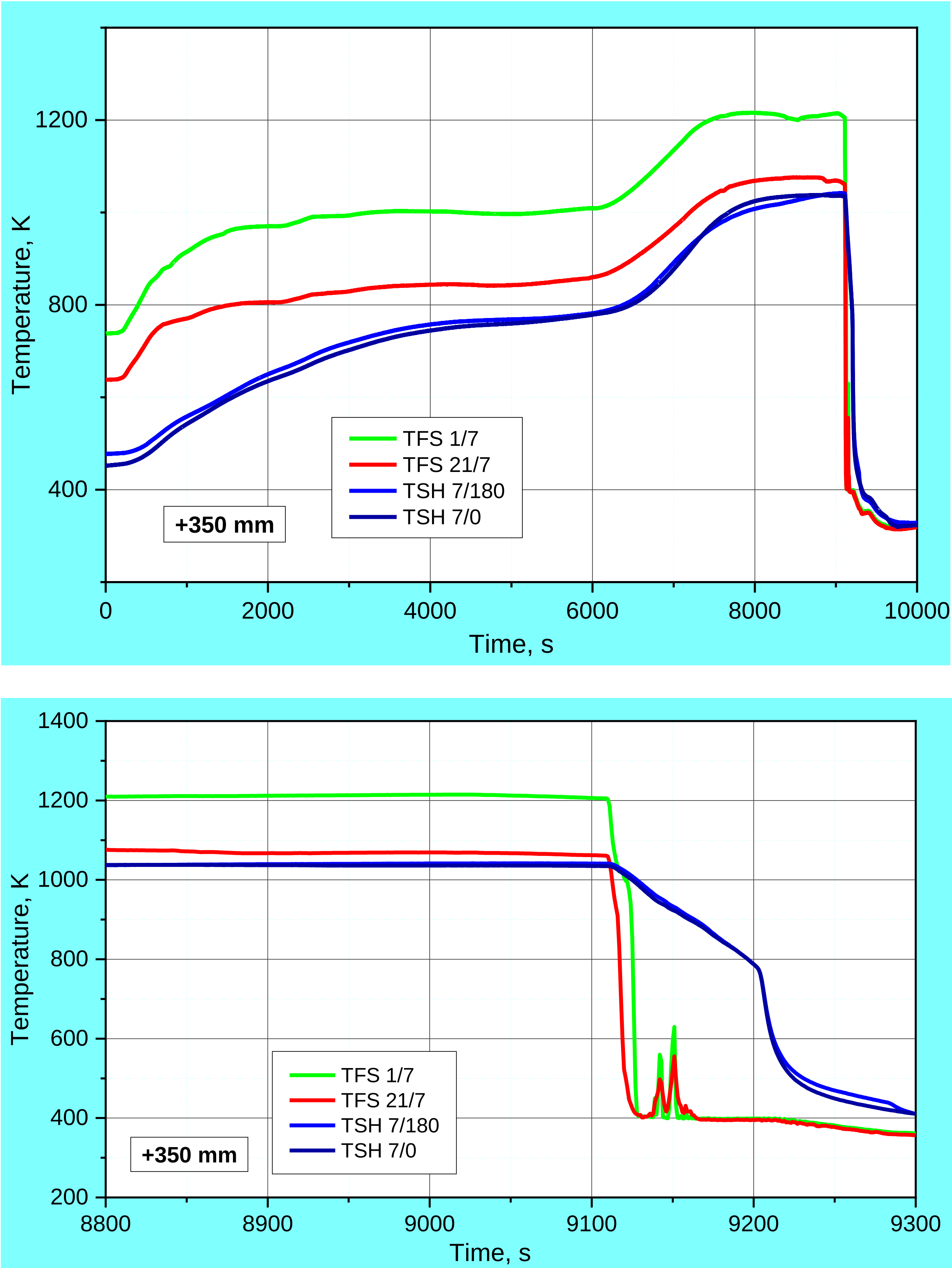

Figure 30 QUENCH-19; Temperatures measured by rod cladding (TFS) and shroud (TSH) thermocouples at 350 mm elevation

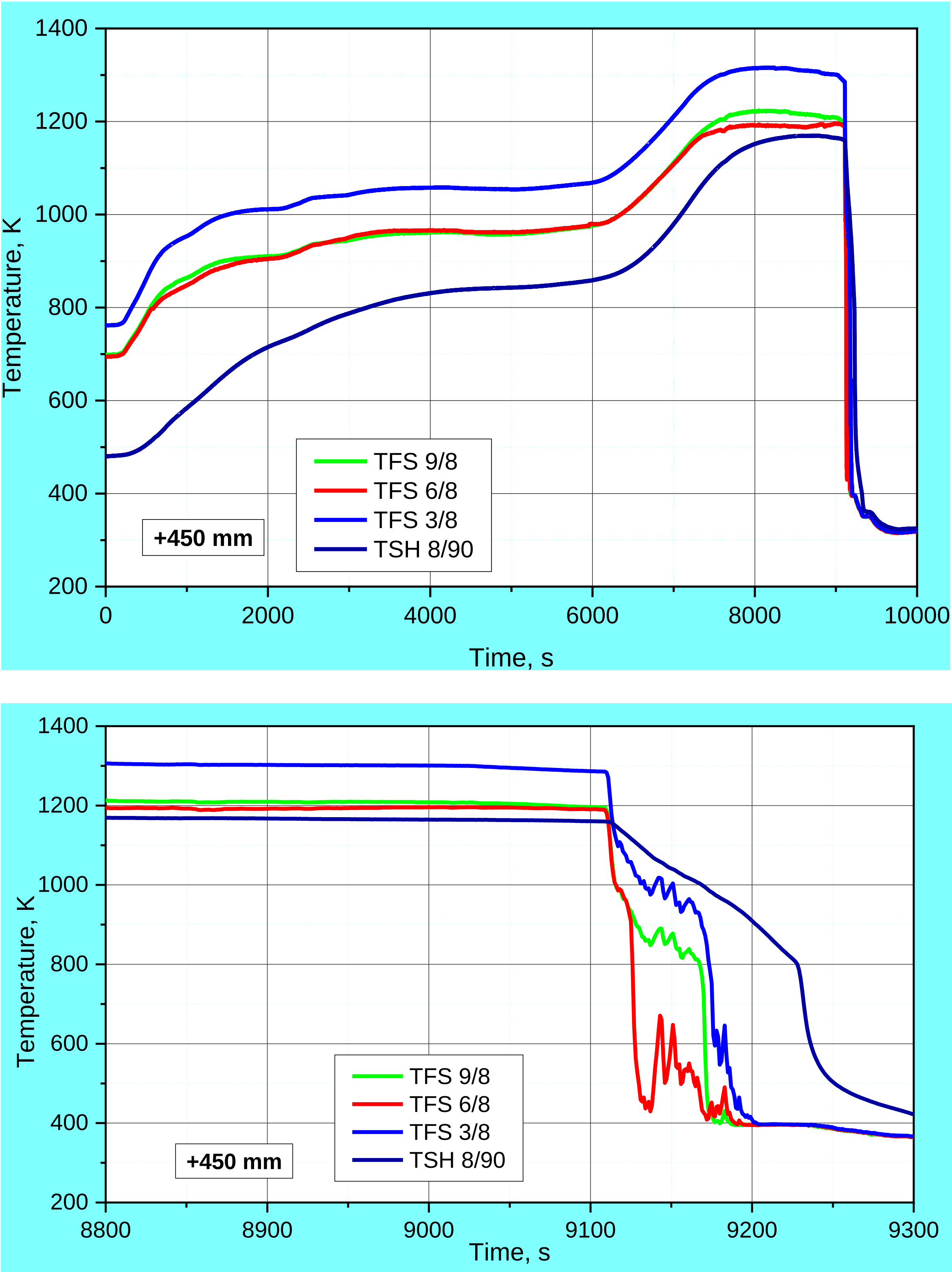

Figure 31 QUENCH-19; Temperatures measured by rod cladding (TFS) and shroud (TSH) thermocouples at 450 mm elevation

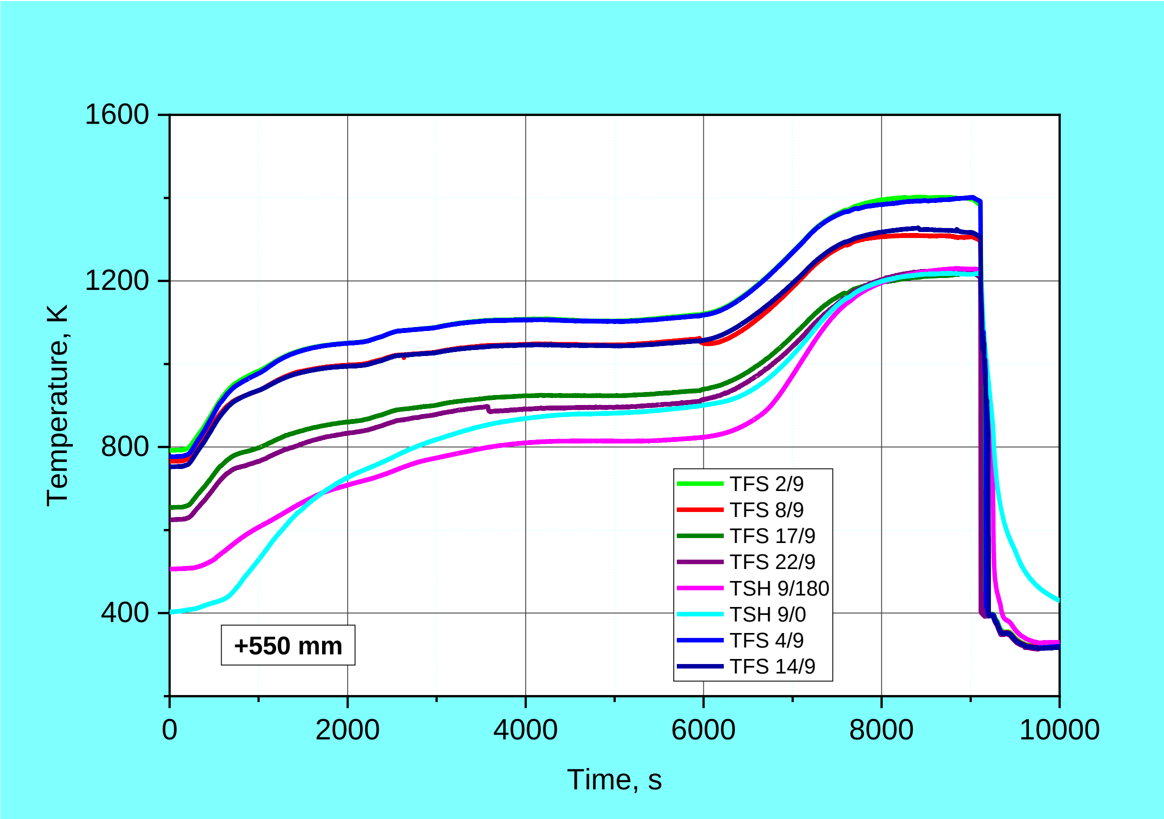

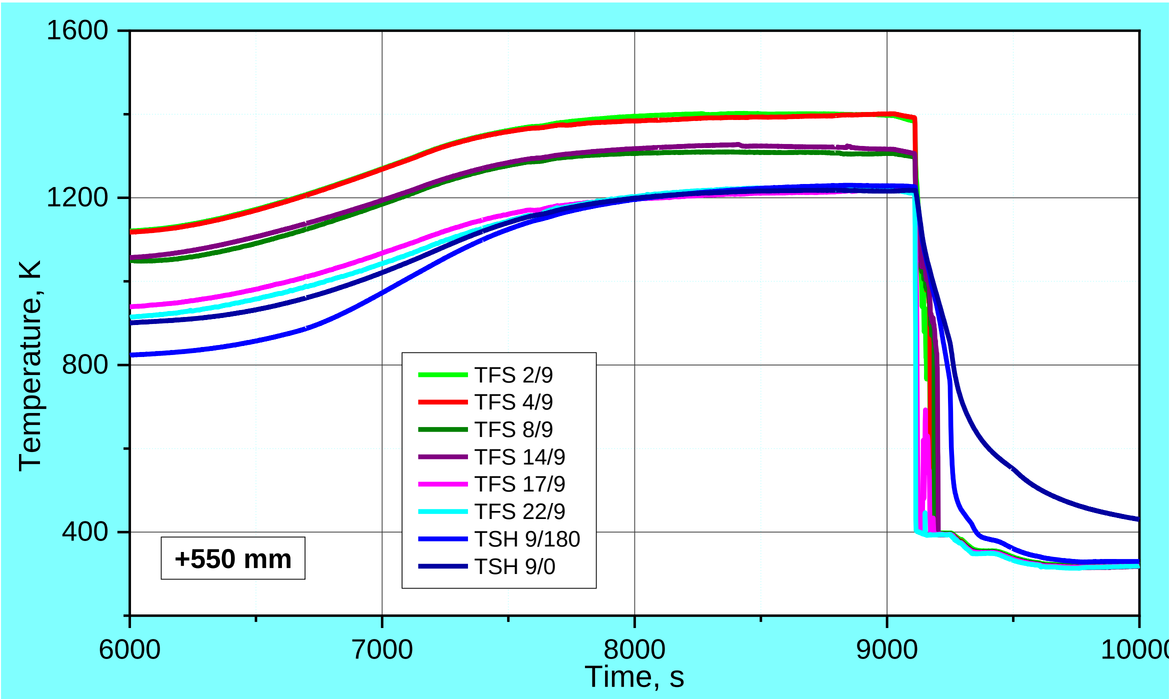

Figure 32 QUENCH-19; Temperatures measured by rod cladding (TFS) and shroud (TSH) thermocouples at 550 mm elevation

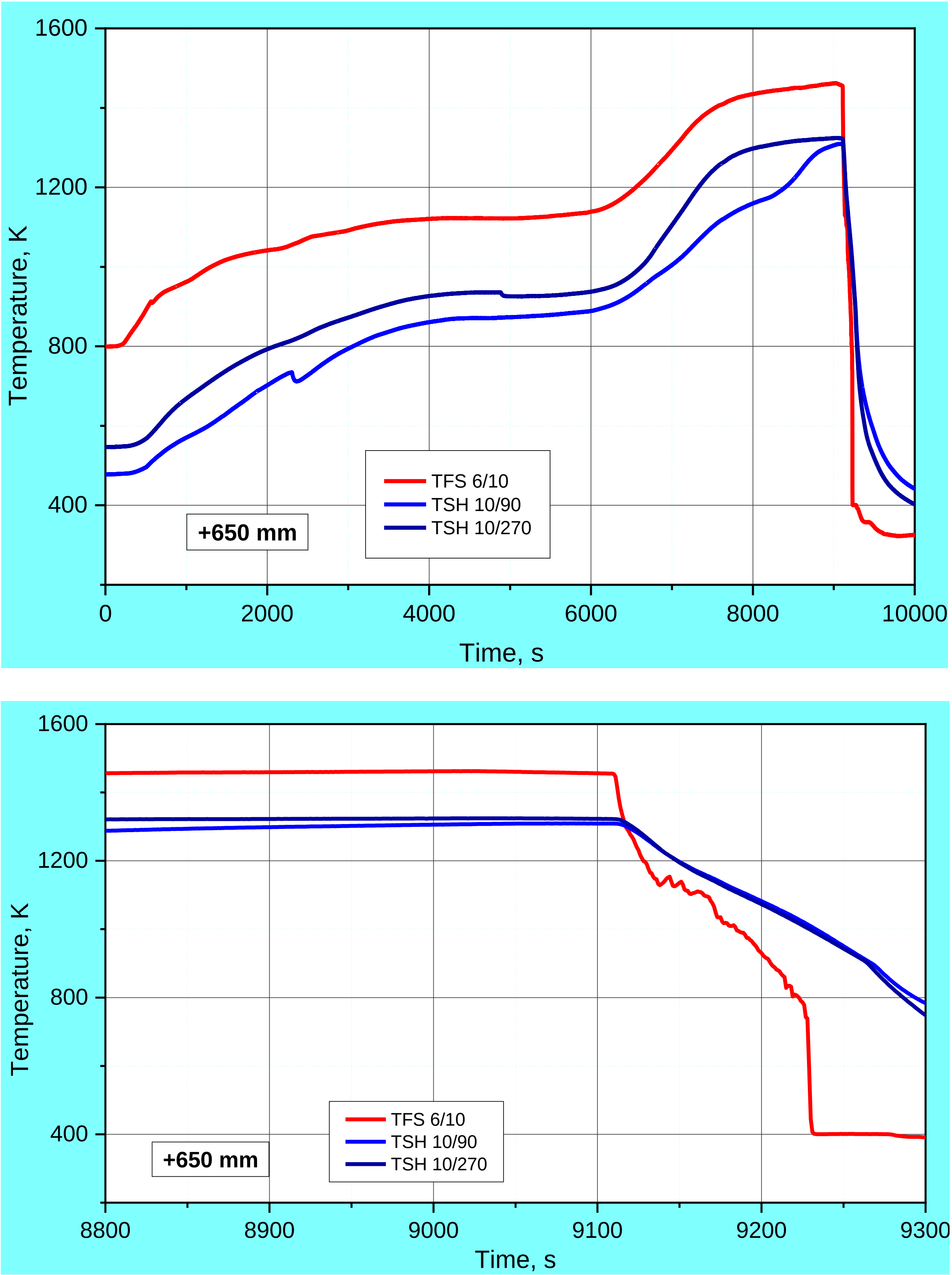

Figure 33 QUENCH-19; Temperatures measured by rod cladding (TFS 6/10) and shroud (TSH) thermocouples at 650 mm elevation

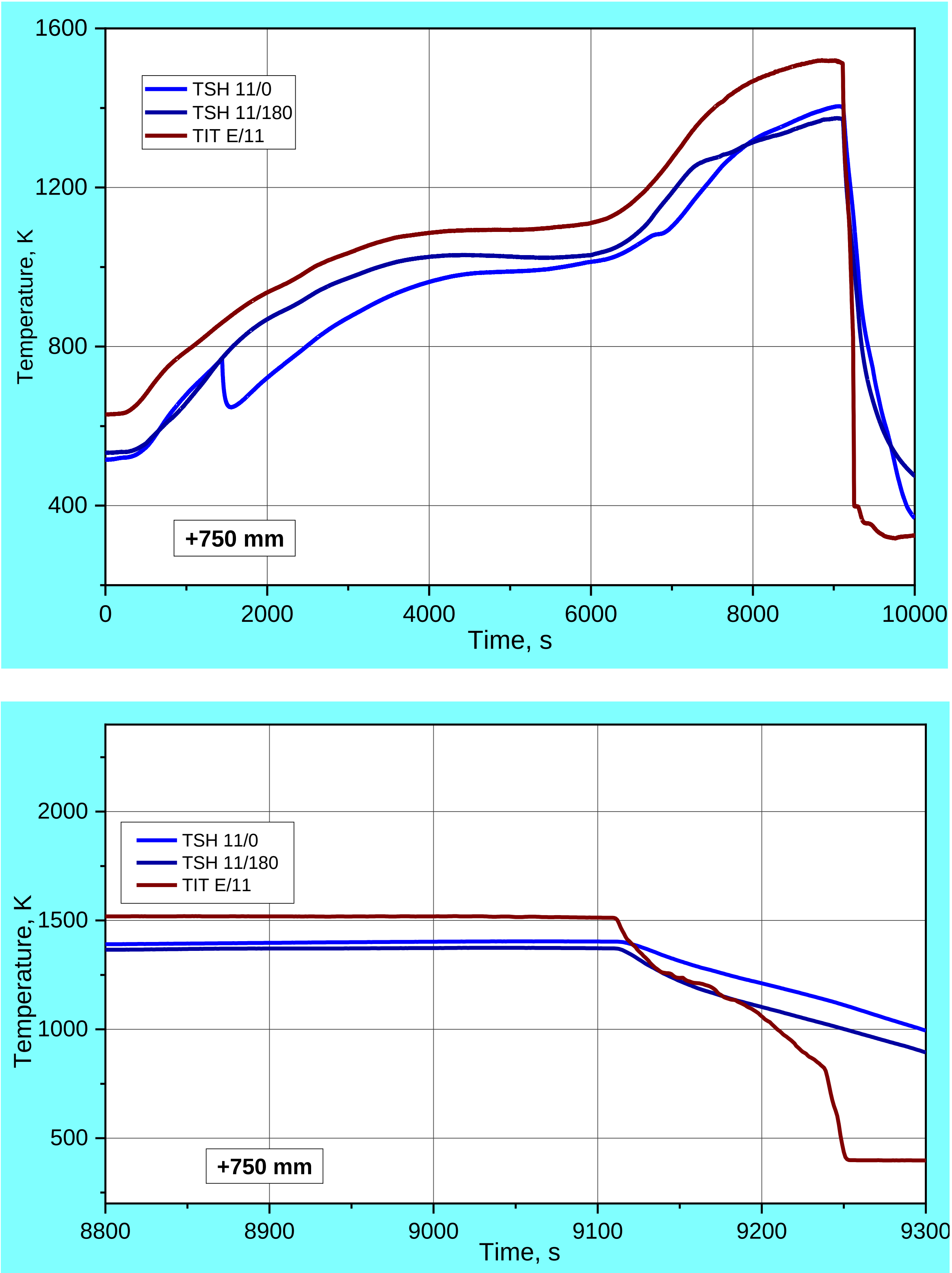

Figure 34 QUENCH-19; Temperatures measured by shroud (TSH), and corner rod internal (TIT E/11) thermocouples at 750 mm elevation.

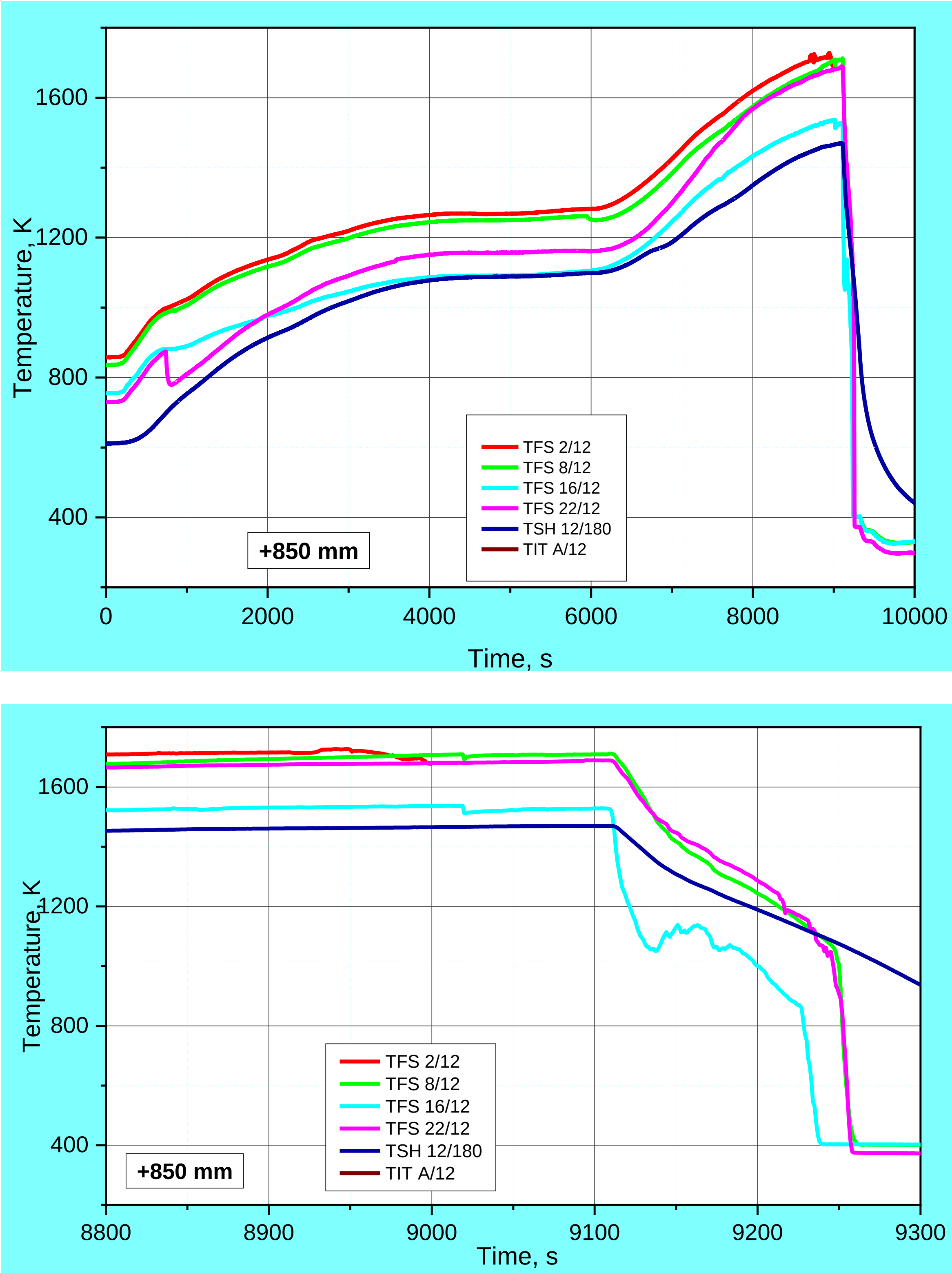

Figure 35 QUENCH-19; Temperatures measured by rod cladding (TFS) and shroud (TSH), and corner rod internal (TIT C/12) thermocouples at 850 mm elevation.

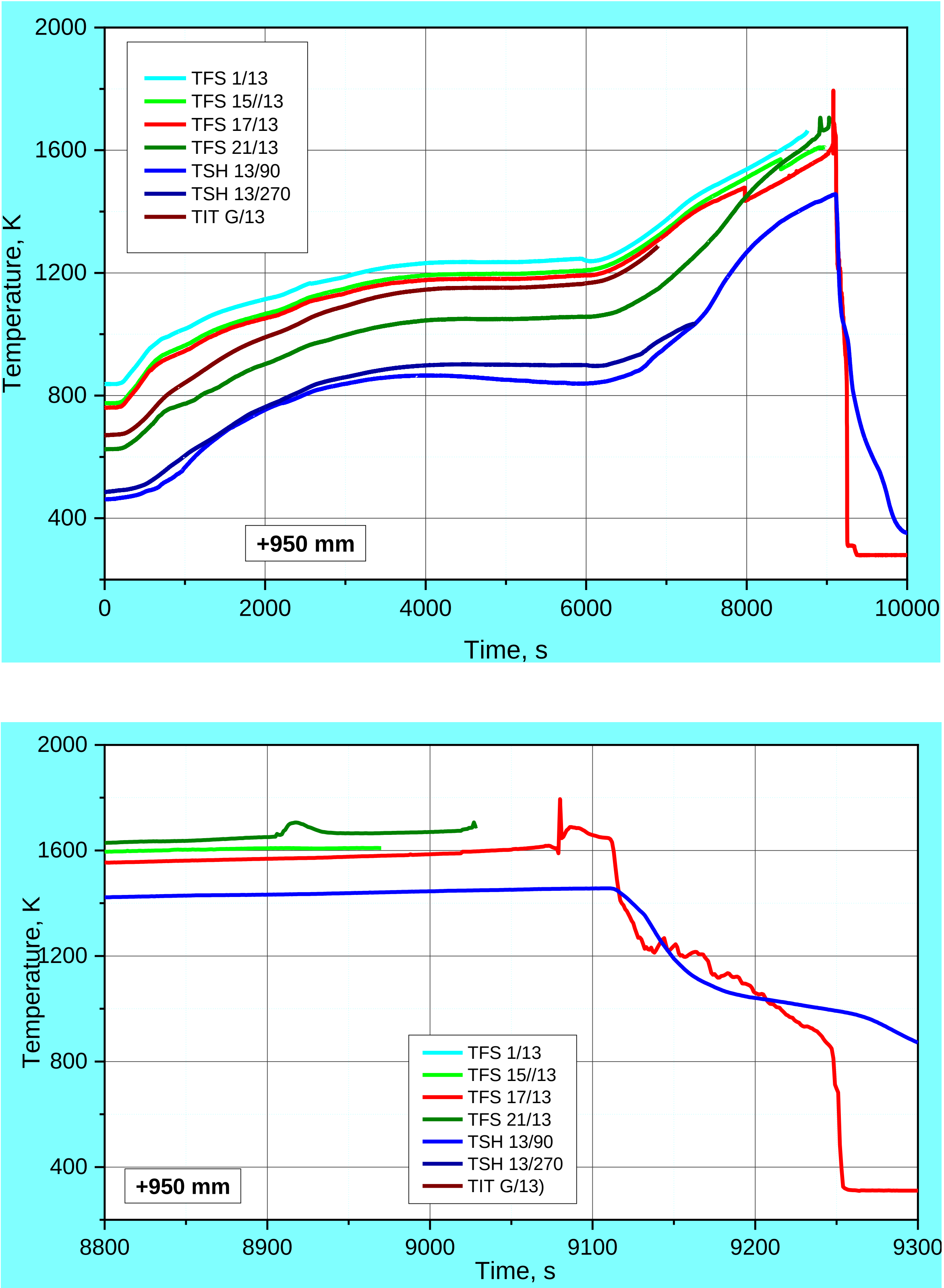

Figure 36 QUENCH-19; Temperatures measured by rod cladding (TFS) and shroud (TSH), and corner rod internal (TIT A/13) thermocouples at 950 mm elevation.

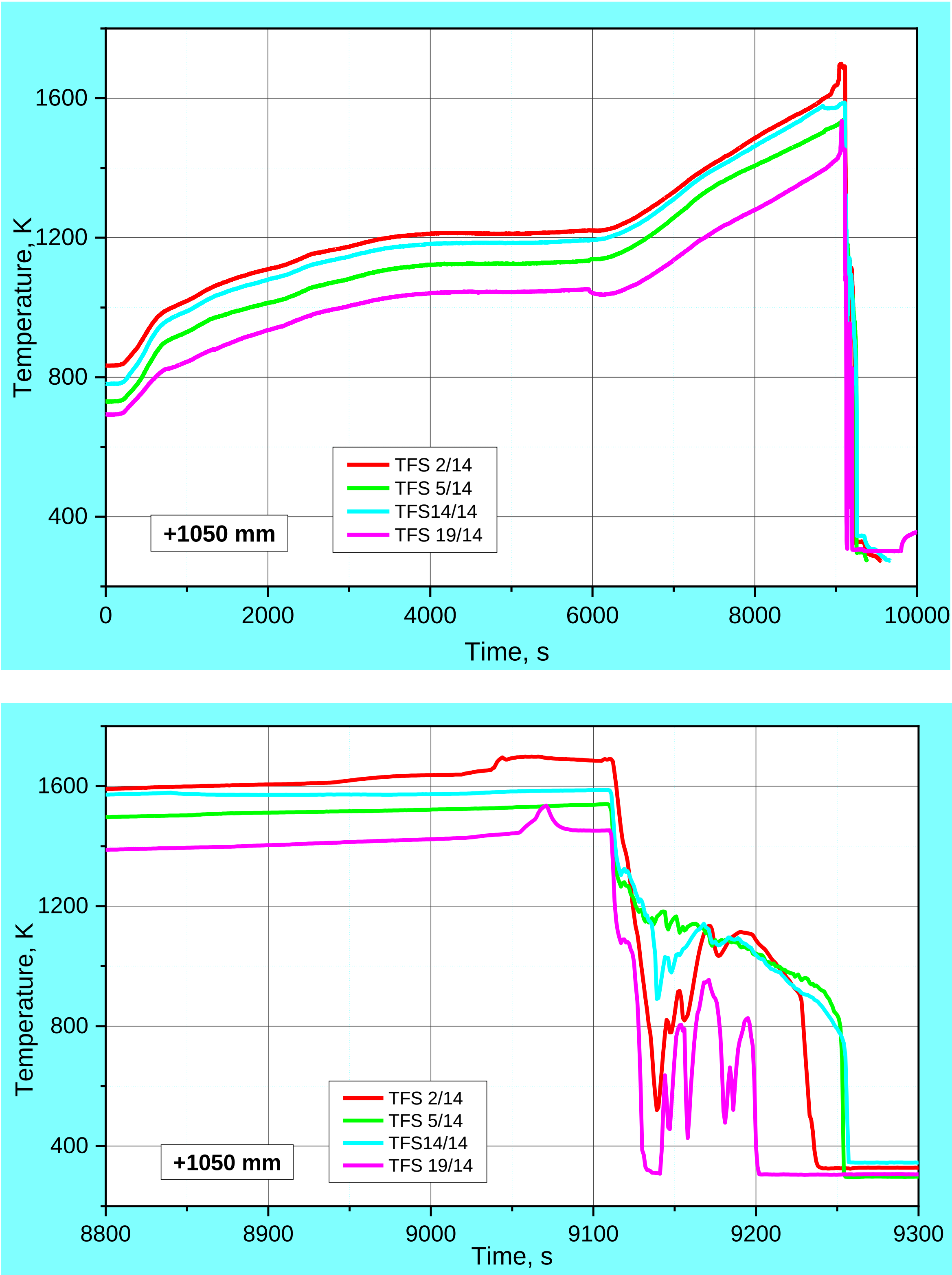

Figure 37 QUENCH-19; Temperatures measured by rod cladding (TFS) thermocouples at 1050 mm elevation

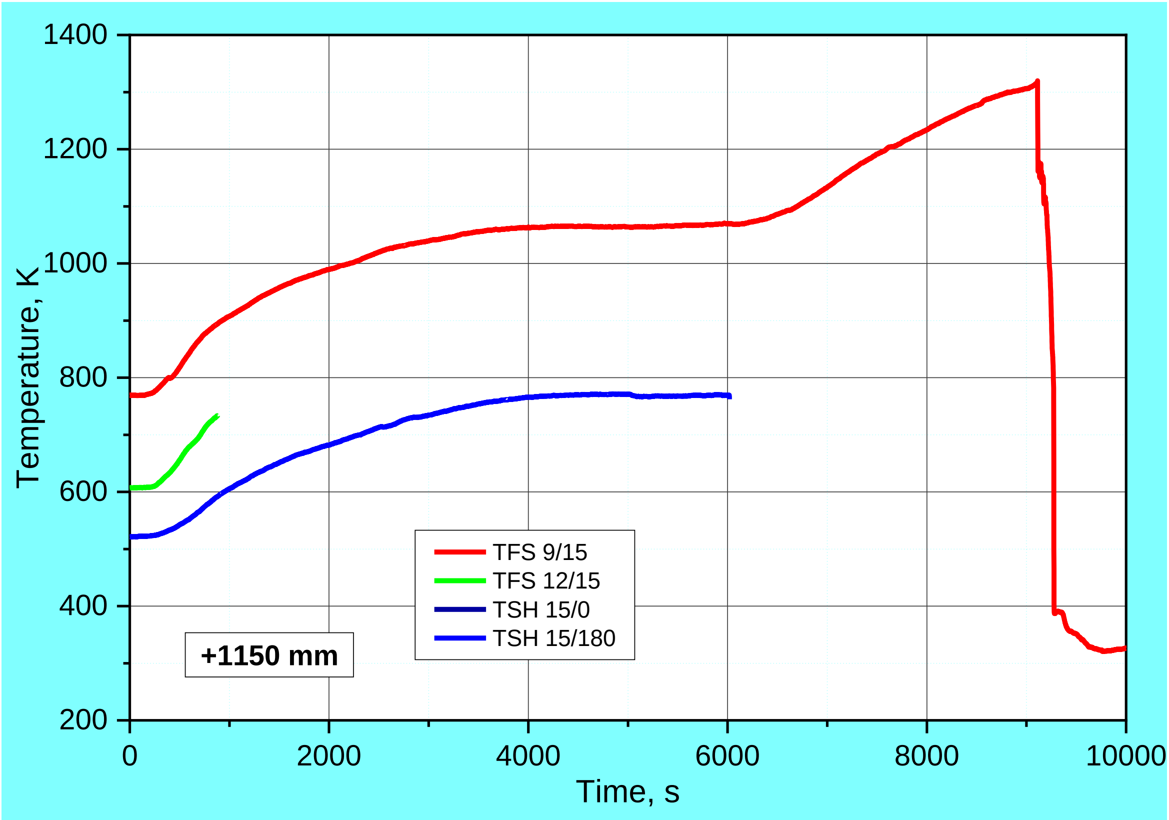

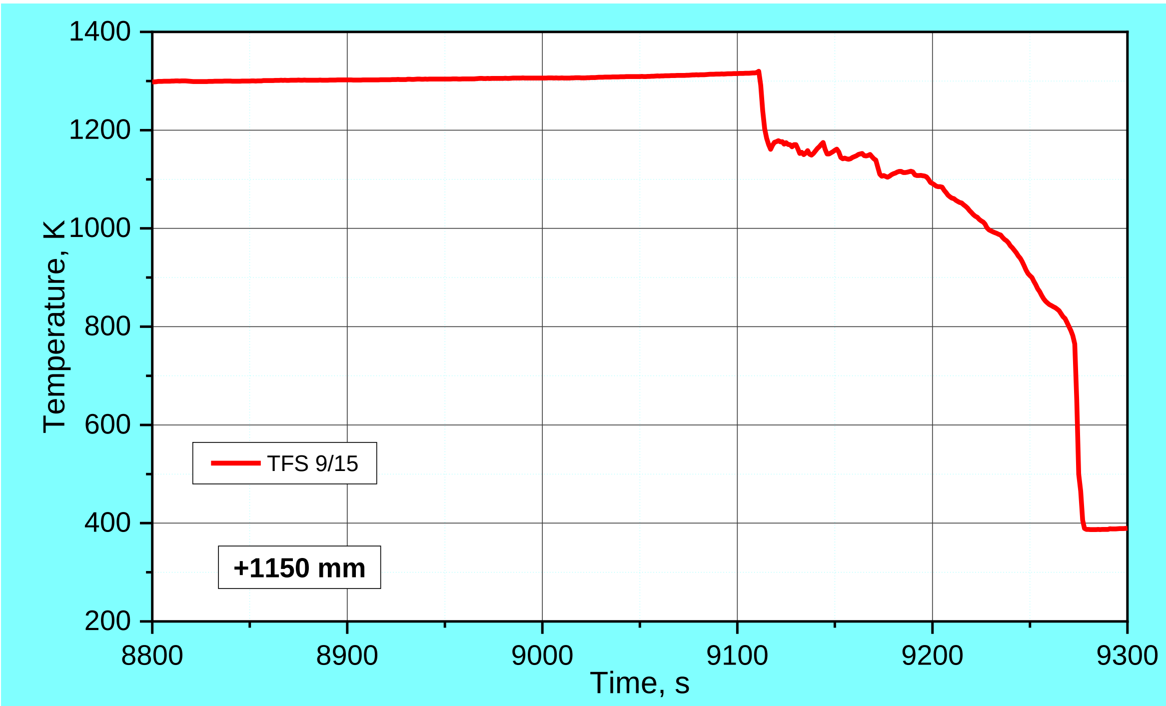

Figure 38 QUENCH-19; Temperatures measured by rod cladding (TFS) and shroud (TSH) thermocouples at 1150 mm elevation

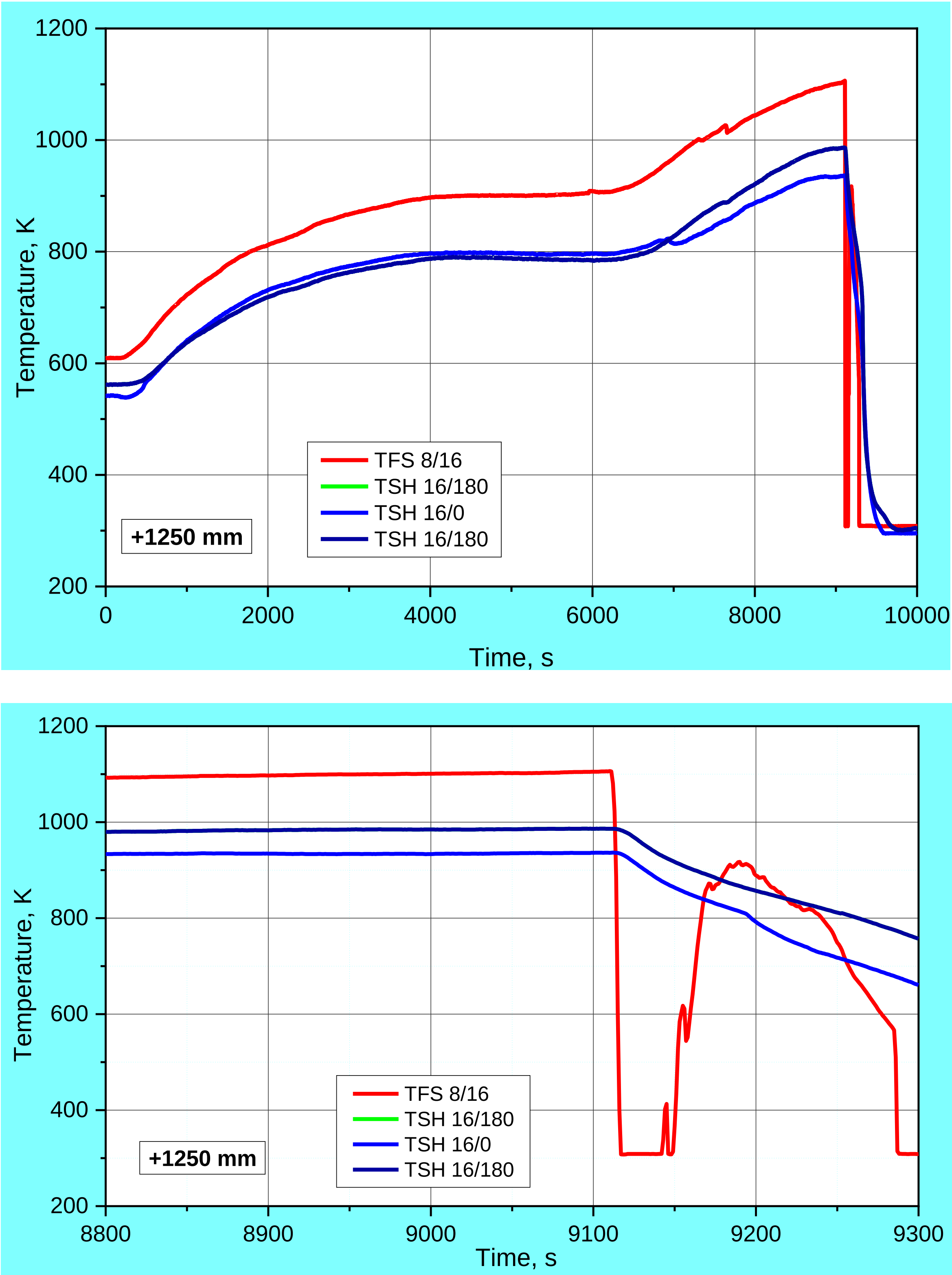

Figure 39 QUENCH-19; Temperatures measured by rod cladding (TFS) and shroud (TSH) thermocouples at 1250 mm elevation.

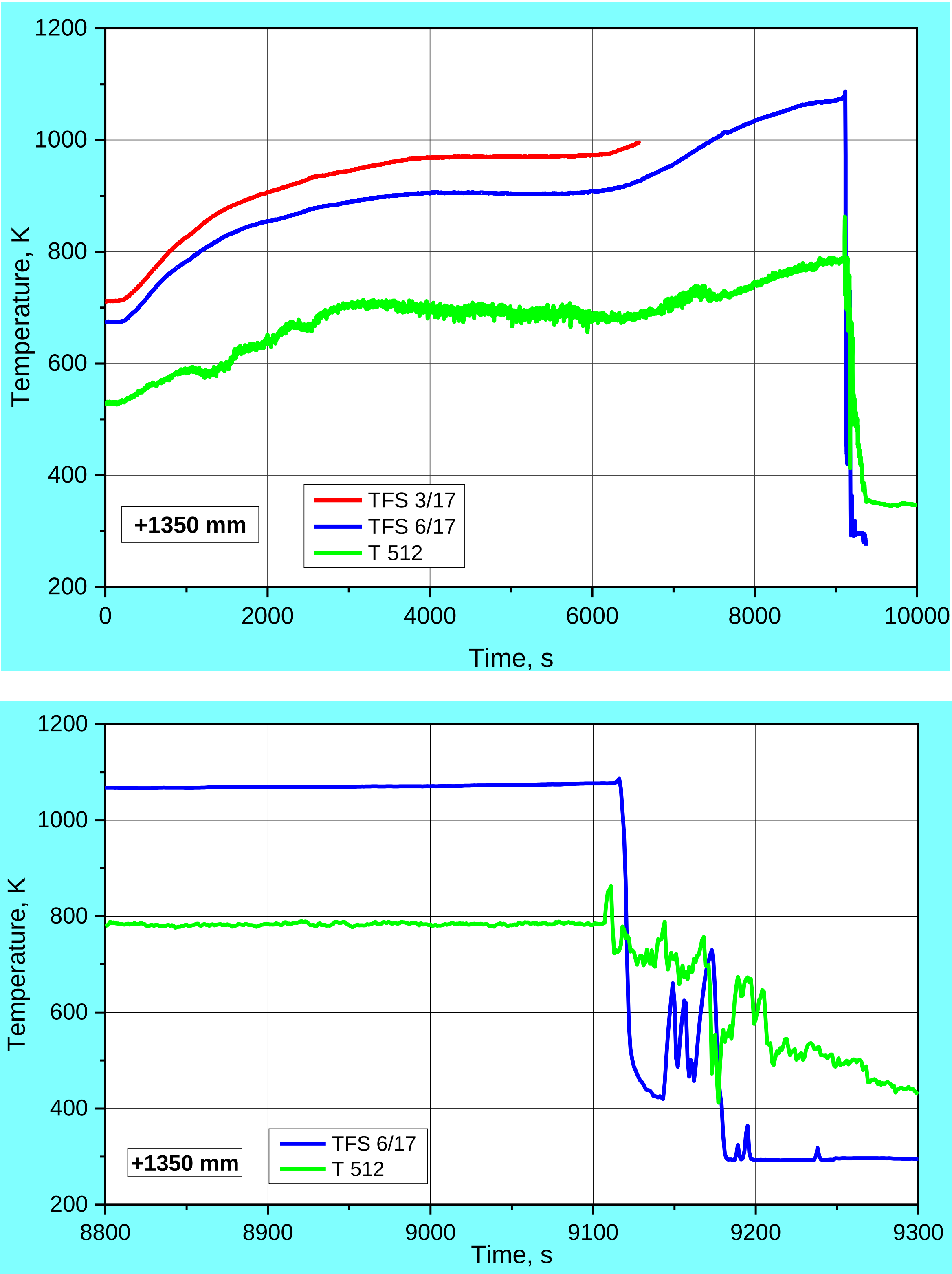

Figure 40 QUENCH-19; Temperature measured by rod cladding thermocouple at 1350 mm elevation (TFS 7/17) and gas temperature (T 512) at 1360 mm between shroud and rod #20

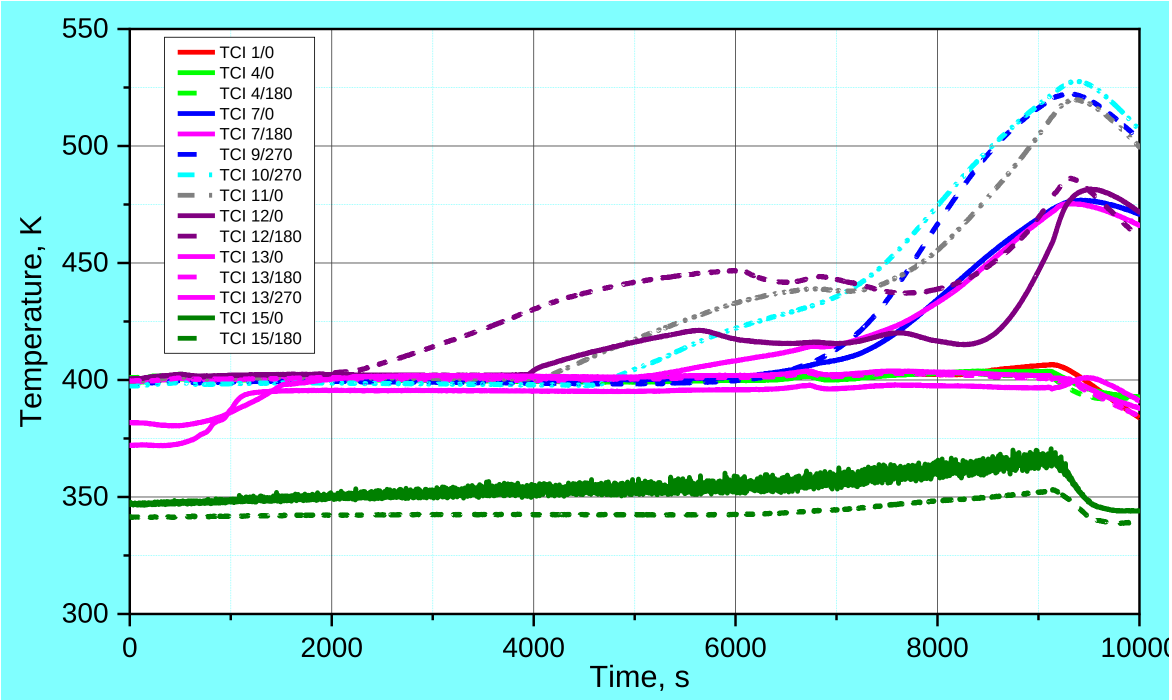

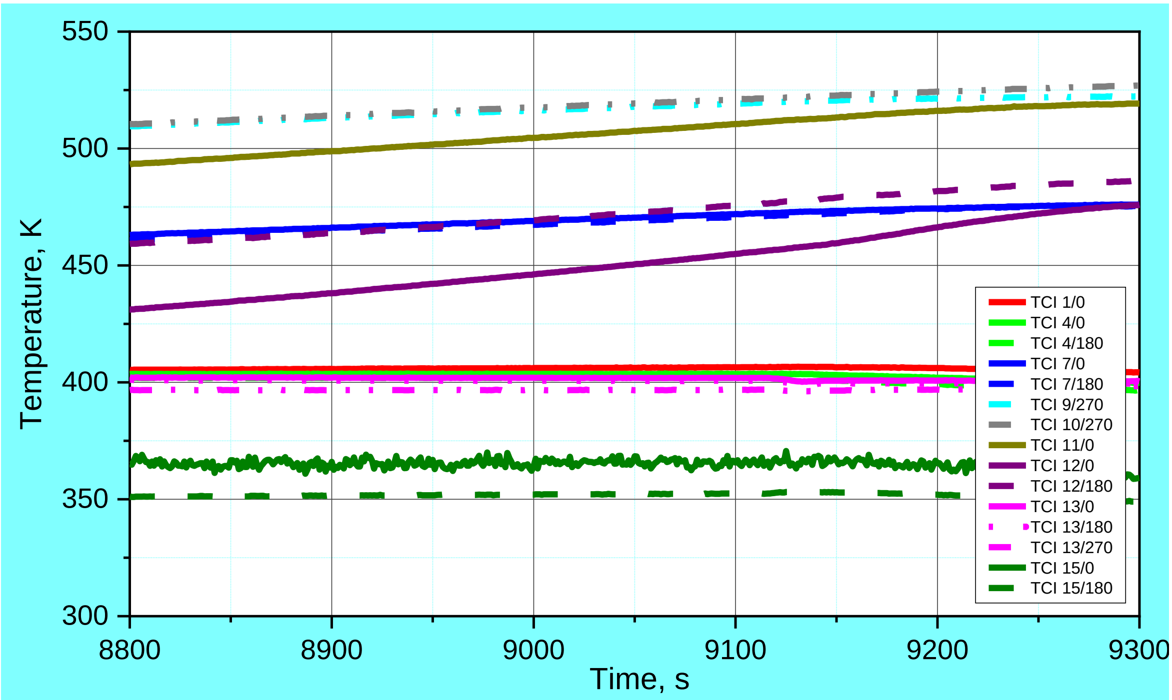

Figure 41 QUENCH-19; Overview of the TCI (inner cooling jacket)

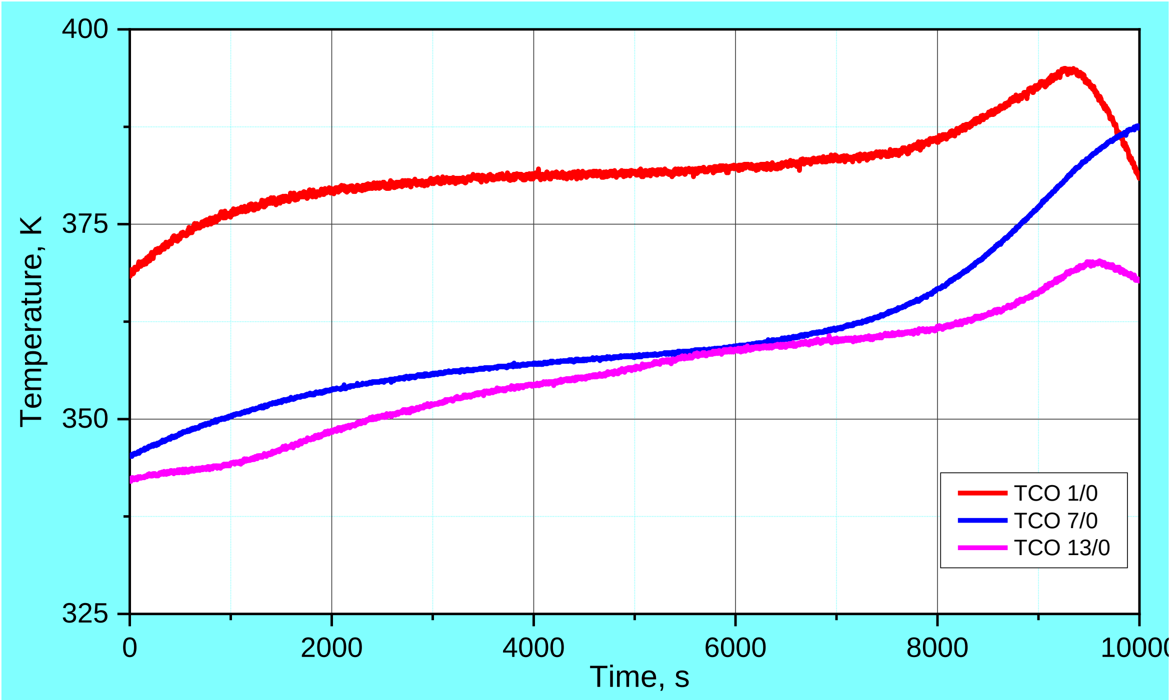

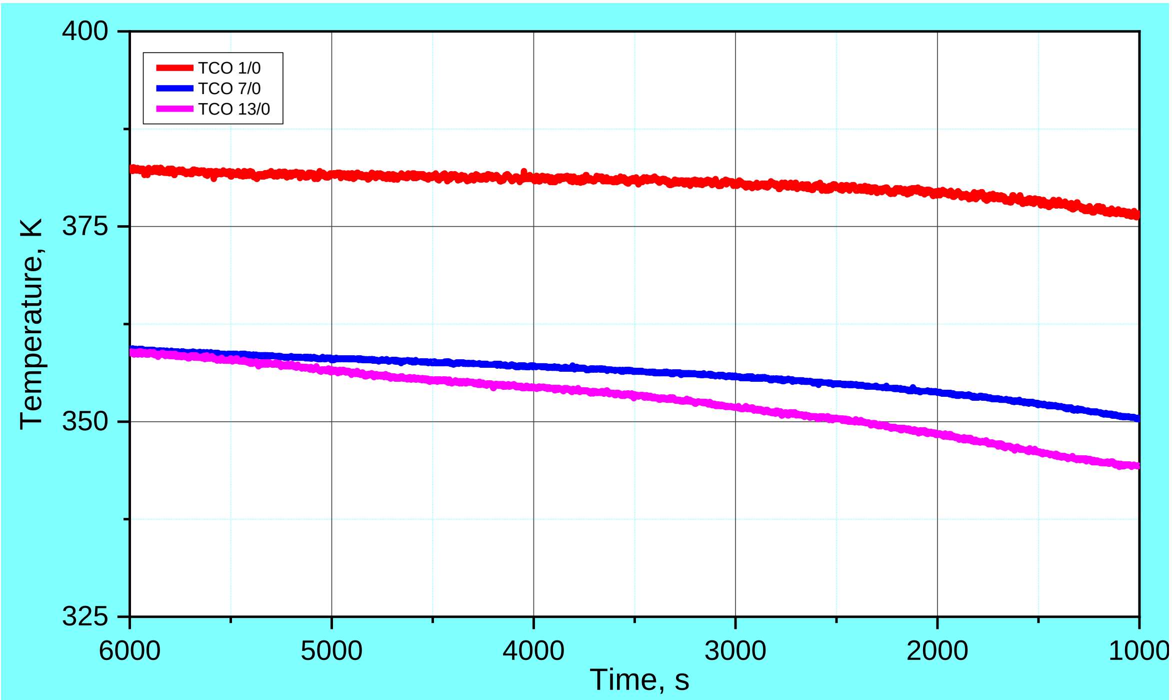

Figure 42 QUENCH-19; Overview of the TCO (outer cooling jacket)

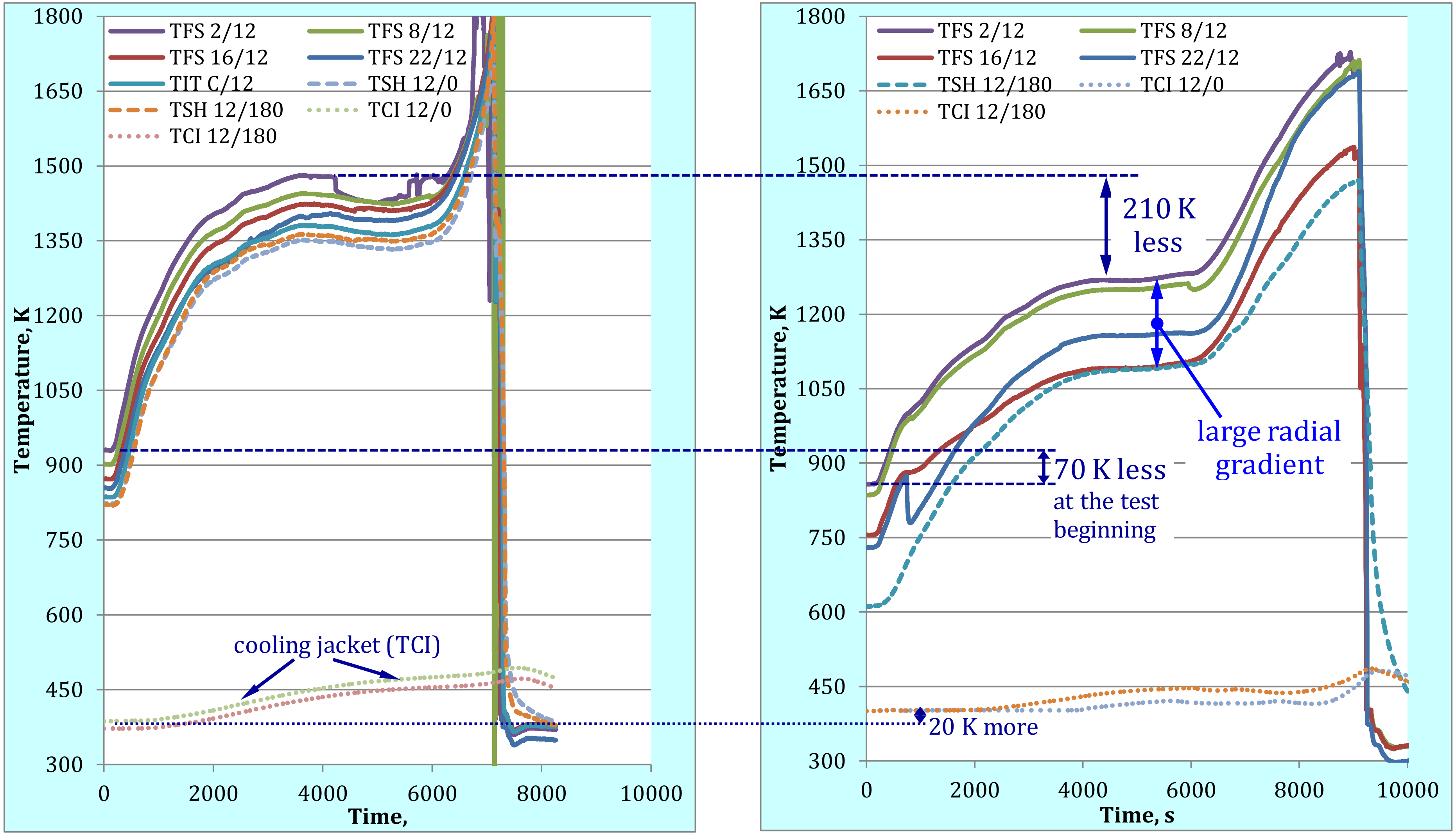

Figure 43 Comparison of readings of thermocouples at 850 mm for QUENCH-15 and -19.

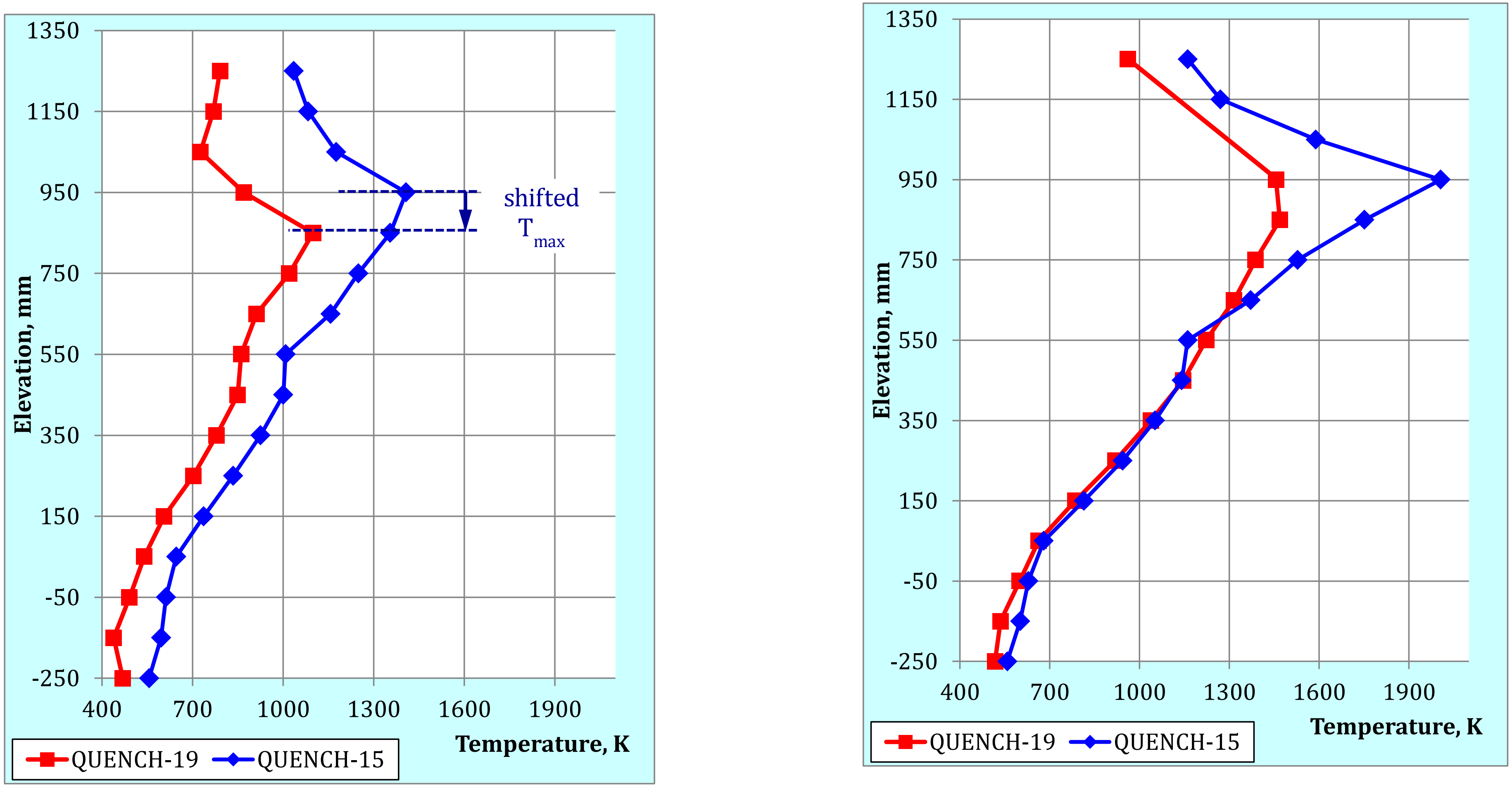

at the beginning of transient (5950 s for both tests)

at the onset of reflood (7111 s for QUENCH-15, 9100 s for QUENCH-19

Figure 44 Comparison of axial temperature profiles at shroud for QUENCH-15 and QUENCH-19.

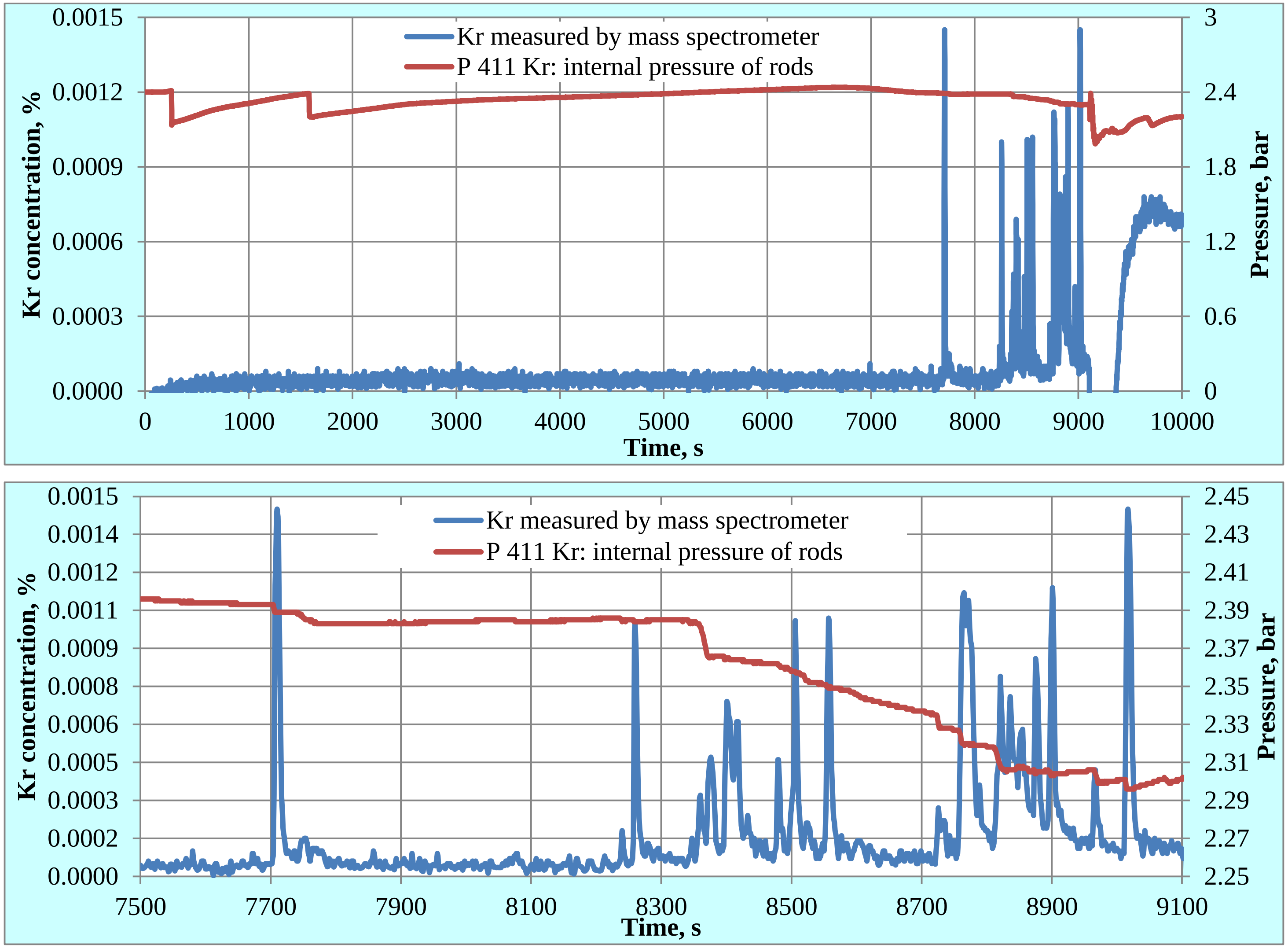

Figure 45 QUENCH-19; indications of rod failures: internal pressure decrease and Kr releases

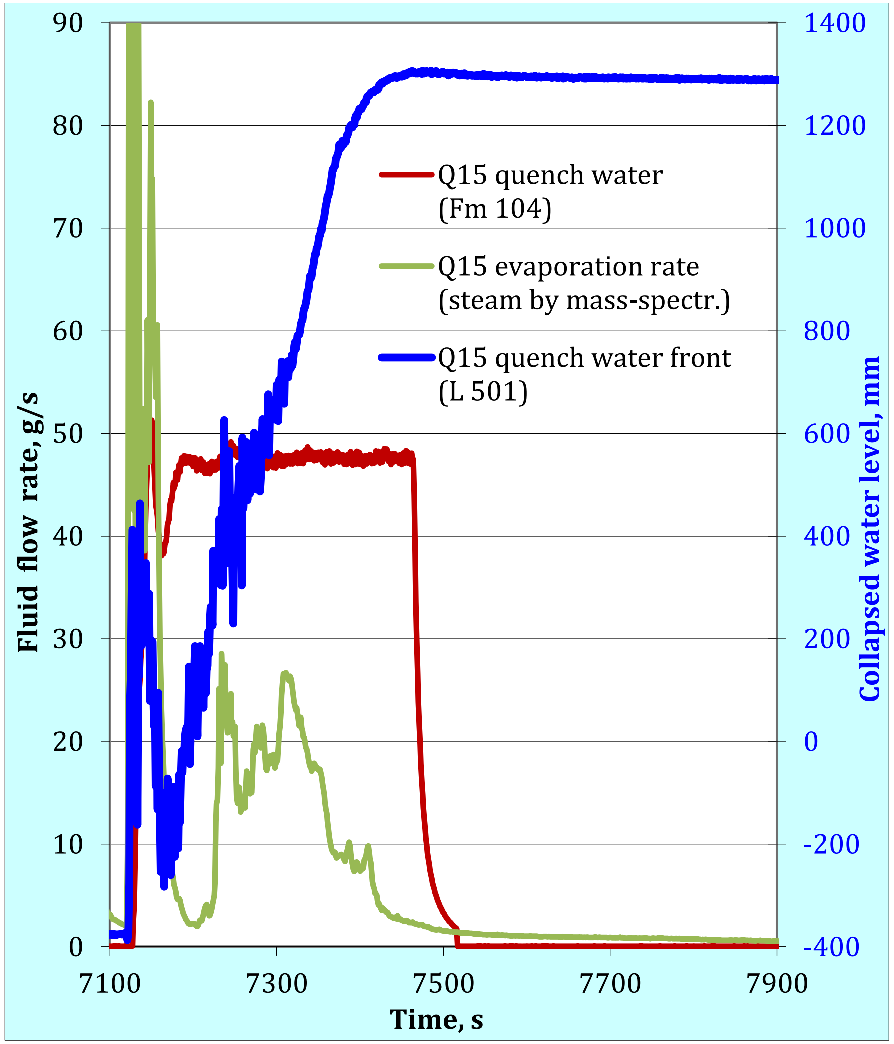

QUENCH-15: water rise duration 330 s (extended due to initial reduced water feed rate)

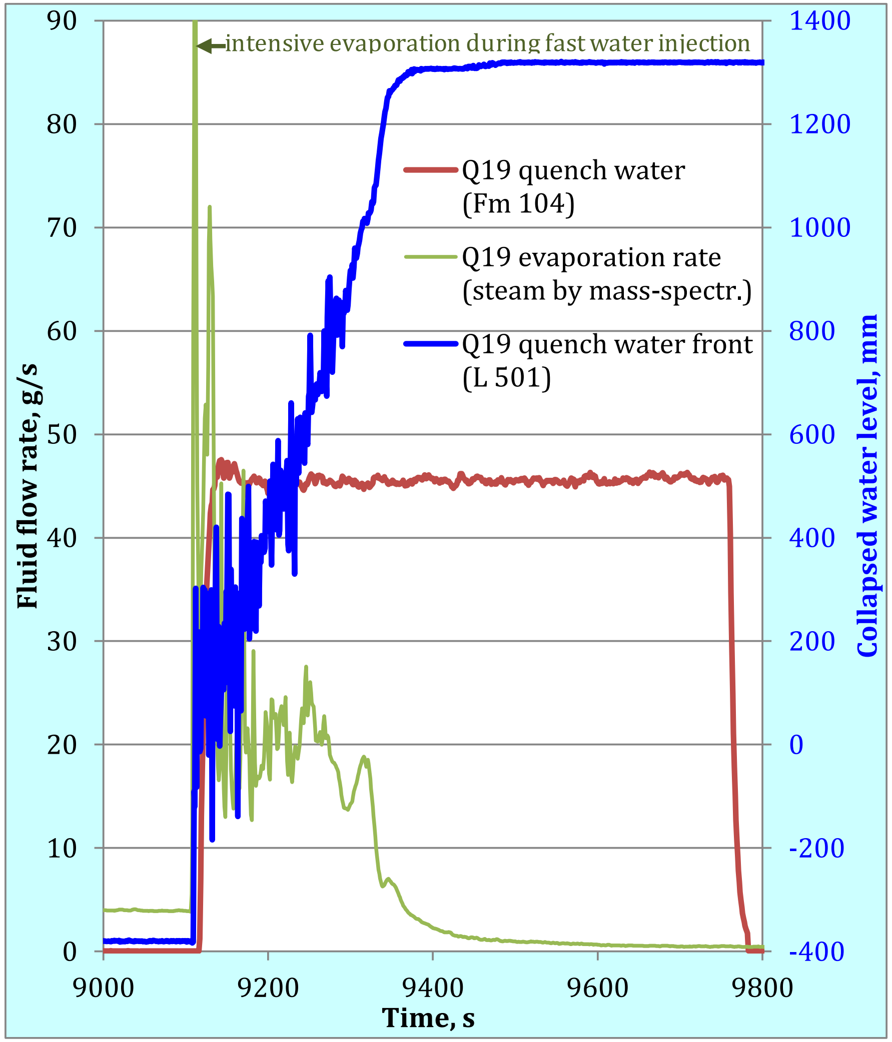

QUENCH-19: water rise duration 270 s

Figure 46 Phenomena during the quench stage of QUENCH-15 and QUENCH-19: evaporation of injected water, collapsed water front progress.

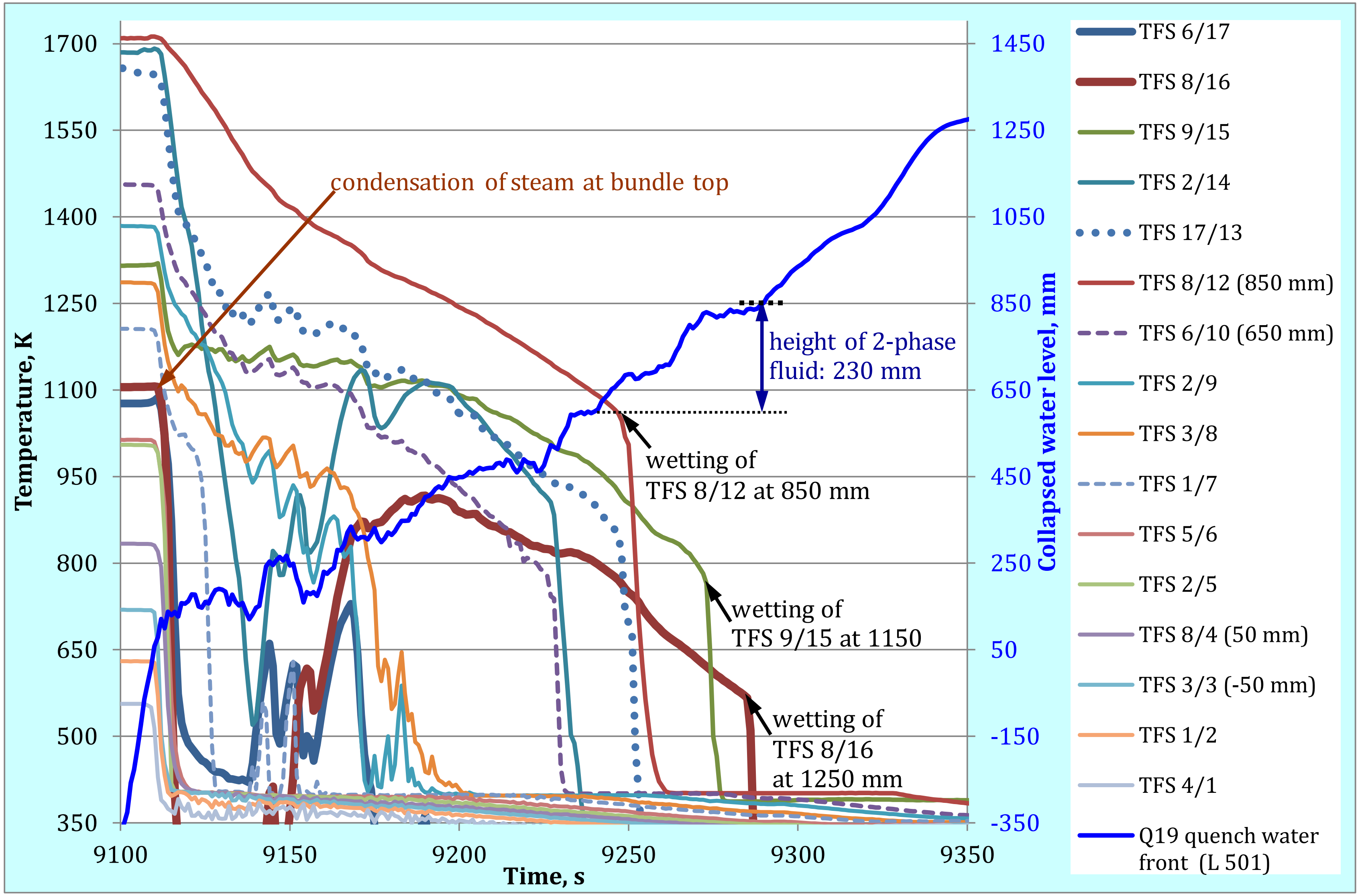

Figure 47 QUENCH-19; Wetting of thermocouples by two-phase fluid.

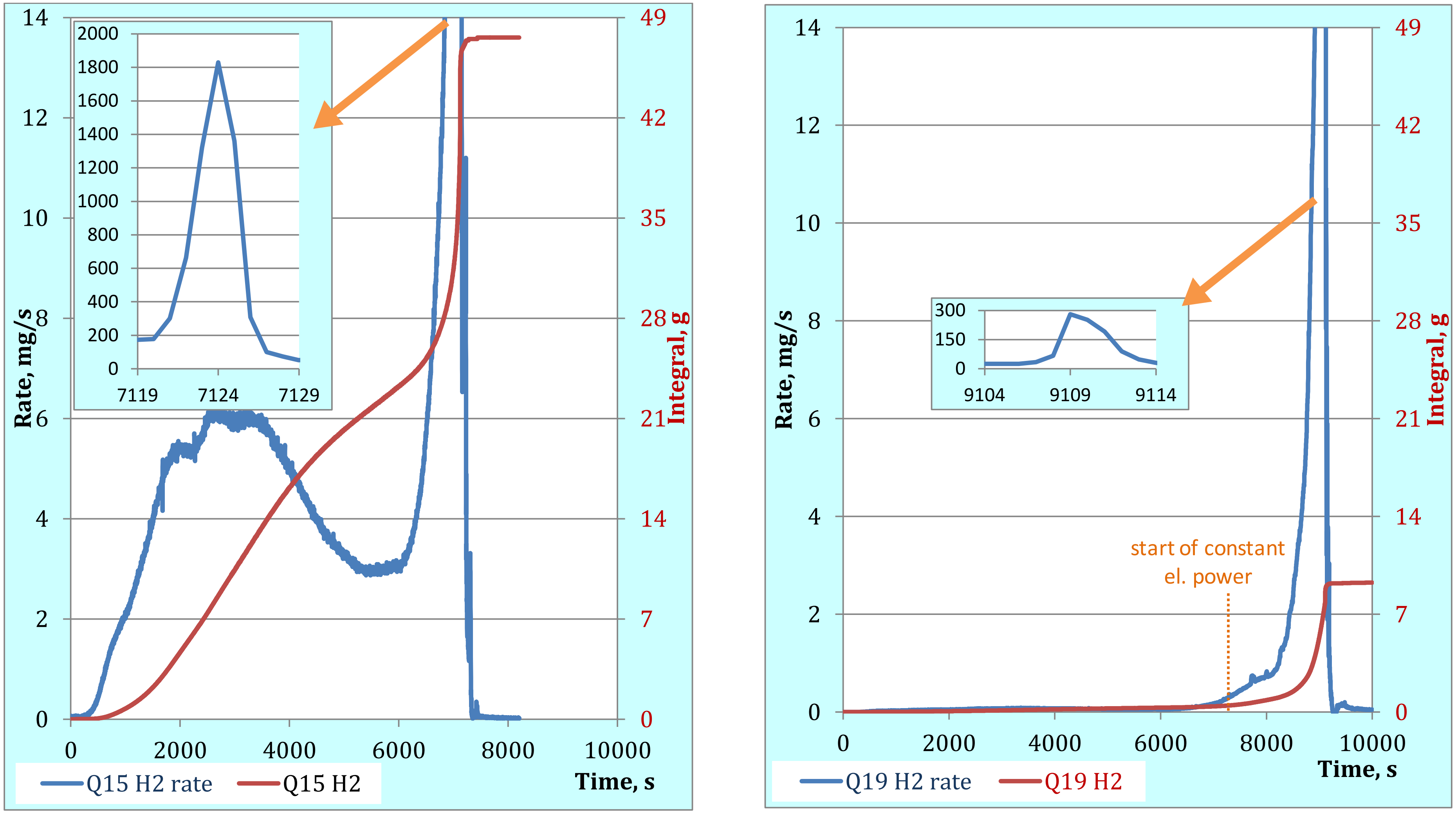

QUENCH-15: max rate 1830 mg/s; totally 47.6 g H_2, during quench 7 g H_2 QUENCH-19: max rate 280 mg/s; totally 9.2 g H_2, during quench 1.2 g H_2

Figure 48 Comparison of hydrogen release during QUENCH-15 and QUENCH-19.

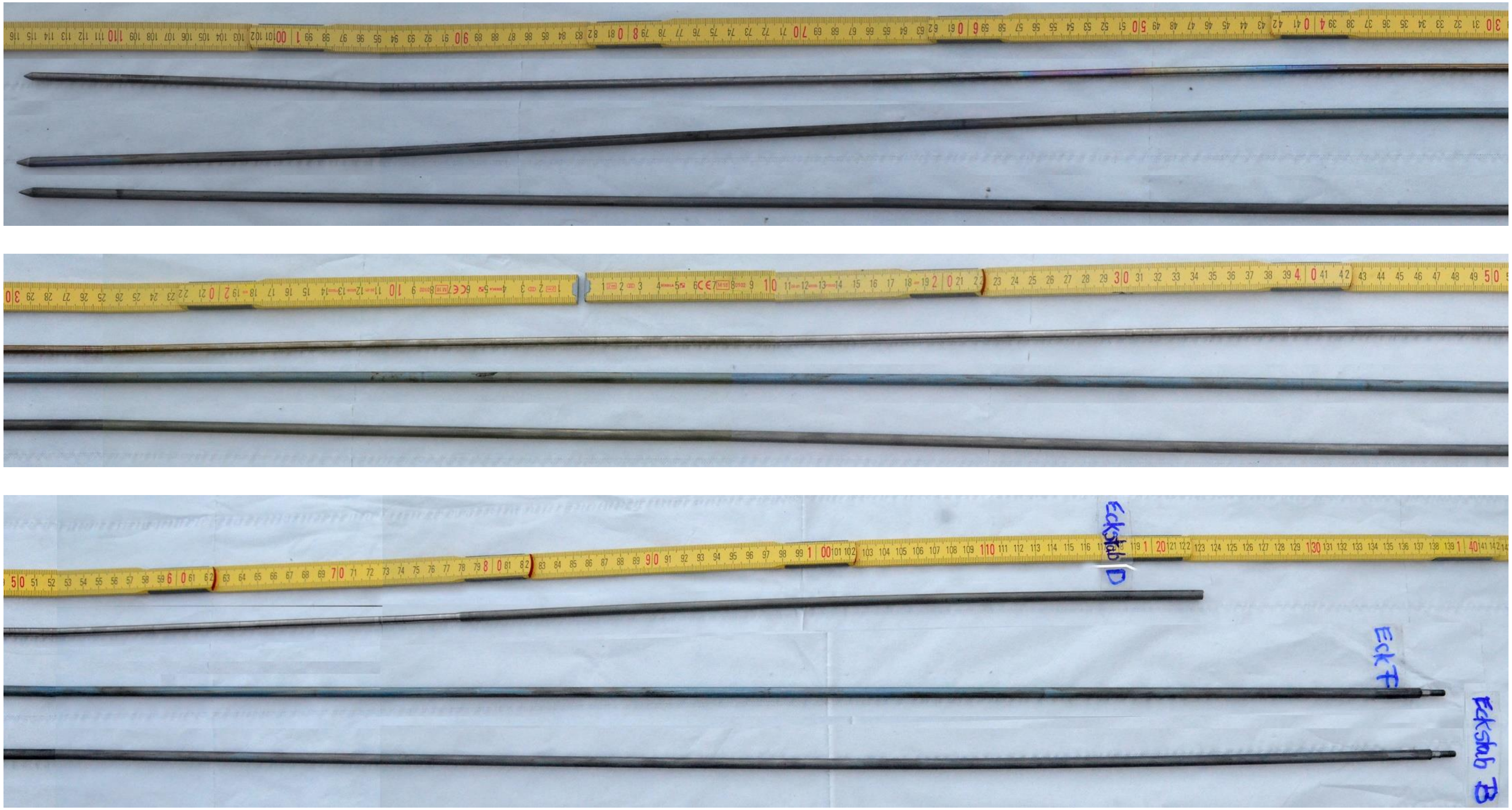

Figure 49 QUENCH-19; drawn corner rods B (after pre-oxidation), F (after transient), D (after test)

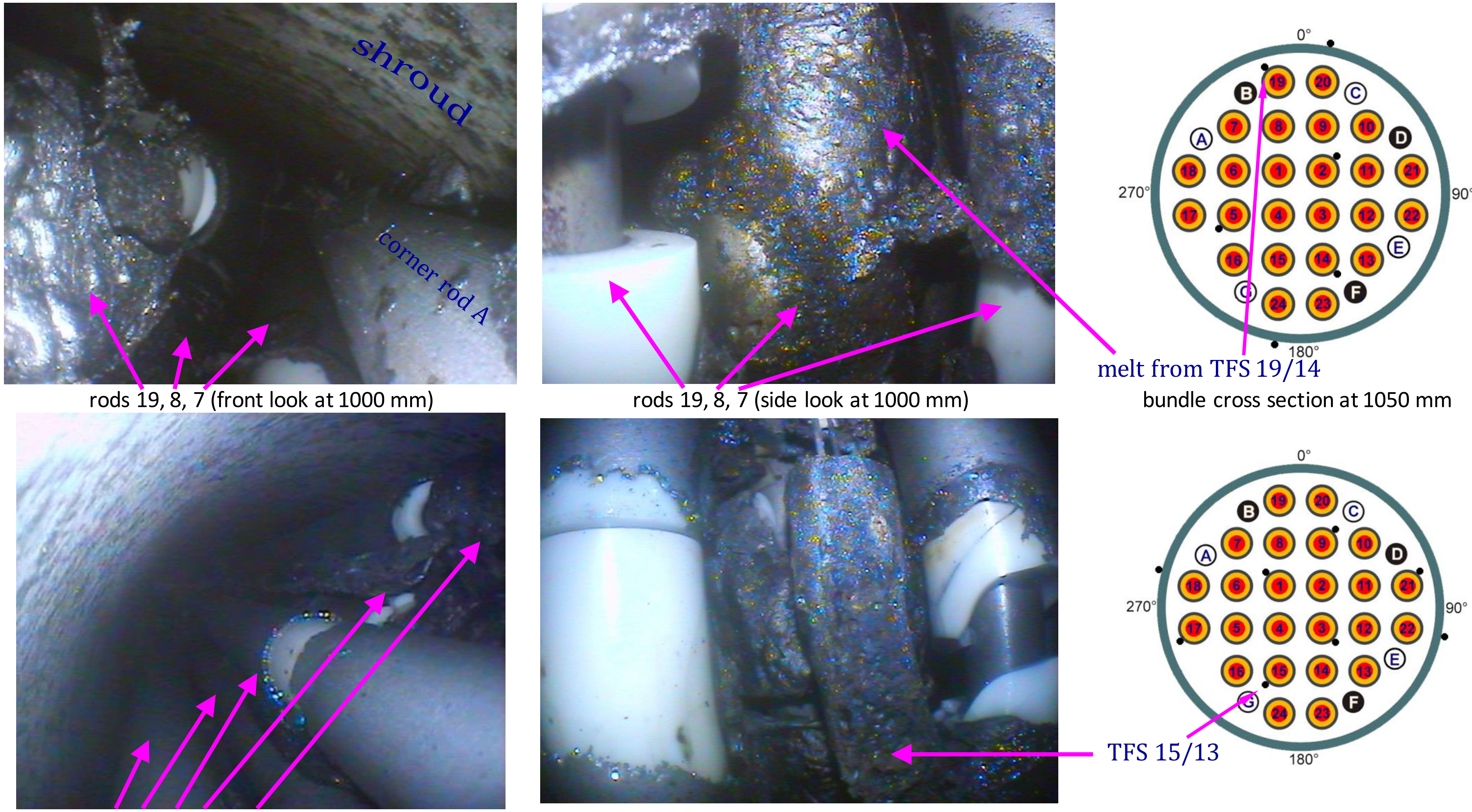

rods 19, 8, 7 (front look at 1000 mm) | rods 19, 8, 7 (side look at 1000 mm) | bundle cross section at 1050 mm

rods 17, 5, 16, 15, 24 (front look at 950 mm) | rods 16, 15, 24 (side look at 950 mm) | bundle cross section at 950 mm

Figure 50 QUENCH-19; observations of damaged (partly melted) claddings at upper part of the heated zone with videoscope inserted instead withdrawn rods B and “E”

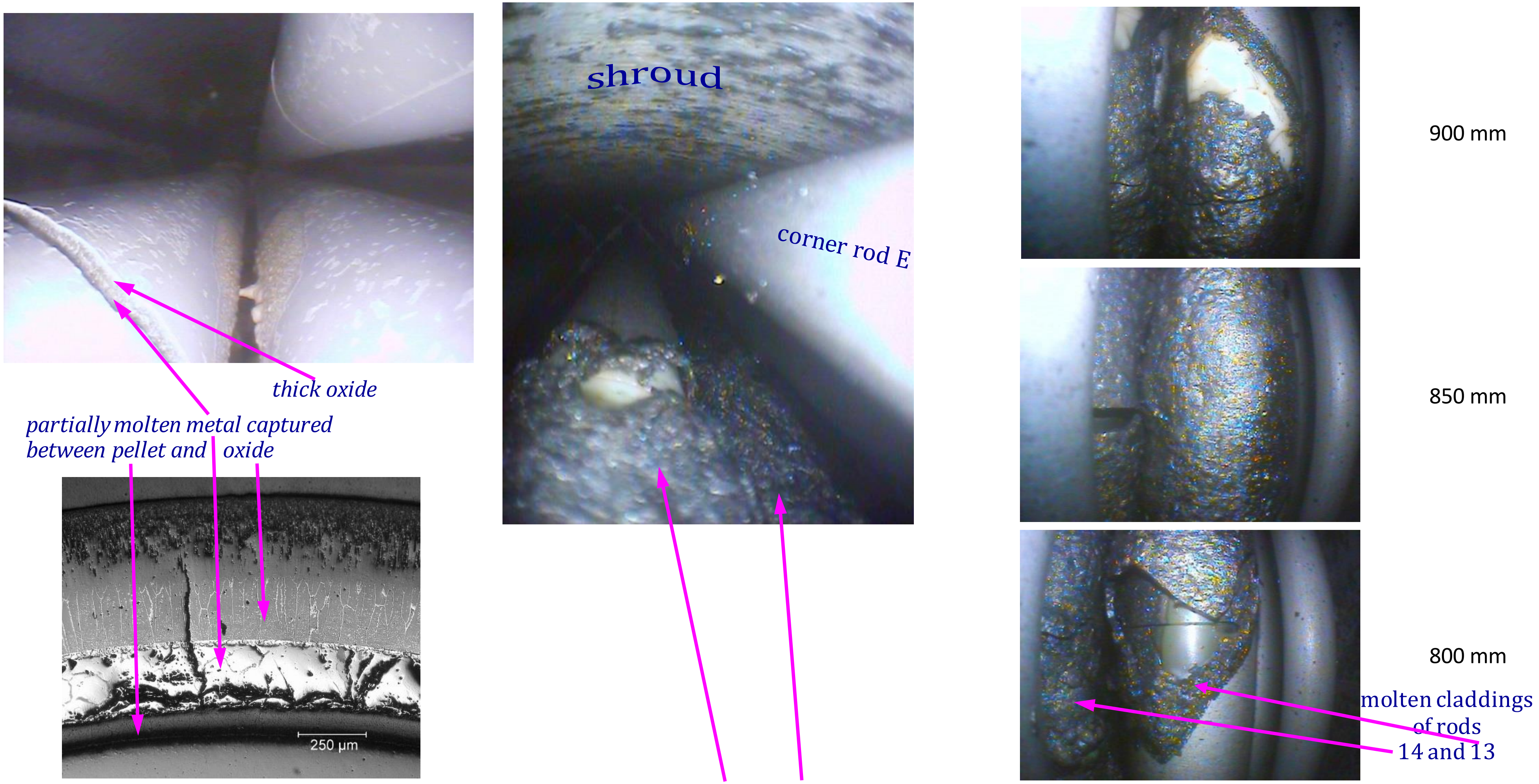

Q15: circumferential cladding cracks at hottest elevation of 950 mm

molten claddings of rods 13 and 12 of QUENCH-19 bundle at 1000 mm

Figure 51 Comparison of observations for QUENCH-15 and QUENCH-19 with videoscope inserted instead withdrawn rod F

bundle surrounded by shroud, insulation and cooling jacket | bundle surrounded by shroud and insulation | bundle surrounded by shroud | bundle

Figure 52 QUENCH-19; stages of extracting an assembly from the test section

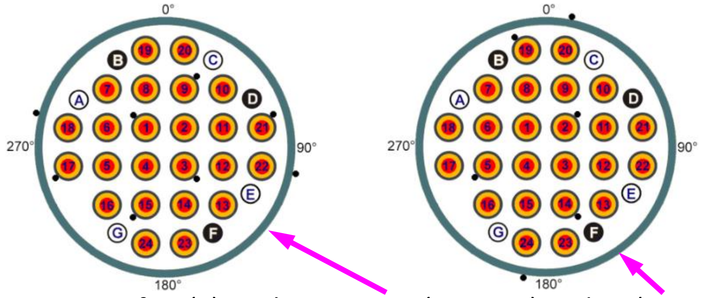

Positions of TC (•) at elevations 13 (950 mm) and 14 (1050 mm)

- the melting range of 304 steel is 1400…1450°C
- the melting range of FeCrAl alloys is 1500…1520°C

0°: TFS 9/13 and 19/14

90°: TFS 3/13, 21/13, 9/13

180°: TFS 15/13 and 14/14

270°: TFS 1/13, 15/13

Figure 53 QUENCH-19: bundle at elevations between 900 and 1100 mm: cladding damages by molten thermocouple steel (AISI 304) sheaths

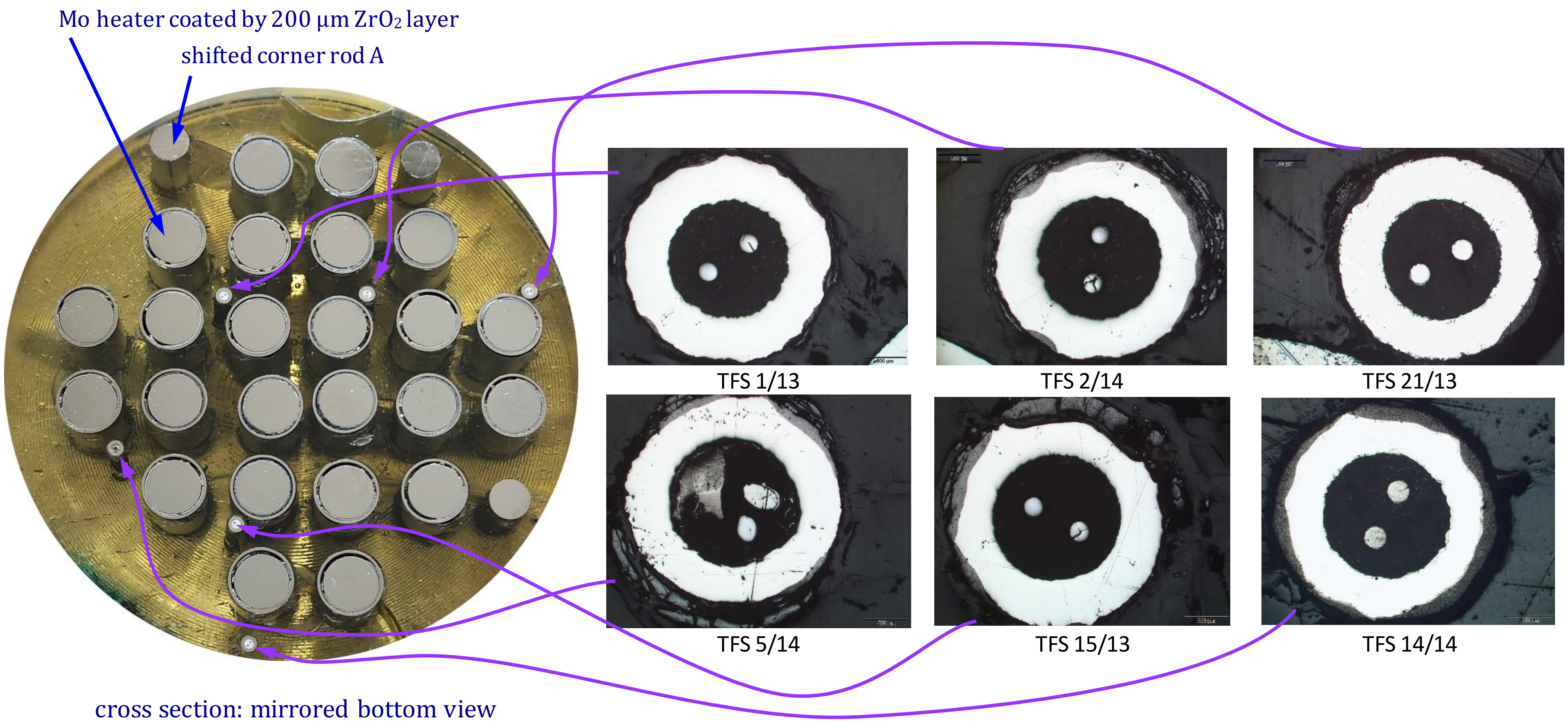

Figure 54 QUENCH-19: oxidation of stainless steel sheaths of thermocouples at the bundle elevation 1050 mm

KIT: bottom view of slice **952**-968 mm, mirrored

KIT: bottom view of slice **854**-870 mm, mirrored

KIT: bottom view of slice **754**-770 mm, mirrored

ORNL: top view of slice 932-**948** mm

ORNL: top view of slice 834-**850** mm

ORNL: top view of slice 734-**750** mm

Figure 55 Pairs of cross sections investigated at KIT and ORNL

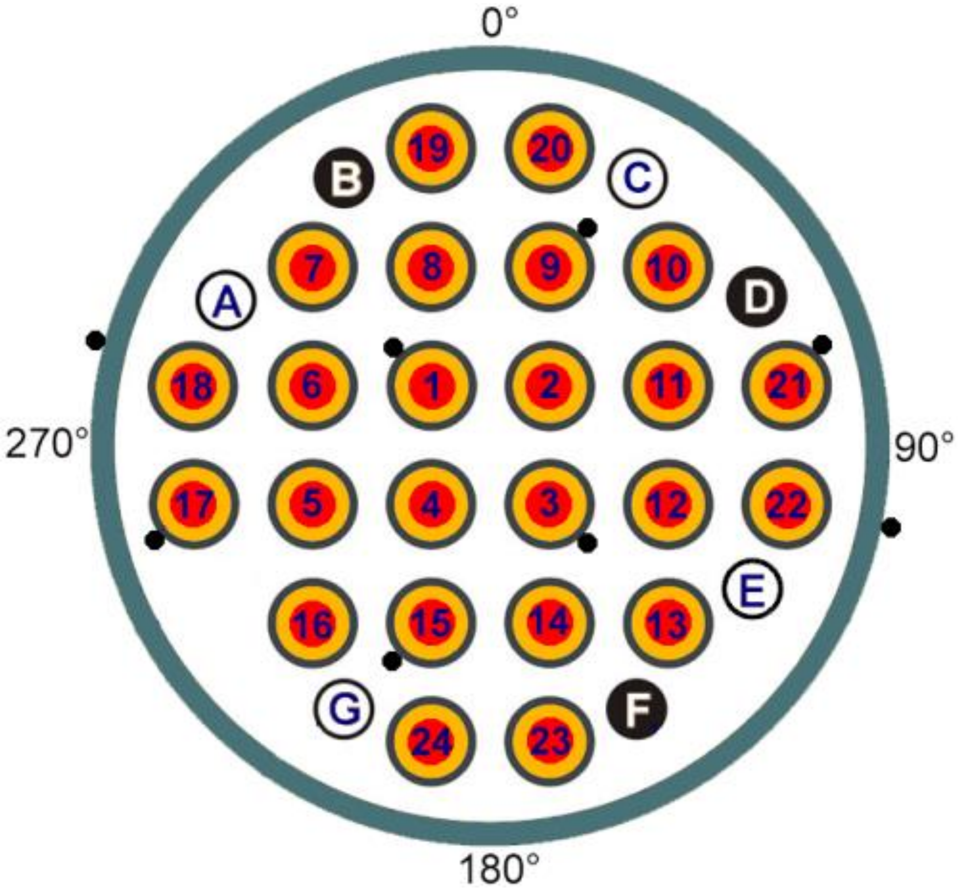

950 mm top view

mirrored bottom view of slice 952-968 mm: dark reduced pellets of rods 17, 18, 23 due to intact claddings, all other claddings failed

Figure 56 QUENCH-19: cross section at elevation 950 mm

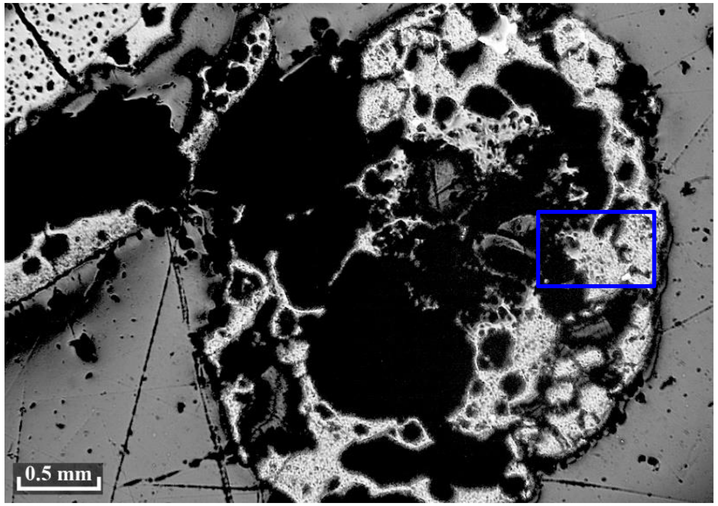

TFS 1/13 with molten sheath detached from rod 1 and contacted rod 7

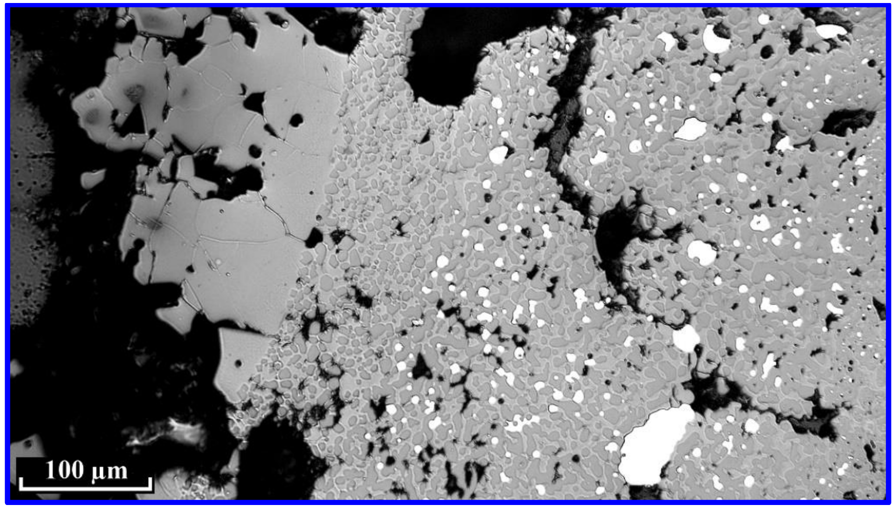

TFS 1/13 melt structure

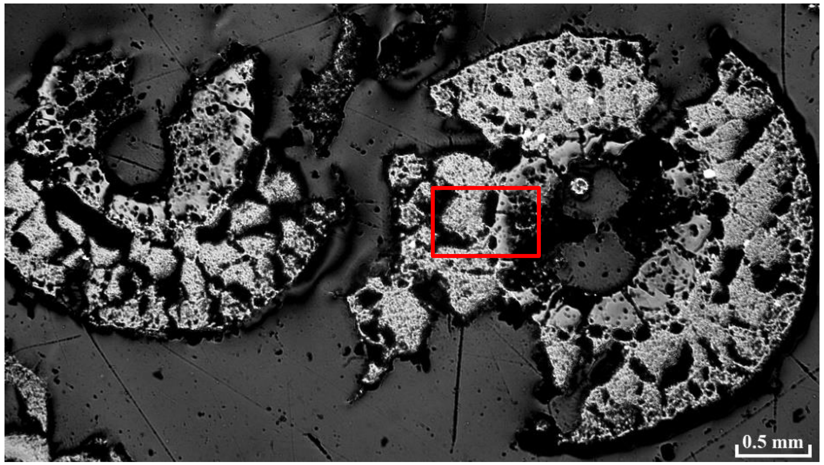

TFS 3/13 with molten sheath detached from rod 3

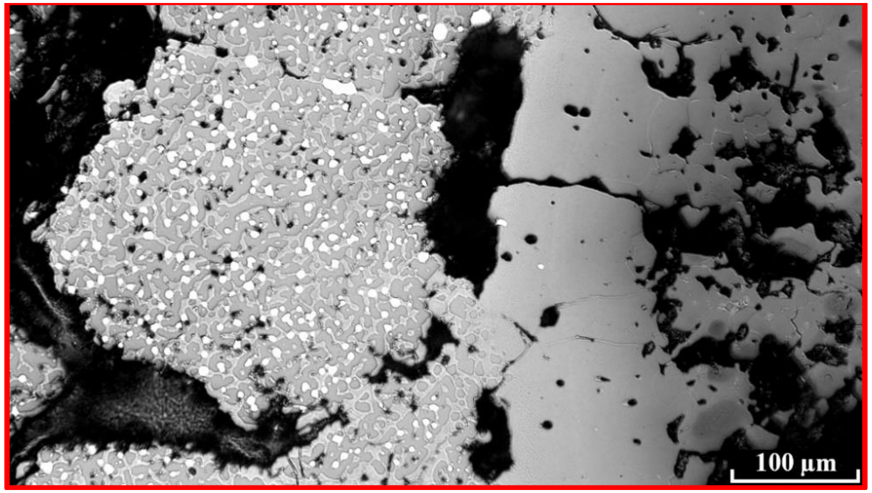

TFS 3/13 melt structure

Figure 57 QUENCH-19: thermocouples at elevation 950 mm

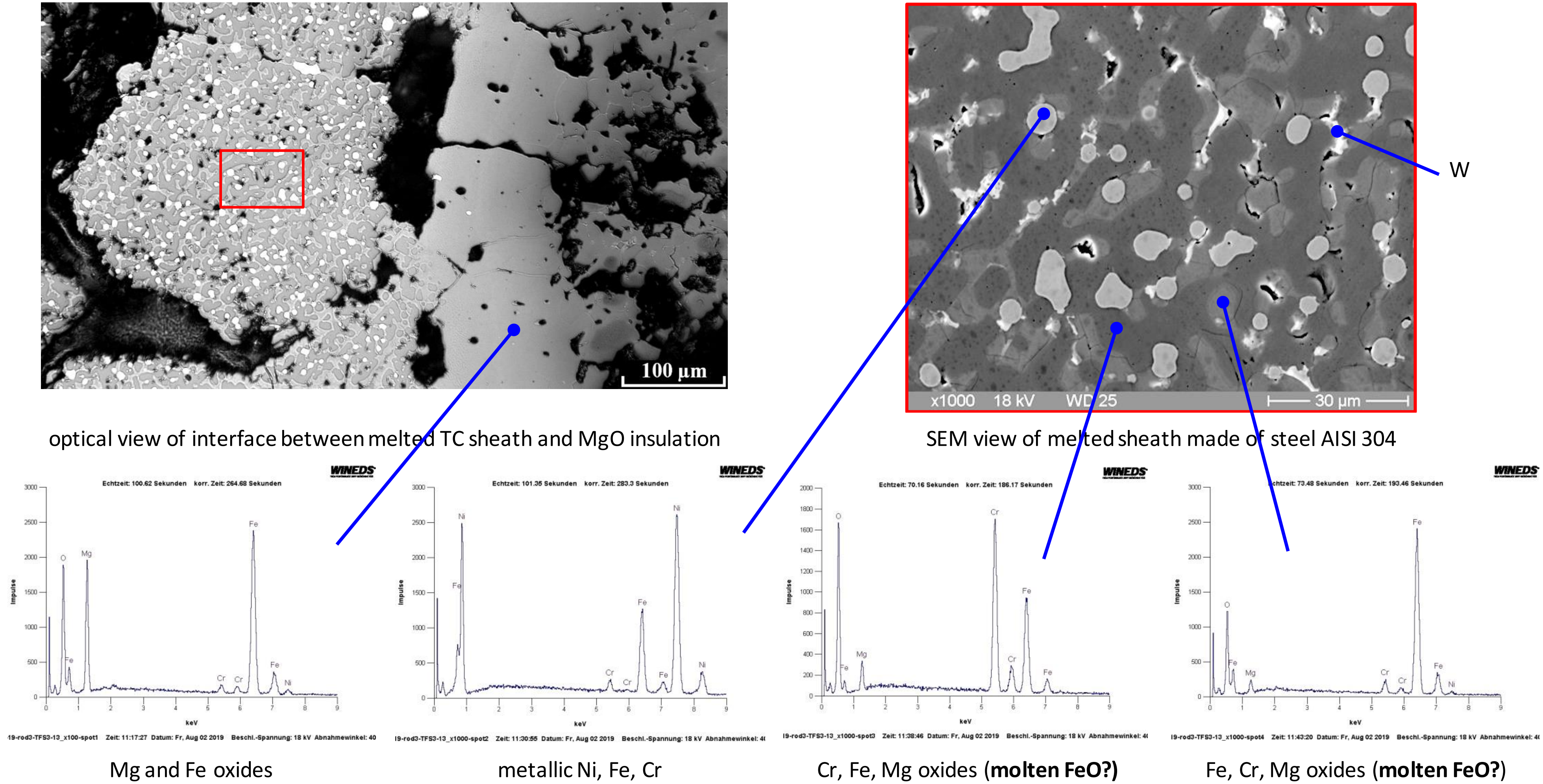

Figure 58 QUENCH-19; SEM/EDX investigation of composition of thermocouple TFS 3/13 failed by sheath melting, elevation 950 mm

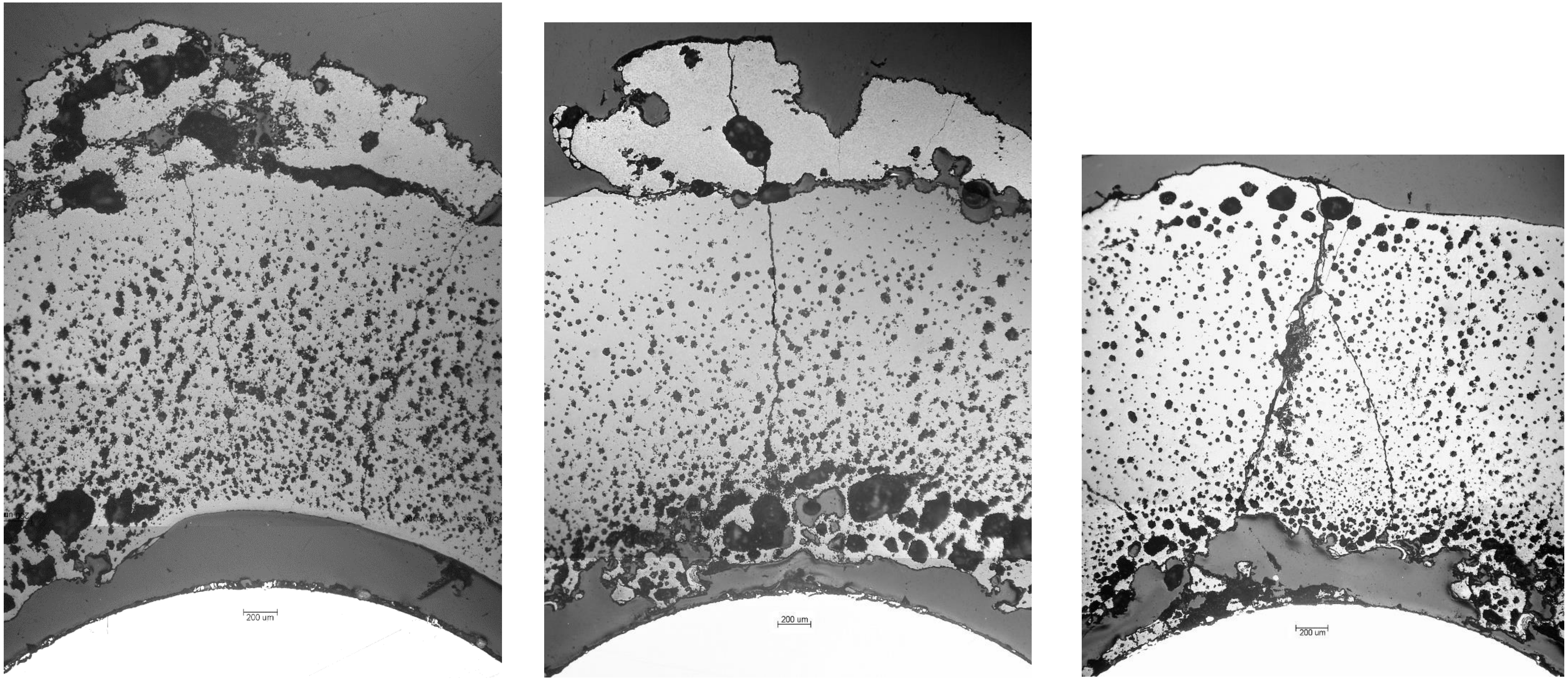

90°: remnants of oxidized cladding and porous pellet

135°: remnants of oxidized cladding and porous pellet

180°: porous pellet; absent of molten cladding relocated downwards

Figure 59 QUENCH-19: metallographic observation of rod 1 at the elevation 950 mm; interaction of oxidized molten cladding with pellet

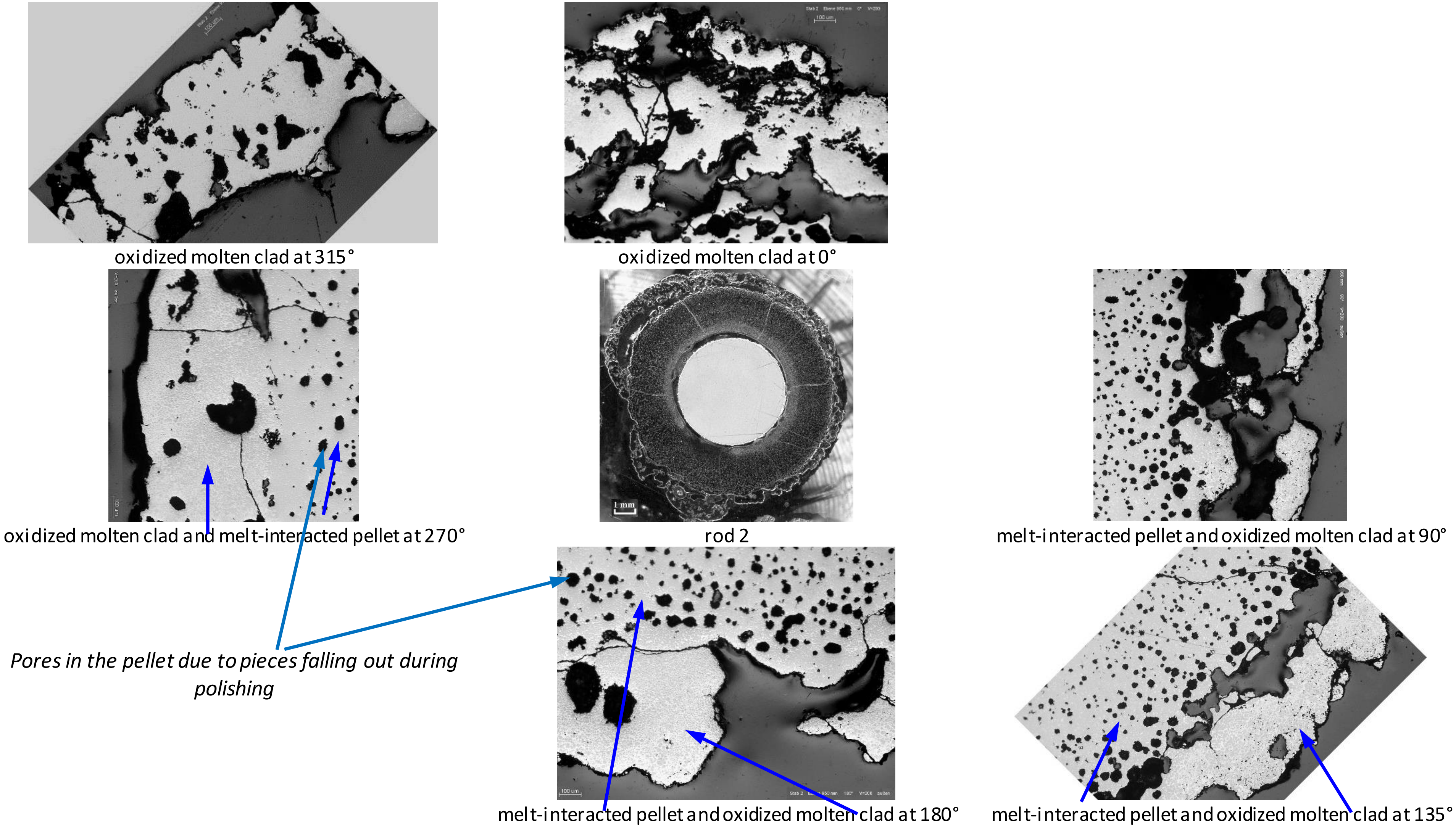

Figure 60 QUENCH-19: metallographic observation of rod 2 at the elevation 950 mm, bottom view mirrored

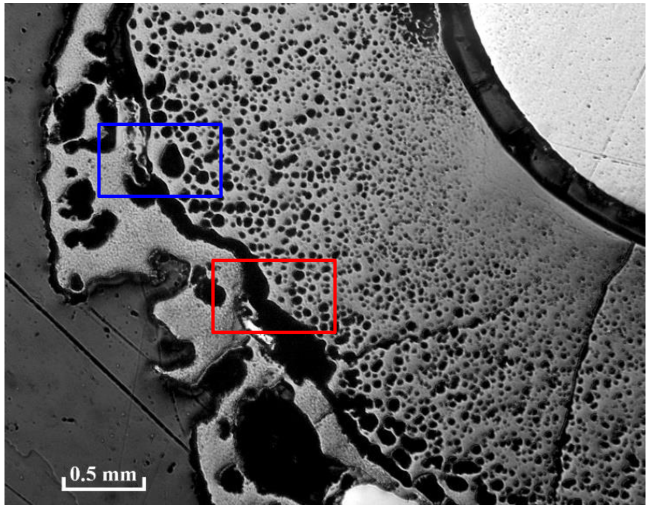

left lower segment of rod 2 with molten cladding and melt-interacting pellet (pores due to grain remove during grinding)

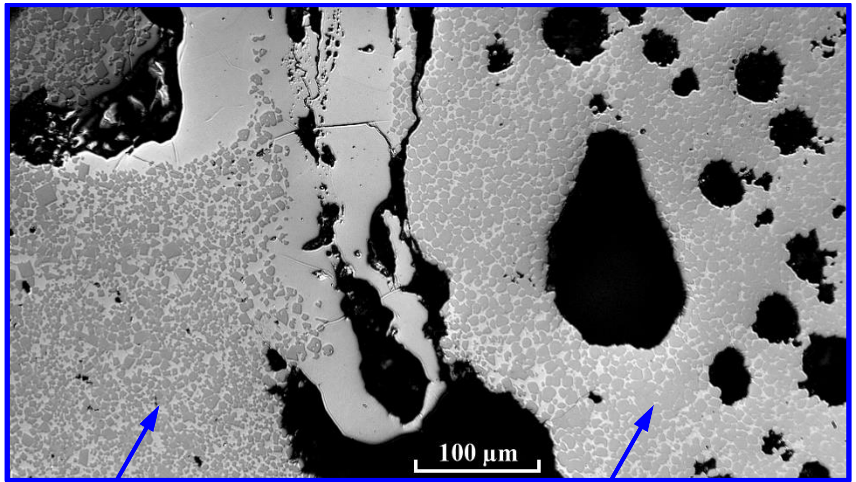

FeO melt with ceramic precipitates; pellet grains surrounded by frozen metal melt

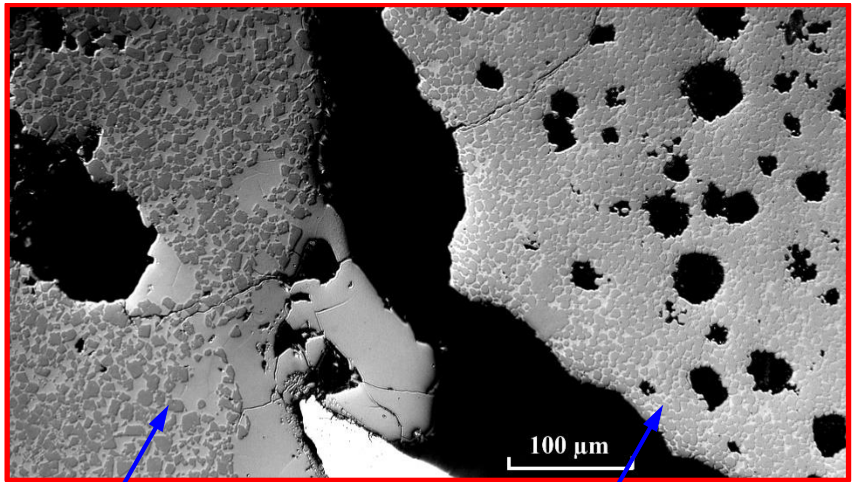

FeO melt with ceramic precipitates; pellet grains surrounded by frozen metal melt

Figure 61 QUENCH-19: metallographic observation of interface between cladding melt and the pellet of rod 2 at the elevation 950 mm, bottom view mirrored

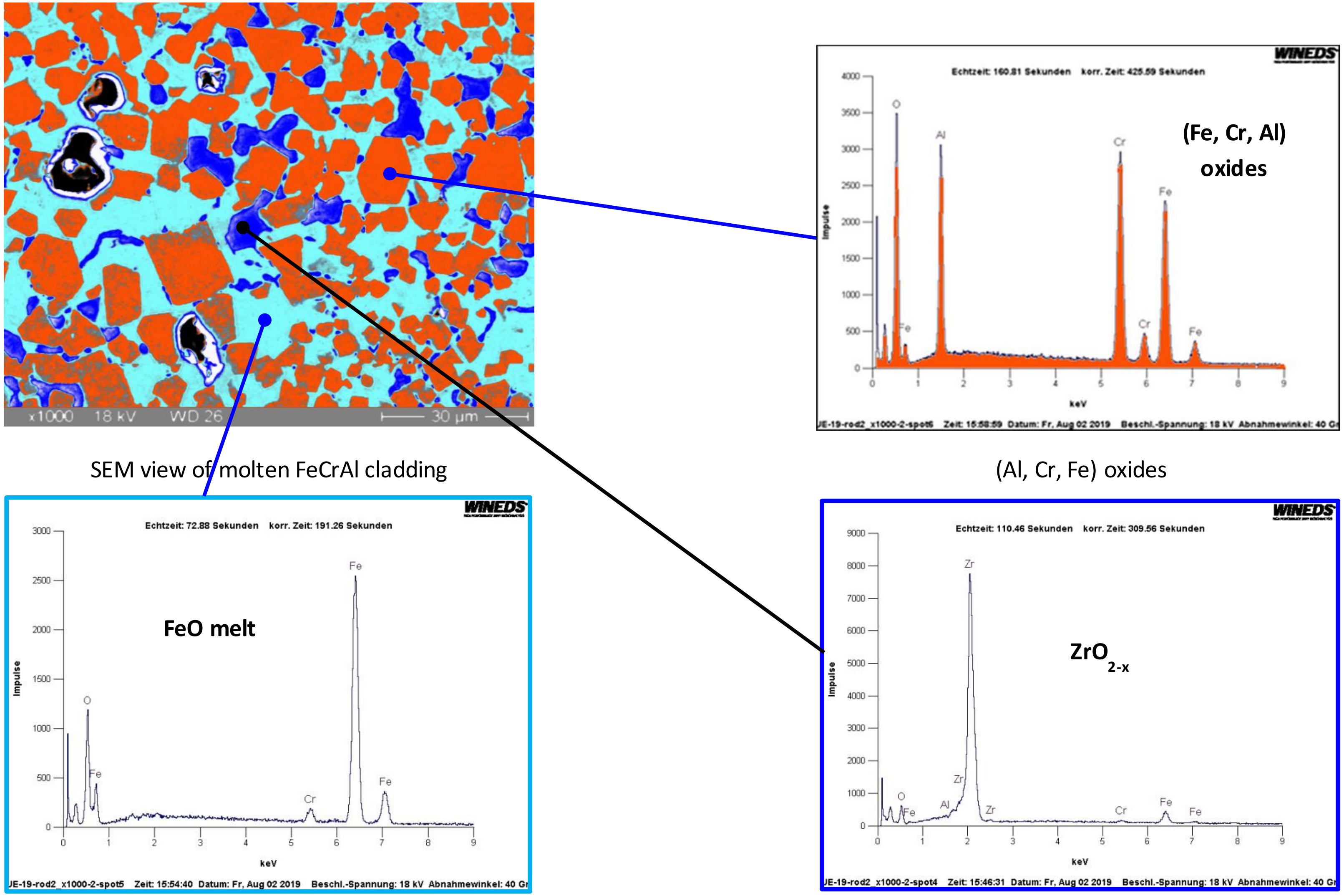

SEM view of molten FeCrAl cladding

(Al, Cr, Fe) oxides

molten FeO

ZrO_{2-x}

Figure 62 QUENCH-19; SEDX investigation of molten cladding structure of rod 2 at elevation 950 mm

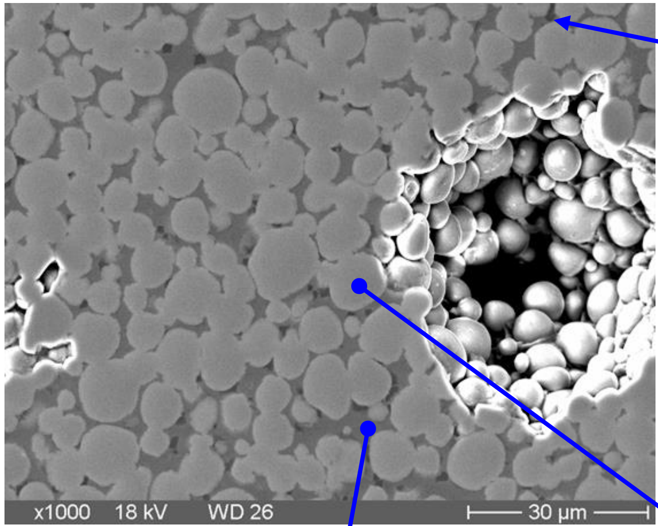

SEM view of ZrO_2 pellet

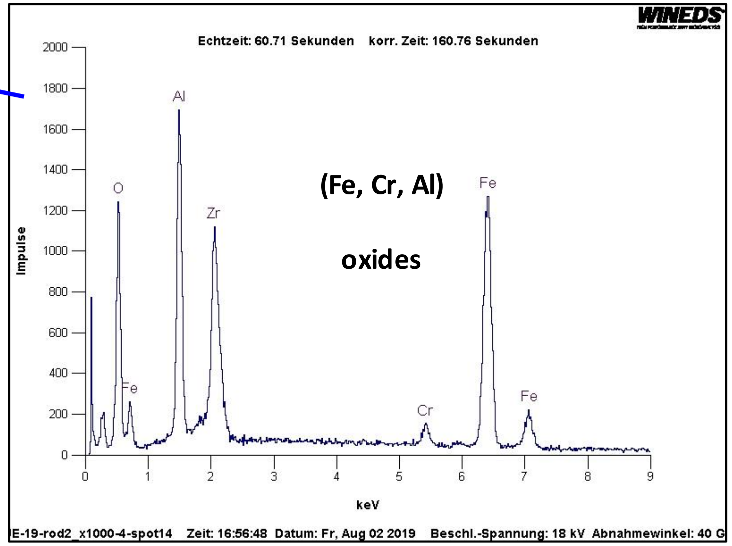

(Al, Fe, Zr) oxides

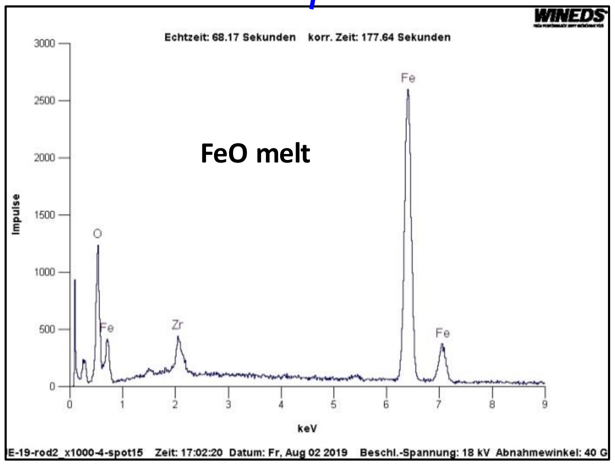

molten FeO

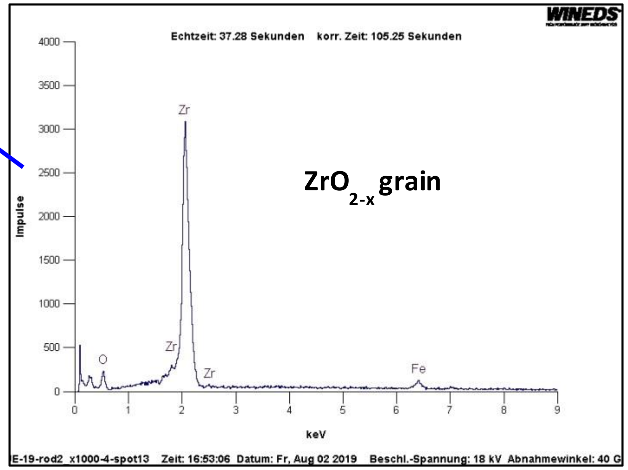

ZrO_{2-x} grain

Figure 63 QUENCH-19; SEM/EDX investigation of friable pellet structure of rod 2 at elevation 950 mm

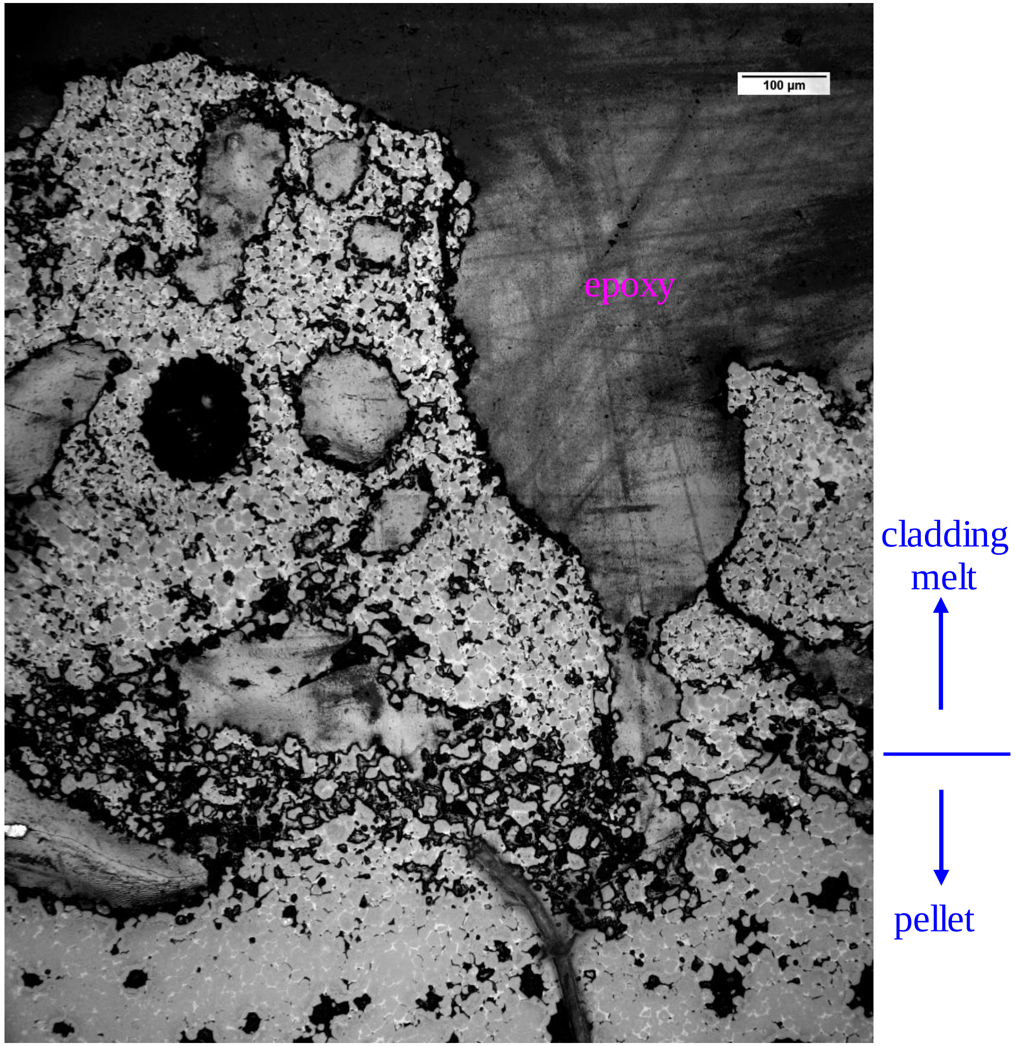

0°, interaction of oxidized cladding melt with pellet

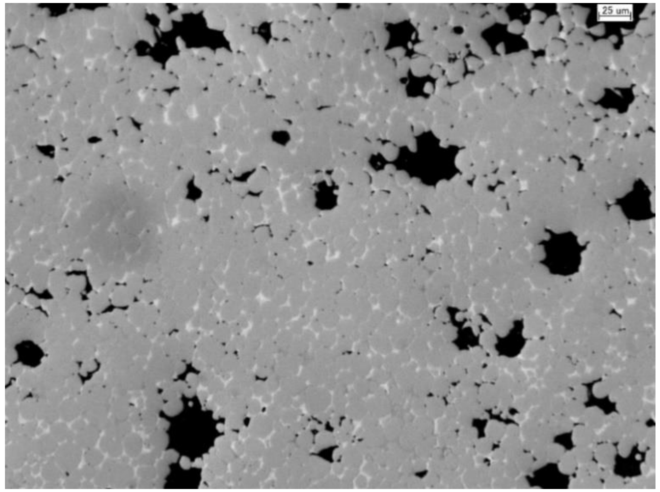

315°, middle part of pellet (ZrO_2 grains surrounded by FeO)

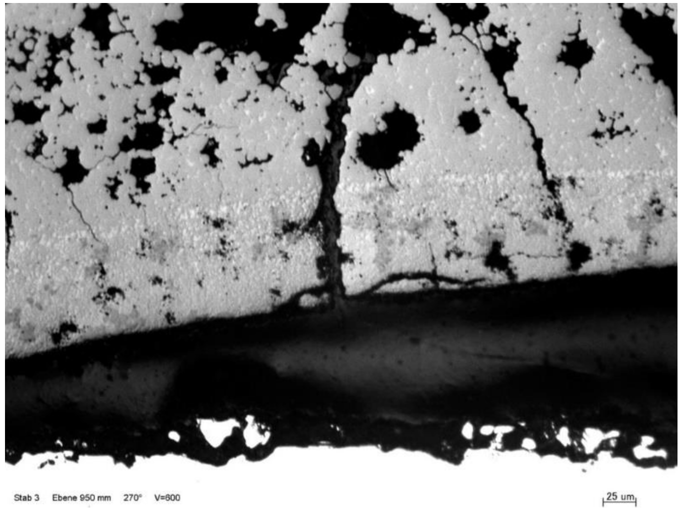

270°, rim at inner pellet edge (oxygen transport to W heater)

Figure 64 QUENCH-19: metallographic observation of rod 3 at the elevation 950 mm; microstructure of pellet: ZrO_2 grains surrounded by molten metal

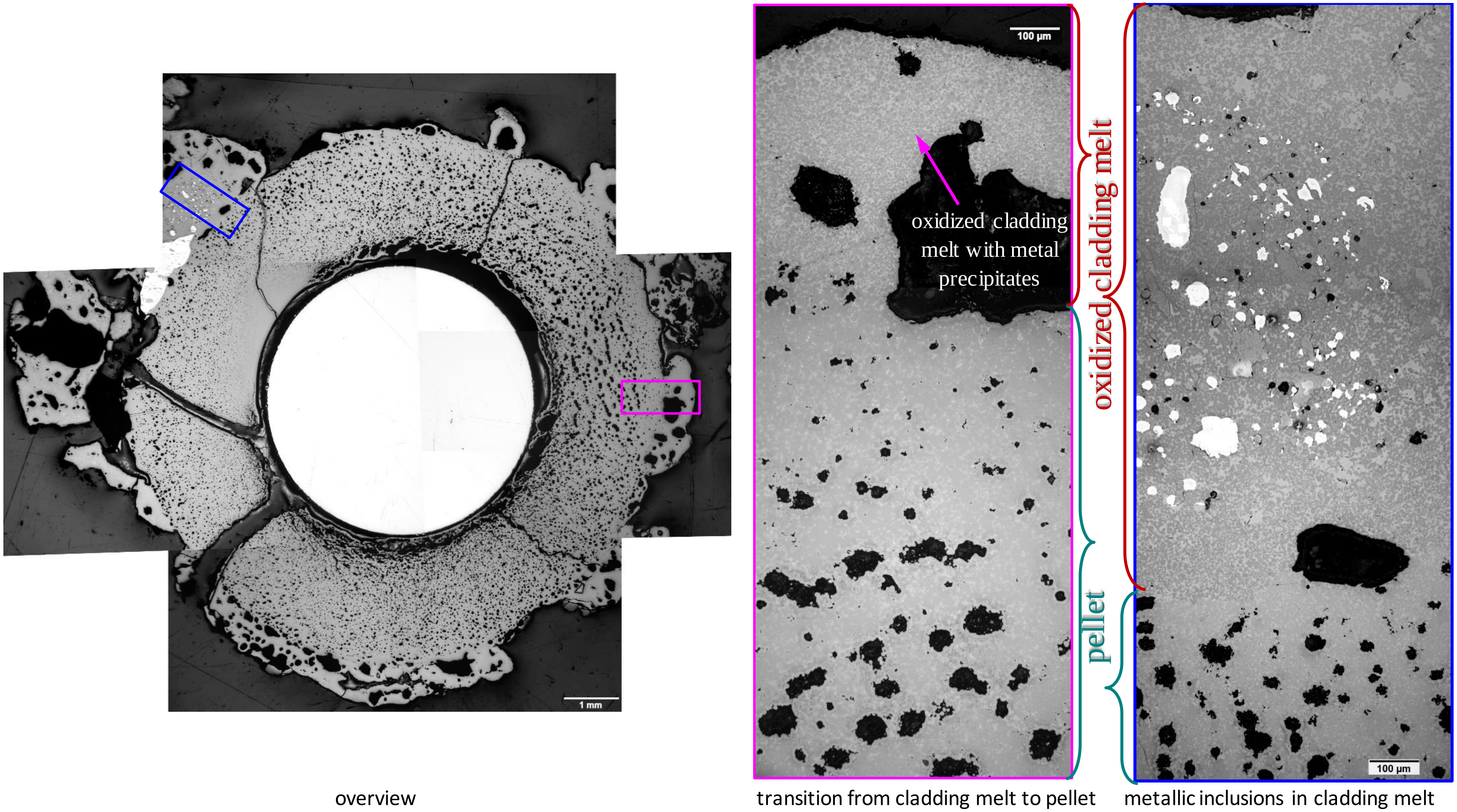

Figure 65 QUENCH-19: metallographic observation of rod 4 at the elevation 950 mm; completely oxidized melted cladding and strong porous pellet

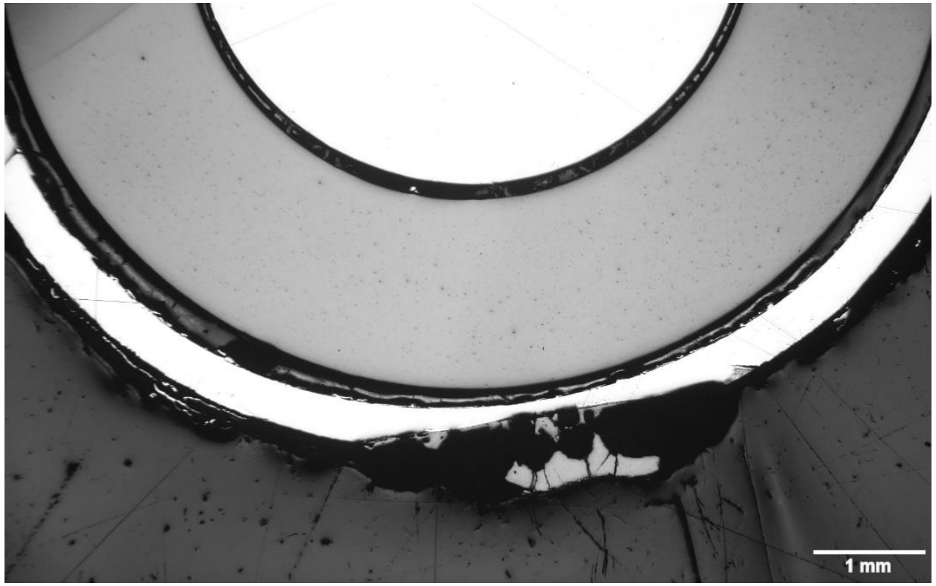

overview

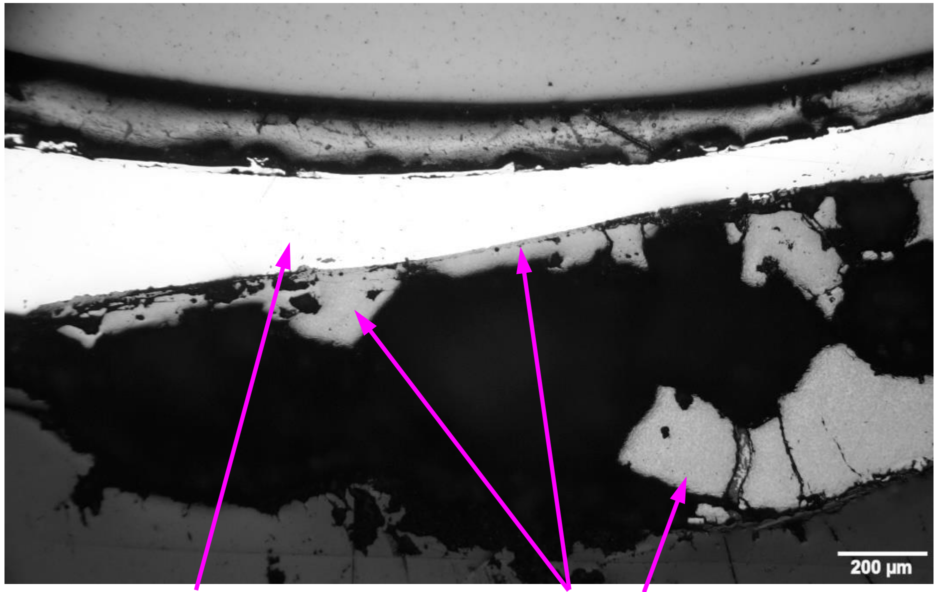

cladding thinning at the contact to melted oxidized part of cladding

Figure 66 QUENCH-19: metallographic observation of rod 5 at the elevation 950 mm, angle 180°: local thinning of cladding due to melting oxidized molten clad; not stoichiometric pellet material

not stoichiometric pellet material; oxidized molten clad

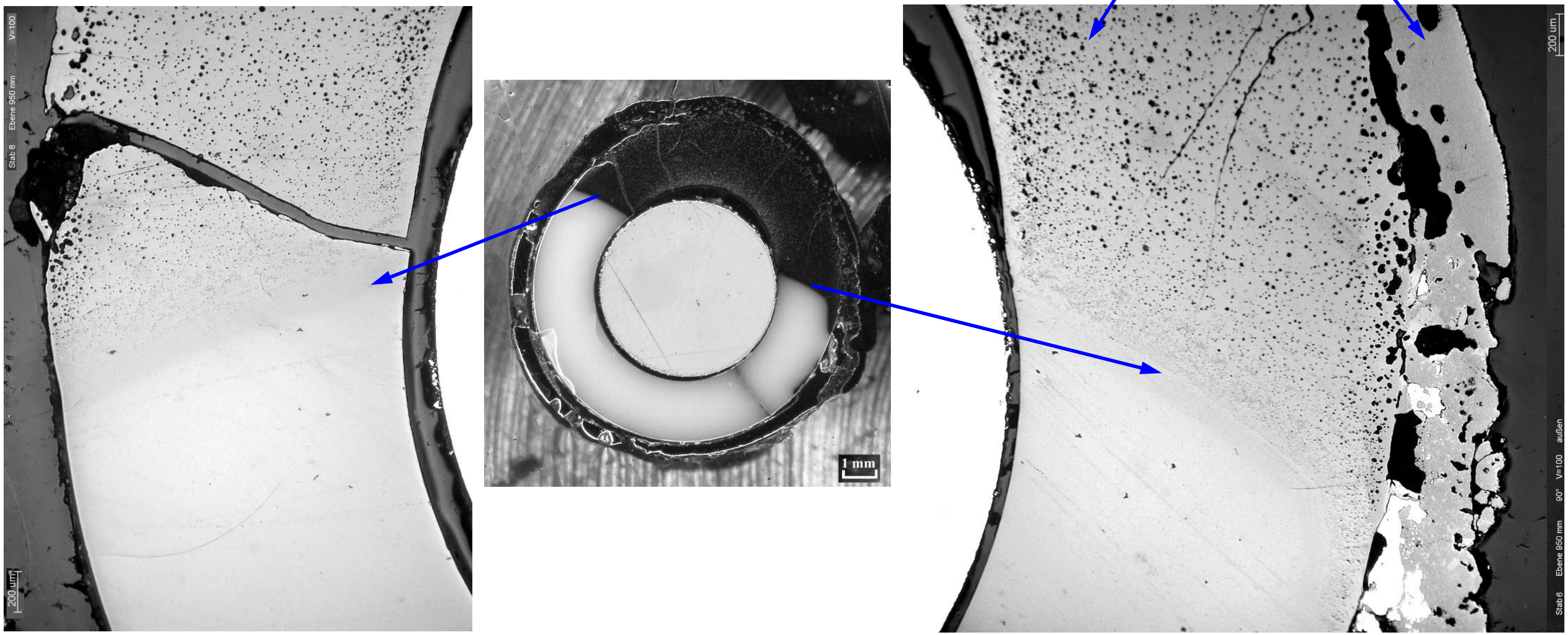

interface between two parts of pellet at 315°

rod 6 at 950 mm with two parts of pellets: interacted with melt (dark) and not interacted with melt (light)

interface between two parts of pellet parts at 100°; frozen cladding melt

Figure 67 QUENCH-19: metallographic observation of rod 6 at the elevation 950 mm, bottom view mirrored

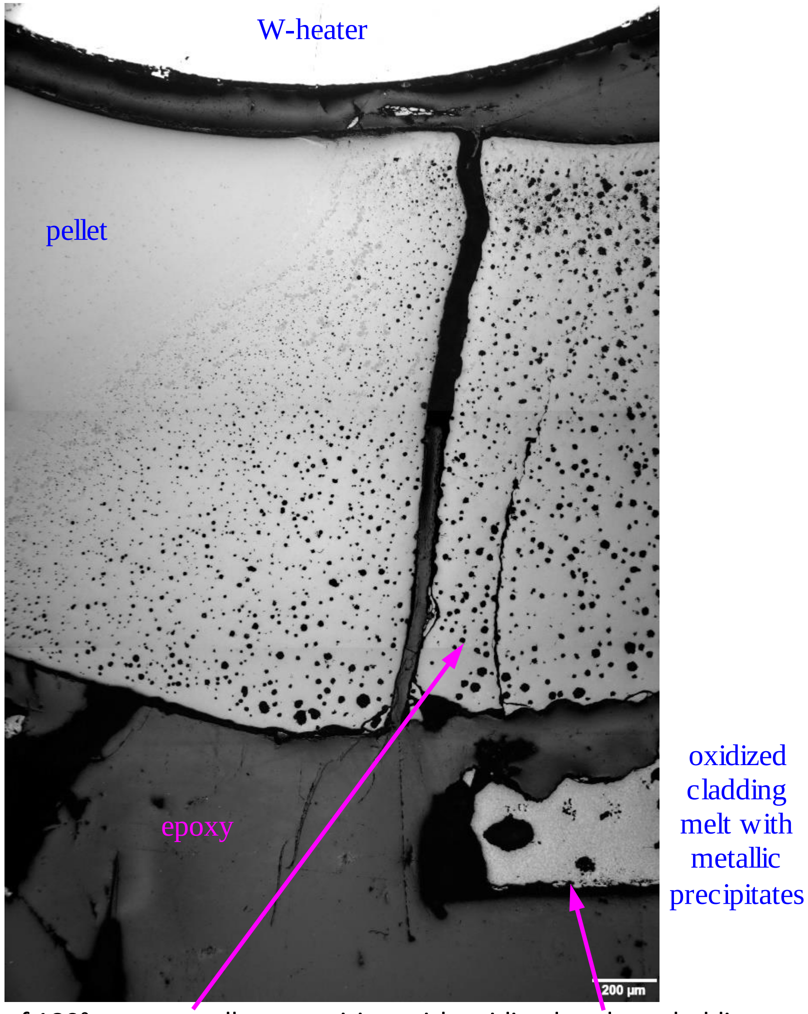

at angle of 180°: porous pellet at position with oxidized molten cladding

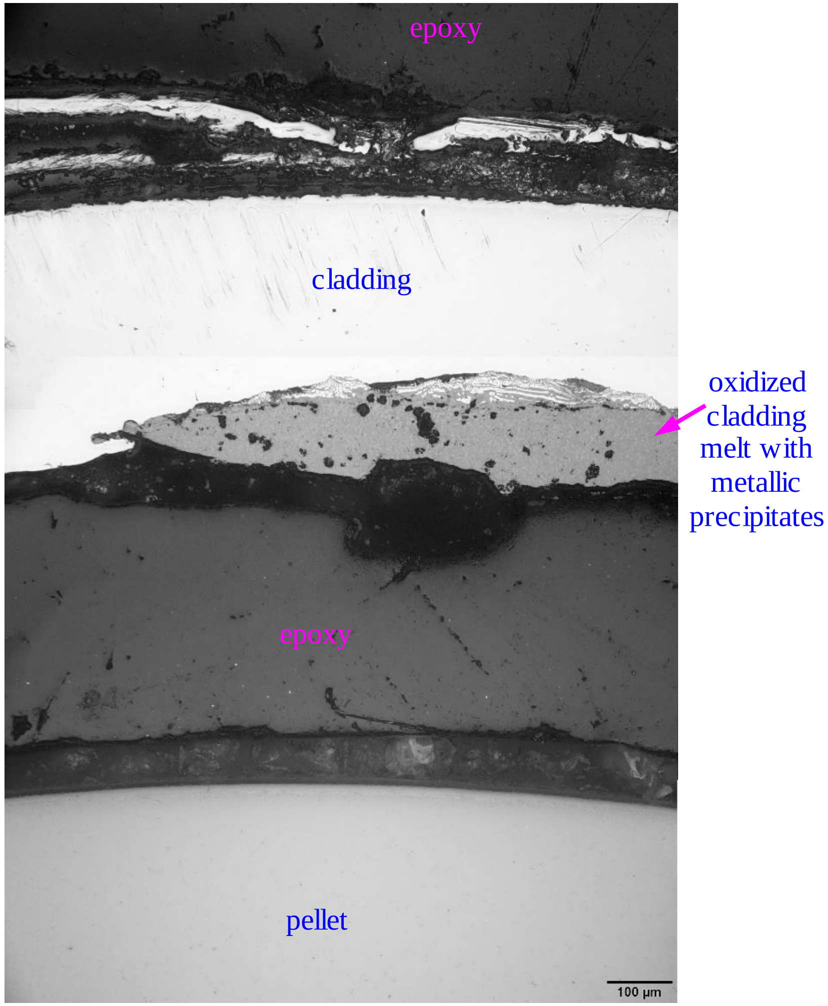

at angle of 315°: oxidized molten spot at the inner surface of cladding

Figure 68 QUENCH-19: metallographic observation of rod 7 at the elevation 950 mm

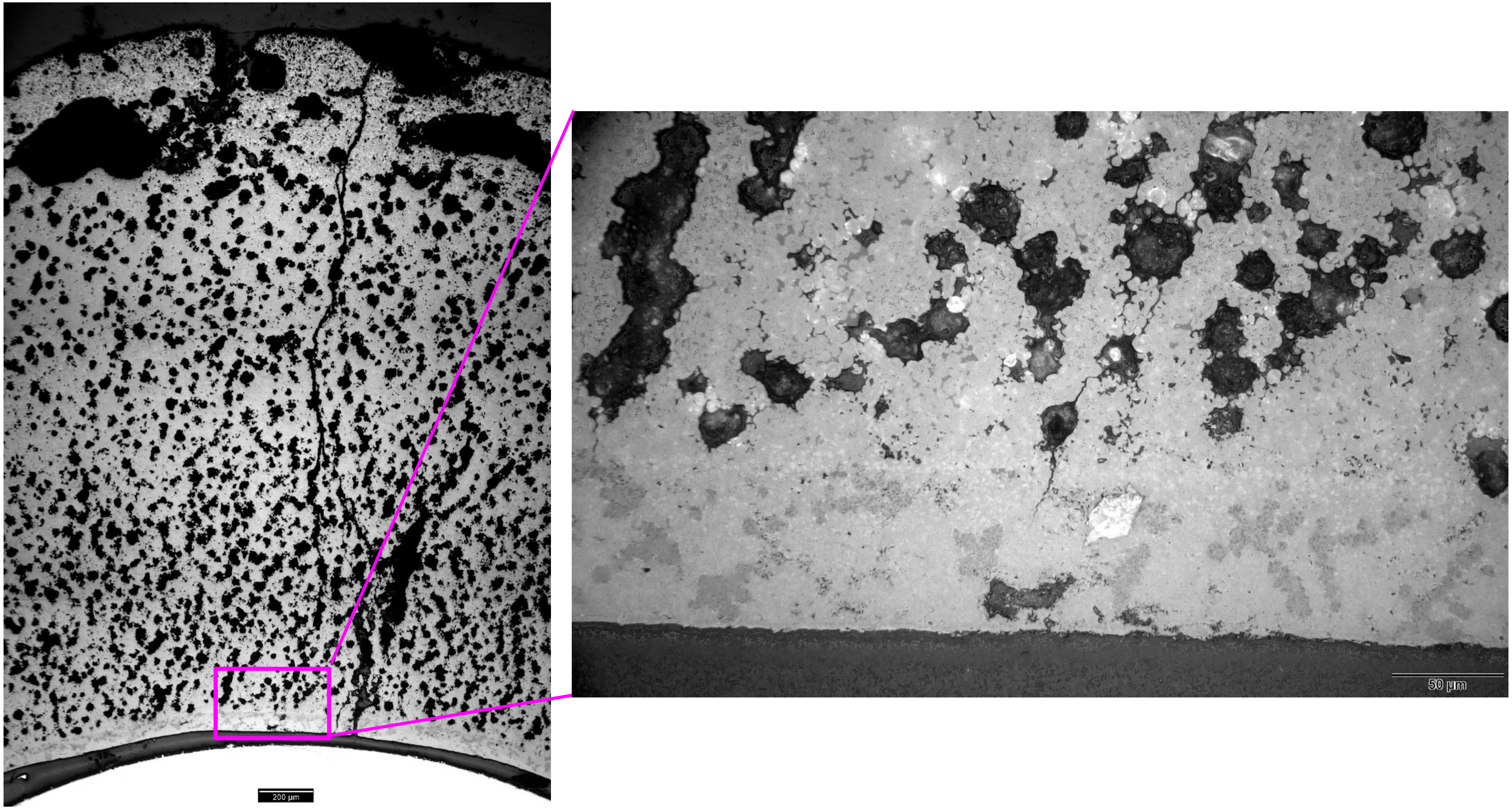

cladding cross section

layer at interface to W heater

Figure 69 QUENCH-19: metallographic observation of rod 9 at the elevation 950 mm, position 0°

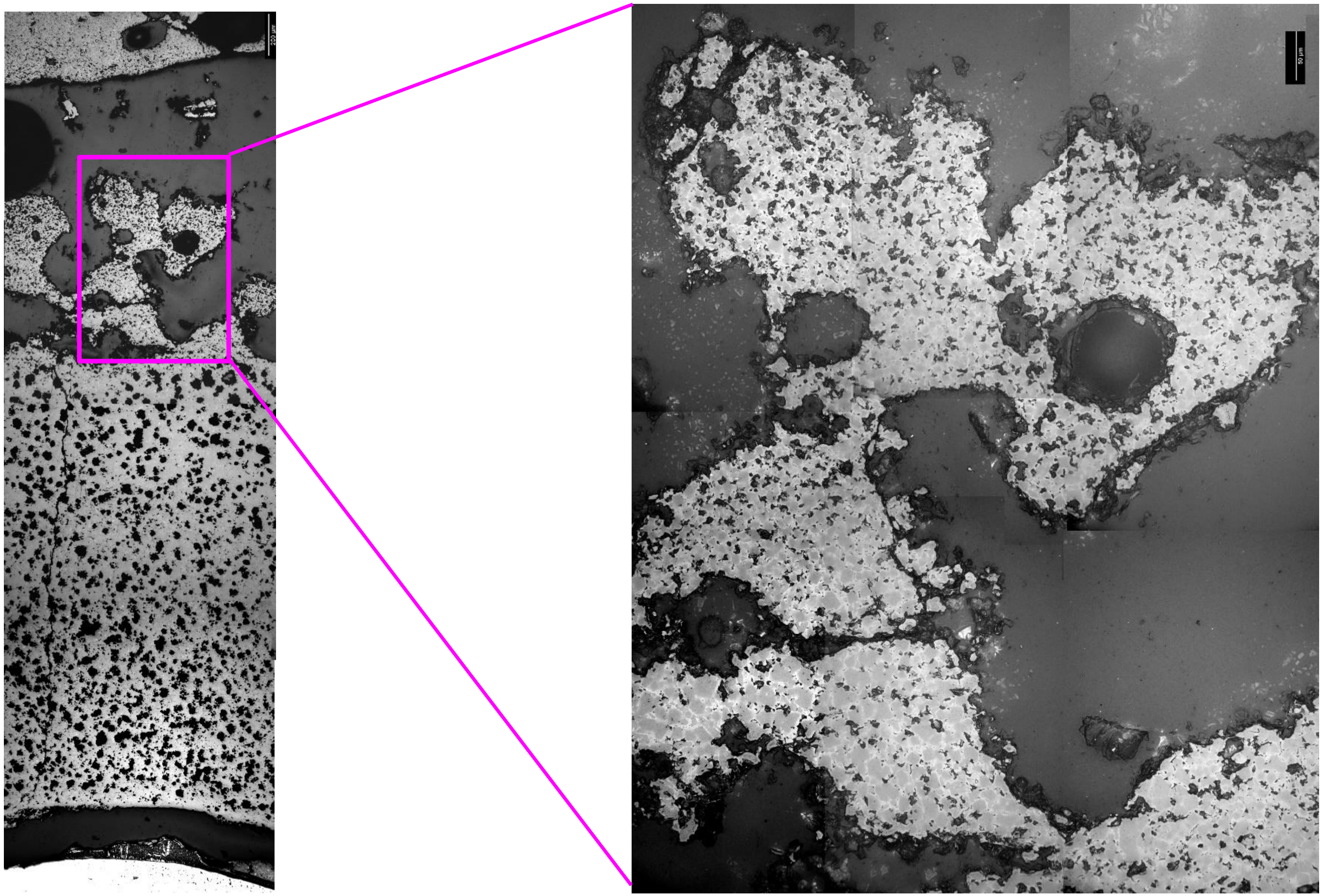

cladding cross section oxidized cladding melt: oxide clusters divided by metal streaks

Figure 70 QUENCH-19: metallographic observation of rod 9 at the elevation 950 mm, position 90°

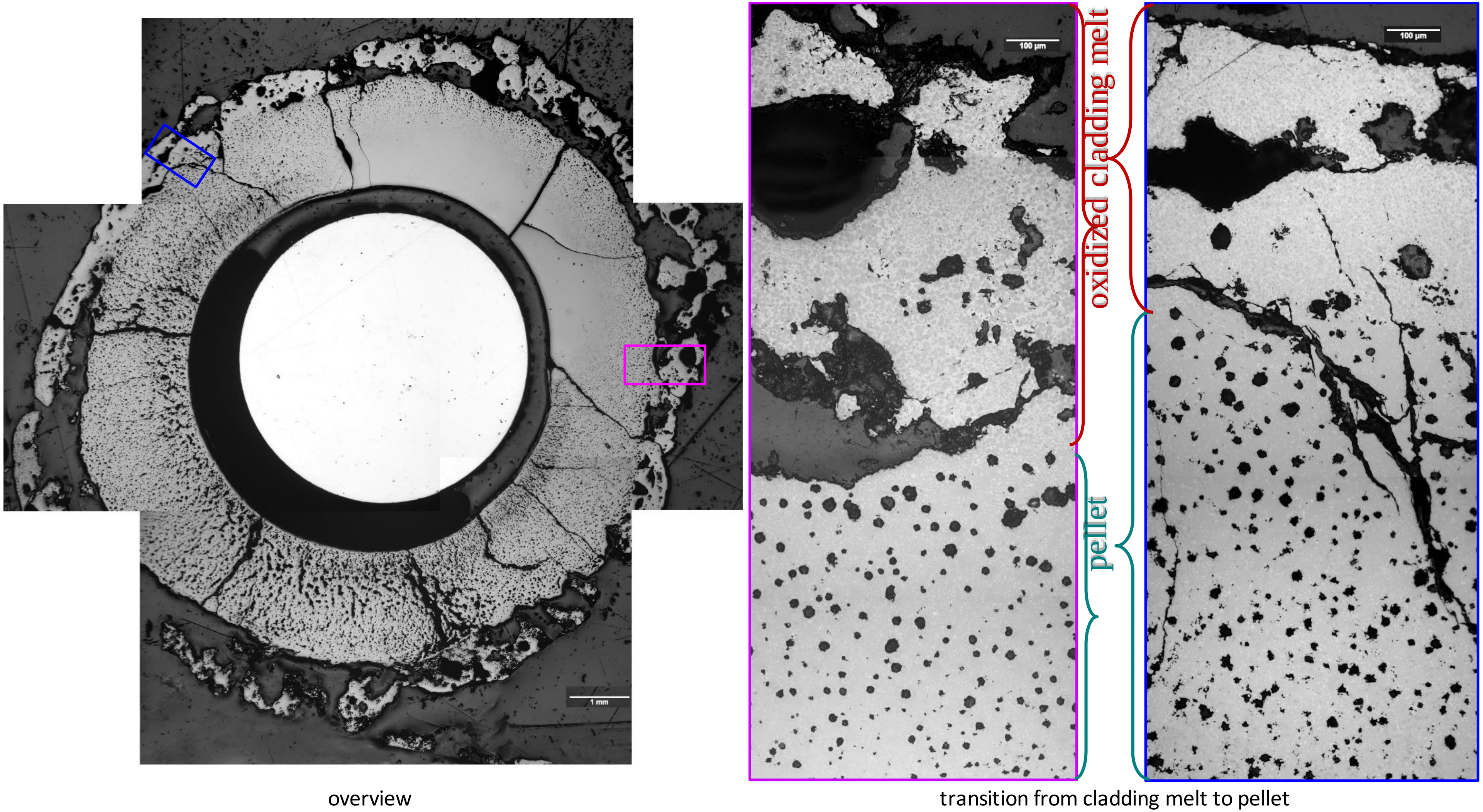

Figure 71 QUENCH-19: metallographic observation of rod 10 at the elevation 950 mm; completely melted and oxidized cladding

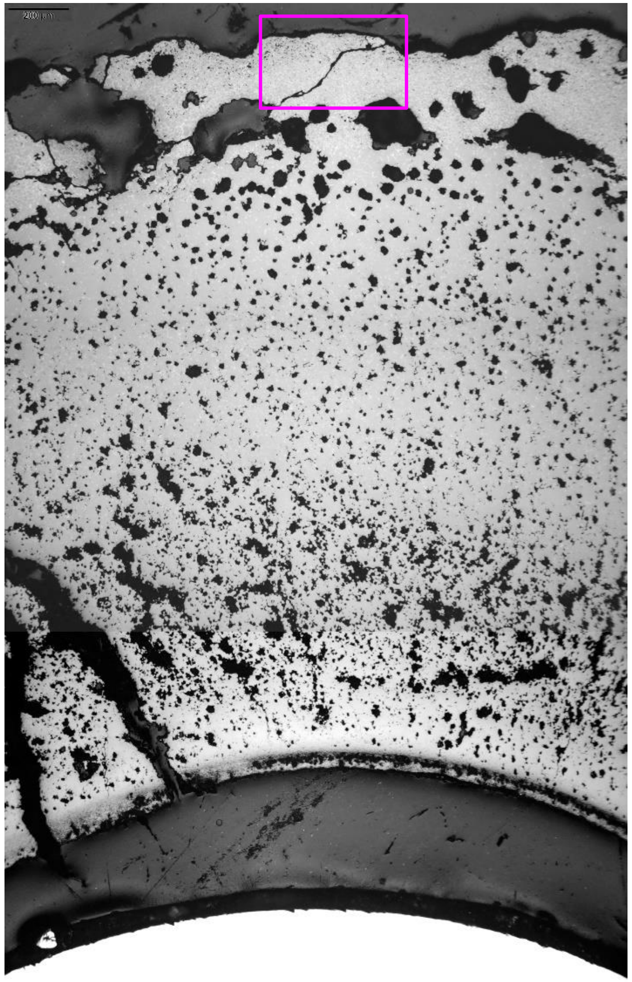

rod segment from cladding to heater

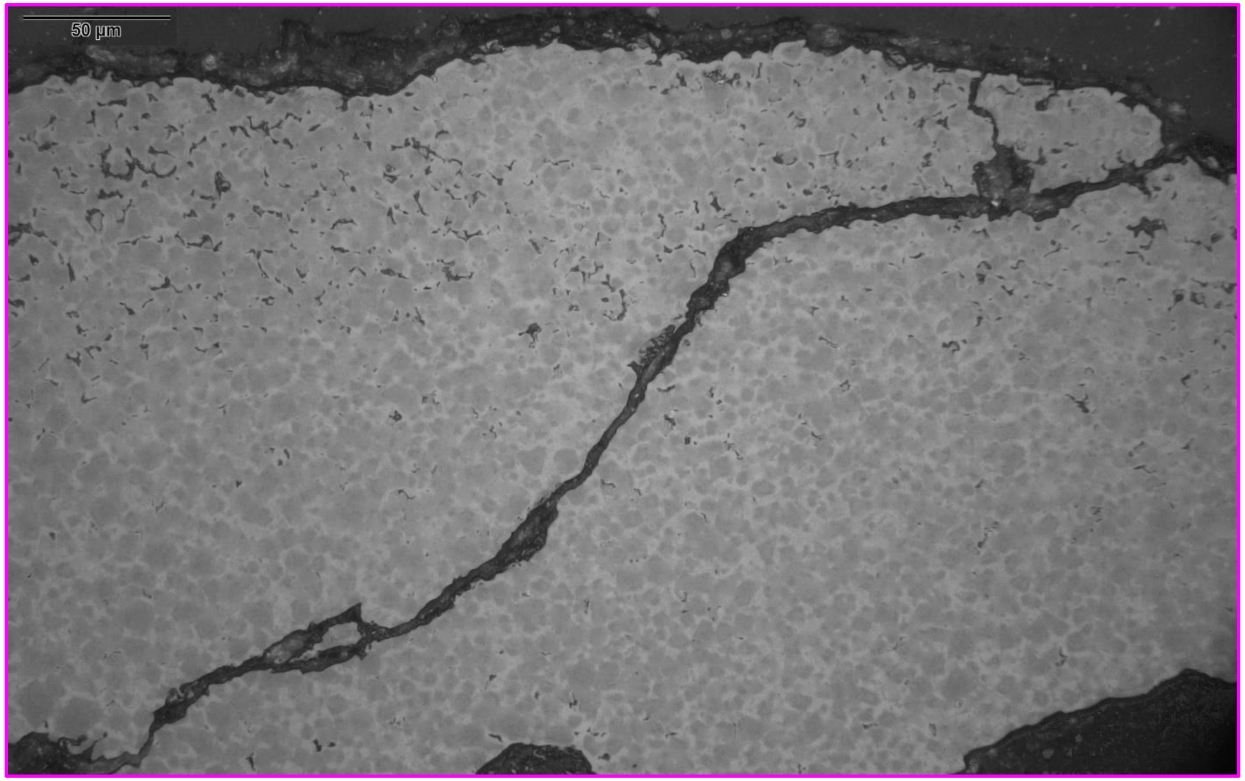

structure of frozen oxidized molten cladding

Figure 72 QUENCH-19: metallographic observation of rod 11 at the elevation 950 mm; completely melted and oxidized cladding

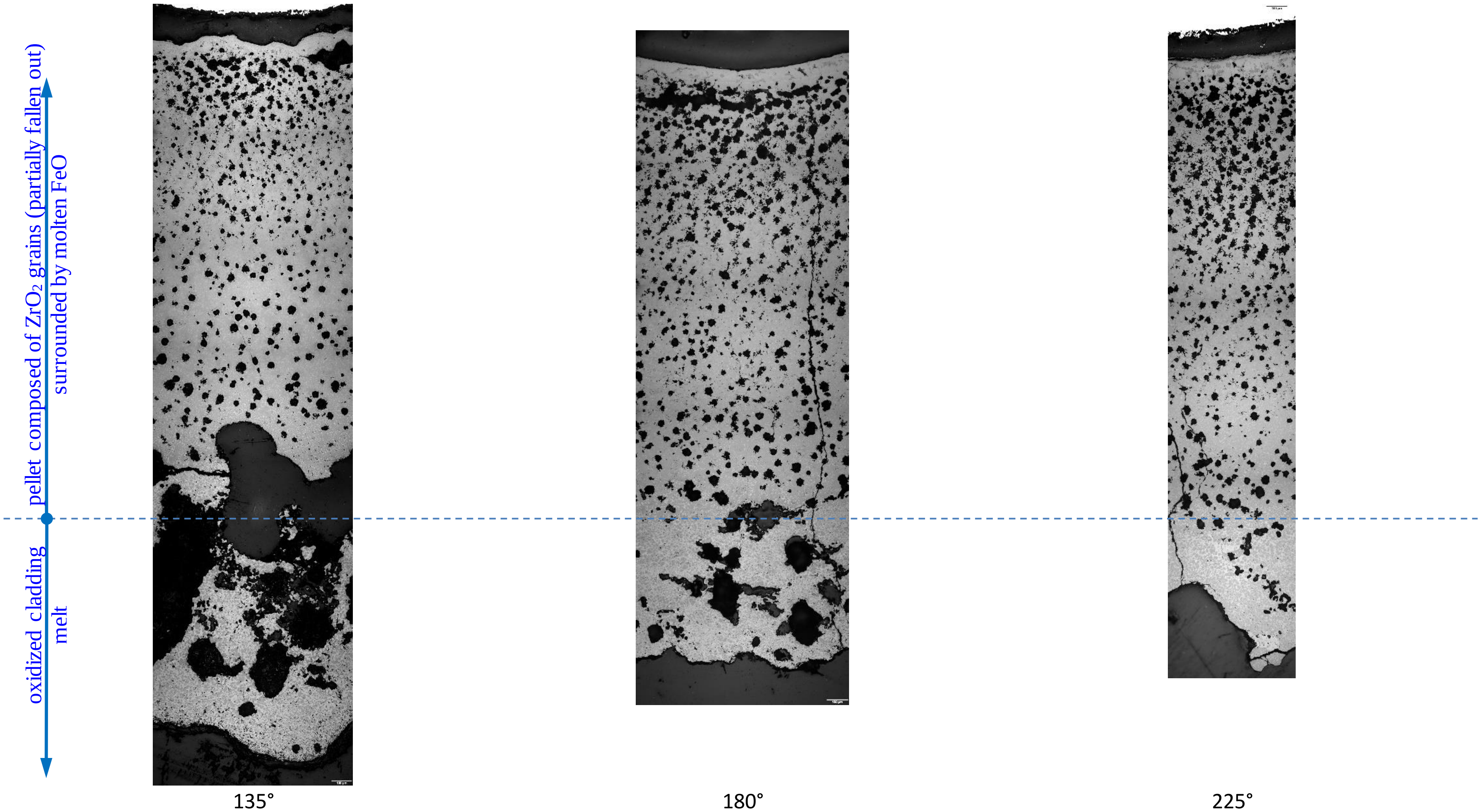

Figure 73 QUENCH-19: metallographic observation of rod 12 at the elevation 950 mm

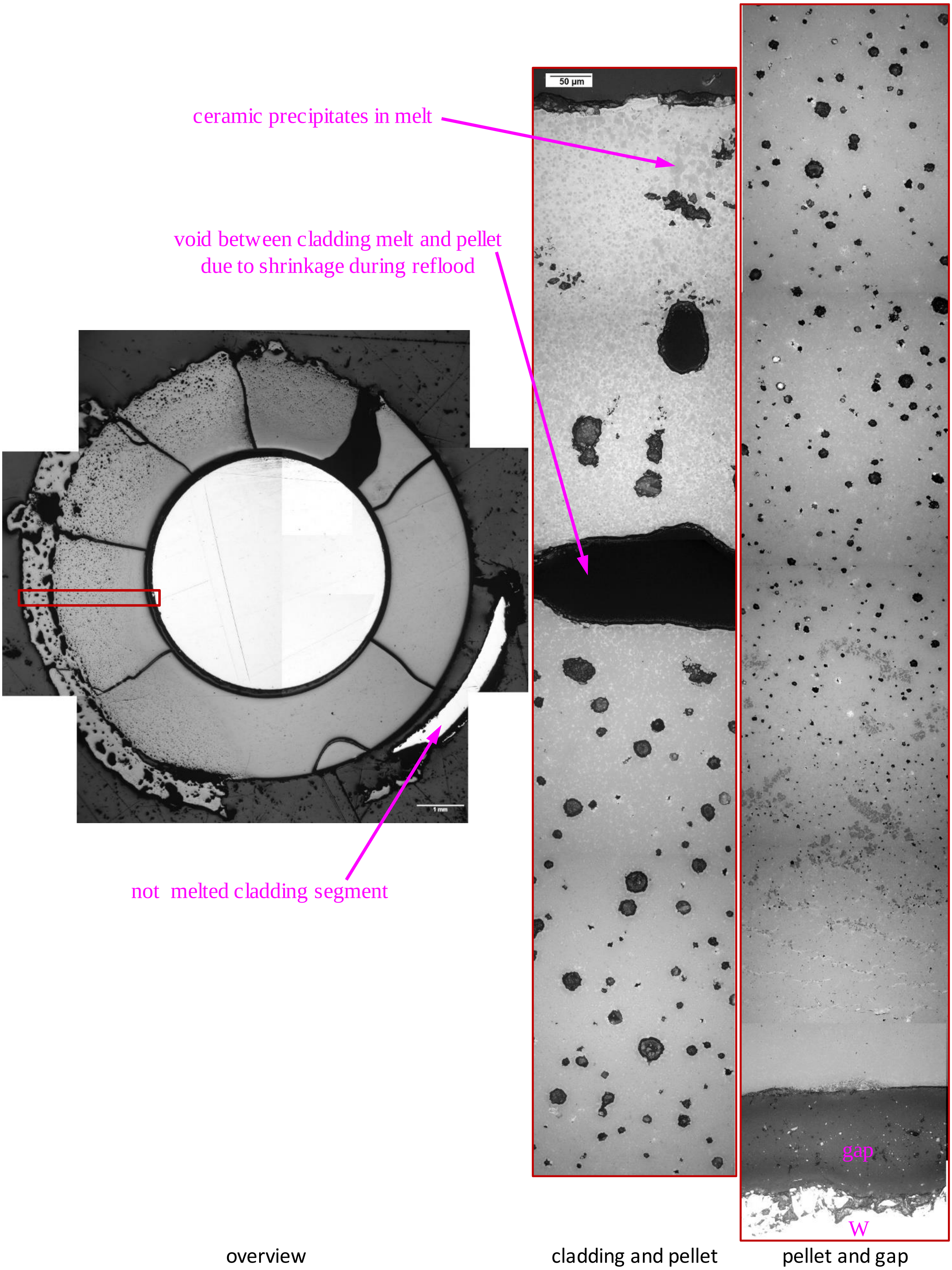

Figure 74 QUENCH-19: metallographic observation of rod 13 at the elevation 950 mm; mostly melted and oxidized cladding

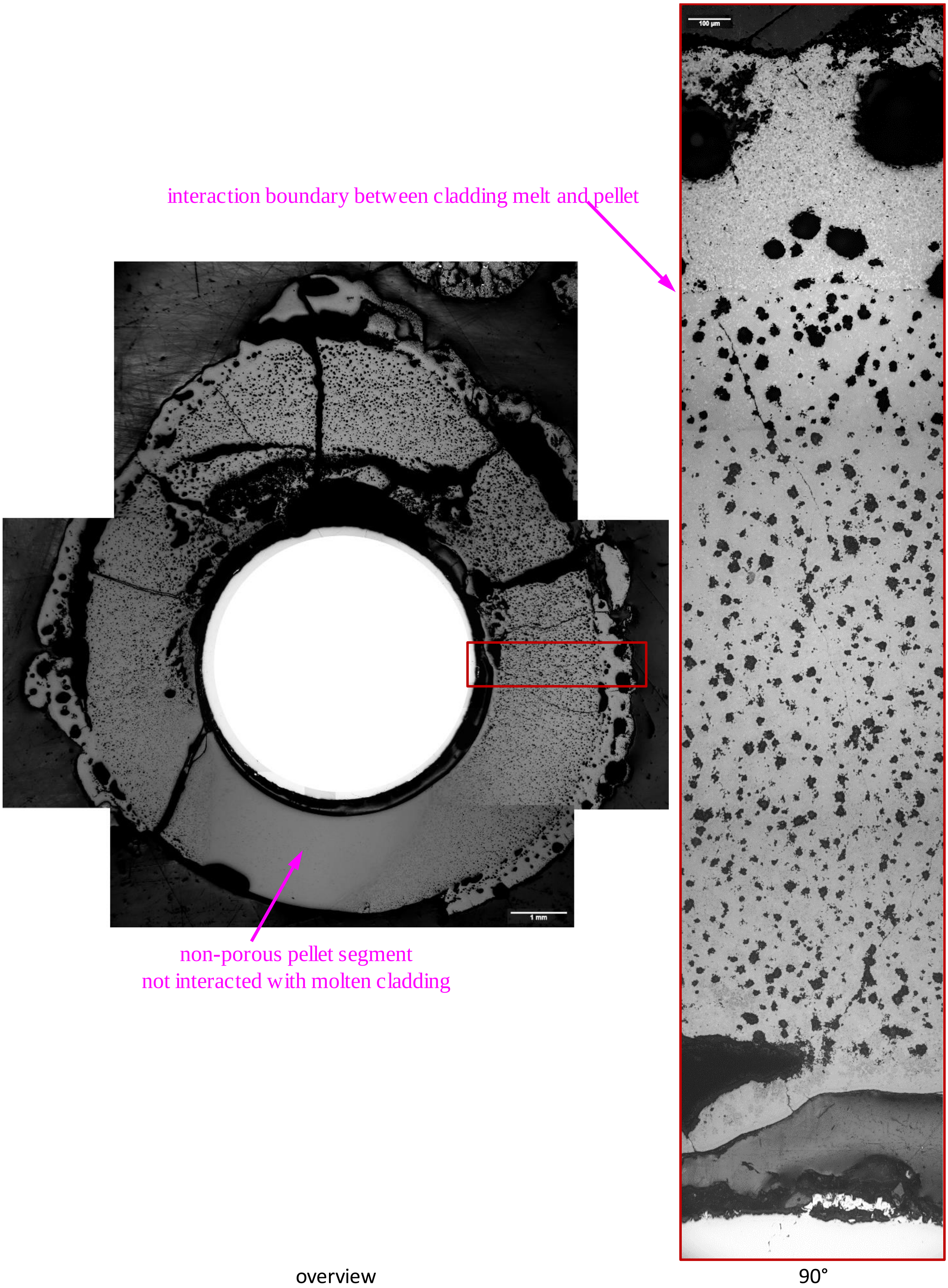

Figure 75 QUENCH-19: metallography of rod 14 at 950 mm; interaction of pellet with cladding melt

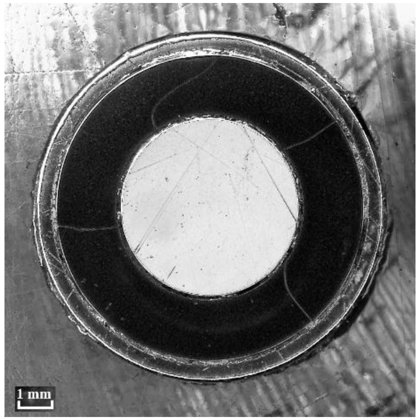

rod 17: dark sub-stoichiometric pellet surrounded by intact clad

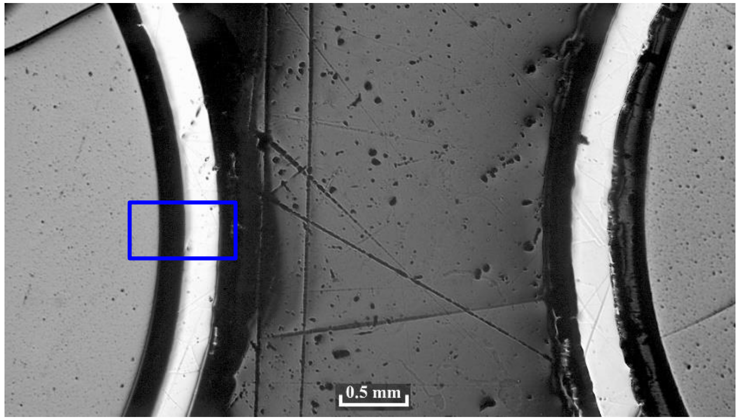

rod 17 (left) and rod 5 (right): metallic claddings

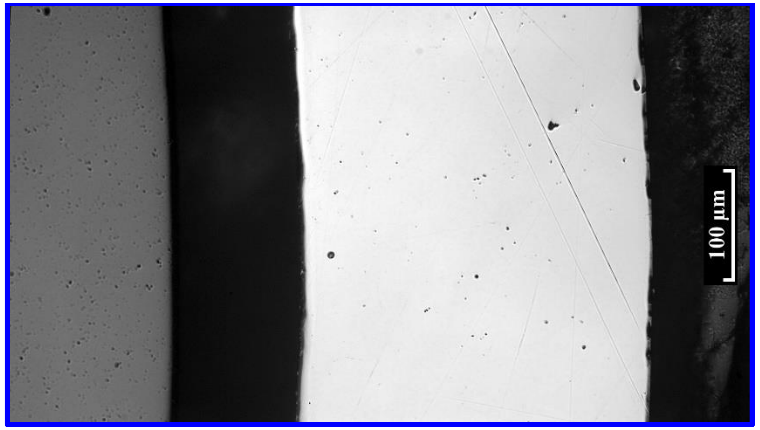

rod 17: intact metallic cladding (right) and intact pellet (left)

rod 15: dark part of pellet in contact with melt

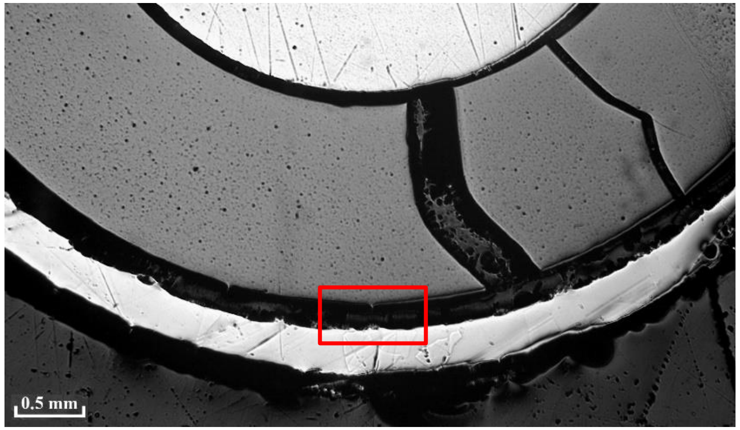

gap of rod 15 between light pellet part and intact cladding segment

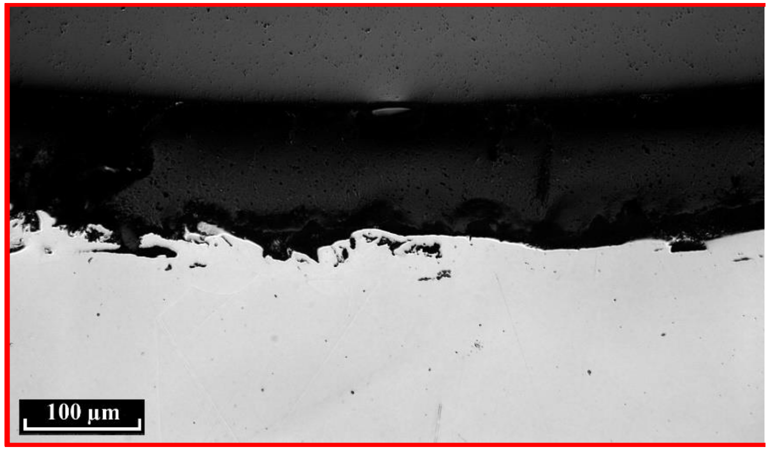

cladding (bottom) and pellet (top) of intact part of rod 15

Figure 76 QUENCH-19, elevation 950 mm: intact rod 17 and intact part of rod 15, bottom view mirrored

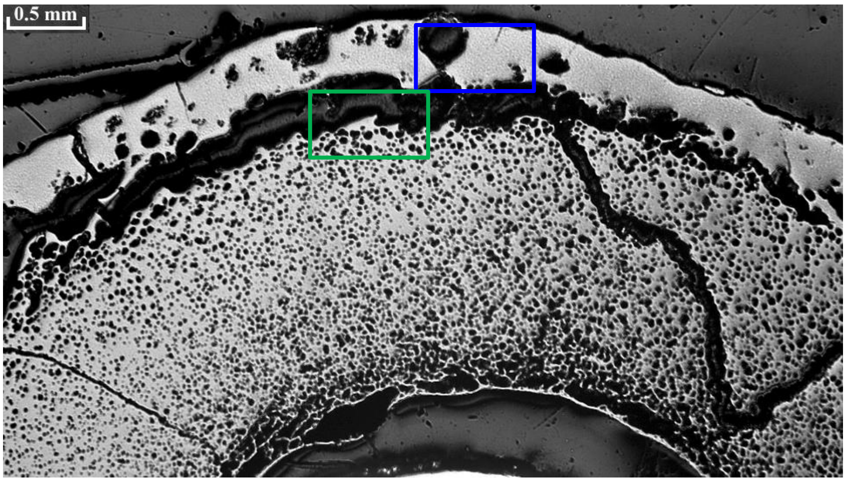

molten cladding and melt-interacted pellet of damaged upper part of rod 15

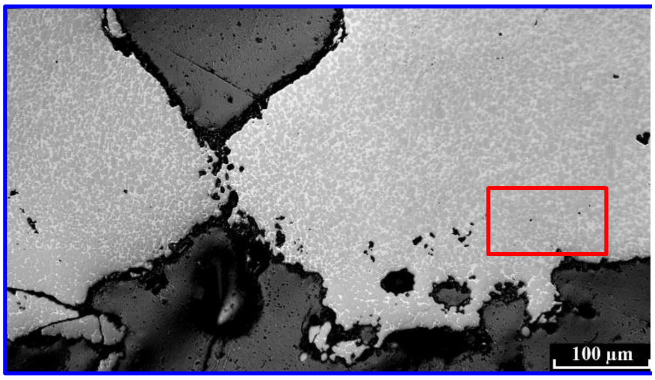

oxidized cladding melt of rod 15

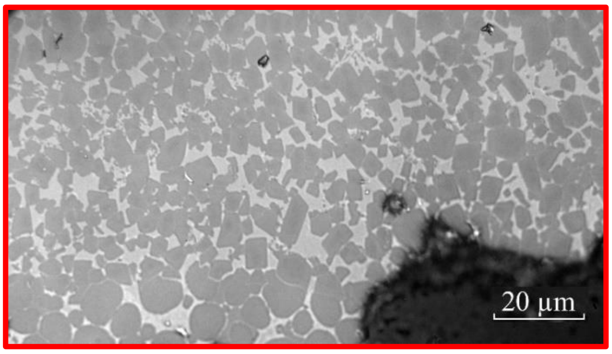

oxidized molten cladding with angular precipitates of oxides and part of melt-interacted pellet (round grains) of rod 15

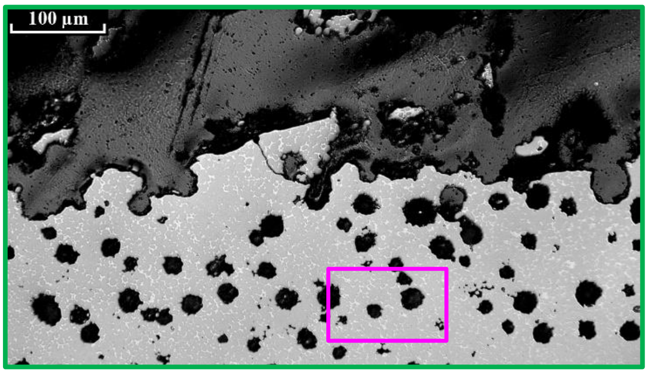

melt-interacted pellet part of rod 15

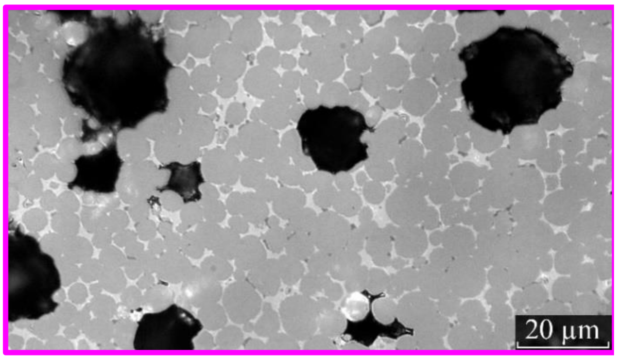

ceramic grains of pellet of rod 15 surrounded by FeO melt

Figure 77 QUENCH-19, elevation 950 mm: damaged part of rod 15, bottom view mirrored

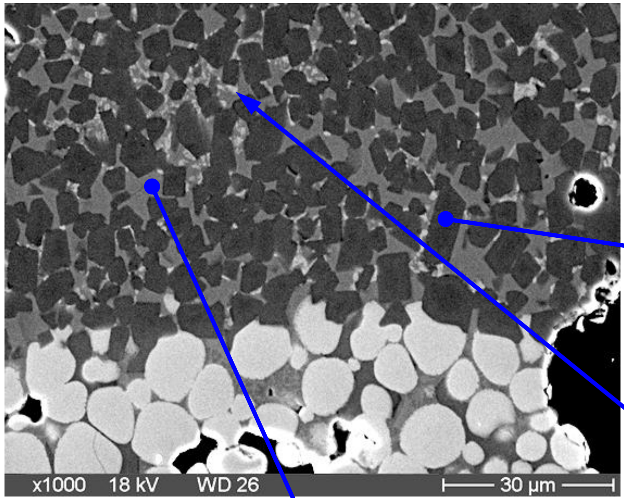

SEM view of interface between molten FeCrAl cladding and pellet

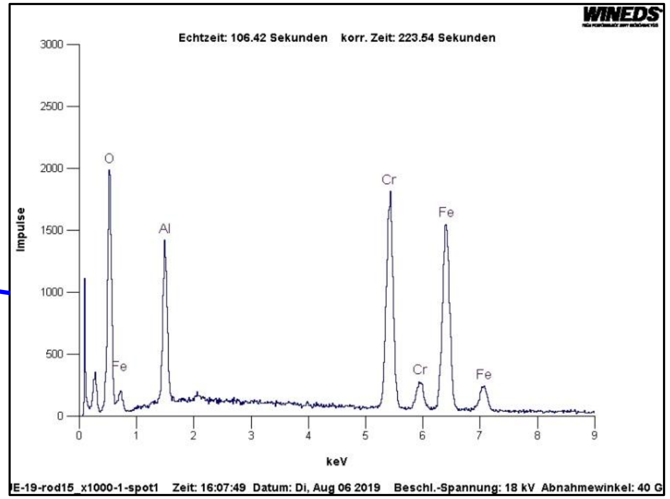

(Cr, Fe, Al) oxides

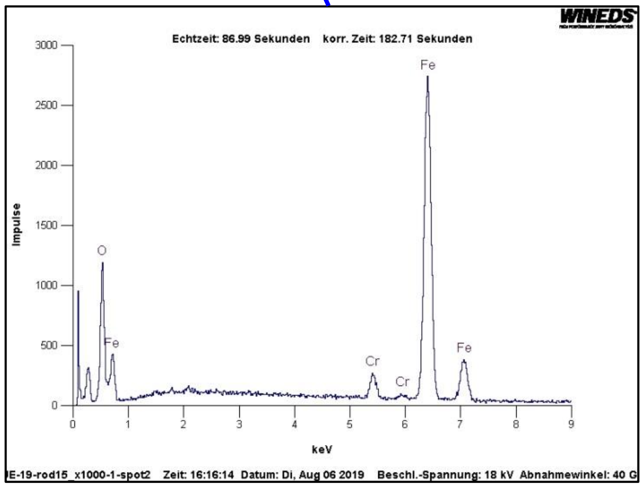

molten FeO

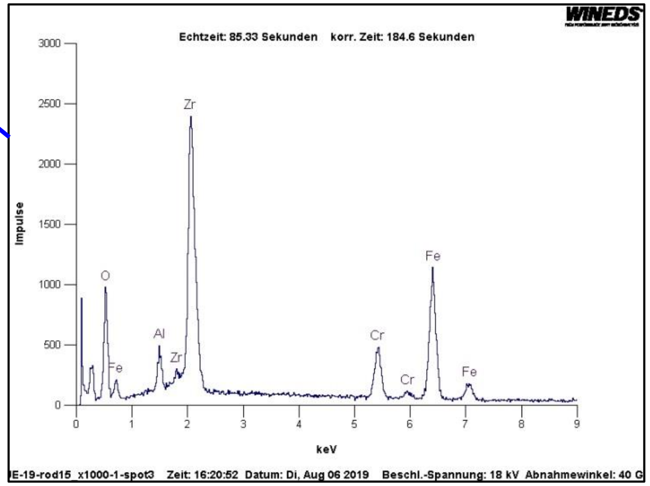

ZrO_{2-x}

Figure 78 QUENCH-19; SEM/EDX investigation of molten cladding structure of rod 15 at elevation 950 mm

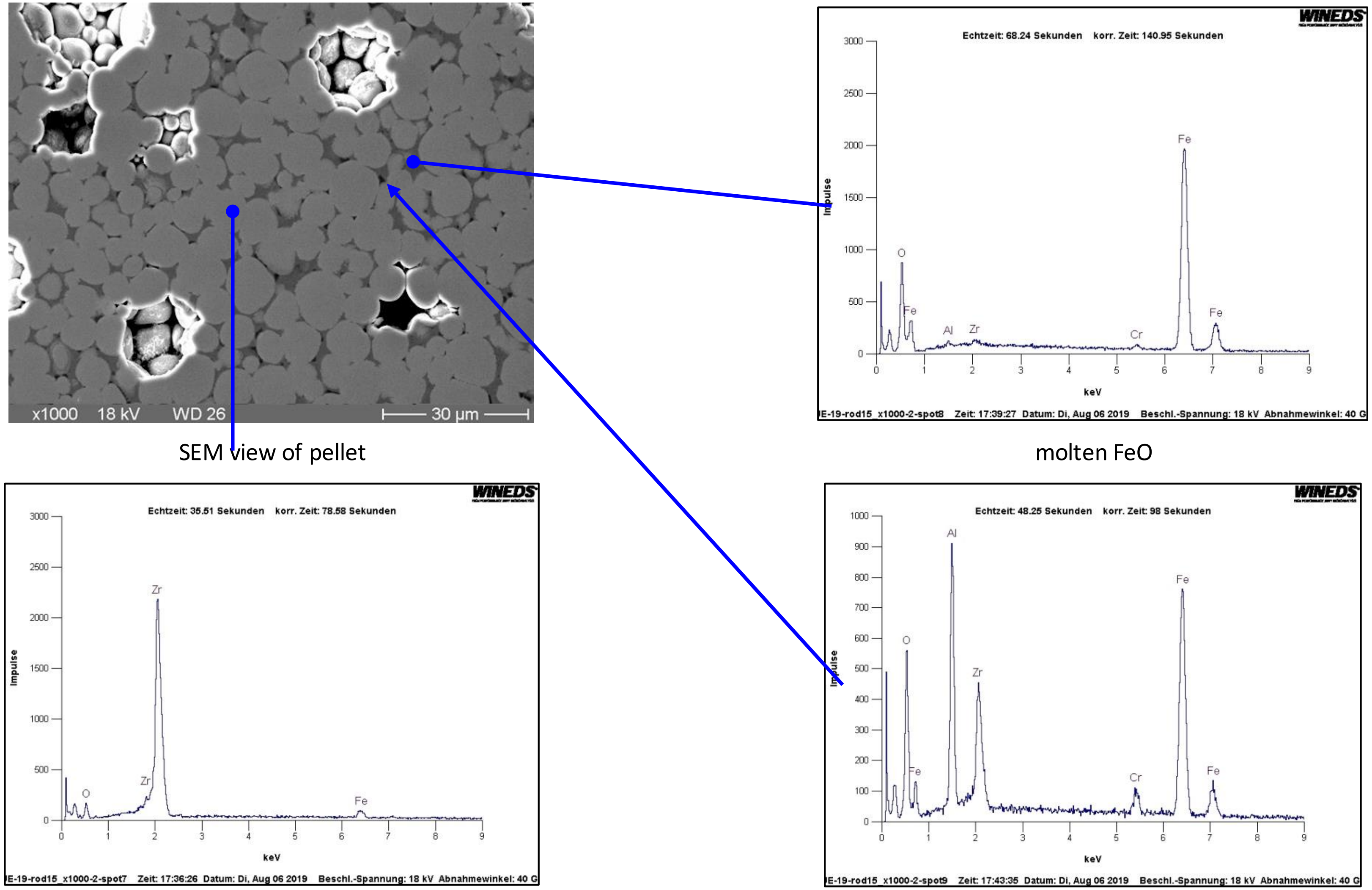

SEM view of pellet

molten FeO

ZrO_{2-x} grain

Al, Fe, Zr oxides

Figure 79 QUENCH-19; SEM/EDX investigation of friable pellet structure of rod 15 at elevation 950 mm

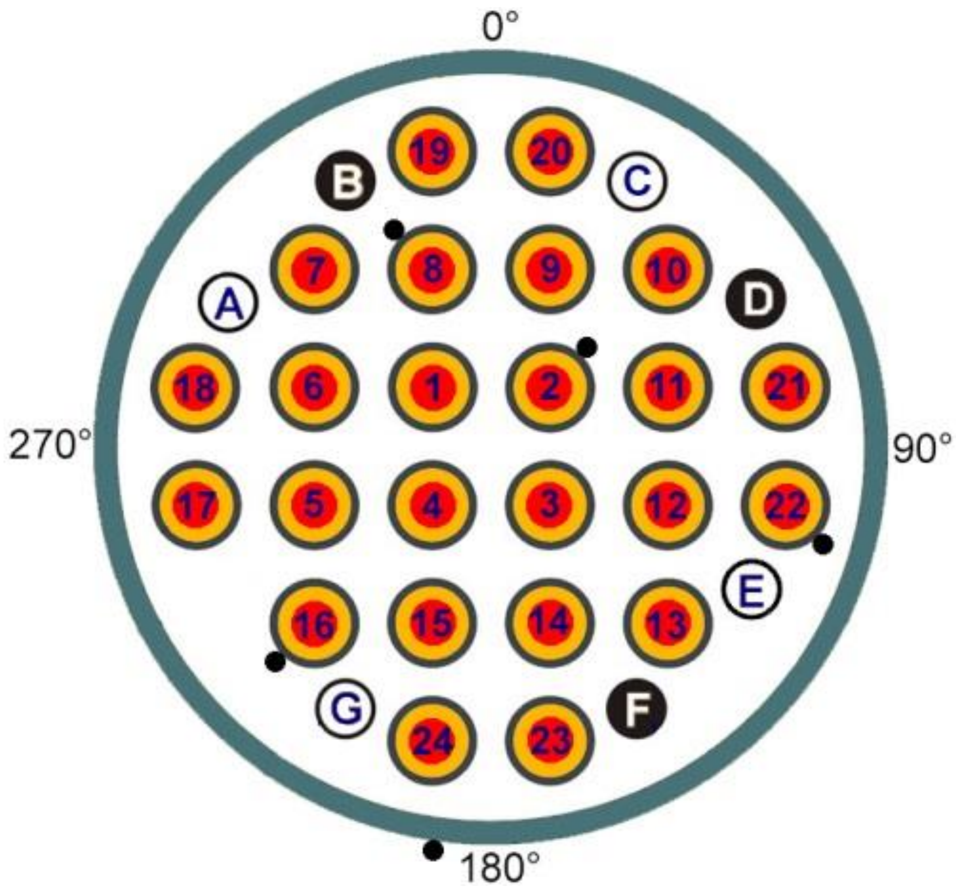

bundle composition, top view

mirrored bottom view of slice 854-870 mm: dark pellets inside rods 17, 18, 23 with intact claddings and relocated melt

Figure 80 QUENCH-19; cross section at elevation 850 mm

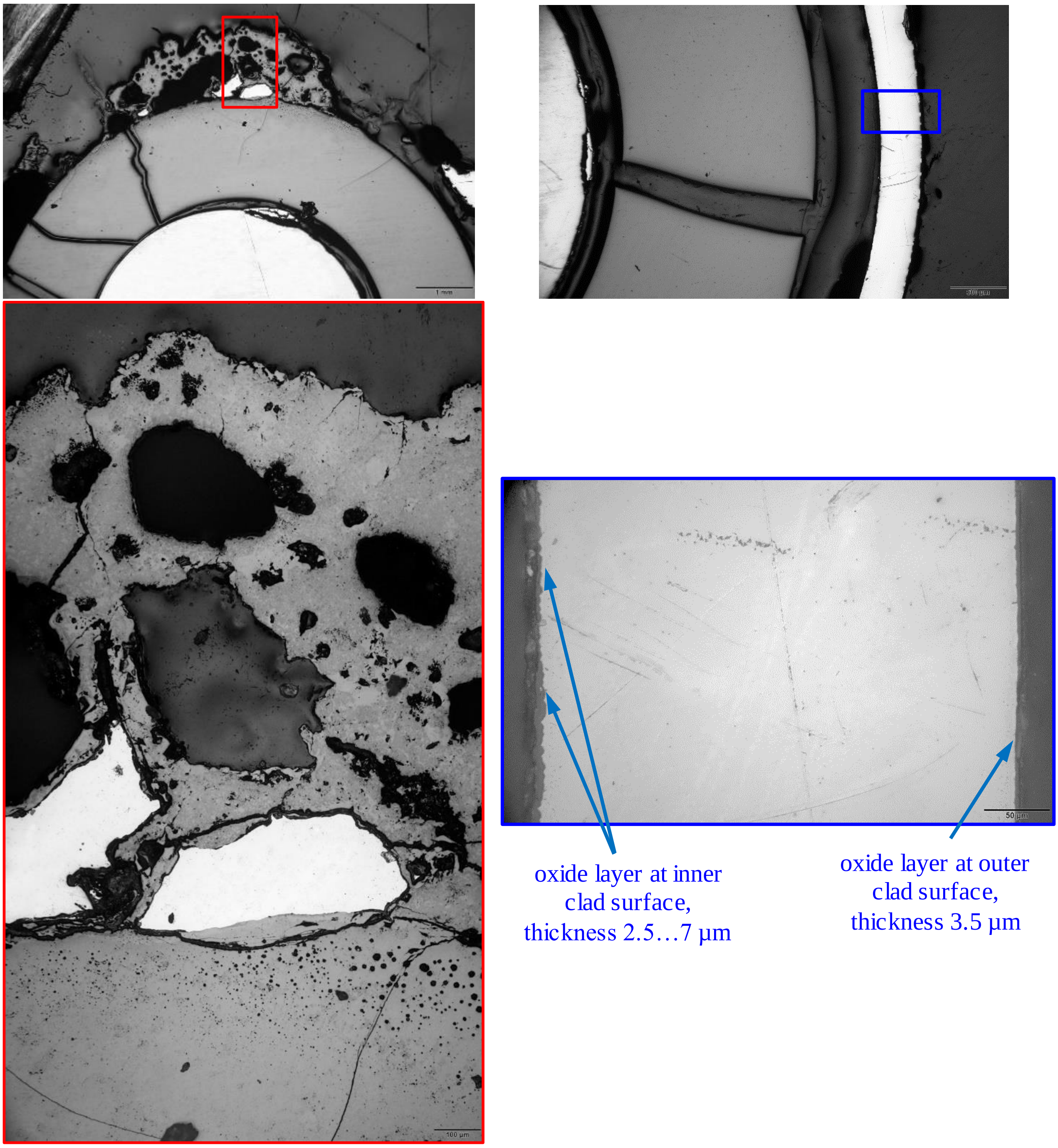

melt at 0°

inner and outer oxide layers at 90°

Figure 81 QUENCH-19; metallographic observation of rod 3 at 850 mm (T_{peak}=TFS 2/12=1700 K), bottom view mirrored; interaction of oxidized cladding melt with pellet; inner and outer oxide layers

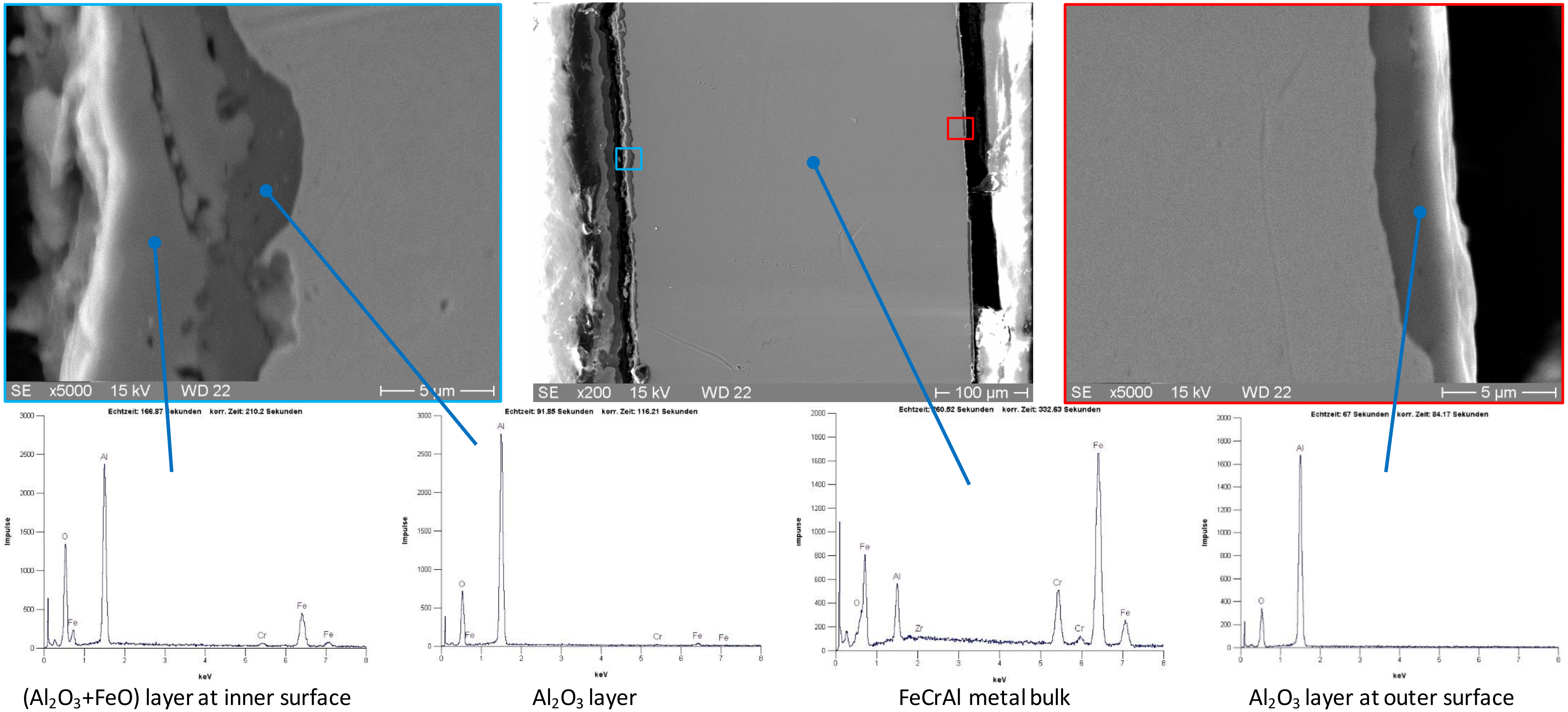

Figure 82 QUENCH-19; REM/EDX analysis of rod 3 at elevation 850 mm at 90°: oxide layers at outer and inner cladding surfaces

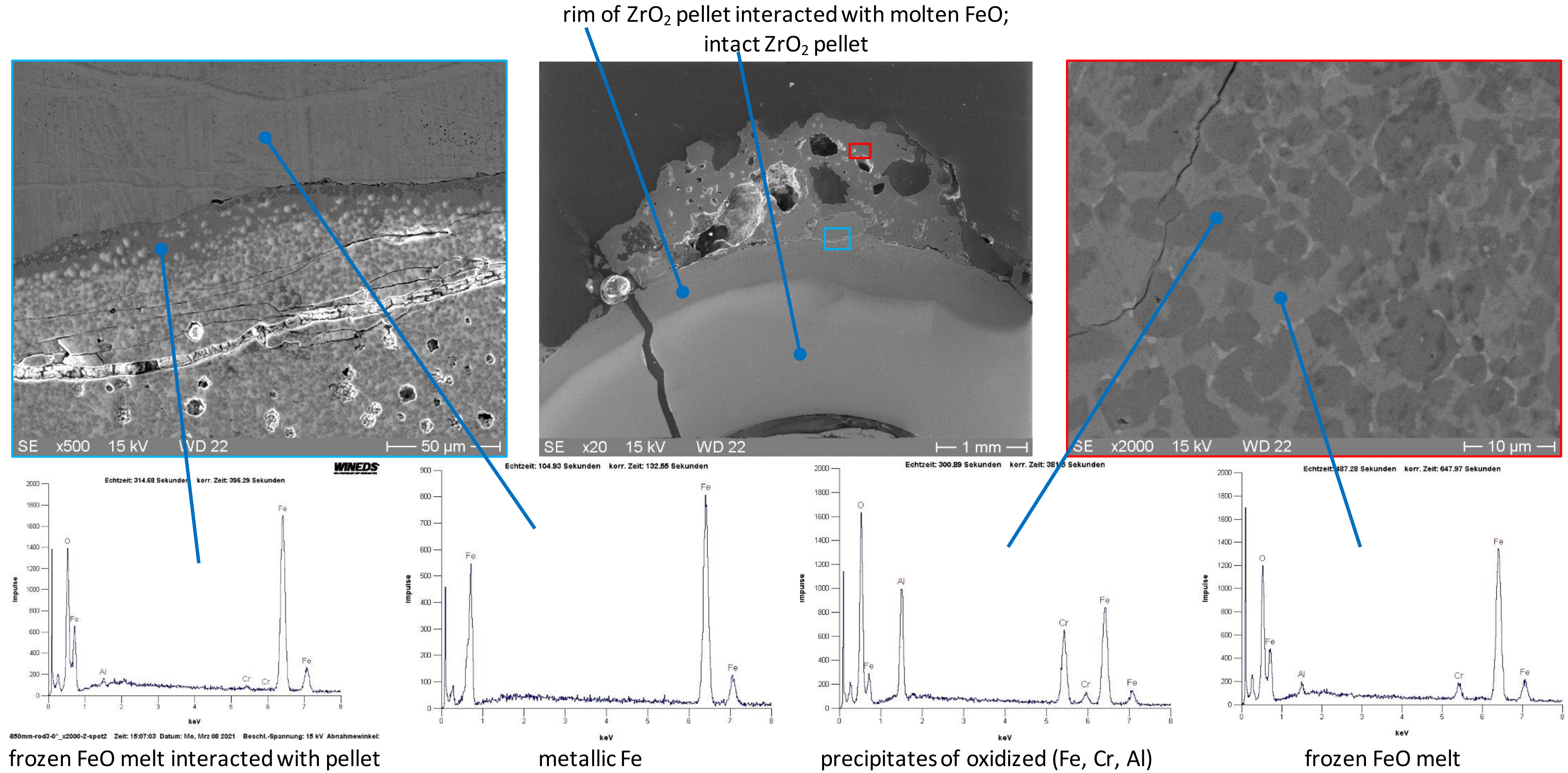

Figure 83 QUENCH-19; REM/EDX analysis of rod 3 at elevation 850 mm at 0°: interaction of molten cladding with pellet

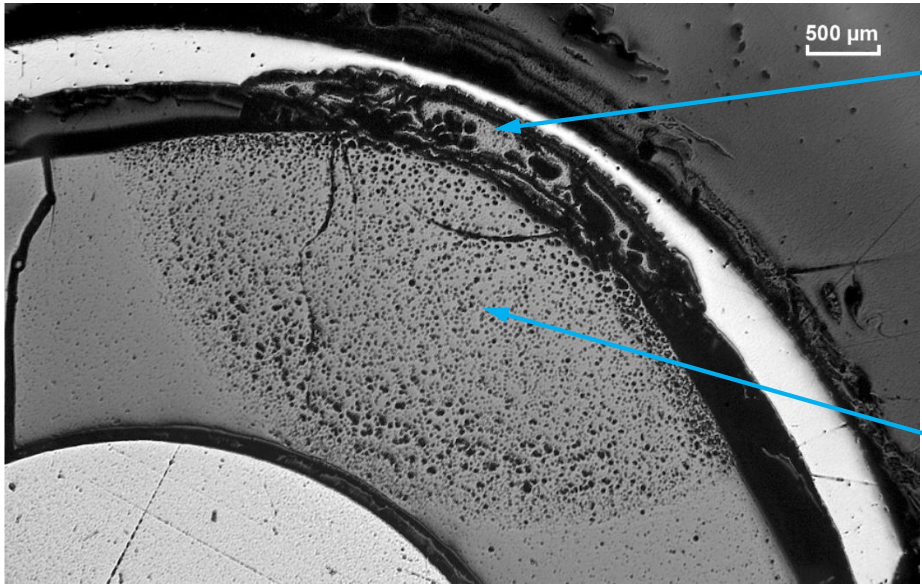

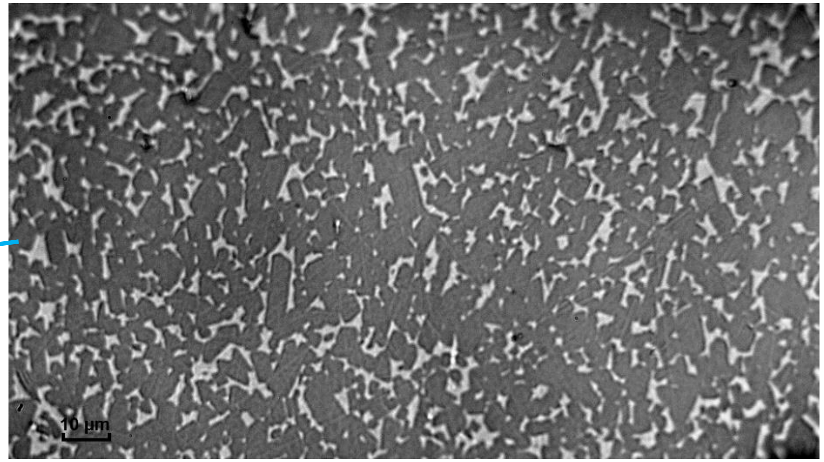

structure of oxidized cladding melt

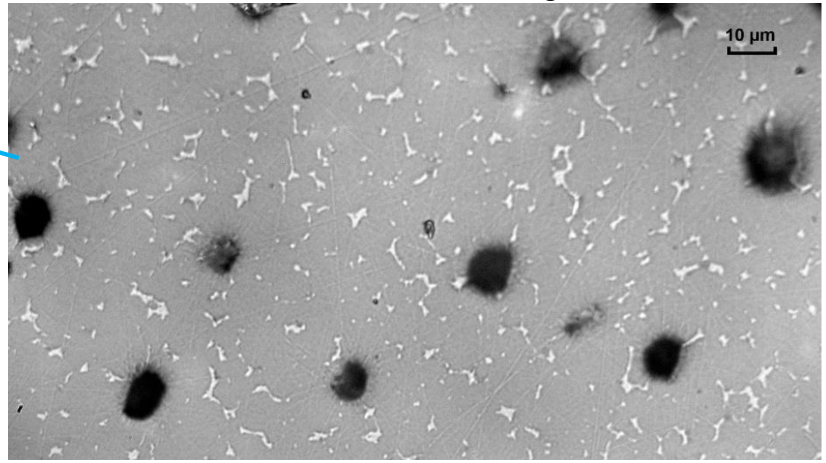

interaction of cladding melt with pellet

structure of pellet attacked by cladding melt

Figure 84 QUENCH-19; metallographic observation of rod 4 at the elevation 850 mm, bottom view mirrored

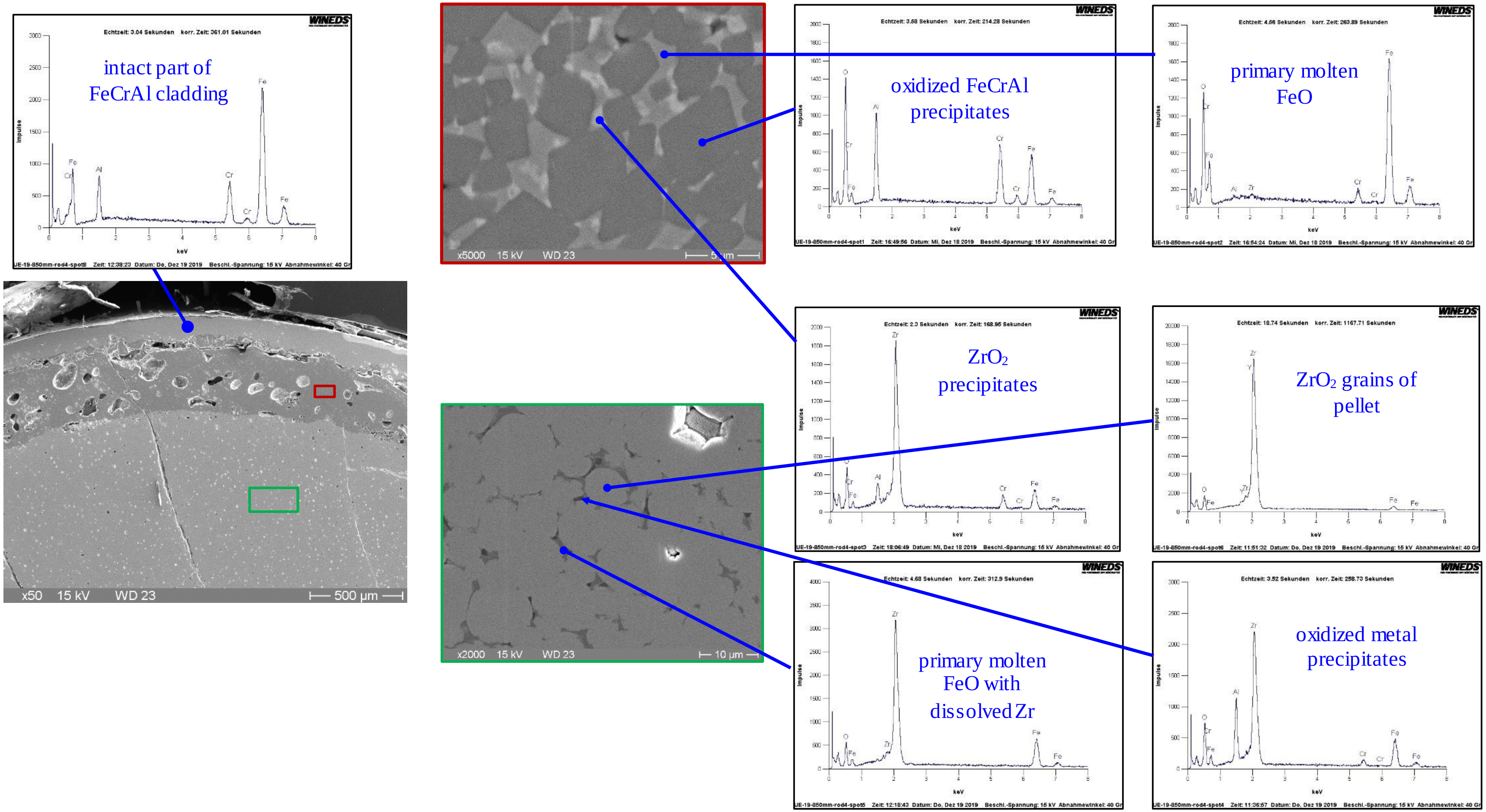

Figure 85 QUENCH-19; SEM/EDX analysis of rod 4 at elevation 850 mm

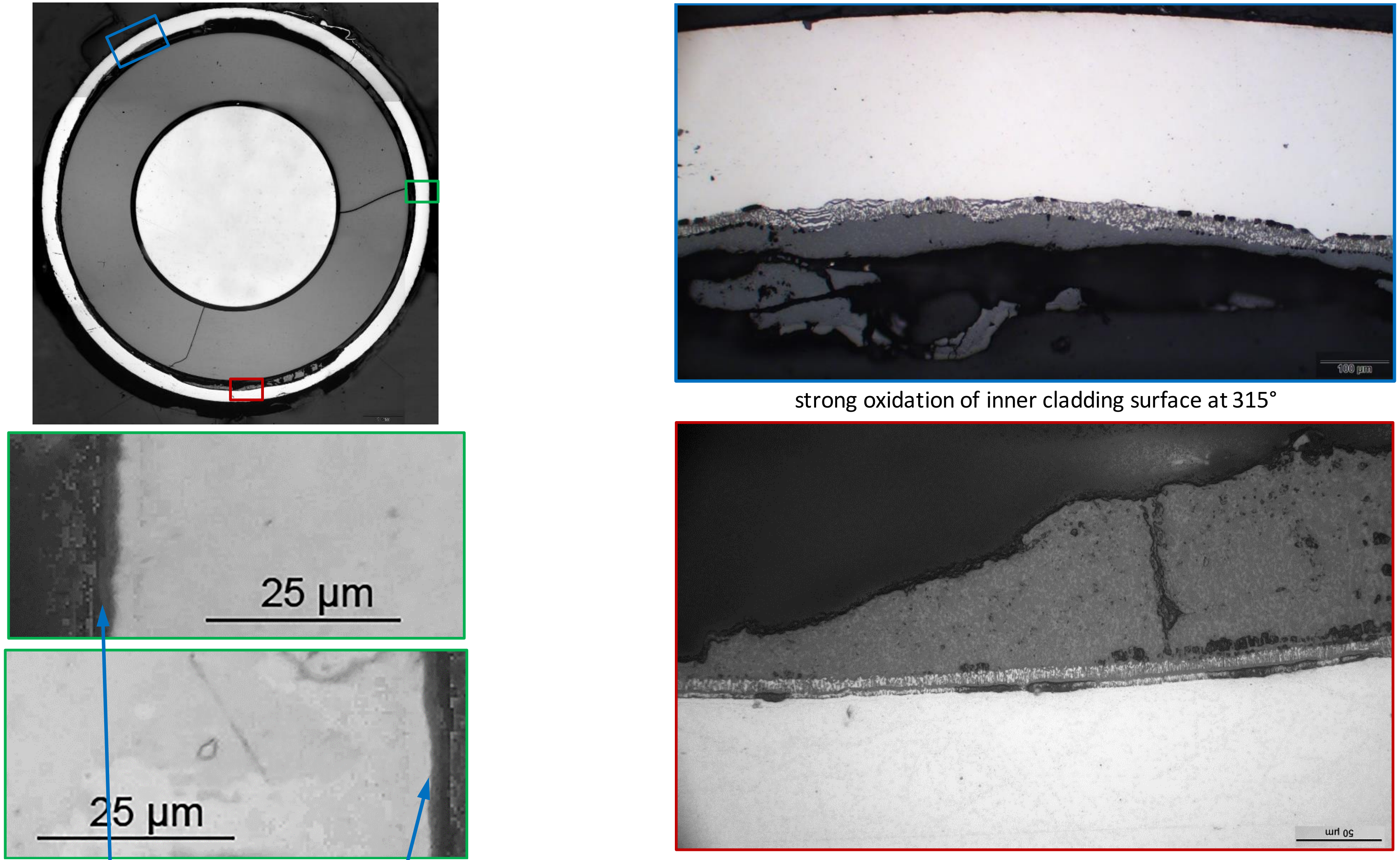

strong oxidation of inner cladding surface at 315°

90°; middle: clad inner oxide 2 µm; bottom: clad outer oxide 2 µm

strong oxidation and melting of inner cladding surface at 180°

Figure 86 QUENCH-19; metallographic observation of rod 16 at the elevation 850 mm (T_{peak}=TFS 16/12=1500 K), oxidation of the inner cladding surface

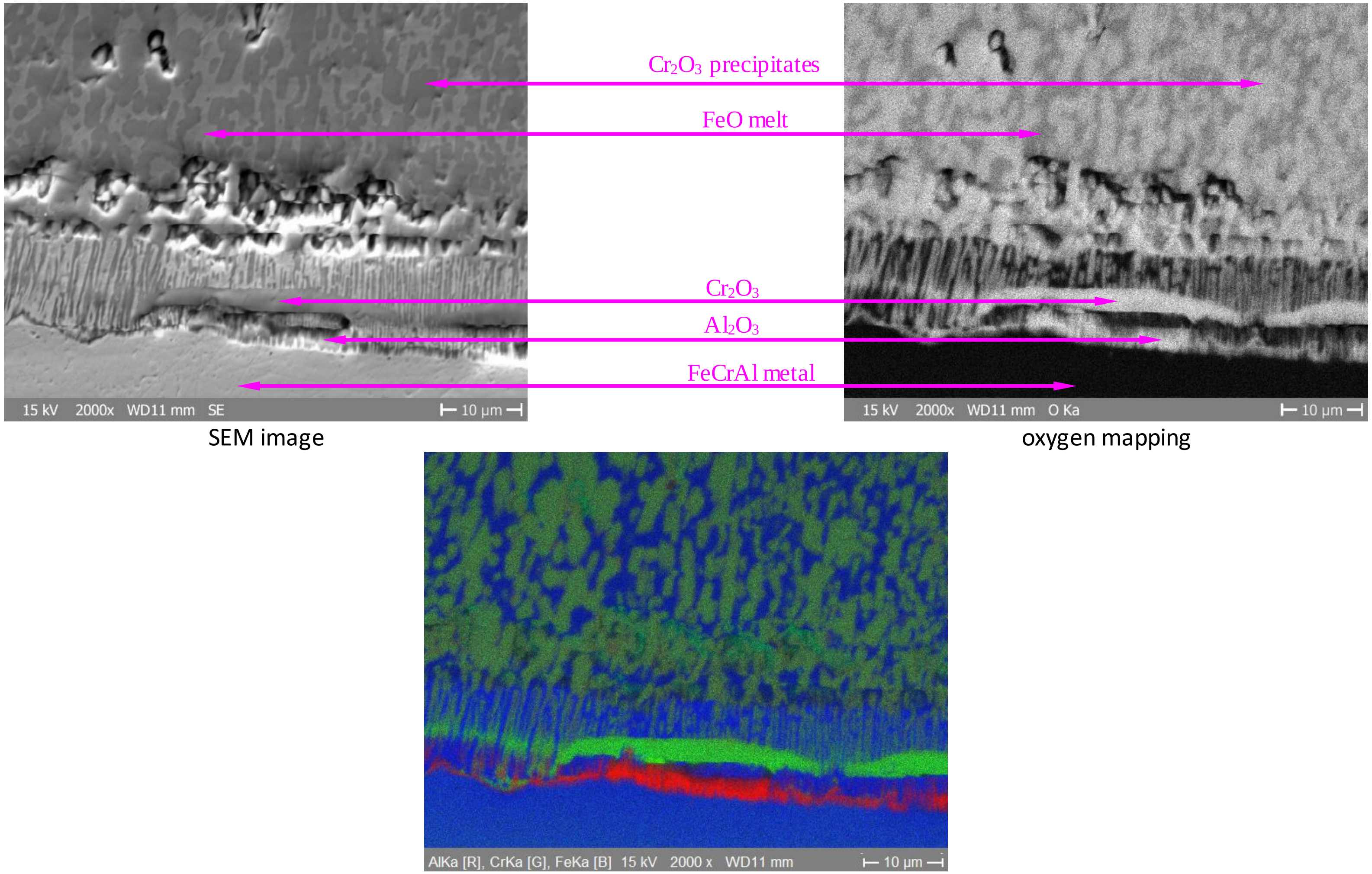

SEM image

oxygen mapping

mapping of Fe (blue), Cr (green), Al (red)

Figure 87 QUENCH-19; SEM/EDX investigation of rod 16 at the elevation 850 mm, angle 180°; interaction of FeO melt relocated from above with cladding

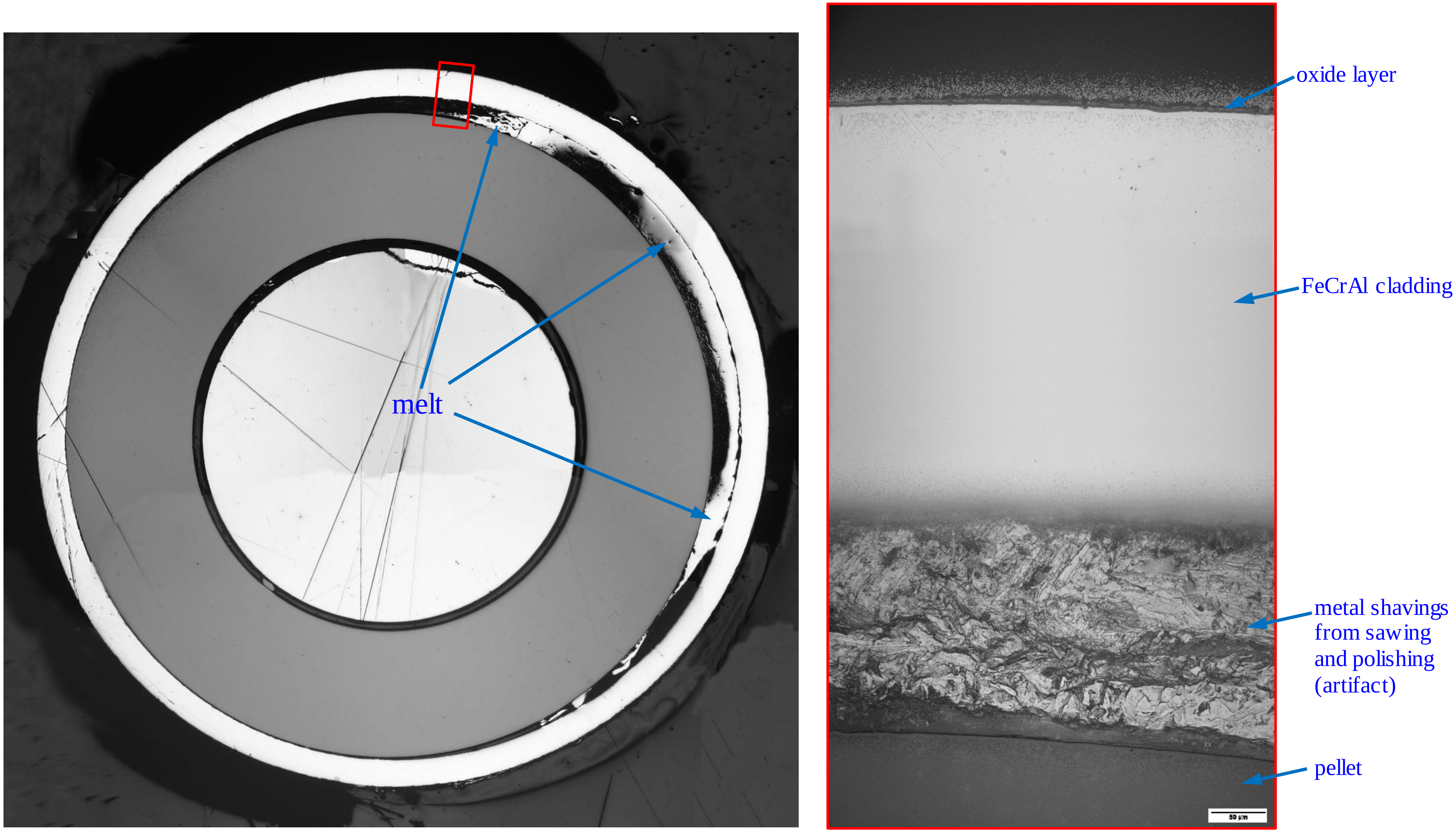

Figure 88 QUENCH-19; metallographic observation of rod 18 at the elevation 850 mm; FeCrAl shavings collected in gap during sawing and grinding (artefact)

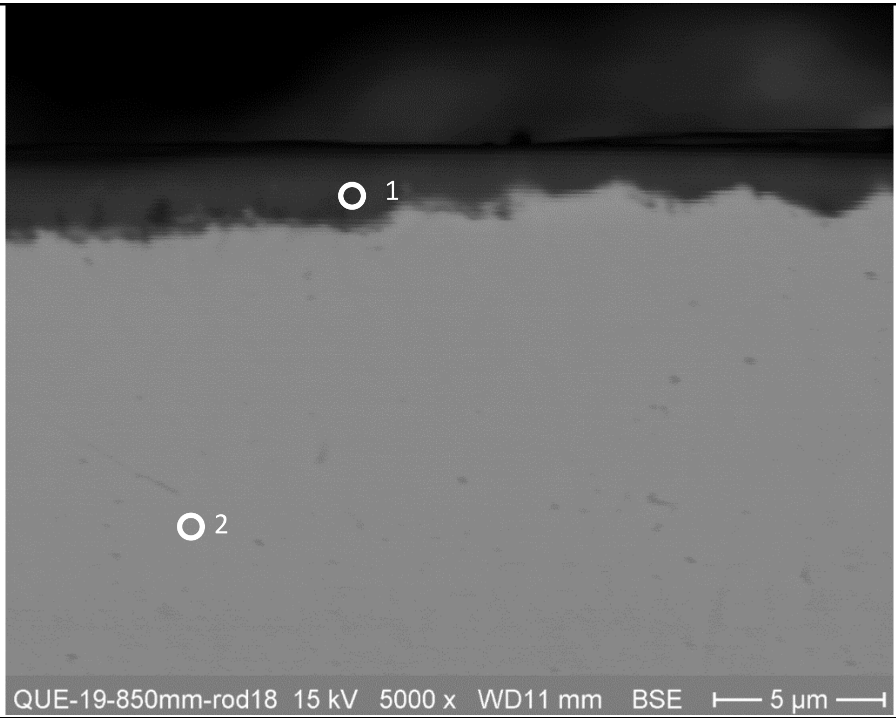

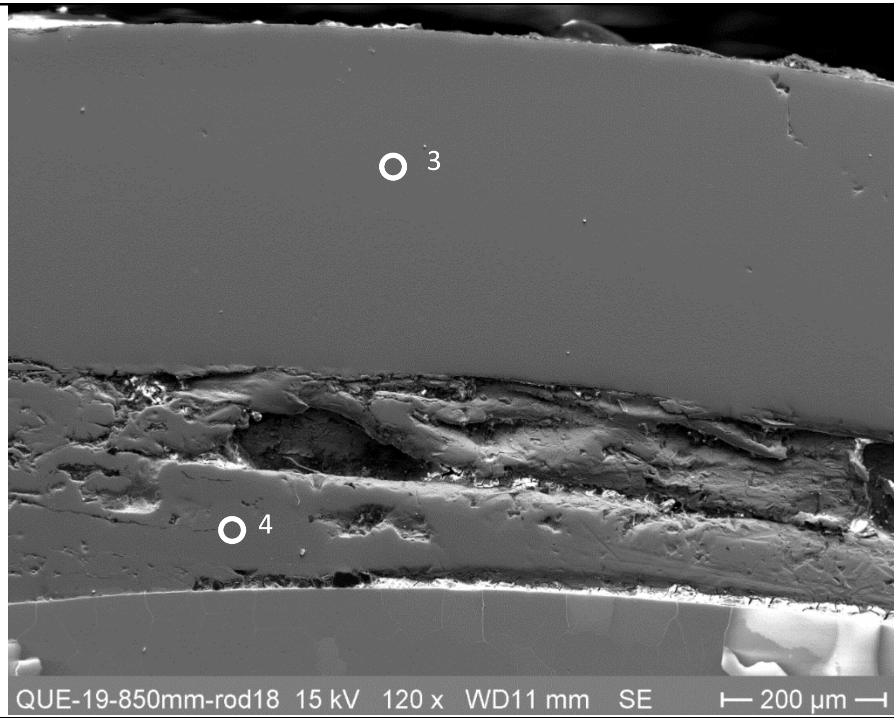

Spot 1; at%:	O ≈70%, Al ≈30%	→ oxide layer **Al_2O_3**	Spot 3; at%:	Al 16%, Cr 13%, Fe 71%	→ cladding
Spot 2; at%:	Al 16%, Cr 13%, Fe 71%	→ cladding	Spot 4; at%:	Al 16%, Cr 13%, Fe 71%	→ metal shavings between cladding and pellet (artefact)

Figure 89 QUENCH-19; SEM/EDX investigation of rod 18 at the elevation 850 mm, angle 10°: outer oxide layer and FeCrAl shavings in the gap

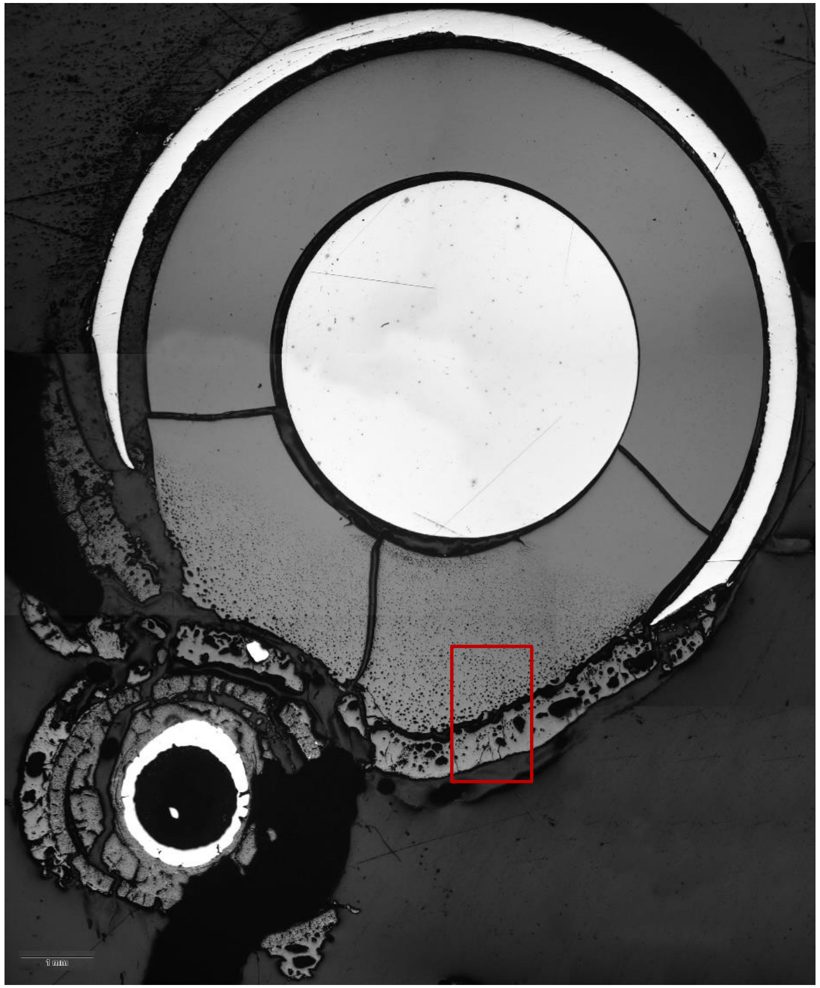

Figure 90 QUENCH-19; metallographic observation of rod 19 at the elevation 850 mm, interaction of cladding with oxidized TC sheath, interaction of pellet with oxidized and melted cladding

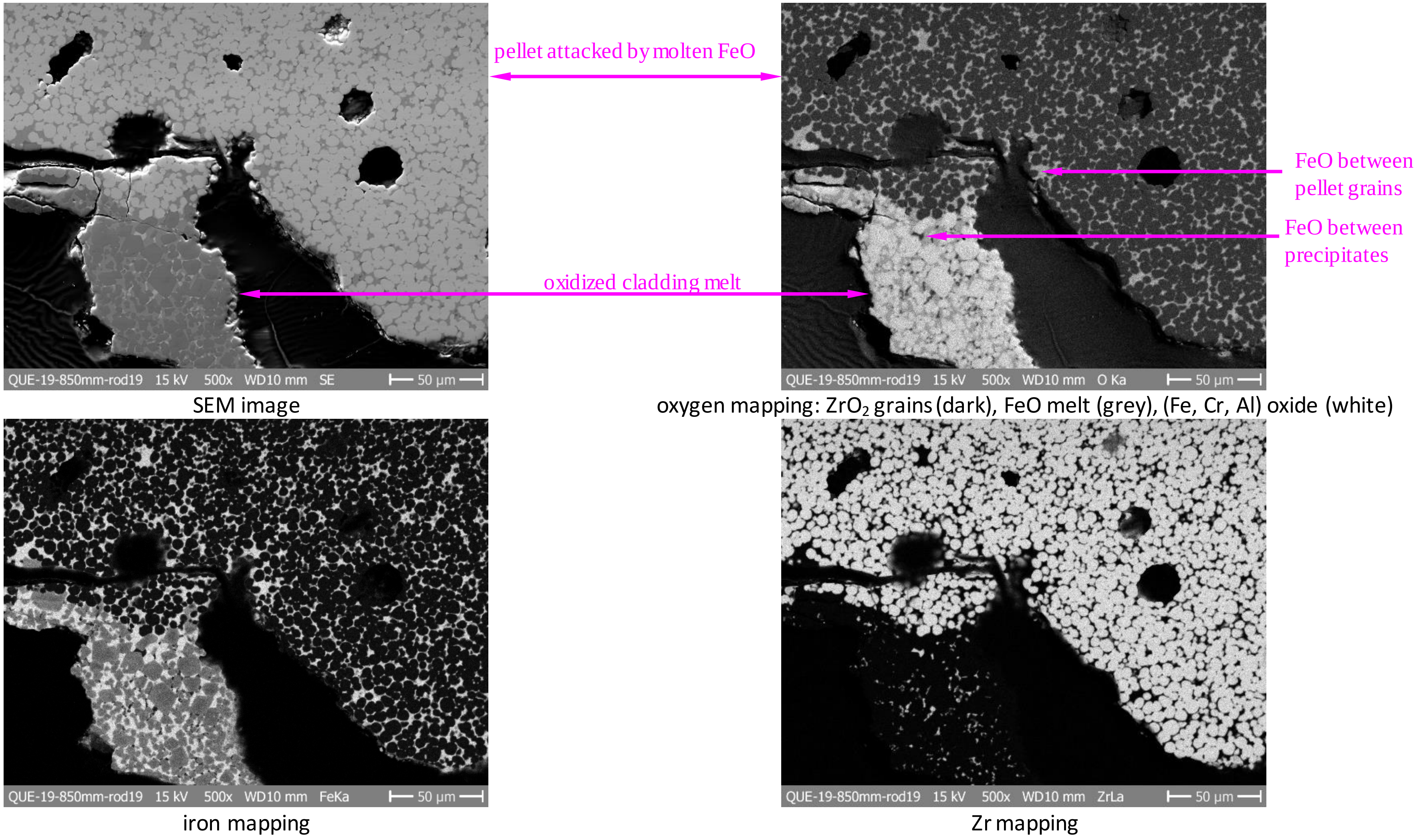

Figure 91 QUENCH-19; interaction of oxidized FeCrAl melt with pellet at elevation 850 mm (rod 19, 170°): penetration of molten FeO between ZrO_2 grains

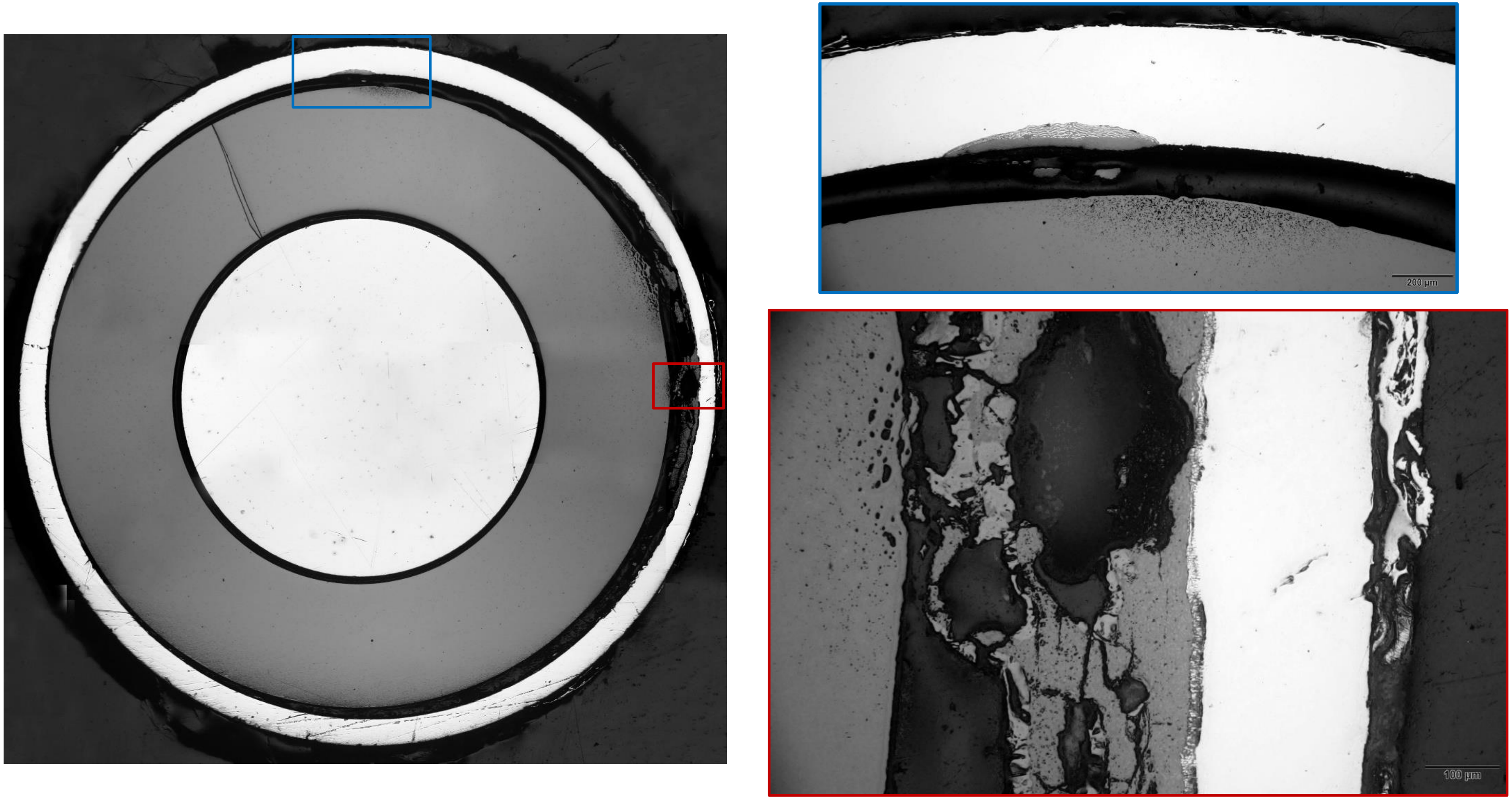

Figure 92 QUENCH-19; metallographic observation of rod 24 at the elevation 850 mm, oxidation of the inner cladding surface, interaction of cladding with pellet

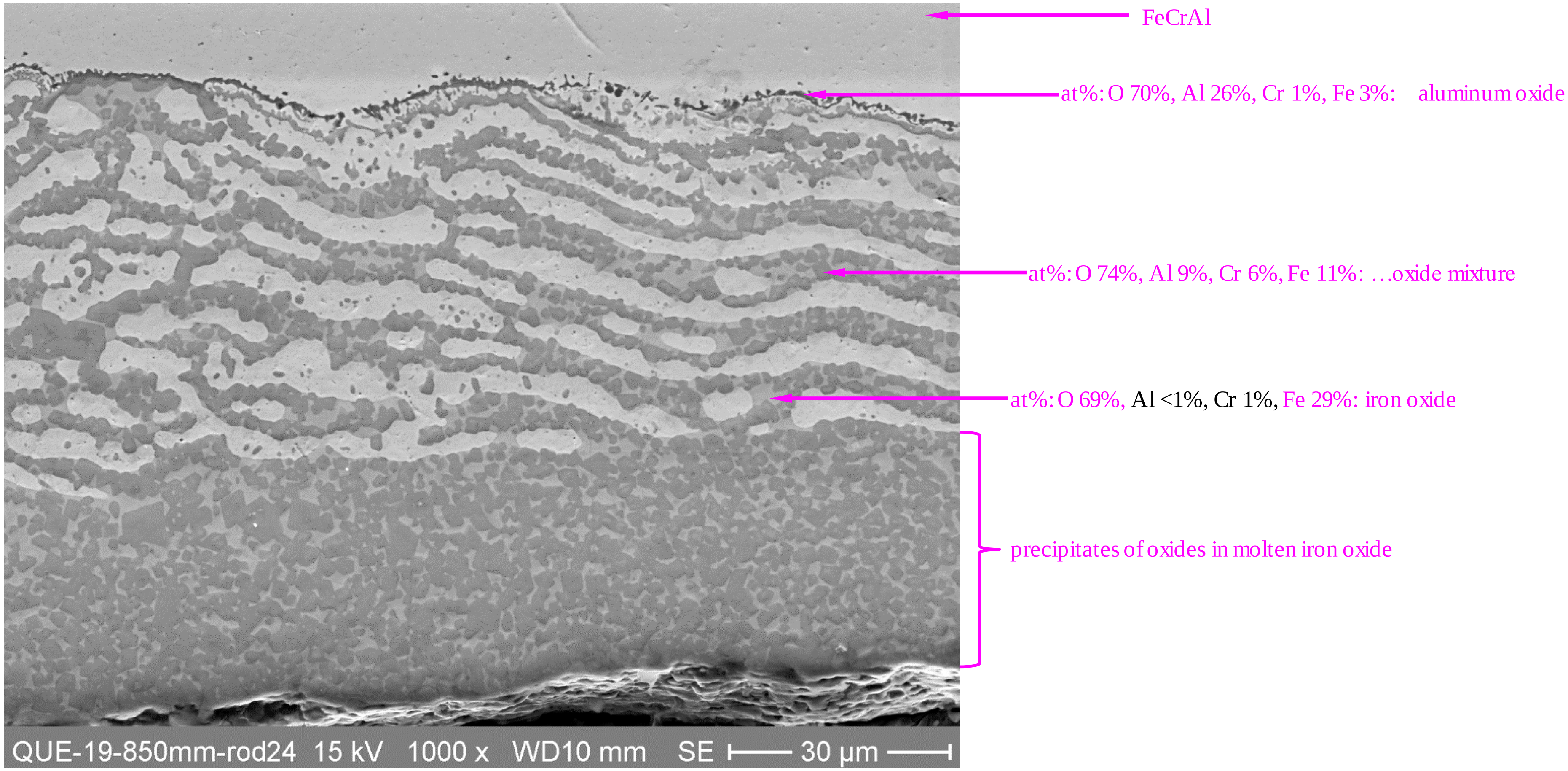

Figure 93 QUENCH-19; multilayer structure of cladding spot (850 mm, rod 24, 0°) at the former contact with pellet: penetration of oxide into cladding from pellet

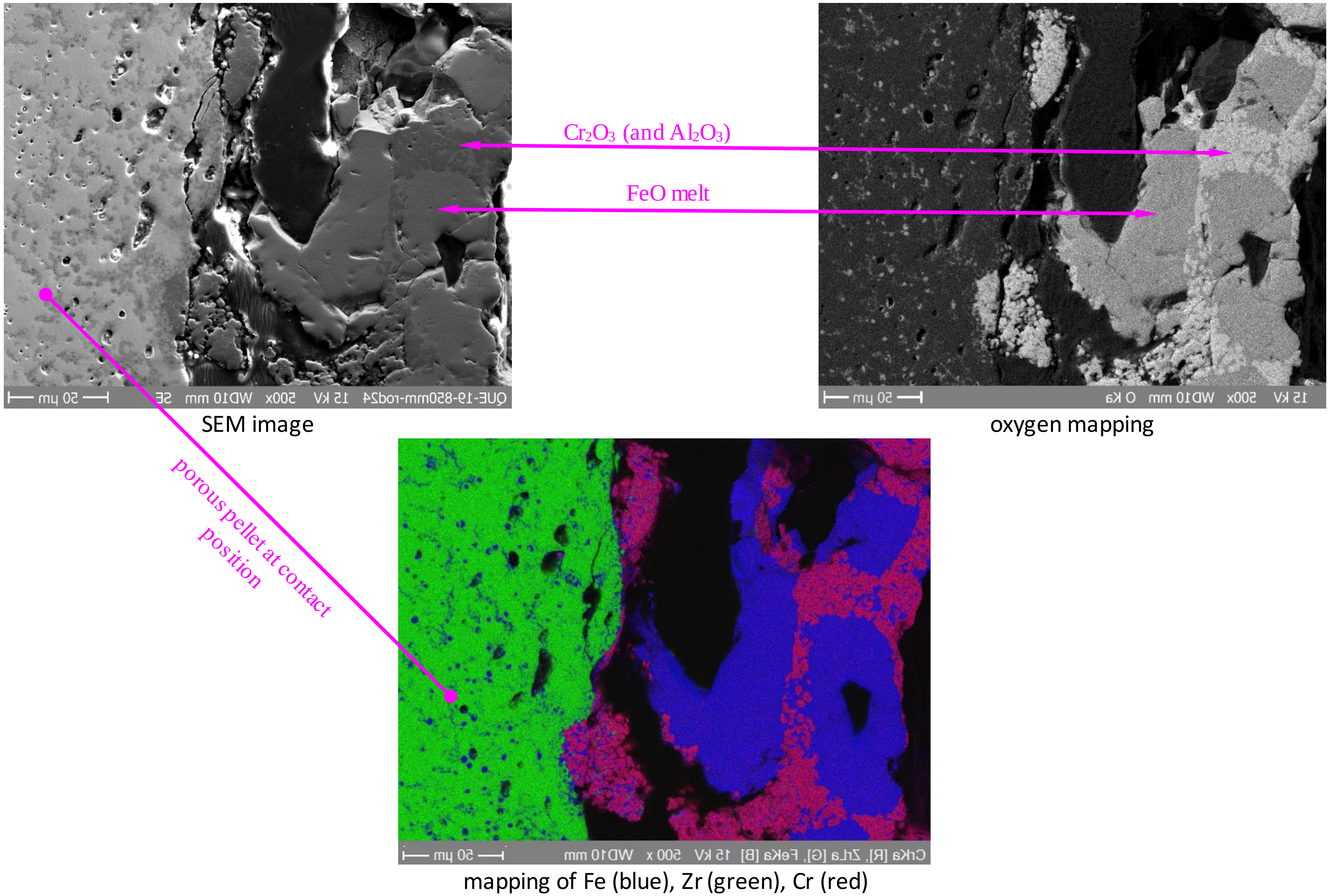

Figure 94 QUENCH-20; interaction of relocated FeCrAl melt with ZrO_2 pellet at 850 mm, (rod 24, 90°), transport of oxygen from pellet to melt

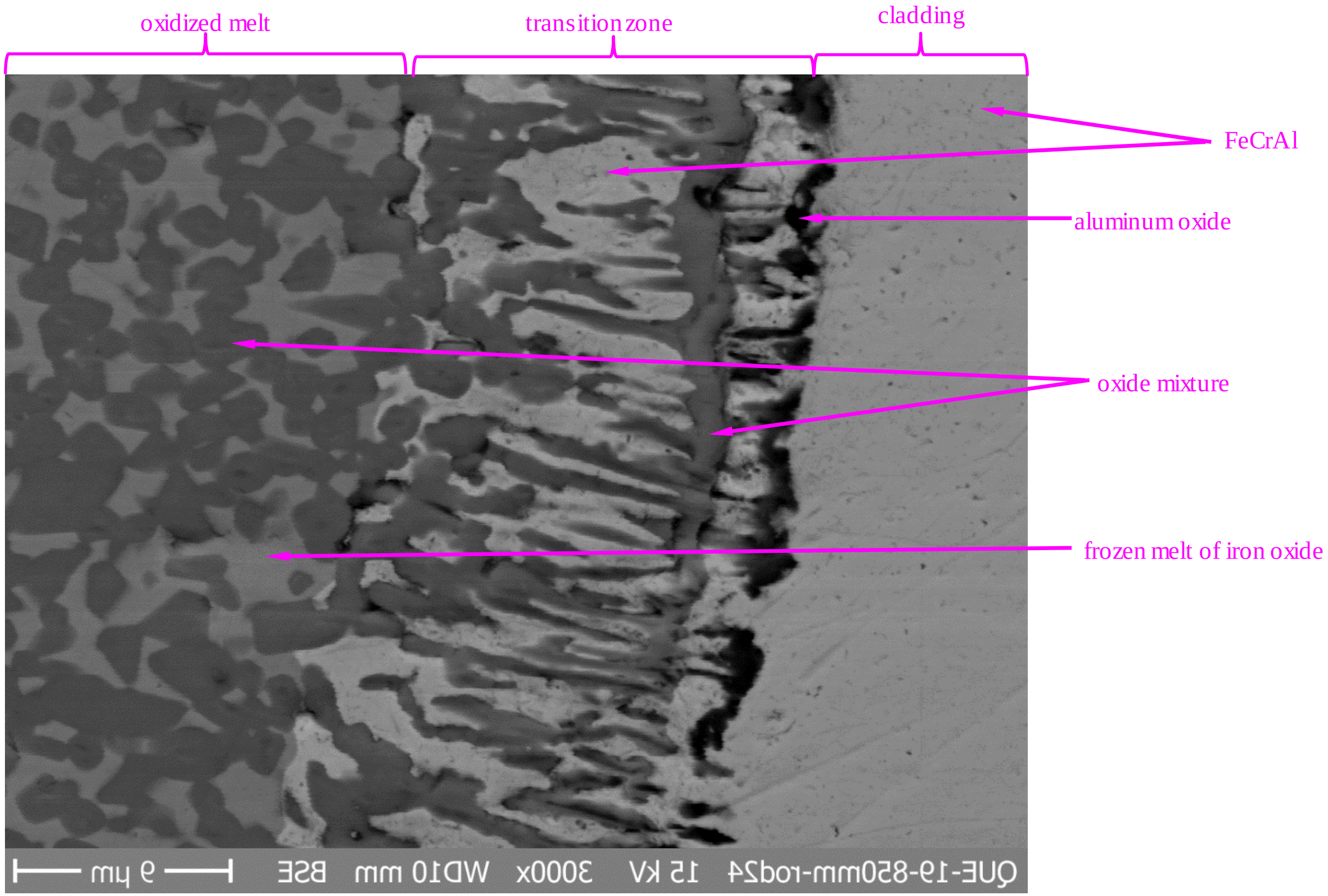

Figure 95 QUENCH-20; interaction of relocated FeCrAl partially oxidized melt with cladding at 850 mm, (rod 24, 90°)

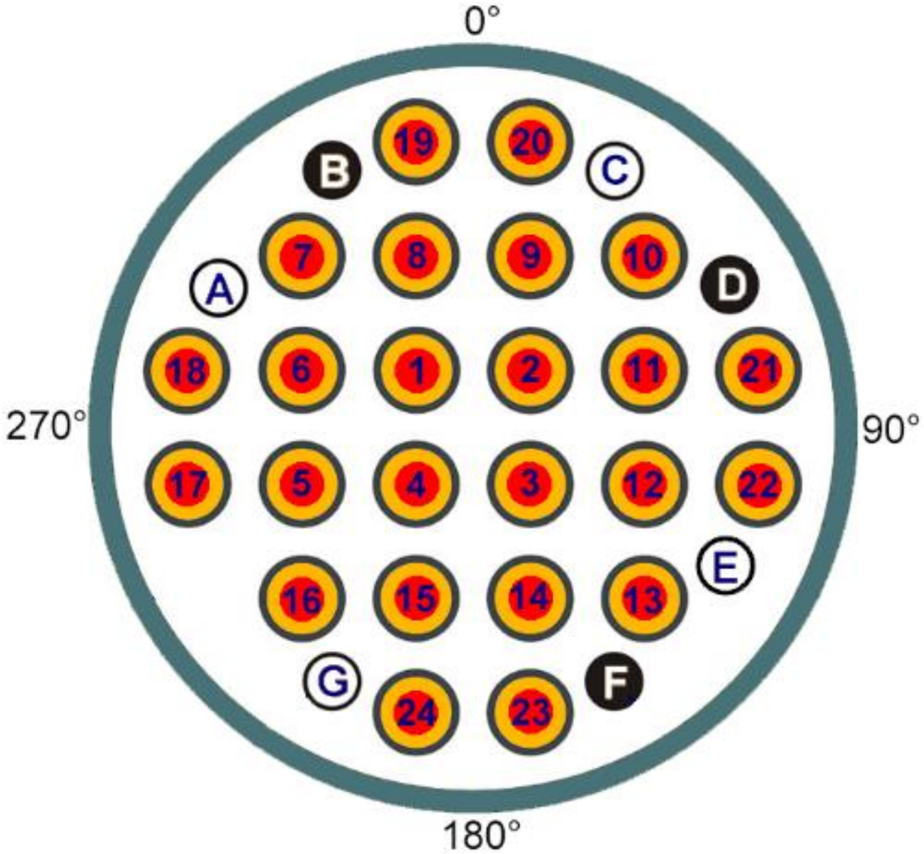

bundle composition, top view

mirrored bottom view of slice **754**-770 mm: dark pellets inside rods 17, 18, 23 with intact claddings and relocated melt; light pellets in all other rods (several rods failed at upper elevations have a local dark spots at the positions of contact to relocated cladding melt)

Figure 96 QUENCH-19; cross section at elevation 750 mm

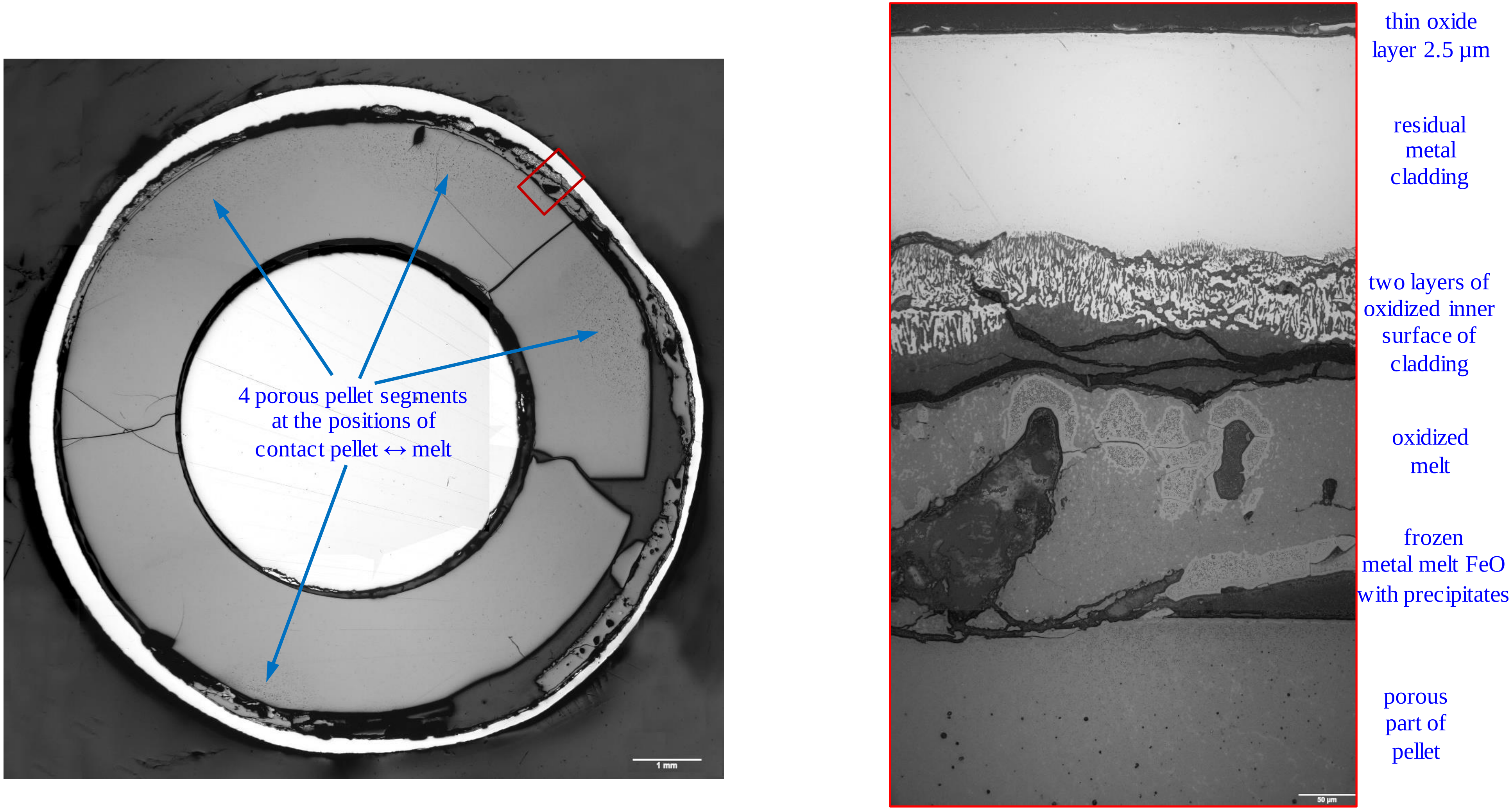

layers at 45°: gap between pellet and residual cladding filled by melt

Figure 97 QUENCH-19; cross section of rod 1 at 750 mm: cladding degradation by melting and oxidation of inner surface

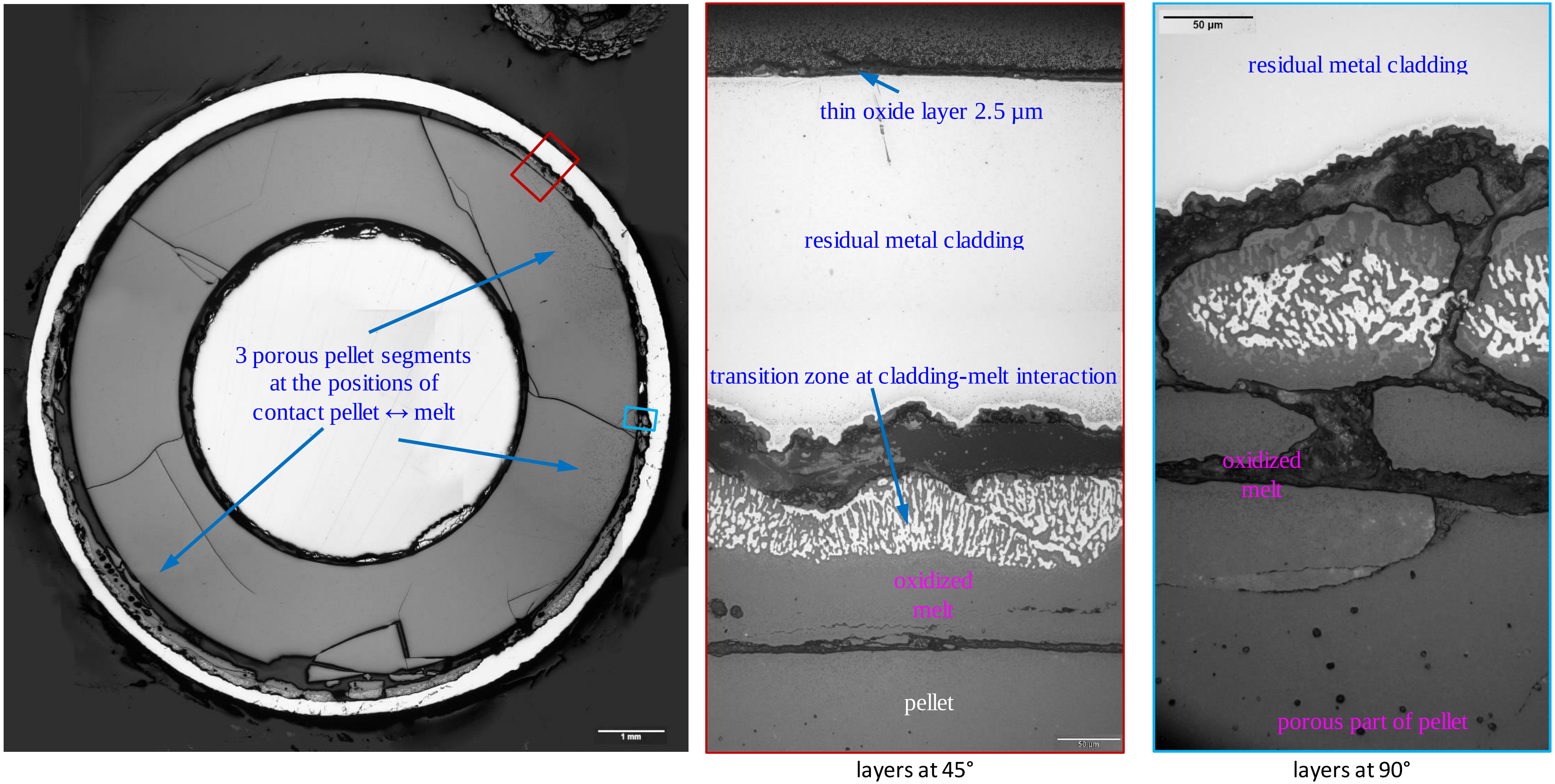

Figure 98 QUENCH-19; cross section of rod 2 at 750 mm: cladding degradation due to interaction with melt relocated from above

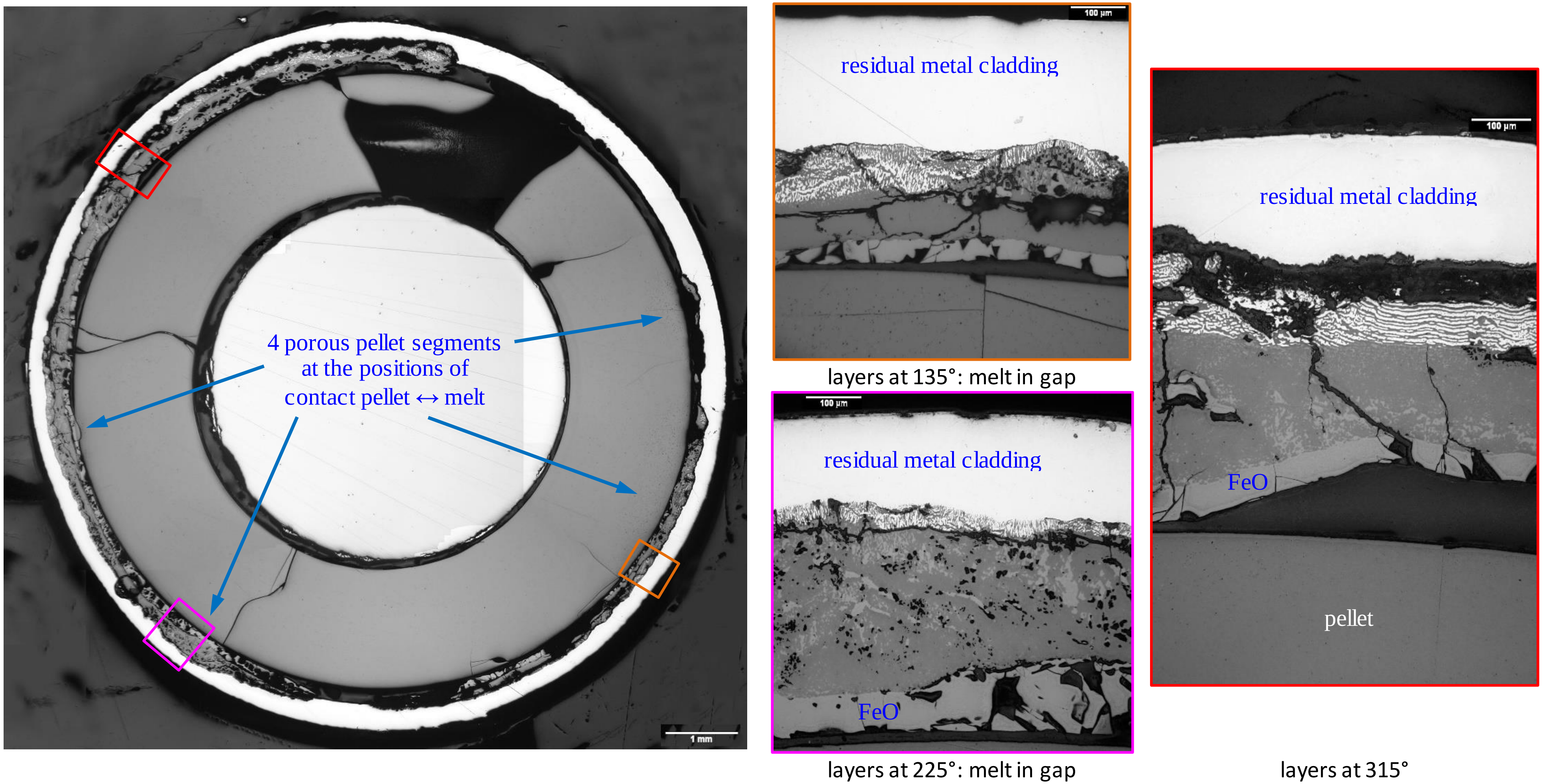

Figure 99 QUENCH-19; cross section of rod 3 at 750 mm: cladding degradation due to interaction with melt relocated from above

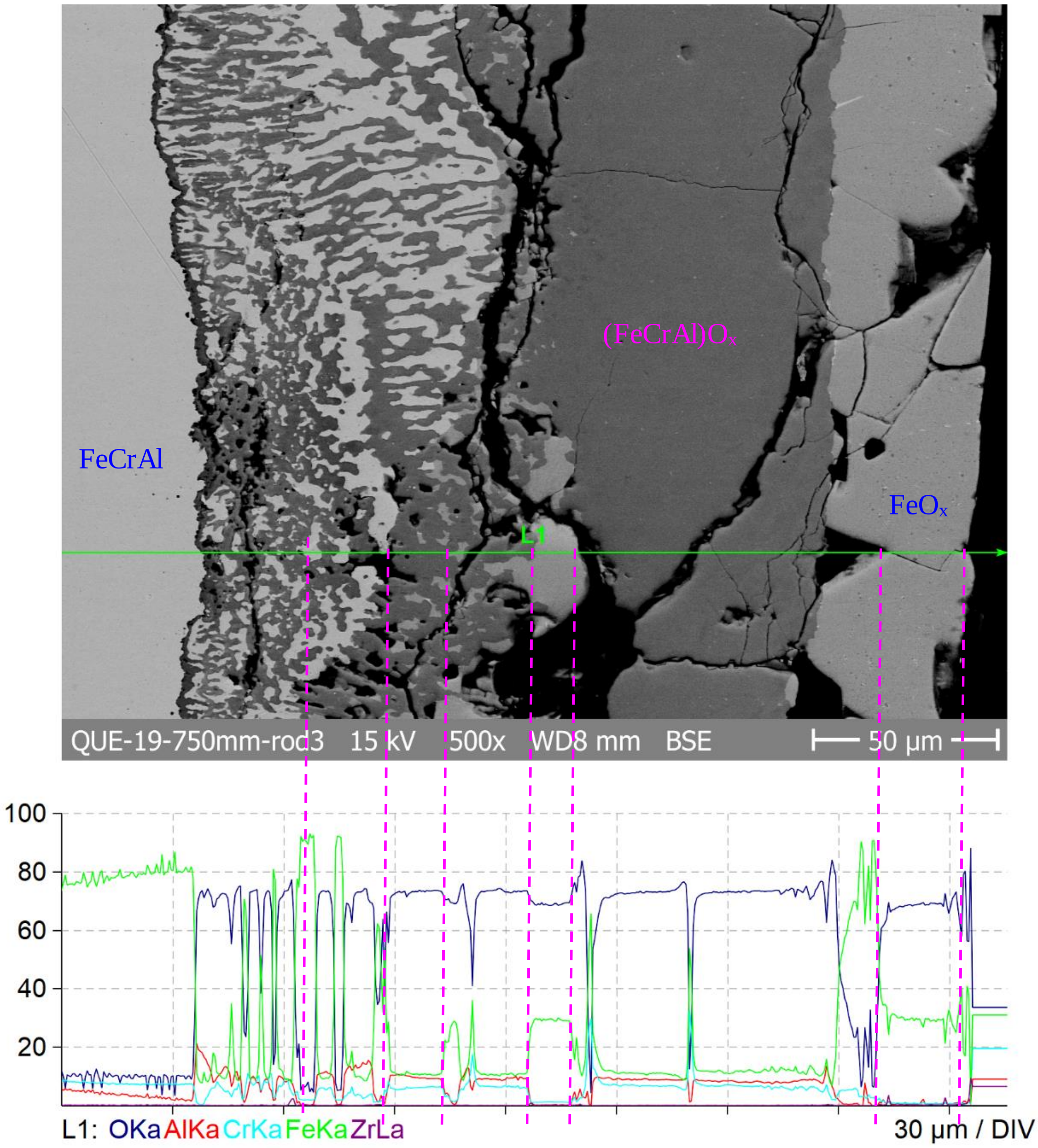

Figure 100 QUENCH-19; cross section of rod 3 at 750 mm, 135°: REM/EDX line scan indication of element distribution (at%)

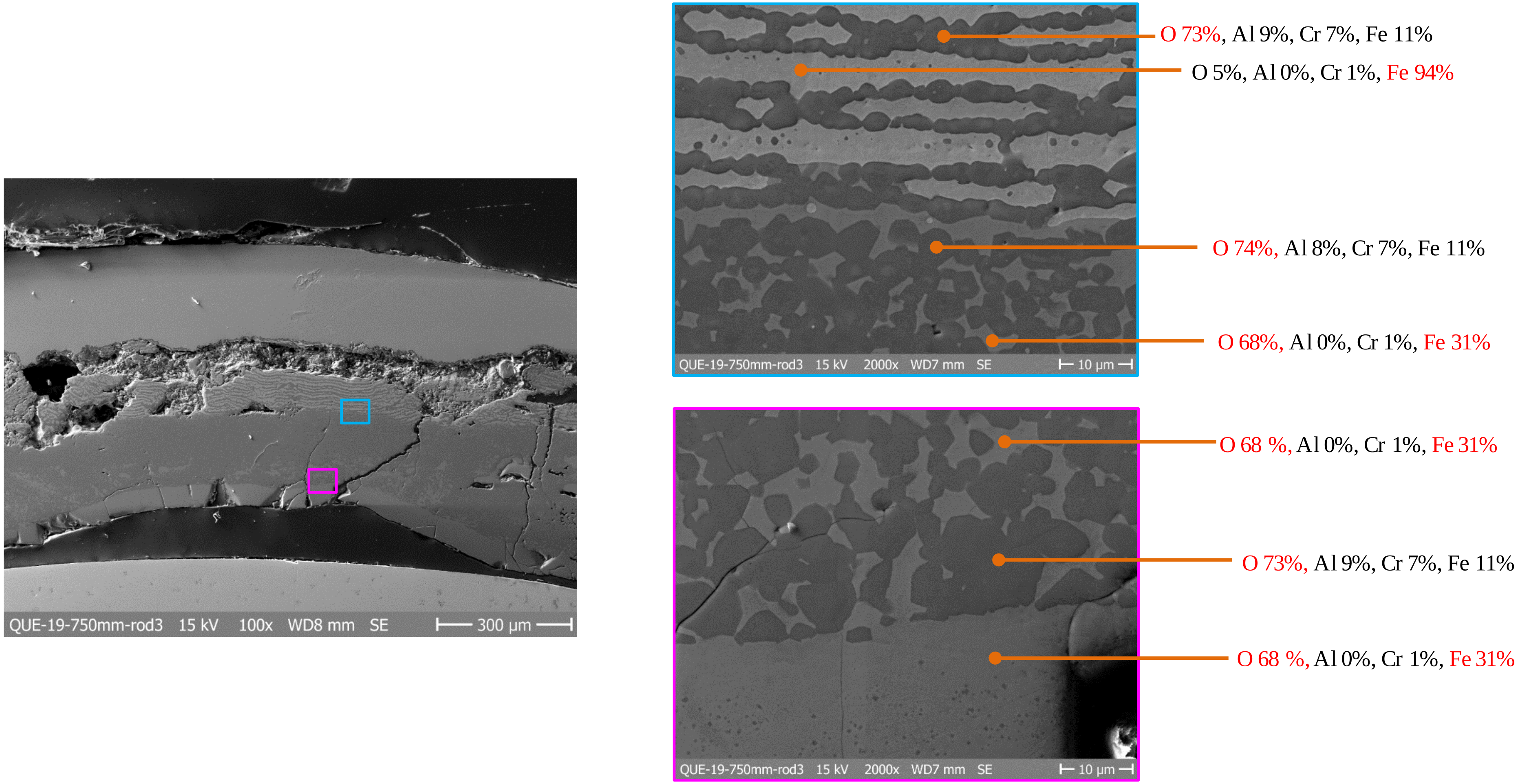

Figure 101 QUENCH-19; cross section of rod 3 at 750 mm, 315°; REM/EDX point analysis of frozen melt (at%): precipitates of (FeCrAl) oxides in FeO_x melt

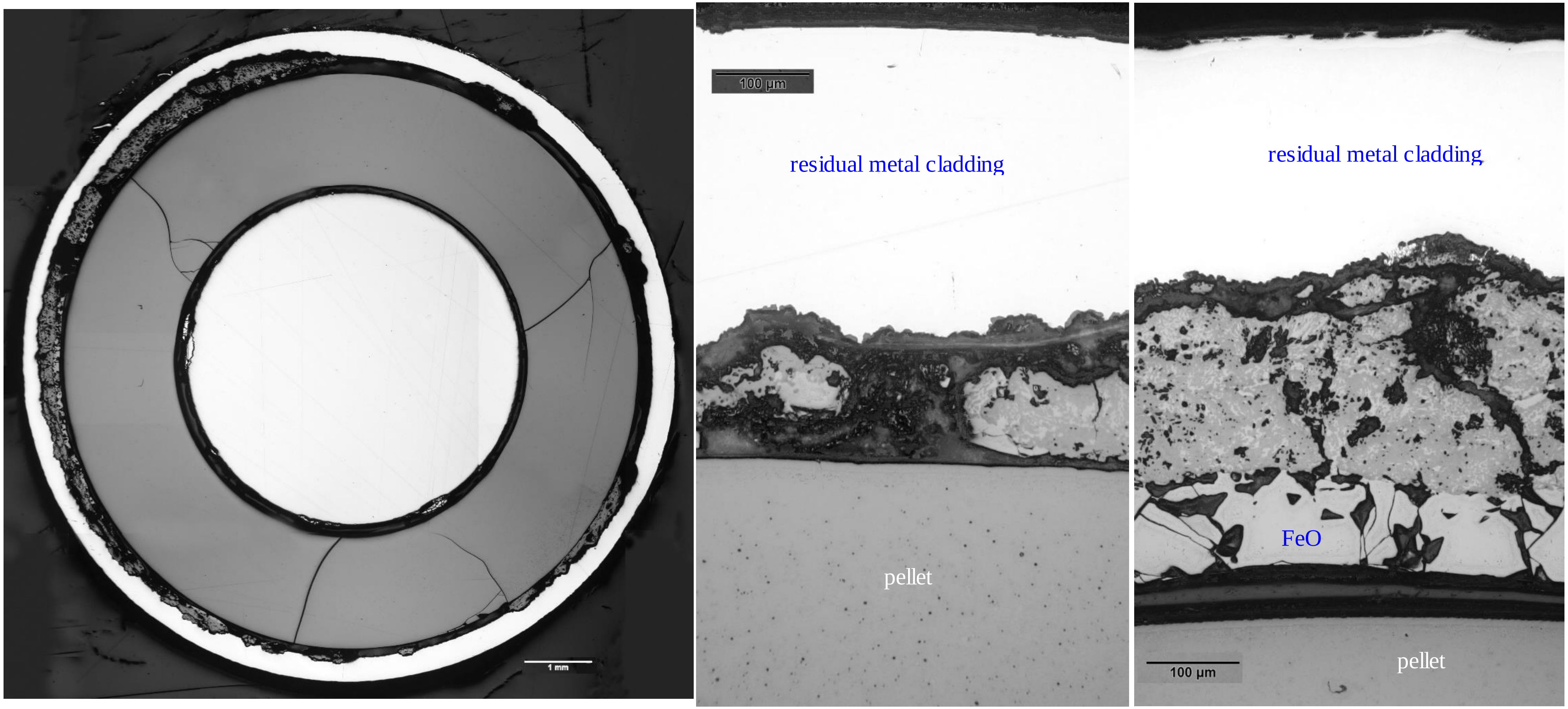

135°: porous pellet at contact to oxidized melt

270°: oxidized melt between residual metal cladding and pellet

Figure 102 QUENCH-19; cross section of rod 9 at 750 mm: cladding degradation due to interaction with melt relocated from above

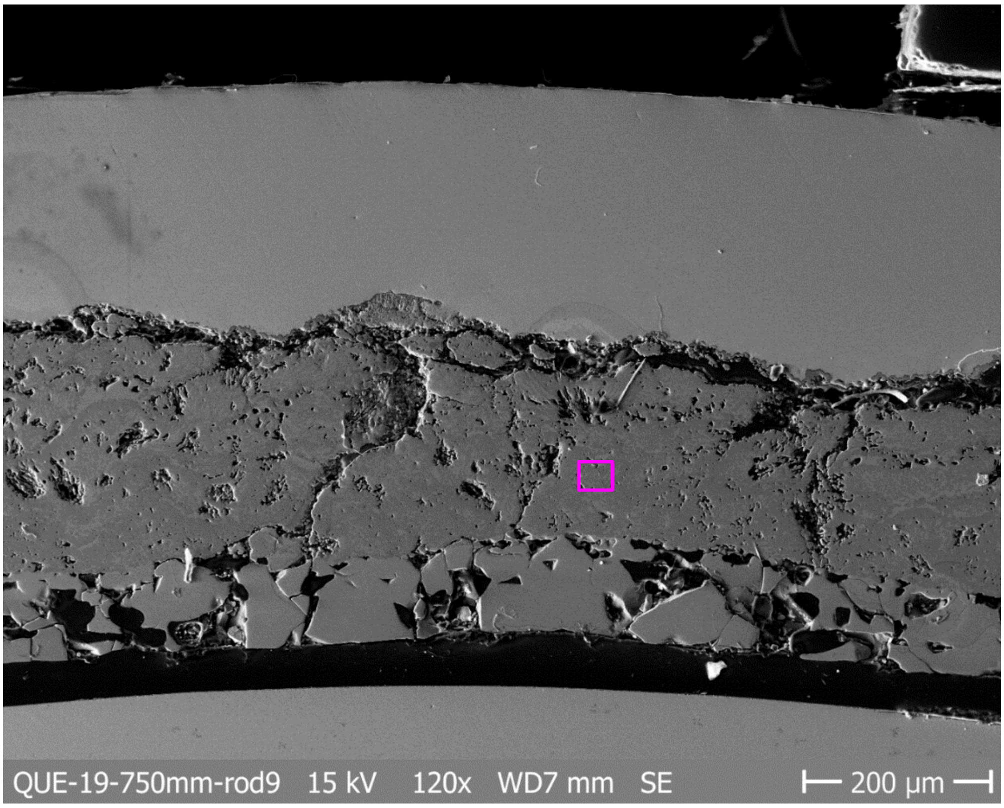

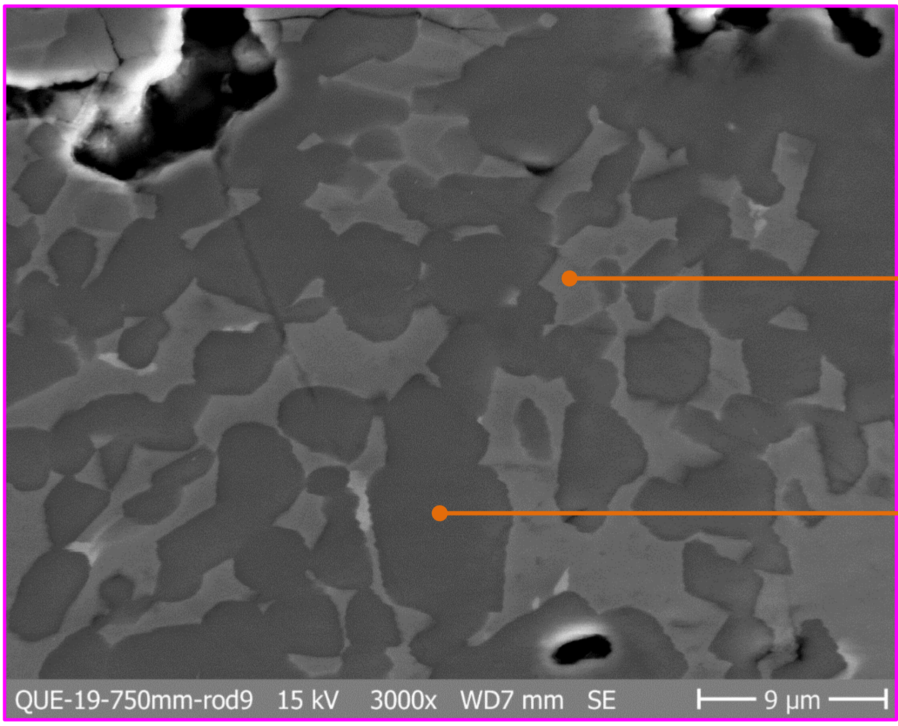

Figure 103 QUENCH-19; cross section of rod 9 at 750 mm, 270°; REM/EDX point analysis of frozen melt (at%): precipitates of (FeCrAl) oxides in FeO_x melt

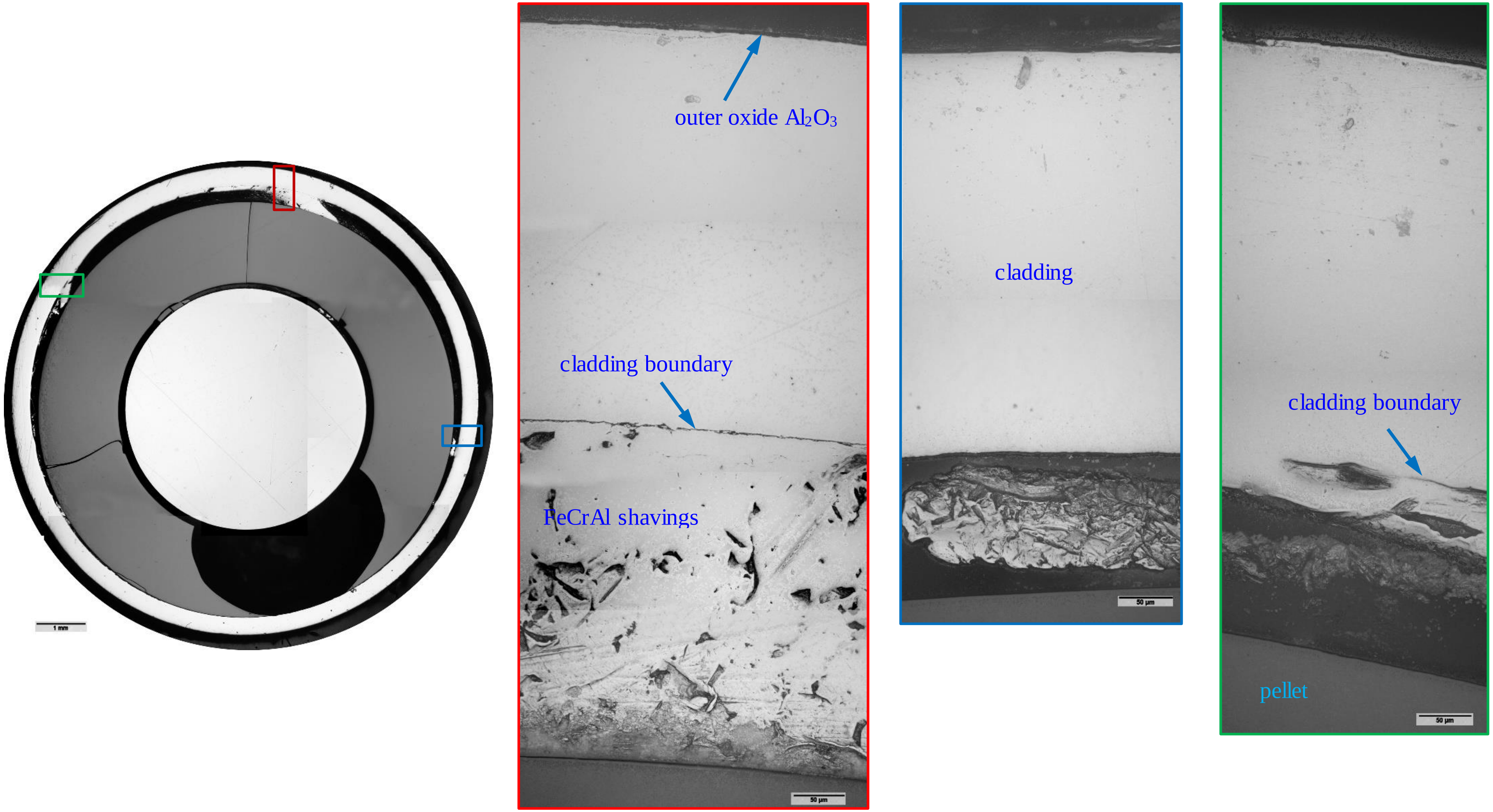

cross section: dark not porous pellet | 10°; outer Al_2O_3 oxide 2 µm | 190° | 290°

Figure 104 QUENCH-19; rod 18 at 750 mm: shavings between cladding and pellet (artefact appeared during the sawing and grinding of "soft" FeCrAl)

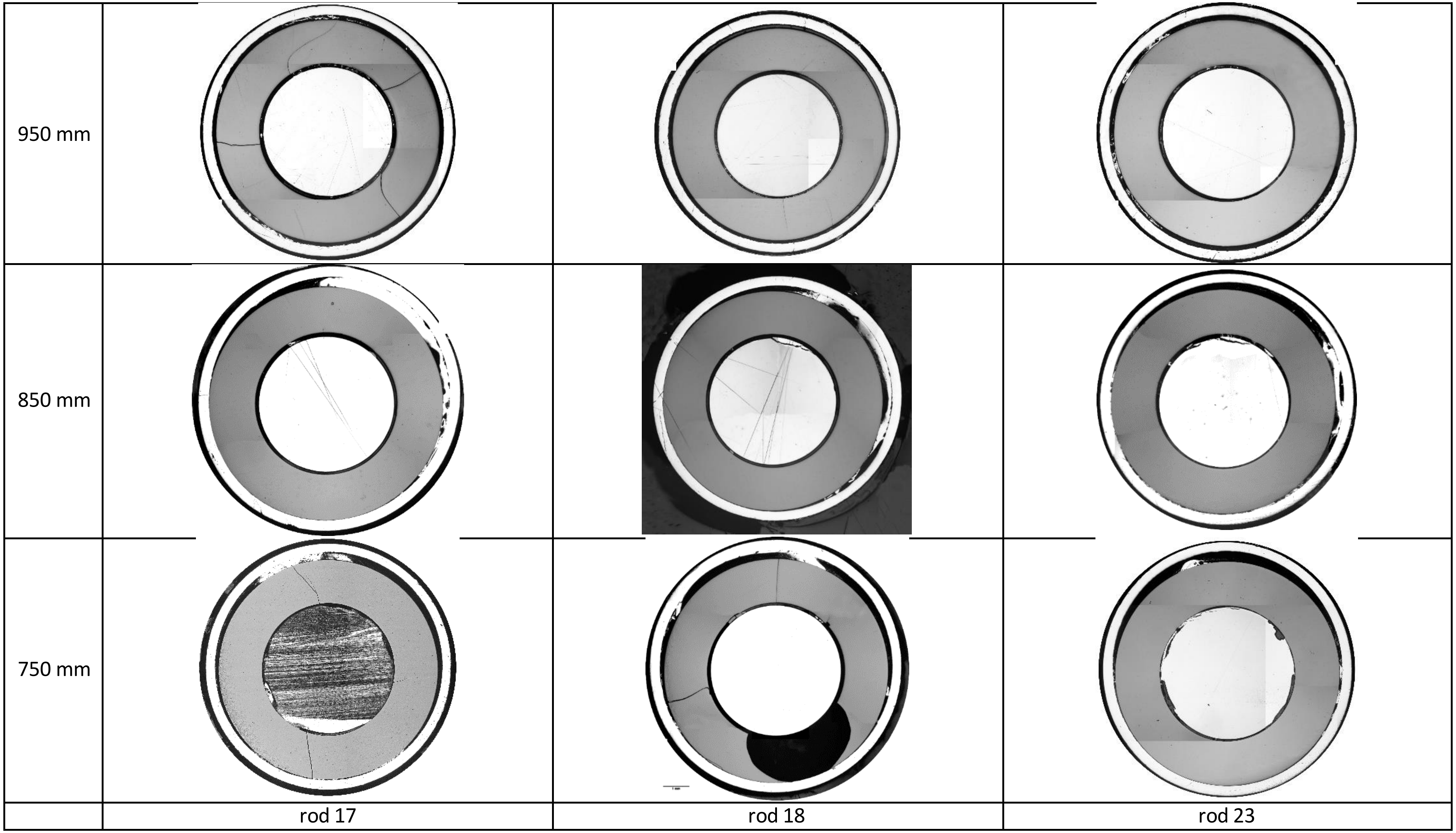

Figure 105 QUENCH-19; shavings in the gap between cladding and pellet of rods 17, 18, and 23 at elevations 950, 850, and 750 mm

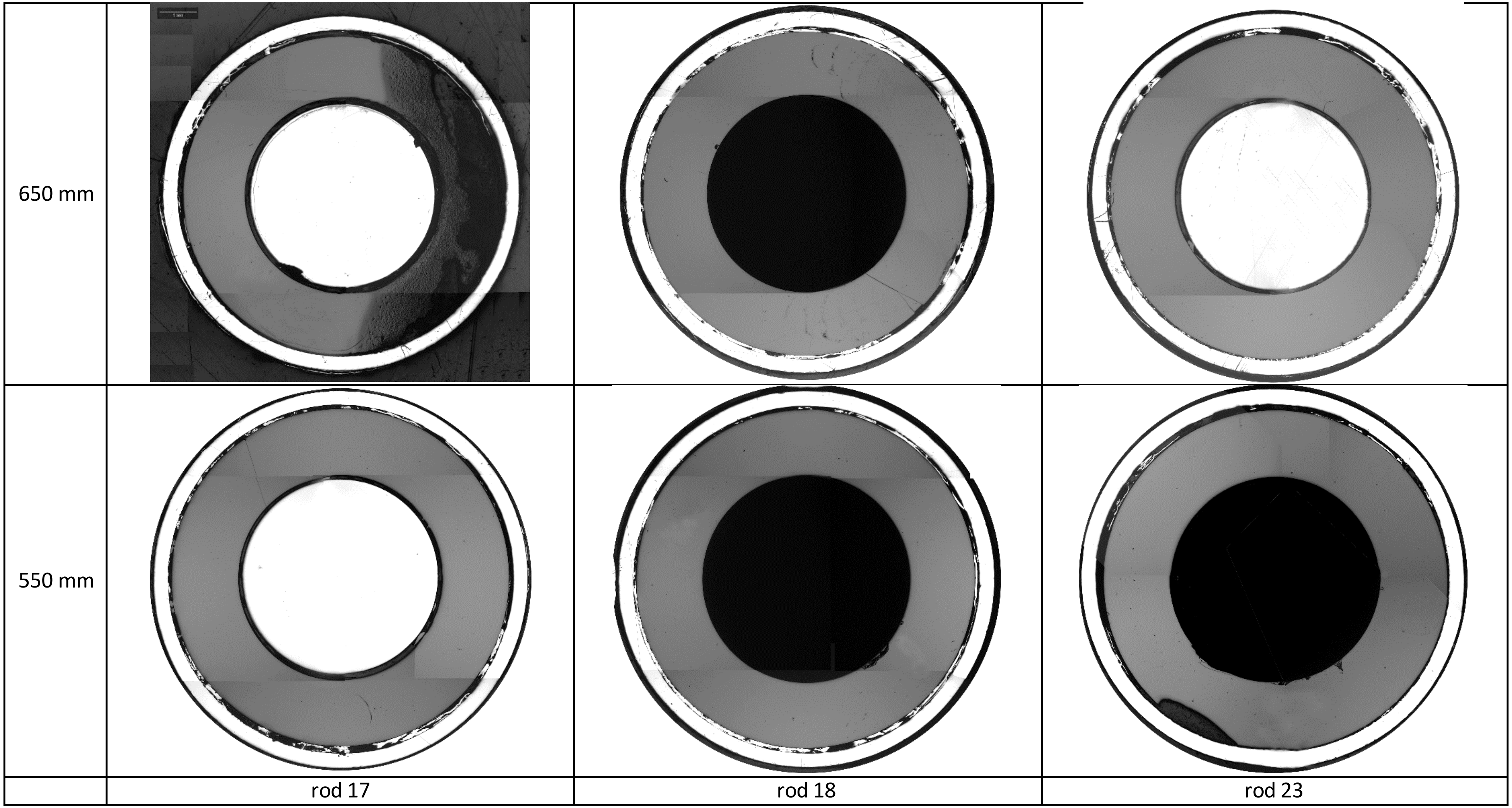

Figure 106 QUENCH-19; shavings in the gap between cladding and pellet of rods 17, 18, and 23 at elevations 650 and 550 mm

The QUENCH-19 test with bundle containing 24 heated rods with B136Y3 cladding tubes and 4 Kanthal AF spacer grids as well as 7 KANTHAL APM corner rods and KANTHAL APM shroud was performed at KIT on August 29, 2018 with similar electrical power history as reference test QUENCH-15 (ZIRLO™ claddings). Non comparable conditions were 1) cooler steam-Ar flow, and 2) moist Ar inside the thermal insulation for QUENCH-19. The QUENCH-19 test was performed in four test stages: 1) pre-oxidation during about 6000 s (similar to QUENCH-15), 2) transient during about 1130 s (similar to QUENCH-15), 3) extended period with constant electrical power of 18.32 kW during 1970 s (to extend the temperature increase stage), 4) test termination by water flooding with rate of 48 g/s (similar to QUENCH-15).

The peak cladding temperatures during the pre-oxidation stage were about 200 K lower in comparison to QUENCH-15. The radial temperature gradient was noticeable larger in comparison to QUENCH-15. The reasons for these test differences could be the different properties of the bundle materials (lower thermal conductivity and higher heat capacity and thermal expansion of FeCrAl) as well as the different boundary conditions (cooler gas flow, humid heat insulation) Compared to QUENCH-15, a much lower heating rate was measured. A temperature of about 1150 °C was reached at the time point as local melting of QUENCH-15 claddings occurred. *No temperature escalation was observed during the extended transient.* Maximum cladding temperature measured before reflood was about 1800 K (extrapolated from measured data at the elevation of 950 mm).

The coping time was about 3200 s (≈1200 s for QUENCH-15). *The conclusion about increased coping time in QUENCH-19 in comparison with the reference test QUENCH-15 is only qualitative*: quantitative assessments for reactor conditions should be made with care due to artificial extension of transient before reflood.

In the axial hottest zone between 800 and 1000 mm, a thin (2-3 µm) protective layer of aluminum oxide formed and remained on the claddings of some peripheral rods. However, in many cases (especially for the inner rods) this layer was destroyed and the claddings were completely oxidized, which is in accordance with results of single effect tests, showing catastrophic oxidation of nuclear grade FeCrAl alloys with lower Cr content already from 1350°C. Many claddings were damaged at elevations between 850 and 1000 mm: 1) by formation of circumferential cracks (probably due to thermal expansion followed by quench shrinkage), 2) by high-temperature inner oxidation in steam, penetrated through the damaged cladding regions, and formation of molten FeO, 3) due to FeCrAl melting and relocation of melt inside the gap between pellet and cladding, 4) due to eutectic interaction of claddings with stainless steel thermocouple sheaths. *The molten FeO penetrated between the grains of the ZrO_2 pellets and dissolved them at their edges. The remaining parts of the pellets became loose and porous due to the penetration of the FeO melt between the grains of the pellets throughout the entire volume of the pellets.* The interaction of the FeO melt with the ZrO_2 pellet is an important degradation effect of the pellet. All four FeCrAl grid spacers were outside the hottest area and remained intact.

A sharp increase of the hydrogen release rate was observed about 800 s before reflooding. The main reasons are the disappearance of the protective layer of aluminum oxide and the melting of the claddings of the inner rods. The maximum hydrogen release rate reached during reflood was 280 mg/s (1830 mg/s for QUENCH-15). The total hydrogen production was 9.2 g (47.6 g for QUENCH-15).